Mechanisms shifting the emission energy of self-assembled quantum dots in nanowires

Thèse N° 9058

LUCA FRANCAVIGLIA

2019

ÉCOLE POLYTECHNIQUE
FÉDÉRALE DE LAUSANNE

To my family.

Acknowledgements

This PhD was not only possible, but also much fun and gratification because I was not alone. I would like to sincerely thank all the people that showed me their professional and human support during these years.

Anna, thank you for your lively presence, already starting with my Master project. Borrowing the words of one of your students from that period (2014!): "you are a successful person who would like to help others to be successful, too". As a PhD student of yours, I learnt a lot in these years. I could benefit from your motivation and supervision, while growing as an independent researcher. You also have the merit of building a team of motivated and friendly people: in the highs and lows of a PhD life, a constant was the pleasure to come to LMSC.

I am thankful to Dr. Paulina Plochocka, Prof. Martino Poggio, Dr. Raphaël Butté, and Prof. Karen Scrivener for the time that they dedicated to my thesis and for providing useful feedback. I thank Martino and his students (Nicola and Davide in particular) also for their warm welcome during a short stay in their lab at the University of Basel. Thank you for the nice discussion and for sharing with me your experience in micromanipulation.

I thank Prof. Richard Warburton for his support and, together with his group members, for the pleasant and fruitful mini-sabbatical in their group. Great thanks to Philipp, for the restless help during my stay: you taught me a lot with fun and brought me some essential results for my thesis.

I acknowledge NCCR QSIT, for funding my PhD and setting the people network that enabled the aforementioned collaborations. Further rewarding collaborations that I would like to acknowledge have been with Martin Hetzl (Walter Schottky Institut) and Nicolas Bologna (EMPA IBM): thank you for making measurements together a nice and fruitful experience that expanded my scientific knowledge and understanding of semiconductors.

My first and main occupation in LMSC was optics. A great deal of what I know still comes from Yannik's teachings. Yannik, thank you for being my first teacher and colleague, who invited me for a glass at SAT already on my first day, when I was a Master student, and for many afterwards. Thank you for your patience during my initial clumsiness with the optical setups and your professional advice in many situations, like during the writing of the book chapter. I think that I had with you some of the most ridiculous laughter ever when coming back home late on the metro! Francesca, thank you for sharing your great experience with Raman. I have nice memories of the time we spent in the same office (two different rooms actually!) and after: thank you for the nice discussion and help to solve some of my organizational doubts, for always taking my opinion into consideration and for sharing yours with me. I had so much

was the first for Elias. Elias, thank you for being a kind colleague and always sharing a sincere smile in the morning. About Raman, now you definitely know more than I do and I hope I could facilitate your start. Your kindness and rigor at the same time and quiet approach to problems always make it a pleasure to discuss with you about science and other topics. Dmitry, thank you for our conversations in Montpellier! Thank you for the discussions about science, I hope I could help in some way about optics and building optical setups! Good luck with your job in Moscow!

Jelena, thank you for your generous presence in LMSC! Thank you for contributing to make the lab a welcoming and friendly place. I also really appreciated the way you valued my time and expertise during our collaborations. And thanks a lot for proposing and taking care of the holidays in Split: they are undoubtedly at the top in the moments of careless happiness during my PhD life! Shahrzad, with you the holidays in Split became even more fun! It was great to have you in the lab and meet again at the summer school in Gstaad and other occasions. Thank you for bringing brightness to all these moments.

Wonjong, I still remember the day of your first and unexpected visit to LMSC! Thank you for performing so much SEM for me; thank you for contributing to a relaxed atmosphere in the office with your smooth sense of humor and for always being a kind colleague also in the busiest moments. I really enjoyed your wedding and wish you and Sol a prosperous life in Switzerland! Mintae, I enjoyed our time together in the office and hope I could help you during your stay. Thank you for your great kindness and flattering comments ("guru") and for the Korean-food dinners. Lucas, thank you very much for being always ready to help, give your opinion and pass by for discussion. Obviously I greatly appreciated sharing advice and impressions about preparing figures for papers and reports! And also non-scientific conversations about movies and art! Thank you for being so generous and for your lively presence in and out of the lab. Akshay, I sincerely appreciated working and discussing with you as well as sharing the same office. You are a thoughtful person and this fact made the conversions with you about different topics always interesting. If I taught you something, that's been a pleasure, at least as much as it's been gratifying to learn from your experience. I wish you a great success for your PhD and Swiss life!

Marco, I still look up to the way you focused on a difficult project and worked hard to obtain something where I had got nothing. Scientific discussion with you was always fruitful: I always discovered some sides of the problem that had not been considered enough. Thank you for sharing tiring working hours with me and for always providing an adult perspective of different topics! Your faceted interests triggered again my curiosity for a plethora of enriching inputs that I had forgot about during a dull period. Thank you for the good time during the many trips and for inviting us in Parma! For sure, I got with you the funniest glass of hot wine ever! Pranit, thank you for your pleasant presence in the lab and beyond. I always appreciated your sincere wonder towards life and your wise approach to some of its challenges. It was fun to have you as a vegetarian buddy in many occasions! Andrea, although you were my student, you were indirectly teaching me a self-confident and resolute approach to problems in research, and maybe life, that I was lacking. I will probably benefit from it in the years to come. Thank you for this and for many insightful questions and discussions. Thank you for

Martine, you may have not realized it, but you had a great importance at the starting of my PhD. Thank you for patiently introducing me to French, a skill that made my life much easier in Lausanne, and for the warm welcome to Switzerland and the Swiss culture. I thank my friends in Italy for welcoming me every time I was back and in spite of my terrible presence (= absence) on any social media. In particular, I thank Marty for finding the time to meet with me when I am back; Massi, thank you for your unconditional friendship and support that, I know, you would give me whenever I may need it. Thanks to Roby, Andrea, Stefano, Elia e Davide for meeting every year and sharing our work and PhD experiences abroad and in Italy. Grazie a Fatmir, Rita e Hasan per la calorosa accoglienza che mi danno ad ogni mio ritorno, facendomi ogni volta sentire a casa. Mamma, papà, Marsi: grazie per essere stati al mio fianco, avermi sostenuto e incoraggiato sempre durante questi anni. Vi devo molto di quanto ho raggiunto e della serenità con cui questo si è realizzato.

Lausanne, 11 January 2019   L. F.

Abstract

This thesis is dedicated to the engineering of the emission energy of quantum dots embedded in core-shell GaAs-AlGaAs nanowires. The goal is to redshift the quantum-dot emission energy in resonance with a gas of Rb atoms.

Segregation processes on the nanowire surface account for the formation of the quantum dots as Ga-rich nanoclusters that behave as optically active single-photon emitters. The study presented in this thesis shows ways to enhance the control on the composition of semiconductor alloys, in order to form homogeneous compounds or to direct segregation and diffusion phenomena at the atomic scale.

The first part of this thesis elucidates the role of crystal defects, namely rotational twins in the nanowire structure, in tuning the diffusion-driven quantum-dot formation. The combination of high-resolution cathodoluminescence and transmission electron microscopy evidences that the quantum-dot occurrence increases in presence of crystal defects, while the quantum-dot emission energy decreases. Simulations of the emission energy of quantum dots crossed by crystal defects as well as the twin-driven adatom-diffusion dynamics on the nanowire surface account for the observed correlation. The control on the occurrence of crystal defects in the nanowires turns into an important parameter to master the composition and light emission of the nanowire shell.

The second part of this work describes two mechanisms used to redshift the quantum-dot emission energy to match the D2 emission line of Rb. By the first mechanism, a silicon-oxide coating deposited on the nanowires applies tensile stress to the embedded quantum dots and redshifts their emission-energy distributions by more than 100 meV. The anisotropy of the strain is evinced from Raman-spectroscopy measurements and correlated with the oxide microstructure. The application range of this simple, yet effective, straining device is expanded by testing further materials and deposition techniques.

The second redshifting mechanism consists in alloying the nanowire shell with indium to form a quaternary AlGaInAs shell. This mechanism redshifts the quantum-dot emission-energy distributions by about 300 meV. The spatially-resolved compositional analysis of the nanowire cross sections reveals that Ga, Al, and In segregate in the quaternary alloy according to a facet- and polarity-driven 3-fold symmetry. Wedge-shaped In-rich segregates, not observed before, form as the result of the competitive diffusion of the group-III adatoms on the nanowire facets. Preliminary measurements on the optical coupling between quantum dots and Rb demonstrate the achievement of the target emission energy, which is the first fundamental step towards the integration of these single-photon emitters into a quantum network.

Abstract

Résumé

Cette thèse est dédiée au contrôle de l'énergie d'émission de boîtes quantiques incorporées dans des nanofils coeur-coquille de GaAs-AlGaAs. L'objectif de cette thèse est de baisser l'énergie d'émission des boîtes quantiques jusqu'à la résonance avec un gaz d'atomes de Rb.

Des procédés de ségrégation à la surface des nanofils expliquent la formation de boîtes quantiques comme des nano-agglomérats riches en gallium, qui sont actifs au niveau optique et ont des propriétés d'émetteurs de photons uniques. L'étude exposée dans cette thèse montre des stratégies utiles au contrôle de la composition d'alliages de semi-conducteurs, lesquelles servent à former des mélanges homogènes ou à diriger les phénomènes de ségrégation et de diffusion à l'échelle atomique.

La première partie de cet écrit clarifie le rôle des défauts cristallins, tels que les macles par rotation dans la structure des nanofils, dans le réglage de la diffusion de surface qui guide la formation des boîtes quantiques. La combinaison de cathodoluminescence et de microscopie électronique en transmission à haute résolution démontre que le nombre de boîtes quantiques est augmentée par la présence de défauts cristallins tandis que leur énergie d'émission diminue. Les simulations de l'énergie d'émission des boîtes quantiques traversées par des défauts cristallins ainsi que la dynamique de diffusion des adatomes sur la surface des nanofils en fonction des macles expliquent la corrélation observée expérimentalement. Le contrôle de la présence des défauts cristallins dans les nanofils est donc un important paramètre pour maîtriser la composition et l'émission lumineuse de la coquille d'AlGaAs des nanofils.

La deuxième partie de cet exposé décrit deux mécanismes utilisés pour baisser l'énergie d'émission des boîtes quantiques jusqu'à s'accorder avec la ligne d'émission D2 du Rb. Dans le premier mécanisme, une couche d'oxyde de silicium, déposée sur les nanofils, exerce une contrainte de traction aux boîtes quantiques incorporées dans les nanofils et baisse leur distribution d'énergie d'émission de plus de 100 meV. L'anisotropie de la déformation est déduite de mesures de spectroscopie Raman et corrélée avec la microstructure de l'oxyde. La gamme d'applications de ce dispositif simple, mais efficace, est étendue par la caractérisation de matériaux et méthodes de déposition supplémentaires.

Le deuxième mécanisme de décalage vers le rouge repose sur l'ajout d'indium dans la coquille des nanofils pour former un alliage quaternaire d'AlGaInAs. Ce mécanisme baisse d'environ 300 meV la distribution d'énergie d'émission des boîtes quantiques. L'analyse de la composition des sections transversales des nanofils, résolue spatialement, révèle que Ga, Al et In se séparent dans l'alliage quaternaire en suivant une symétrie de rotation ternaire, fonction des facettes et de la polarité de la surface du nanofil. De nouvelles typologies de ségrégation en

forme de coin et riches en indium résultent de la compétition entre les adatomes du groupe III pendant la diffusion de surface sur les facettes du nanofil.

Des mesures préliminaires du couplage optique entre les boîtes quantiques et le Rb démontrent l'obtention de l'énergie d'émission souhaitée, un pas essentiel vers l'intégration de ces émetteurs de photons uniques dans un réseau quantique.

Mots-clefs : nanofils · boîtes quantiques · semiconducteurs III-V · émetteurs de photons uniques · déformations élastiques · ségrégation d'alliages · cathodoluminescence · photoluminescence · spectroscopie Raman · microscopie électronique en transmission

Riassunto

Questa tesi è dedicata al controllo dell'energia di emissione di punti quantici incorporati in nanofili coassiali di GaAs rivestiti di AlGaAs. L'obiettivo è ottenere il redshift dell'energia di emissione dei punti quantici fino alla risonanza con un gas di atomi di Rb.

Processi di segregazione sulla superficie dei nanofili determinano la formazione dei punti quantici come nano-agglomerati ricchi di gallio, i quali mostrano attività ottica e si comportano come emettitori a singolo fotone. Lo studio presentato in questa tesi individua strategie utili al controllo della composizione di leghe di semiconduttori, le quali servono a formare composti omogenei o a dirigere i processi di segregazione e diffusione su scala atomica.

La prima parte di questa tesi chiarisce il ruolo di difetti cristallini, quali twin di rotazione della struttura dei nanofili, nel regolare la diffusione superficiale che guida la formazione dei punti quantici. La combinazione di catodoluminescenza e microscopia elettronica a trasmissione ad alta risoluzione prova che l'osservazione dei punti quantici aumenta in presenza dei difetti cristallini, mentre decresce la loro energia di emissione. Simulazioni dell'energia di emissione dei punti quantici attraversati da difetti cristallini, nonché la dinamica di diffusione degli adatomi sulla superficie dei nanofili legata ai twin, rendono conto della correlazione osservata sperimentalmente. Il controllo della presenza di difetti cristallini nei nanofili si rivela un importante parametro per padroneggiare la composizione e l'emissione luminosa del rivestimento di AlGaAs dei nanofili.

La seconda parte di questo lavoro descrive due meccanismi usati per abbassare l'energia di emissione dei punti quantici fino a coincidere con la linea di emissione D2 del Rb. Mediante il primo meccanismo, un rivestimento di ossido di silicio, depositato sui nanofili, applica uno sforzo di trazione ai punti quantici incorporati nei nanofili e ne abbassa le distribuzioni di energia di emissione di oltre 100 meV. L'anisotropia della deformazione è dedotta da misure di spettroscopia Raman e correlata con la microstruttura dell'ossido. La gamma di applicazioni di questo semplice, ma efficace, dispositivo è ampliata dall'esame di ulteriori materiali e metodi di deposizione.

Il secondo meccanismo di redhsift consiste nell'aggiunta di indio nel rivestimento dei nanofili per formare una lega quaternaria di AlGaInAs. Questo meccanismo abbassa di circa 300 meV le distribuzioni di energia di emissione dei punti quantici. L'analisi della composizione delle sezioni trasversali dei nanofili risolta spazialmente rivela che Ga, Al e In si separano nella lega quaternaria seguendo una simmetria di rotazione tripartita, funzione della facce e della polarità della superficie del nanofilo. Nuove tipologie di segregazione a forma di cuneo e ricche di indio risultano dalla competizione tra gli adatomi del gruppo III durante la diffusione

superficale sulle facce del nanofilo.

Misure preliminari dell'accoppiamento ottico tra punti quantici e Rb dimonstrano il raggiungimento dell'energia di emissione prefissata, passo essenziale per l'integrazione di questi emettitori a singolo fotone in una rete quantica.

Parole chiave: nanofili · punti quantici · semiconduttori III-V · emettitori a singolo fotone · deformazioni elastiche · segregazione delle leghe · catodoluminescenza · fotoluminescenza · spettroscopia Raman · microscopia elettronica a trasmissione

Contents

Contents

List of Figures

Acronyms

APT Atom probe tomography

BEP Beam equivalent pressure

BF Bright field

CB Conduction band

CL Cathodoluminescence

CX Charged exciton

EDX Energy dispersive X-ray spectroscopy

EELS Electron energy loss spectroscopy

FCC Face centered cubic

FFT Fast Fourier transform

FIB Focused ion beam

FSS Fine structure splitting

HAADF High angular annular dark field

HH Heavy hole

HRTEM High-resolution transmission electron microscopy

LH Light hole

LHe Liquid helium

LO Longitudinal optical

MBE Molecular beam epitaxy

MOCVD Metal-organic chemical vapor deposition

NA Numerical aperture

NIR Near infrared

NW Nanowire

PECVD Plasma enhanced chemical vapor deposition

PL Photoluminescence

QD Quantum dot

QW Quantum well

SAE Selective area epitaxy

SAED Selected area electron diffraction

SAG Selective area growth

SDD Silicon drift detector

SEM Scanning electron microscope

SOFI Super-resolution optical fluctuation imaging

SP Single photon

SPAD Single-photon avalanche diode

STED Stimulated emission depletion microscopy

(S)TEM (Scanning) transmission electron microscope

TO Transversal optical

UHV Ultra-high vacuum

UV Ultraviolet

VB Valence band

VLS Vapor-liquid-solid

WZ Wurtzite

X Exciton

XRF X-ray fluorescence

XX Biexciton

ZB Zinc-blende

1 Introduction and motivation

Semiconductors establish health and prosperity in our lives: the access to clean electricity, efficient lighting, smart energy consumption and the Internet relies on the steady progress in the understanding and manufacturing of semiconductors. In the wide panorama of semiconductor materials, silicon has a pivotal role thanks to its abundance and low cost as well as the deep comprehension and wide control achieved on its properties.

III-V semiconductors, such as GaAs, AlGaAs, and InGaAs, outperform silicon at least in two aspects: higher carrier mobility and brighter light emission. The combination of silicon with III-V semiconductors is thus appealing to fabricate low-cost and high-performance devices for, e.g. light emission. Yet, the on-chip integration of the two is not straightforward; in particular, the mismatch in lattice constant and polarity hinders the epitaxial growth of one class of semiconductor on the other. Nanostructures tackled this challenge: for instance, the epitaxial growth of GaAs elongated nano-crystals, i.e. nanowires (NWs), on silicon is demonstrated by several growth methods [1, 2, 3, 4, 5] and is reaching a mainstream level nowadays .

In addition to enabling the fundamental integration of direct-bandgap semiconductors with silicon, NWs are a versatile platform to study novel semiconductor properties and to fabricate solid-state devices with wider or improved functionalities. NWs demonstrate an unprecedented elastic response to external stress: thanks to their high surface-to-volume ratio, NWs stand impressively high strain before plastic relaxation takes place [6]. This property makes strain-tuning a highly desirable mechanism to modify the bandgap of a semiconductor in the NW form [7]. For similar reasons, the integration of highly mismatched alloys is facilitated in NW heterostructures [8]. An original NW property is to induce the growth of III-V semiconductors in crystal phases, like wurtzite (WZ), different from the zinc-blende (ZB) phase found in the bulk under normal growth conditions [9]. By the control over the formation of different phases (polytypism), homostructures are demonstrated on the NW axis. The band alignment between the two phases may localize the semiconductor charge carriers; if the size of the segments of different phases is shorter than the charge-carrier de Broglie wavelength, they undergo quantum confinement. Such a homostructure is a crystal-phase quantum dot (QD) [10] that would be virtually impossible to achieve in the bulk. Not limited to homostructures,

QDs are embedded in NWs also as heterostructures of different materials in several forms, e.g. along the NW longitudinal axis or on the NW sidewalls [11, 12, 13, 14]. QDs as light emitters embedded in NWs can take advantage of improved functionalities with respect to the bulk. NWs of engineered photonic design overcome one of the main limitations in planar light-emitting diodes (LEDs): the reduced light outcoupling due to total internal reflection. NWs can act as waveguides that enhance the transmission of light outside the NW [15] and increase the brightness of embedded quantum emitters by broadband coupling with the NW waveguiding modes [16]. By further engineering the NW tip geometry, the intensity of the light emitted by an embedded QD can be tuned to an ideal Gaussian profile for the optimal collection by commercial optics [17].

Inside a QD, quantum confinement has a profound impact on the semiconductor electronic bands and density of states: charge carriers can only have discrete energies, the manipulation of which is achieved through the engineering of the size and composition of the solid-state QD. Thanks to their peculiar electronic structure, QDs have found application into lasers, LEDs, and photovoltaic panels as well as into fundamental research on quantum mechanics.

As light emitters, QDs are envisioned as the future source of single and entangled photons that are required in certain quantum-technology implementations [18]. Quantum technologies revolve around the manipulation of matter according to the laws of quantum mechanics. For instance, a quantum computer processes a superposition of quantum states as input in order to speed up algorithms that involve the analysis of many cases in parallel. This capacity promises to revolutionize some specific problems, such as factoring large numbers, searching extensive datasets and simulating complex physical systems. By analogy with classical computing, the fundamental information unit in quantum computing is called qubit. Although the distribution of quantum computers into the market is still at a seminal stage, few-qubit quantum computers are currently sold or available to academic and industry users. For instance, IBM has demonstrated 20-qubit and 16-qubit computers that, through cloud-based platforms, are available to its clients and to the public respectively [19]. Concomitantly, the governments invest in quantum research for competitive health, security and energy applications. The European Union has supported quantum research with a cumulative investment of €550 million over the past 20 years [20] and, in the frame of the program for Future Emerging Technologies, will dedicate further funding for €1 billion to enable the transition of quantum technologies from the research level to the market [21, 20]. The goals are ambitious: in the Strategic Research Agenda of the European Union on quantum technologies, quantum computing is predicted to outperform classical computing within the next 10 years [20].

The realistic implementation of quantum technologies relies on the interconnection of several components that define the nodes of a so-called quantum network. For instance, quantum cryptography relies on the distribution of a quantum key between two physically distant actors, while quantum computers can connect and cluster together: a sort of quantum Internet is also foreseen to operate over long distances exceeding 1000 km [20]. So-called flying qubits carry the information between the nodes of a quantum network. Single photons (SPs) are

envisioned as the physical carriers of flying qubits, with QDs as the ideal source. Over long transmission lines, quantum communication would benefit from brighter sources. With this regard, QDs in NWs would represent a significant step forward. Furthermore, the operation of a quantum network relies on the synchronization of all its components; quantum memories would harmonize the functioning of a quantum network by storing and releasing on demand flying qubits without affecting their quantum state. Gases of alkali atom, such as Rb or Cs, match the physical and technological requirements of a quantum memory, as already demonstrated in the laboratories [22, 23].

The goal of this thesis is to engineer the emission energy of self-assembled QDs embedded in core-shell GaAs-AlGaAs NWs (NWQDs) by taking advantage of the degrees of freedom and improved performance offered by the NW host. The target is to redshift the NWQD emission energy in resonance with the D2 transition of a gas of Rb atoms as a proof of principle of the use of these quantum emitters in a realistic quantum network.

This thesis is structured as follows:

Chapter 1 frames the topic of this thesis in the wide perspective of semiconductor quantum technologies.

Chapter 2 provides an overview on NWs and QDs; a description of the combination of QDs in NWs follows, with details on the specific (Al)GaAs NWQDs that are the object of analysis in this thesis. Theoretical details on the mechanisms of tuning a semiconductor bandgap by strain and composition engineering are given. A description of the working principle of Rb as a quantum memory concludes this introductory chapter.

Chapter 3 describes the main experimental techniques and setups used in this thesis, including photoluminescence (PL), Raman spectroscopy, cathodoluminescence (CL), transmission electron microscopy (TEM), and energy dispersive X-ray spectroscopy (EDX).

Chapter 4 to **Chapter 7** report the experimental work conducted in this thesis:

Chapter 4 is dedicated to the study of the NWQD occurrence and emission energy as a function of the density of crystal defects along single NWs.

Chapter 5 is dedicated to the strain tuning of the NWQDs by the deposition of a SiO_2 shell, which allowed to redshift the NWQD emission energy by more than 100 meV.

Chapter 6 is dedicated to the alloying of the AlGaAs shell with different amounts of indium, a strategy that allowed to redshift the NWQD emission energy by about 300 meV.

Chapter 7 is dedicated to the preliminary experimental proof of optical coupling between the emission of the engineered NWQDs and the absorption of a gas of Rb atoms.

Chapter 8 concludes this dissertation with a summary of the experimental work described in the previous chapters and outlooks for future developments.

2 Quantum dots in nanowires

In this chapter, the growth methods and optical properties of NWs and QDs are described. The integration of QDs in NWs is then addressed, the advantages are discussed and the state-of-the-art properties are reported. Specific focus is given to SP emitters embedded in NWs and to the system studied in this thesis. The mechanisms employed to redshift the NWQD emission energy are discussed from a theoretical point of view. The description of atomic gases as slow-light media concludes this chapter.

2.1   Nanowires

NWs are elongated crystals with length usually exceeding by at least one order of magnitude the diameter: NWs have a diameter in the nanometer range, up to few hundreds nanometers, while the length is generally in the micrometer range. In the 60's, Wagner and Ellis [24] reported the first vapor-liquid-solid (VLS) growth of NWs, here discussed in subsection 2.1.1, and laid the basis of the research that was to exponentially grow during the last twenty years. NWs offer advantages and additional degrees of freedom with respect to their bulk counterparts. For instance, NWs can act as waveguides and thus tackle one of the main drawbacks of light emitters in the bulk: the low light extraction efficiency into the outer environment. More details on the optoelectronic and photonic properties of NWs and emitters embedded in NWs are provided in subsection 2.3.3. NWs also have interesting mechanical properties: they can strikingly support stress yields much higher than the same materials in the bulk [6, 7]. This is of particular interest because crystals with large differences in lattice constants can be combined by epitaxy without or with minimized stress-induced defects and plastic relaxation [25, 8]. A wider range of material combinations is thus available, which opens to a variety of heterostructures and provides additional functionalities to the NWs [26]. These heterostructures include quantum wells (QWs) as well as QDs defined on [27, 28, 29, 30, 31, 32, 33, 34, 16, 35, 36] and off [13, 14, 2, 37, 38] the NW longitudinal axis, as discussed in section 2.3.
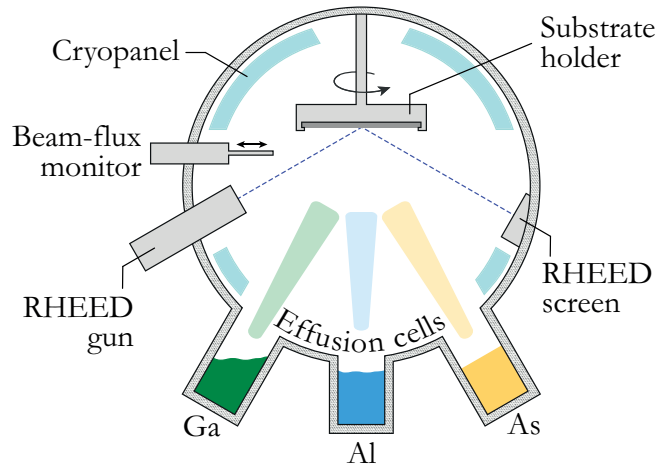
Figure 2.1 – Sketch of the main components of an MBE chamber.

2.1.1 Nanowire growth

Epitaxy is a method of growing crystals: two crystals have an epitaxial relation if the lattice of the first is in a well-defined spatial relation with the lattice of the second [39]. Metal-organic chemical vapor deposition (MOCVD) and molecular beam epitaxy (MBE) are the two main methods of epitaxial growth. They both rely on providing fluxes of the grown material to a substrate placed into a chamber under controlled temperature and pressure. In particular, MOCVD and closely related variants, such as metal-organic vapor-phase epitaxy (MOVPE), are based on the decomposition of organic precursors at the growth surface. MOCVD is more common in industrial applications with respect to MBE because of less strict constraints on the growth pressure and consequently easier scalability. A drawback that affects MOCVD is that parts of the organic precursors can be incorporated in the deposited material. Organic contamination is a concern in some applications that require highly pure materials. On the contrary, MBE supplies material to the growth substrate by molecular beams of the pure elements; at the same time the growth chamber is kept in ultra-high vacuum: thanks to cryopumps and liquid-nitrogen-cooled cryopanels on the chamber walls, the base pressure is in the order of 10^{-10} Torr [39]. At this pressure most contaminants are taken away and the molecular beams are highly directional: they can reach the growth substrate in almost ballistic conditions. A sketch of an MBE chamber and its main components is presented in figure 2.1. MBE growth rates are low (often less than 1 Å/s), which facilitates the growth of sharp interfaces between layers of different materials and finely tuned thickness. NWs are crystals with a high aspect ratio: in the work described here, they are typically between 4- and 10-micron long and less than 200 nm in diameter. MOCVD and MBE have been extensively used for the planar deposition of semiconductor layers and thin films; more recently, they have been successfully adapted to grow NWs. The transition from planar to NW growth is possible if the deposition is constrained only in specific areas of the substrate. One method to achieve this is to deposit a mask that prevents the material deposition on the substrate and define openings where the supplied material is in contact with the substrate; the material grows in epitaxial relation
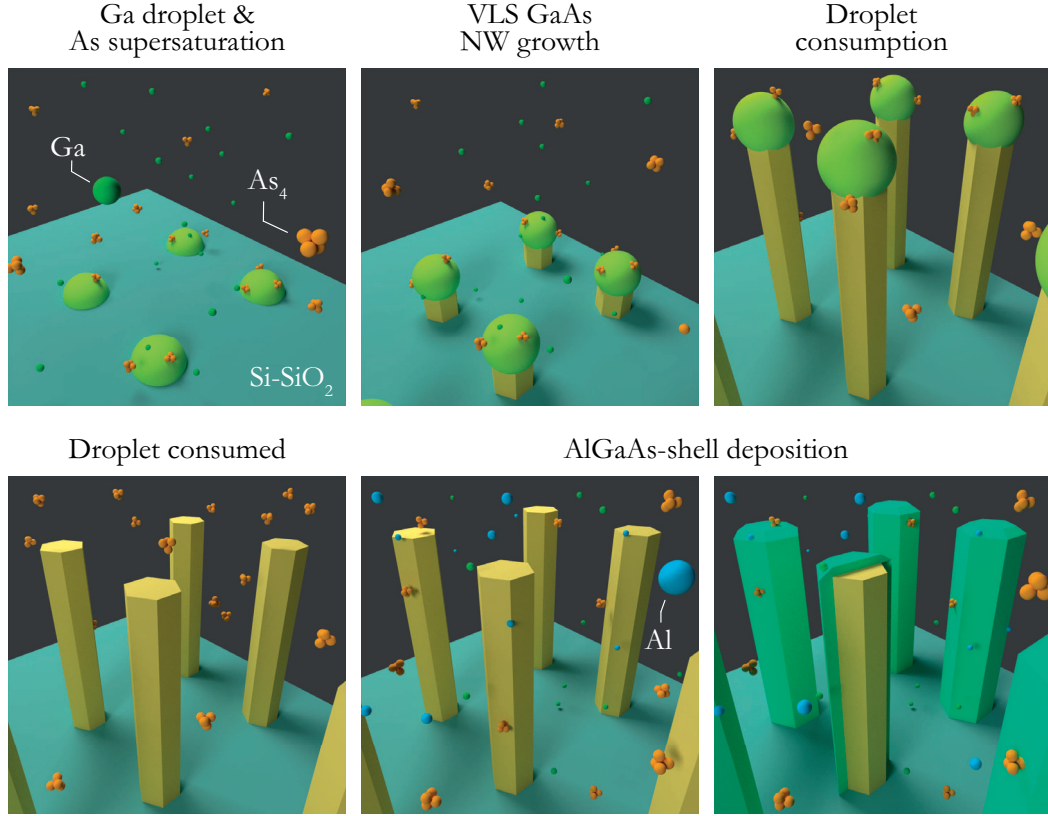
Figure 2.2 – Steps of the VLS growth of a GaAs NW coated by an AlGaAs shell. From top to bottom and left to right: Ga-droplet formation and supersaturation with As; precipitation of solid GaAs at the liquid-solid interface and NW vertical growth; droplet consumption by As supply; droplet consumed and interruption of vertical growth; Al supply in addition to Ga and As to deposit an AlGaAs shell on the GaAs core sidewalls.

with the substrate and, under adequate growth conditions, forms an elongated crystal with diameter constrained by the opening size. This NW-growth method is known as selective area epitaxy (SAE) or selective area growth (SAG) [40]. Another strategy was defined by Wagner and Ellis in 1964 [24]. The material deposition is localized by catalytic sites in the form of liquid droplets on the growth substrates. In their seminal work, Wagner and Ellis used gold droplets. From the vapor phase, the material supply preferentially diffuses into the catalytic droplet, where it reaches supersaturation conditions. Therefore, the supersaturated species precipitate at the droplet-substrate interface as a solid crystal. Layer by layer, the materials precipitation under the liquid droplet grows a filamentary crystal. The growth time determines the NW length: the longer the growth time, the higher the NW aspect ratio. Being based on the transition of the growth materials from vapor to solid through a liquid solution in the catalytic droplet, this process is known as the VLS growth method. The material that composes the catalytic droplet is not limited to gold. It is in general a metallic seed that is liquid at the growth temperatures and defines a preferential site where the growth material diffuses [41, 42]. Metal atoms in the droplet can be incorporated in the semiconductor precipitate. The incorporation of metals, gold in particular, is detrimental for the semiconductor optoelectronic properties
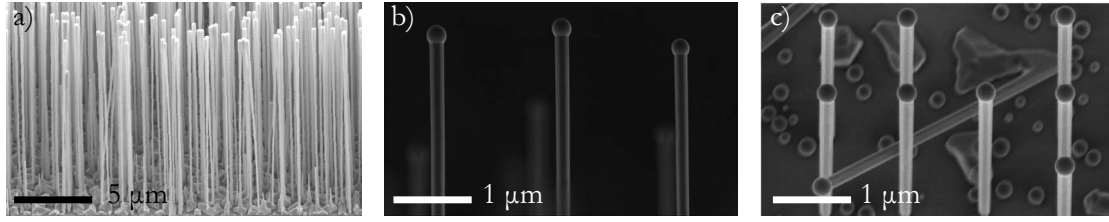
Figure 2.3 – a) 20°-tilted SEM micrograph of highly dense as-grown self-assembled GaAs-AlGaAs core shell NWs: the shell is tapered, thicker at the top and thinner at the bottom. b) Close-up side-view SEM micrograph of as-grown self-assembled GaAs NWs: the Ga droplet is visible at the NW tops. c) 20°-tilted SEM micrograph of an as-grown GaAs-NW array with Ga droplets at the NW tops.

because they form deep bandgap levels.

New materials have been exploited as a catalyst of the VLS NW growth in order to replace metals. This is the case of the method known as self-catalyzed VLS growth. It consists in using one of the components of the semiconductor NW as a liquid catalyst. A noticeable example is the Ga-assisted growth of GaAs NWs [43, 44], for which Ga is used as a liquid catalyst. The GaAs cores of the core-shell GaAs-AlGaAs NWs studied in this work are grown by this method in a DCA P600 MBE machine following the steps sketched in figure 2.2. The growth begins with the formation of liquid-Ga droplets on the growth substrate. In this thesis, Si (111) wafers were used as growth substrates, while GaAs wafers were used in the past [43]. They were covered by a thin layer of native oxide. Pinholes are naturally present in the oxide and define sites where the Ga droplets form and the NWs can grow in epitaxial relation with the growth substrate. A specific oxide thickness slightly thinner than 1 nm ensures the highest yield of vertical NWs [5, 45]. NWs obtained in this way are referred to as self-assembled, because their distribution on the growth substrate depends on the distribution of pinholes naturally present in the native oxide. Alternatively, a 10-nm-thick oxide mask can be patterned to induce the catalytic droplets to position in the e-beam-defined openings of an ordered array [46, 4, 47, 48]. In this thesis, the NWs have been grown both as self-assembled and in order arrays.

In both cases, the Ga droplet acts as a catalyst of the GaAs NW axial growth: As diffuses through the droplet until supersaturation and precipitation of the GaAs crystal underneath (upper left panel in figure 2.2). The growth temperature of the substrate is about 630°C; the Ga beam equivalent pressure (BEP) is about 1×10^{-7} Torr and the As_4 BEP is about 4×10^{-6} Torr. In these conditions the typical growth rate is about 2.8 nm/s for the self-assembled NWs and 1.4 nm/s for the array NWs. Once reached the desired length of the core (upper mid and right panels in figure 2.2, the growth is interrupted by closing the Ga supply and consuming the catalytic droplet with As (lower left panel in figure 2.2). This allows to proceed with the engineering of the NW by depositing a shell of a different material on its surface (lower mid and right panels in figure 2.2). This can be used to define radial NW heterostructures, such as QWs on the NW sidewalls [26] or QDs [13], but can also be used to passivate the NW surface [49, 50, 51, 52]. In the NWs studied here, the GaAs core of about 80 nm in diameter is surrounded by an AlGaAs shell. The shell deposition is the equivalent of planar MBE growth using the NW-core sidewalls
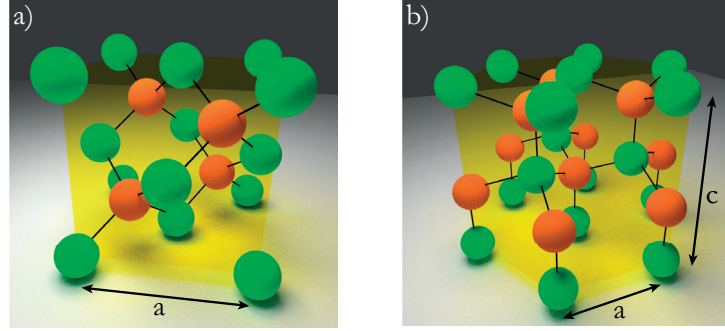
Figure 2.4 – a) 3D model of the unit cell of GaAs in the ZB phase. b) 3D model of the unit cell of GaAs in the WZ phase.

as a deposition substrate. The shell grows in epitaxial relation with the NW facets [53, 54]. The substrate temperature is lowered to about 460°C, with Al BEP of about 2×10^{-7} Torr, Ga BEP of about 1.4×10^{-7} Torr and As BEP of about 1×10^{-5} Torr. These conditions result in a radial growth rate of about 0.2 Å/s and nominal Al content of 33%. An outer 5-nm GaAs capping is deposited to prevent oxidation of the Al in the AlGaAs shell. The shell thickness can be controlled by the deposition time. In this work, we report on NWs with 30 nm-, 50 nm-, and 100 nm-thick shells. We also engineered the shell alloy by adding indium to obtain a quaternary-alloy shell. The indium content in the AlGaInAs shell was varied between 0 and 25%. More details are reported in chapter 6. Illustrative scanning-electron-microscope (SEM) images of GaAs and GaAs-AlGaAs NWs are reported in figure 2.3.

SAE and VLS are bottom-up growth methods: they assemble new nanostructures on the substrate. On the opposite, a top-down approach defines the desired structures by removing material from a pre-existing bulk, by means of, e.g., lithographic methods. A top-down growth is in general more expensive and complex than the bottom-up one, since it involves several processing steps that are unnecessary to define bottom-up nanostructures. In addition, the surface quality can be lower in top-down structures because of the roughness and damage introduce by the lithographic steps. Having a high surface-to-volume ratio, NW properties are very sensitive to the quality of the surfaces. In particular, dangling bonds at the etched surface and adsorbed species such as oxygen can introduce surface states whose energy levels lie in the GaAs bandgap. These levels may act as efficient non-radiative recombination centers and hinder the PL response of NWs and other nanostructures with a high surface-to-volume ratio.

2.1.2 Nanowire crystal structure

Top-down NWs inherit their crystal structure from the one of the bulk material from which they are formed. ZB is the only crystal structure observed in bulk GaAs in normal conditions: its unit cell is face centered cubic (FCC), with a two-atom base set occupied by Ga and As (figure 2.4a). It is energetically unfavorable to form the WZ phase during the growth of bulk III-arsenide crystals. In NWs, the high surface-to-volume ratio and the VLS growth method
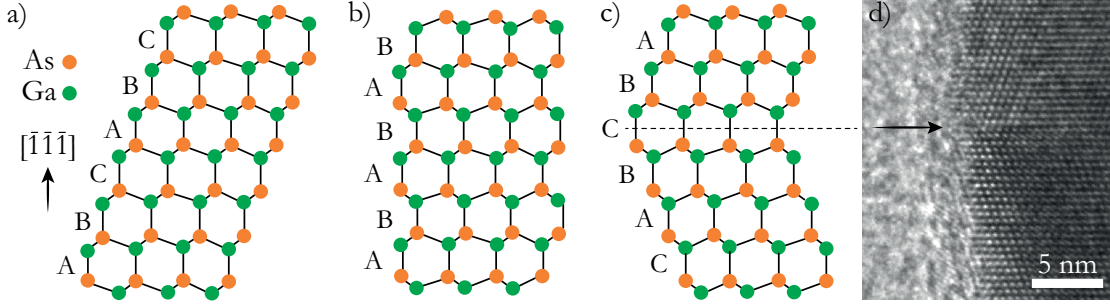
Figure 2.5 – a) Scheme of the atom stacking of Ga and As atoms along the (111) direction in (a) GaAs ZB, (b) GaAs WZ and (c) GaAs ZB in presence of a rotational twin. d) HRTEM micrograph of ZB rotational twin in a core-shell GaAs-AlGaAs NW.

allow the formation of GaAs WZ crystals. In general, the occurrence of the WZ phase has been related with the NW diameter, the supersaturation of the catalyst droplet and its contact angle at the liquid-solid interface [9, 55, 56]. WZ has a four-atom-base hexagonal unit cell fully determined by the two lattice constants a and c (figure 2.4b), while the ZB unit cell is described by a single lattice constant a. WZ and ZB segments can coexist in the same NW, a characteristic that is referred to as polytypism. The similarity between ZB and WZ GaAs is appreciated by applying a rigid rotation that orients the ZB [111] direction as the WZ c direction. The difference between the two crystal structures is the atom stacking in the ZB <111> direction, that is the growth direction in the NWs described in this thesis: ZB alternates atoms with an A-B-C-A-B-C stacking, while WZ shows an A-B-A-B stacking. Figures 2.5a and b sketch the atom stacking in defect-free GaAs ZB and WZ, respectively.

Stacking defects are also common in NWs. A simple stacking fault is the interruption of the ideal sequence by skipping one layer followed by immediate recovery of the ideal atomic ordering: e.g. in A-B-C-B-C-A-B-C, A is skipped at the fourth position. Rotational twins correspond to a 180° rotation of the lattice cell around the <111> direction. In the NWs studied in this thesis, rotational twins in the ZB phase were commonly observed. The twin perturbs the ZB stacking in the <111> direction and results in the A-B-C-B-A-C atomic sequence. Farther in the sequence, the repetition of the same defects brings the stacking back to the original one A-B-C-B-A-C-B-A-B-C. Figure 2.5c shows the atomic sequence of a twin in GaAs ZB. By comparison between figures 2.5b and c, one can notice that the twin plane has the stacking of the WZ phase. Different crystal phases (ZB and WZ) and stacking defects can be detected by TEM. In order to image the NW crystal structure by TEM, a practical configuration consists in aligning the electron beam parallel to the <110> crystal direction, that is, perpendicular to one of the six facets on which a NW typically lies on a TEM grid. High-resolution (HR) TEM micrographs in this configuration as said to be in the <110> zone axis and allow to observe the atom stacking sequence in the <111> direction. An illustrative example of a twin in a ZB NW observed by HRTEM in this is configuration is reported in figure 2.5d: the twin plane is indicated by an arrow aligned with the sketch in figure 2.5c. The fast Fourier transform (FFT) of HRTEM micrographs and selected-area electron diffraction (SAED) images can be routinely
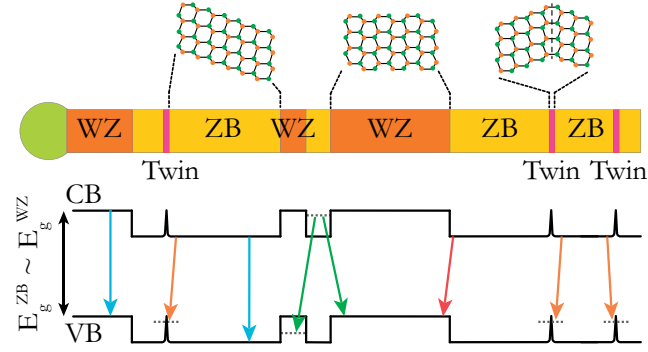
Figure 2.6 – Sketch of the band-edge alignment between GaAs ZB and WZ. Twins are shown in the ZB regions. The possible radiative transitions are sketched.

used to undoubtedly distinguish the NW crystal phase and the presence of stacking defects.

Although the control of the NW crystal structure has been demonstrated by several groups to form defect-free NWs and embed homostructures in NWs [10, 55, 57, 58], this is not the primary interest in this thesis. Here, the focus is on the impact that crystal defects and different crystal phases have on the NW electronic structure [59, 60, 61] and on the deposition of a shell around the NW core [62, 54]. A sketch of the band alignment in a polytypic NW is presented in figure 2.6. In particular, it sketches the effect of different phases and twins on the charge-carrier localization and recombination energy. WZ and ZB have a staggered band alignment; most experiments and simulations agree that the WZ band edges are upshifted with respect to the ZB, while the bandgap in the two phases are similar or equal [59, 60, 61]. This alignment favors the localization of electrons in ZB and holes in WZ. Electrons and holes that radiatively recombine across the WZ-ZB interface emit photons at lower energy with respect to the WZ or ZB bandgap. Electrons in short ZB segments and holes in short WZ segments may undergo quantum confinement. Twins behave as very localized perturbations of the band edges and provide bound states for holes to which electrons can recombine. This topic is further developed in chapter 4.

2.2 Quantum dots

QDs are nanostructures that define a potential well where charge carriers undergo quantum confinement in all three spatial directions. QD research was initially supported by the interest in their optoelectronic applications and in fundamental research. For instance, as laser gain medium [63], QDs ensure low and almost temperature-independent lasing thresholds. With the growth of light-based schemes of quantum computing and encryption, another characteristic rising from the peculiar QD electronic structure attracted much interest: QDs are ideal sources of on-demand SPs. A solid-state QD is formed by the inclusion of a semiconductor inside a matrix made of a different semiconductor of larger bandgap. In all three spatial directions, the surrounding matrix acts as a barrier that localizes electrons and holes inside

the lower-bandgap semiconductor inclusion. Solid-state QDs often range between 10 nm and 30 nm, which is small enough for electrons and holes to undergo quantum confinement in all spatial directions. Colloidal QDs are widely used for biological labeling [64] and light emission, including lasing [65]. They are often less than 10 nm in size and the trapped charge-carriers undergo strong confinement. The fabrication of colloidal QDs by chemical synthesis is less expensive than the growth of solid-state QDs by epitaxy; it is also quicker and allows to obtain a wide range of compositions. However, the solid-state QD growth comes with the great advantages of material purity and the direct integration in solid-state devices.

2.2.1 Quantum-dot epitaxial growth

The most common strategy to obtain semiconductor solid-state QDs is the Stranski-Krastanov (SK) growth mechanism. In SK QDs, strain is the driving force for the QD formation. In the exemplary case of InGaAs QDs in a GaAs matrix [66], few monolayers of InAs are deposited on GaAs; the lattice mismatch between the two materials builds up strain; at a critical thickness, the strain is plastically released by the formation of 3D InAs islands. The increase in the surface energy of the system due to the island formation is compensated by the energy released by the strain relaxation. A layer of InAs, the wetting layer, is left below the QDs. It is thinner than the critical thickness and behaves as a QW. The InAs QDs are then capped again with GaAs that provides the barrier to confine the excitons. Residual strain propagates through the GaAs capping and is used to guide the formation of another layer of SK InAs QDs: stacks of aligned SK QDs can form in this way. The QDs can then be encapsulated between Bragg reflectors or placed in the active region of a diode. As an alternative approach, droplet epitaxy allows to grow QDs in semiconductor systems that are lattice matched [67, 68]. This case is exemplified by GaAs-AlGaAs QDs: a Ga droplet is deposited on AlGaAs; a GaAs crystallite is formed by As supply and finally capped with AlGaAs. SK QDs also lack an easy control on their site position and feature rather broad emission-energy distributions due to the inhomogeneity among the single QDs. MOVPE-grown QDs defined by the segregation of different species in pyramidal recesses lithographically obtained on the growth substrate naturally solve these challenges. Symmetric QDs of finely tuned size and composition can be obtained at the positions defined by the substrate pattern [69, 70, 71, 72]. The control on the QD position is a fundamental step towards realistic on-chip QD photonics and industry scale-up. Alternatively, complex methods must be implemented to track the position of SK QDs during top-down post-growth processing [73].

2.2.2 Quantum-dot optics

Quantum-dot energy levels

The band structure of a direct-bandgap semiconductor, like GaAs, is described by the electron (e) and hole (h) dynamics at the Γ point (wave vector k equal zero) of, respectively, the conduction and the valence bands (CB and VB). The focus is here on ZB GaAs, as a meaningful
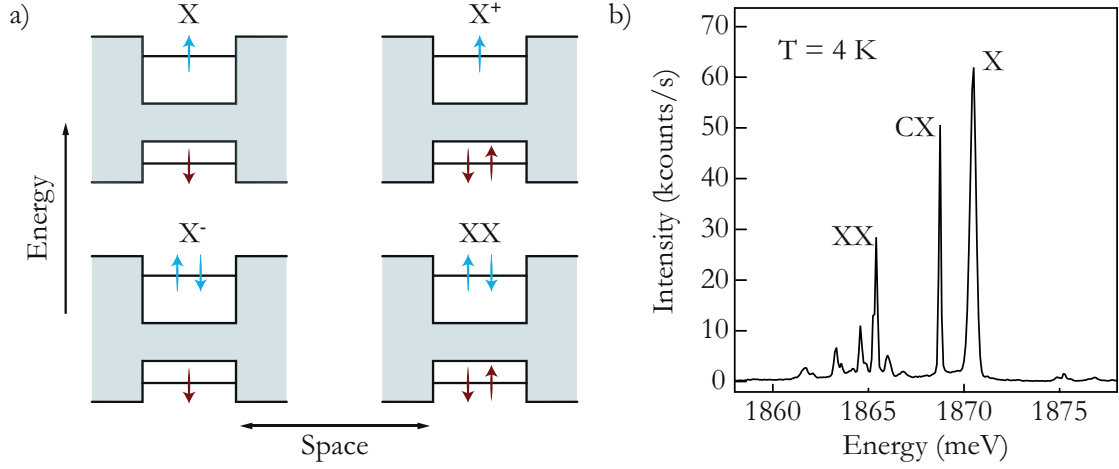
Figure 2.7 – a) Sketch of the bright-state occupation of a 2-level QD (not all the possible spin combinations are shown) and b) corresponding PL emission.

case for the NWs studied in this thesis. The GaAs VB is composed of the heavy-hole (HH), light-hole (LH), and split-off bands: while in relaxed GaAs the HH and LH bands are degenerate, the split-off band is downshifted by 340 meV at 300 K. The electronic structure of a GaAs QD results from the quantization of the electronic structure of bulk GaAs. In a similar fashion as atoms, each quantized level is described by a radial quantum number $n = 0, 1, 2, \ldots$ and an angular momentum quantum number $l = 0, \pm 1, \pm 2, \ldots$ The level with lowest energy has $n = l = 0$ and is referred to as the QD s-shell to recall the symmetry of the s-shell in atoms. Following the same analogy, the levels at higher energy form the QD p- and d-shell. For realistic values of the confinement barrier for GaAs-AlGaAs QDs, the split-off band is delocalized and not confined. GaAs LHs are about 6 times lighter than HHs: since the energy of quantized levels depends on the mass of the charge carrier, quantum confinement lifts the LH and HH degeneracy in a QD and leads to the LH delocalization out of the QD barrier.

A priori, electrons and HHs can be hosted on s-shell and higher states. However, here only the s levels are considered: there is no evidence of population of higher levels in the QDs studied in this thesis [74]. Moreover, low-energy acoustic phonons mediate the fast relaxation of electrons and holes from excited states to the ground state. Therefore, unless in conditions of high excitation, electron-hole primarily recombination between s-shell levels. This leads to the representation of the QD electronic structure as a 2-level system, shown in figure 2.7a. On each electron (hole) level 0, 1 or 2 electrons (holes) can be loaded. When two fermions are on the same level, they must obey the Pauli principle. Electrons and holes can recombine by emission of a photon. Since the photon does not carry spin, electrons and holes can radiatively recombine only if they have antiparallel spins, that is, the sum of their spins is zero: $| e \rangle = \downarrow$ with $| h \rangle = \Uparrow$ or $| e \rangle = \uparrow$ with $| h \rangle = \Downarrow$. The QD levels can be loaded in four possible configurations (or excitonic complexes) that can emit light, as shown in figure 2.7a: exciton (X), that is: 1 e + 1 h; positive trion (X$^+$), that is 1 e + 2 h; negative trion (X$^-$), that is 2 e + 1 h; biexciton (XX), that is 2 e + 2 h. The e-h Coulomb attraction is known as exciton

13

binding energy; the free-X binding in bulk GaAs is ~ 4 - 5 meV [75] and reduces the X energy with respect to the non-interacting e-h pair. Coulomb and exchange interactions among the charge particles on the QD levels are responsible for lifting the energy degeneracy of the four excitonic complexes described here. The Coulomb interaction causes the largest shift, that is measured as the energy difference between the emission line of one complex from the X emission line; it is repulsive or attractive according to the relative charge of the particles involved, which respectively increases or decreases the overall energy of the excitonic complex. In simple terms, tightly confined particles in a QD cannot freely rearrange their wavefunctions to minimize their interactions, but details on the QD shape and size must be known to accurately calculate the Coulomb interactions. In figure 2.7b an illustrative emission spectrum from a single (Al)GaAs NWQD studied in this thesis is presented; the X, XX lines are distinguishable as well as a charged-X line (CX, either X^+ or X^-). In the specific case reported in figure 2.7b, the Coulomb interaction reduces the CX and XX emission energy by 5 meV at most with respect to the X line.

The exchange interaction between the e and h spins brings an additional shift to the X energy levels into the bright (e and h with antiparallel spins) and the dark (e and h with parallel spins) X states. The hybridization of the bright states further splits their energies. This is known as fine-structure splitting (FSS) or anisotropy exchange interaction, since its magnitude depends on the asymmetry of the QD potential. Since some quantum-information protocols [18] require to cancel the FSS, there is interest to grow highly symmetric QDs with FSS = 0. Considerations on the NW symmetry and growth direction predict a vanishing FSS for QDs embedded on the main NW axis [76]. This topic will be discussed in more details in subsection 2.3.4. In the bulk, the symmetry of the pyramidal recesses mentioned in subsection 2.2.1 provides an excellent template to limit the FSS of the QDs grown at the pyramid bottom. The average FSS value reported is 2.9 μeV, with records of 0.7 μeV, 0.4 μeV, and 0.2 μeV [71]. In a similar way, highly symmetric GaAs QDs grown by MBE in circular holes etched in AlGaAs show an average FSS of 3.9±1.8 μeV, with the lowest measured FSS of 1.2±0.5 μeV [77]. Alternatively, post-growth treatments can reduce or cancel the FSS in anisotropic QDs. For instance, annealing was shown to reduce the FSS of InGaAs QDs to 8 μeV [78].

Quantum dots as single-photon emitters

A two-level QD can host only one of the four excitonic complexes at a given moment; each excitonic complex can emit only one photon. Therefore, QDs can only emit a SP at a given moment in time, that is, QDs are ideal SP sources. In addition, they can be controllably excited and emit SPs on demand. Experimentally, the QD emission consists of a stream of anti-bunched photons and the time spacing between two photons depends on the lifetime of the emitting excitonic complex. SP emission is fundamental to encode information in photons as, e.g., flying qubits and implement any photon-based quantum scheme. The experimental test of the SP nature of the QD emission is performed by measuring the second-order correlation

function ($g^2(\tau)$) of the light, which correlates the light intensity in time:

$$g^2(\tau) = \frac{\langle I(t)I(t+\tau)\rangle}{\langle I(t)\rangle\langle I(t+\tau)\rangle} = \frac{\langle n(t)n(t+\tau)\rangle}{\langle n(t)\rangle\langle n(t+\tau)\rangle} \tag{2.1}$$

where t is time, I is the light intensity, equivalent to the number of photons n, and τ the time delay between two detections of consequent photons. $g^2(0) < 0.5$ is possible only for SP emitters, where $g^2(0) = 0.5$ is the upper limit, corresponding to the case of uncorrelated SP emitters. The $g^2(\tau)$ measurements in usually performed in the Hanbury-Brown-Twiss (HBT) experimental setup, as further discussed in section 3.1. The SP emission is not restricted to QDs. Attenuated lasers can be used to generate de facto a stream of SPs, while the first proof of SP emission was demonstrated on real atoms [79]. Spontaneous parametric down-conversion in non-linear crystals is the most common mechanism to produce entangled photon pairs with large entanglement fidelity and brightness [77]. Yet, a great advantage of QDs is that they are SP emitters on demand; they are solid-state emitters, which facilitates the technology scalability and the engineering of desired optical properties; in addition, the typically long lifetime ($\sim$ 10 ns) of the atomic excitation limits the repetition rate of the atomic emission [80, 81]. Recent advancement in QD engineering improved the purity, indistinguishability and entanglement fidelity of the SP QD emission. The second-order correlation function of the QD emission can be near to the ideal case, that is, $g^2(0) = 0$. Background-subtracted $g^2(0)$ of about 0.007 and 0.002 from the X and XX lines of GaAs QDs respectively are reported [77]. These values are longer than the state-of-the-art background-subtracted $g^2(0)$ of 3 x 10^{-4} obtained with trapped atoms [82]: the QD SP emission suffers from multi-photon contributions. In GaAs QDs, the efficient suppression of multi-photon emission resulted in the state-of-art value of $g^2(0) = 7.5\pm1.6$ x 10^{-5} [81]. This record value was achieved under two-photon excitation matching XX absorption in order to suppress background recombination; in addition, superconducting SP detectors were used to suppress noise and false-coincidence counts. The reported values demonstrate that QDs are excellent sources of SPs and that a large part of the improvements in the measurements of the autocorrelation function of the emission in state-of-the-art QDs is actually related with the detector performance and excitation scheme. The deposition of electron- or hole-injection layers allows to observe QD electroluminescence. An interesting $g^2(0) = 18.5\%$ is obtained from pyramidal QDs electrically excited. After removing overlapping events due to the QD re-excitation by long electric pulses, the $g^2(0)$ reduces to 7.8% [1].

The light emission from the NWQDs studied in this thesis is visible at temperatures below $\sim$ 50 K [74]: at higher temperatures, the thermal energy of the charge carriers prevents to trap excitons on the QD electronic levels. The spectrum reported in figure 2.7b was acquired from a sample kept at 4 K. In many III-V QDs, light and SP emission is possible only at temperatures achieved by liquid-helium (LHe) cooling [14, 77, 81]. The QD brightness and SP purity gradually degrade as a function of temperature. Yet, QD optics at liquid-nitrogen or higher temperatures is cost effective and technologically simpler. QD optical activity is

---

[1]Oral presentation at the 34th International Conference on the Physics of Semiconductors (ICPS 2018 - Montpellier) by Gediminas Juska from Emanuele Pelucchi's group, Cork - Ireland)

demonstrated up to room temperature in semiconductors of wider bandgap, where the exciton binding energies are typically larger. As an example, nitride-based QDs showed promising characteristics as room-temperature SP emitters in the UV range (room-temperature g^2(0) = 33%) [83].

Quantum dots in microcavities

A common way to affect the QD optical properties without any modifications to the QD structure or composition is to modify the QD surrounding environment. In subsection 2.3.3, more details are provided on the way a NW modifies the emission of an embedded QD by acting as a waveguide or an antenna. Here, more focus is given to the physics of QDs positioned in cavities [84]. Microcavities such as Fabry-Perot resonators, whispering galleries and photonic crystals are used to confine the light emitted by a QD. Microcavities in particular are employed to tune the directionality of the QD emission and increase the rate of its spontaneous emission. This second phenomenon is called Purcell effect [85]: the cavity supports an increased density of final states for the QD spontaneous emission.

This strategy is often used to enhance the QD brightness and to shorten its lifetime. Brighter emission was demonstrated for QDs positioned in cavities, also thanks to the increased extraction efficiency [73]. A microcavity can also be exploited to facilitate the QD manipulation by, e.g., applying an external bias to reduce the charge noise [73]. Record QD lifetimes of 22 ps were recently reached by Purcell effect [86]. Yet, strong Purcell effects only work in a narrow bandwidth of photon energies, which represents a limit for, e.g., room-temperature broad-linewidth emitters and poses a fabrication constraint to precisely match the QD emission energy with the cavity mode.

The plethora of additional degrees of freedom that come with QDs as solid-state SP emitters involves an important drawback: the QD states can couple with the surrounding environment or with additional degrees of freedom present in the QD. This coupling can be represented by the interaction between the QD charge-carrier spins and the spins of the nuclei that constitute the QD matrix. The QD-state coherence is destroyed. In order to avoid the decoherence of their states, QDs are put in microcavity to shorten their radiative lifetime τ_R below their coherence lifetime τ_C and allow the collection of the emitted photons in the desired state. The ideal threshold is defined by the fundamental radiative limit that corresponds to $\tau_C = 2\tau_R$ [87]. An alternative approach tackles the strength of the spin coupling by engineering the QD composition. SK In(Ga)As QDs are common as bulk semiconductor QDs, but the ensemble of randomly oriented nuclear spins of the indium atoms that constitute the QD can strongly couple with the spins of the charge-carriers in the QD excitons [88]. To extend the exciton coherence, more attention was recently devoted to GaAs QDs buried in AlGaAs [77]: these materials avoid the use of indium in favor of Ga and Al that have weaker nuclei-spin interactions.
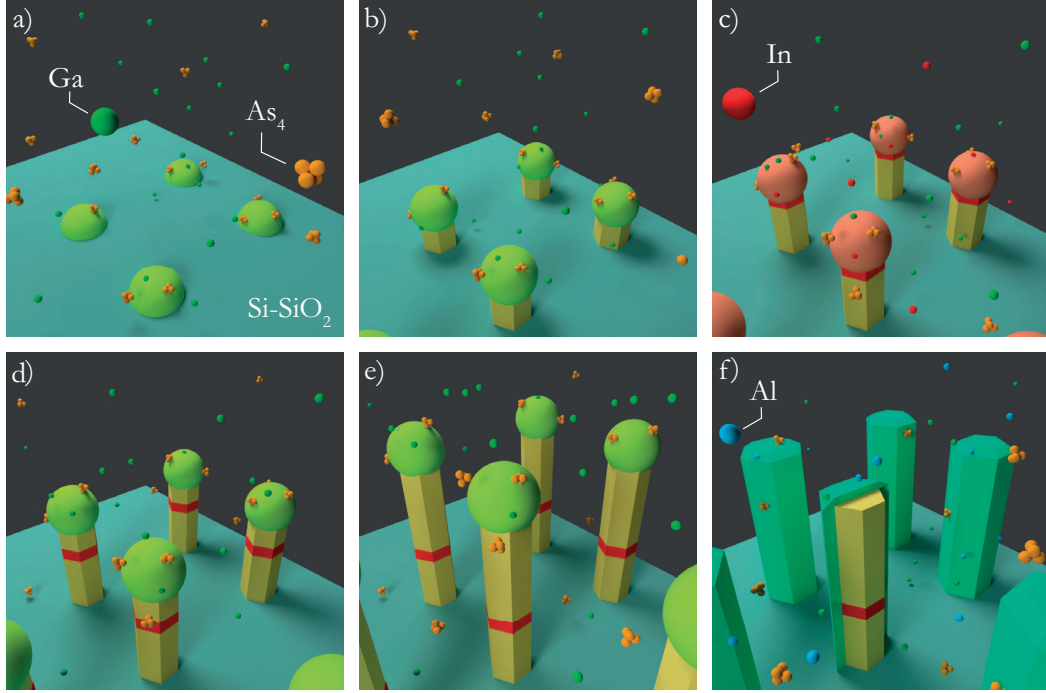
Figure 2.8 – Steps to form InGaAs QD in a GaAs NW as an illustrative case of the formation of an axial NWQD: a) Ga-droplet formation and supersaturation with As; b) VLS growth of a GaAs NW segment; c) indium supply to the catalyst droplet to grow an In-rich segment; d) interruption of the indium supply and growth of GaAs segment; e) elongation of the GaAs NW; f) passivation by a shell of higher bandgap, e.g. AlGaAs, after interruption of the axial growth.

2.3 Quantum dots embedded in NWs

QDs in NWs or NWQDs come in two main configurations. They are referred to as axial and radial NWQDs and are described in the following. The advantages of NWQDs are discussed, especially with respect to their optical properties, and an overview on the relative state of the art is provided. Specific space is dedicated to describe the NWQDs used in this thesis.

2.3.1 Axial nanowire quantum dots

The VLS NW-growth method offers a natural way to tune the NW composition in the axial direction. The composition of the catalyst droplet can be controlled during the growth to change the NW composition in a short segment and form a Z-Y-Z heterostructure along the NW, where Z and Y are different materials. Y has a smaller bandgap than Z, ideally with a type-I band alignment that confines both holes and electrons in the segment Y. If this segment is short enough to show charge-carrier quantum confinement, then Y is an axial QD in a NW of material Z. Laterally, the confinement is given by the NW diameter or an outer shell of a higher-bandgap material. The growth steps necessary to form an axial NWQD are sketched in figure 2.8. Several combinations of Z and Y materials have been reported for III-V semiconductors grown by both MBE and MOCVD. In the case of binary compounds, they can be grouped

in those that change the group-III [28] or the group-V element [30, 29]. More combinations are possible when either Z or Y is a ternary alloy, such as GaAs QDs in AlGaAs NWs [31, 32], InAsP QDs in InP NWs [16, 33, 34, 35] and InGaAs QDs in GaAs NWs [36]. In spite of the wide range of axial-NWQD examples, the element solubility in the catalyst droplet hinders the formation of a short lower-bandgap segment with sharp interfaces. Elements that should only compose material Z are still present in the catalyst droplet when material Y is supplied. The same may happen while moving from Y to Z again. This phenomenon is called reservoir effect [89, 90]: it forms shallow Z-Y interfaces and increases the length of the lower-bandgap segment. Nevertheless, it is possible to form sharp interfaces and control the QD length and emission energy [29, 36]: slow growth rates, and even the interruption of the growth, were used to abruptly switch material. Close-to-atomically sharp interfaces are demonstrated by using this expedient and switching group-V material rather than the group-III [29]. The reservoir effect is limited for the group-V element because of their high vapor pressure and lower solubility in the catalyst droplet: upon interruption of the group-V supply, these elements quickly precipitate in the solid phase and deplete the catalyst. Recently, a theoretical proposal envisioned to take advantage of the presence of a miscibility gap to sharpen the transition between different group-III materials [91]. In the case of the miscibility gap between InAs and GaAs, not all the InGaAs compositions in between the two binaries are achievable. In particular, the composition of the NW crystal is not directly proportional to the one of the catalyst. The indium content of an InGaAs NW is expected to be below 20% for a large range of indium concentrations in the liquid catalyst. A sudden increase above 80% is simulated as soon as the indium concentration in the liquid crosses a specific value that depends on the growth temperature. Two NW segments with low and high indium content can be obtained with a sharp interface. Turning to top-down methods, an alternative approach to embed QDs in NWs consists in etching NWs from a bulk material with buried QD, such as SKQD layer [92]. Depending on the QD density, one or more QDs may be positioned within the etched NW. While the precise QD alignment on the NW main axis is straightforward in bottom-up NWs, the top-down approach is more challenging: it requires the accurate localization of the QD in order to precisely etch the NW waveguide around it.

2.3.2 Radial nanowire quantum dots

Although axial QDs represent the most common NWQD configuration, the NW sidewalls offer a substrate for the growth of QD offset with respect to the NW axis. This configuration is referred to as off-axis or radial QDs. The formation of radial QDs does not rely on the control of the liquid catalyst. Two cases are presented in the following: InAs [13] SKQDs and the Ga-rich AlGaAs QDs employed in this thesis. Optically active InAs SKQDs are demonstrated on the sidewalls of GaAs NWs by MBE [13]. This approach is not the direct translation of planar SKQDs to the NW sidewalls. The SK method works on (001) GaAs substrates. NWs grown in the <111> direction have {110} and {112} facets that are not energetically favorable to the SK method. A 5-nm thick AlAs layer was predeposited on the {110} NW facets to allow the SK growth of InAs QDs, as in planar growth [93]. The presence of both the X and XX emissions
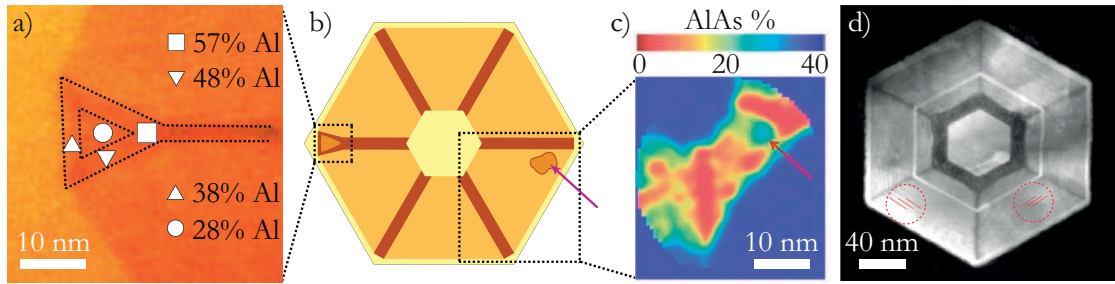
Figure 2.9 – a-c) Candidate NWQDs for the GaAs-AlGaAs core-shell NWs studied in this thesis. a) HAADF STEM micrograph of a corner of NW cross section. The false-color HAADF contrast shows an Al-rich pyramidal nanostructure that surrounds an Al-depleted region. b) Sketch of the two candidate nanostructures observed in the NW shell that may account for the observed QD-like emission. c) Atom-probe-tomography (APT) reconstruction of a portion of the NW shell. The red arrow indicates an Al-depleted nano-cluster. d) HAADF STEM micrograph of a NW cross section. The red arrows indicate the layering of the AlGaAs shell on the sidewalls highlighted by the HAADF contrast. Adapted from a) [97] and b) [95].

was confirmed in these QDs. On the contrary, InAs SKQDs are reported on the sidewalls of GaAs NWs grown by MOCVD without the predeposition of AlAs [2, 37]. Interestingly, a wetting layer is observed, which confirms the SK method, and is reported to be thicker than in the case of SKQDs grown on planar substrate. This difference may depend on the efficient strain relaxation on the NW facets thanks to the high surface-to-volume ratio of the NW geometry.

Figure 2.9 illustrates the specific type of self-assembled GaAs-AlGaAs NWQDs studied in this thesis [14]. Being self-assembled QDs embedded in bottom-up NWs, these QDs need minimal post-growth processing. However, the spontaneous QD formation also requires extensive characterization to understand and control the QD properties. The signature of QD-like emission from GaAs-AlGaAs core-shell NWs was initially represented by sharp emission lines in the shell PL spectra. The physical origin of the lines was originally debated. Point-like defects were proposed as a candidate [94], as well as Ga-rich nanoclusters at the ridge between two facets [14] (figure 2.9a) or randomly dispersed in the shell [95] (figure 2.9c). The first option could be discarded: the PL mapping of the QD emission-energy and occurrence distributions supported the fact that the QD-like emission originates from nanoscale shell clusters [96]. CL maps, some of which are reported in chapter 4, further support this conclusion by showing the shape and size variability of the emitters. The two NWQD candidates are sketched in figure 2.9b.

In the GaAs-AlGaAs core-shell system considered here, the segregation of different adatoms during the shell deposition is well documented. In particular, Al-rich planes form at the ridge between two NW sidewalls both in MBE-grown [94] and MOCVD-grown [98] NWs. Two factors concur to this result. On the one hand, aluminum has a lower surface mobility than gallium and arsenic [99, 100]. On the other hand, the surface chemical potential μ is not uniform on the prismatic surface of the NW. The increased curvature at the ridge between two {110} NW sidewalls locally alters μ; in addition, {112} nanofacets were found at this position, which, because of their different crystalline direction, also affect μ [101]. The Al-rich planes

have an overall constant thickness, but do not precisely follow a unique crystal direction. In ref. [98], it is shown how the profile of the Al-rich planes is indented and not perfectly stable. This detail may support that the formation of the Al-rich planes continuously slightly deviates from a perfectly straight <112> direction. Larger deviations from the <112> crystalline direction may account for the opening of the Al-rich planes into two {$1\bar{1}\bar{2}$} and {$\bar{2}\,\bar{1}1$} branches [14]. Figure 2.9a reports the HAADF scanning TEM (STEM) micrograph of one of these local openings of the Al-rich planes. This bifurcation hosts a Ga-rich alloy and is closed by a (121) Al-rich plane. Such a configuration defines a pyramidal Al-rich barrier that surrounds a Ga-rich nanocluster of very few nanometers in all three spatial directions. Such a structure can host and confine excitons and may account for the observed QD-like emission stemming from the AlGaAs shell. Atom probe tomography (APT) is a destructive technique that allows to reconstruct the 3D distribution of different atomic species in small volumes 10^4-10^7 nm^3. The analysis of the alloy components is based on mass spectroscopy and is very sensitive also to diluted amounts of atoms in the alloy. APT shows a different kind of Ga-rich nanoclusters with respect to those observed in ref [14]. An example of the reconstruction of a 3D volume of the shell is reported in figure 2.9c. Their size is in the few-nanometer range and can confine excitons. These clusters are in positions that do not correlate with the Al-rich planes and their formation seems independent from the branching of the Al-rich features [95, 102]. The formation of these clusters may be related with variations of the shell composition in laminar features along the ⟨110⟩ direction, that is, perpendicular to the NW sidewalls. These features are highlighted by red arrows in the HAADF STEM micrograph of a NW cross section in figure 2.9d. They appear as bright and dark lines parallel to the sides of the NW hexagon. Similar features in HAADF STEM micrographs were regarded as possible fluctuations in the Al-to-Ga ratio [94] and were correlated with the enhanced compositional fluctuations also observed in planar systems on the (110) crystal direction [103]. This was proposed to result from a miscibility gap in AlGaAs. In particular, atomic ordering of Al and Ga was observed in both MBE- and MOCVD-grown planar layers [104]. The reported nanoscale composition fluctuations in NWs are probably related with similar phenomena in the bulk, but the NW prismatic surface enhances this Al-Ga segregation. It is important to notice that NWs can show polytypism and recent reports show that Al tends to concentrate on the ZB segments of WZ NWs [62]. This finding provides a further source of Al-Ga segregation in NWs and in chapter 4 is related to the experimental results on the NWQDs studied in this thesis.

2.3.3 Advantages of quantum dots in nanowires

NWs are a natural connection between the nano- and the microscale thanks to their diameter ranging between few to hundreds nanometers [48] and length in the micrometer range. This characteristic is advantageous for the manipulation of nanostructures embedded in the NW, such as NWQDs. With proper control on the composition of the catalyst droplet, p-n or p-i-n axial junctions can be formed along NWs and an axial QD placed in the active region of the device. The whole current injected or collected at the end tips of the NW goes through the NWQD, ideally with no possibility of losses along different paths. III-V NWQDs have been
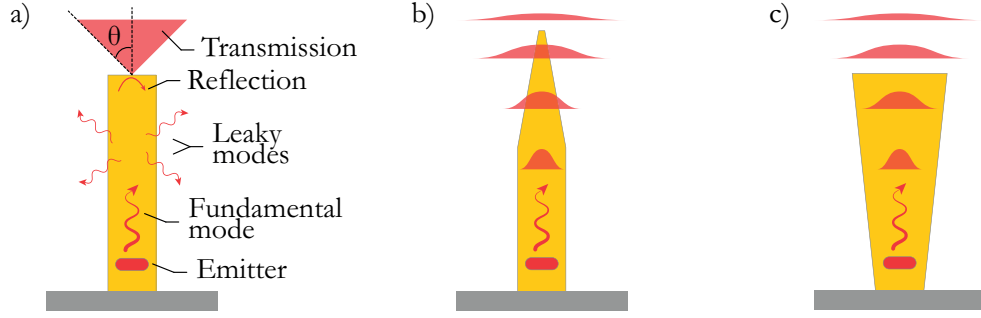
Figure 2.10 – a) Scheme of the coupling of the light emission of a NWQD with the fundamental NW-waveguide mode and higher-order leaky modes. The light transmission is limited by back-reflection at the NW top end. The abrupt change in refraction order between the NW and the surrounding environment scatters the transmitted light at large angles θ. Adapted from [15]. b-c) Schemes of the light outcoupling through expansion of the fundamental photonic mode in the needle- (b) and (c) trumpet-shaped NWs [92, 16].

demonstrated as components for electronic devices, such as LEDs [34], avalanche photodiodes [105], and single-electron transistors [106].

All the components necessary for integrated photonics purely based on Si are available, with the significant exception of a light source [107]. On the contrary, III-V semiconductors, such as (Al)GaAs and In(Ga)As, have excellent optoelectronic properties and QDs grown with these materials are attractive as triggered SP sources. The integration of III-V direct-bandgap light emitters on Si is not straightforward. One challenge concerns the lattice-constant mismatch between Si and III-V semiconductors. NWs and NWQDs can effectively tackle this issue by reducing the interface area between the two lattice-mismatched semiconductors and by offering a high surface-to-volume ratio to relax the accumulated stress.

Turning to NW photonics, the large difference of refractive index between the NW semiconductor and the surrounding medium turns the NW into a light waveguide. An axial NWQD can be precisely positioned on the NW axis by VLS growth. In this position, the QD emission can strongly couple with the fundamental HE_{11} mode of a NW waveguide (figure 2.10a). The coupling between the QD emission and the NW-waveguide modes affects the rate of the spontaneous emission of the embedded QD. A convenient way to describe the coupling efficiency is to consider the fraction β of emitted photons that is channeled into the desired mode, as the HE_{11} mode for an axial NWQD [15]. The interesting aspect of this outcoupling scheme is that it is broadband: the coupling efficiency is relatively high in a wide range of emission energies of the embedded QD. In quantitative terms, the QD emission in a NW waveguide has been simulated at different emission wavelengths λ in vacuum by considering a dipole positioned on the main axis of a waveguide of diameter D and calculating the fraction β of photons coupled to the HE_{11} mode [15]. These simulations show that β is above 90% for a broad range of values of $\frac{D}{\lambda}$ ranging between 0.20 and 0.29. This result is almost wavelength-independent and only relies on the efficient coupling of the dipole emission into the HE_{11} mode. The highest coupling corresponds to $\frac{D}{\lambda}$ of about 0.22. In thinner waveguides the coupling efficiency is hindered by the leakage into a continuum of nonguided modes [108], sketched as

leaky modes in figure 2.10a. On the contrary, for thicker diameters higher-order modes are supported by the NW waveguide and subtract photons from the targeted HE_{11} mode. The broadband operation of the NW waveguiding effect is particularly advantageous if compared to the Purcell effect. A waveguided mode is established in the NW as a consequence of the total internal reflection of light in the NW, which, in turn, relies on the difference of refractive index between the NW material and the surrounding. The refractive index is a function of the light wavelength with a smooth dependence. On the contrary, the Purcell effect relies on interference phenomena that are strictly sensitive to the wavelength-dependent formation of a resonant mode in the cavity. Therefore, the coupling with waveguide modes allows to enhance the whole spectrum of relatively broadband quantum emitters, while in the Purcell effect only a small fraction of the light stemming from a broadband emitter can couple to the cavity mode and be enhanced. Experimentally, the QD lateral size can be tuned independently from the NW diameter, by growing an outer shell around the NW after the QD formation. The shell growth can either happen by enhancing the lateral overgrowth during the axial NW growth [16] or by a two-step process in which the axial growth of the NW is stopped and a shell is deposited on the NW sidewalls [35]. With both strategies it is possible to tune λ and D independently. PL measurements on InAsP QDs positioned on the axis of InP NWs of different diameters confirm that the best coupling of the QD emission lies around $\frac{D}{\lambda} = 0.24$ [16]. The estimated enhancement of the spontaneous emission corresponds to a quantum efficiency of about 92%.

Because of total internal reflection, only ~ 2% of the light stemming from an emitting dipole in the bulk escapes from a solid cone of limited aperture; the rest of the light is trapped inside the device. On the contrary, the waveguiding effect of a NW is used to enhance the light outcoupling and overcome the low light extraction from planar devices. However, the light inside the NW is constrained within a sub-wavelength space and, when it crosses the flat end of the NW, the abrupt decrease in refractive index makes it scatter at large angles θ (figure 2.10a). The broad scattering prevents the efficient collection by optics with small numerical aperture (NA). In order to overcome this issue, the shape of the NW tip has been engineered to gradually expand the waveguide mode into the surrounding medium. Resorting the concept of refractive index, the engineered shape of the NW tip slowly decreases the effective refractive index of the NW until it matches the one of the external environment. This effect is currently achieved by two methods: by reducing the NW diameter in a needle-like tip [35, 92] or by expanding the NW into a trumpet-like shape [109]. These two configurations are reported in figures 2.10b and c, respectively. In the needle-like tip, the photon transmission is a function of the tapering angle: the smaller the angle, the better the transmission. Tapered NW needles were demonstrated by both top-down [17] and bottom-up [35] engineering of the NW diameter. In the bottom-up approach, it is easier to obtain very small angles: 1.5°±0.2° tapering angles were demonstrated in this way and a first-lens extraction efficiency of 0.42 is reported [35]. The NW tapering is not the only factor to consider to enhance the light extraction. A bottom mirror is useful to collect the light travelling to the opposite NW end. Gold is an optimal material for the light reflection at near-infrared (NIR) wavelengths, with a thin SiO_2 layer to prevent the dissipation

of the photon into plasmonic coupling with the metal [92, 15]. In presence of the bottom mirror, the NW becomes a half-cavity, which brings further constraints to optimize the light extraction. In particular, the mirror sets a stationary wave in the NW and the QD must be precisely positioned at a wave antinode [17], which means accurate control on the QD position along the NW. Light extraction efficiency of 0.72 is reported for a needle-tip NW obtained by top-down etching and integrated on a SiO_2-Au mirror [92]. A very high external efficiency of 0.75±0.1 is also reported for the trumpet geometry [109].

A further concern is that the light should outcouple with an intensity profile that optimizes the collection by commercial optics. In the ideal case, the light intensity should decrease from the center of the beam to the edges with a Gaussian profile. From both trumpet-like [109] and needle-like NWs [110] the emitted light closely matches the intensity profile of a Gaussian free-space beam. Thanks to this effect, a record coupling of 0.93±0.03 was achieved between the light emission from a needle-like NW and a single-mode optical fiber [110]. As a demonstration of the importance of the shape engineering of the NW tip, the intensity profile of the light emitted from an InP NW with a flat top facet has a maximum at an angle of 49° from the direction of the NW longitudinal axis [111]. This may depend on the fact that the NW environment selects the outcoupling polarizations and favors the dipoles aligned along its longitudinal axis [111]. By engineering the NW cross section, the NW is used to tune the polarization of the emitted light. Only the light polarized along the major axis of an asymmetric NW cross section can outcouple if the short axis is small enough not to support an electromagnetic mode. The polarization selection has been demonstrated by growing NWs with anisotropic cross sections by both the top-down [112] and bottom-up [113] methods.

Off-axis NWQDs weakly couple with the fundamental mode of a NW waveguide. However, their peripheral position offers interesting opportunities. Radial QDs can couple to higher order modes, air modes and the continuum of the radiation modes of the NWs [17]. For instance, the NW TE_{01} mode, a peripheral mode, has been coupled into SiO_2 waveguides to obtain III-V NW lasers integrated on Si chips. The same mode can couple strongly with radial QDs, which suggests the possibility of coupling the radial-QD emission into the waveguide [114]. The luminescence of radial QDs was observed in NW cross sections of controlled thickness obtained by ultramicrotomy [115]. These NW cross sections support peripheral cavity modes that could be coupled with the optically active QDs. A further advantage of radial NWQDs is that they offer enhanced sensitivity to external fields, thanks to their proximity to the NW surface. NWs are attractive probes to scan external fields [116], such as electric fields, with spatial resolution defined by their diameter. Radial NWQDs add further functionalities, such as the possibility to read out the local electric field at the QD position by the emission Stark shift. As mechanical resonators, NWs have ideal characteristics: small masses, high resonance frequencies and low dissipation. Radial QDs strongly couple to strain fields induced by the static bending [117] or by oscillations of the NW [118]. Large optomechanical coupling between radial QDs and a NW oscillator are reported for the same kind of NWQDs studied in this thesis [118]: the NWs were clamped at a piezoelectric actuator and the emission energy of the embedded radial QDs shifted as a function of the oscillation frequency. The QD-NW

optomechanical coupling offers a way to read out the mechanical status of the NW; if the NW displacement is driven by an external field, the same read-out scheme is a protocol to map the external field.

2.3.4 State of the art in nanowire-quantum-dot optics

In this subsection, a brief overview of the state of the art of the performance of NWQDs as SP emitters is provided. Specific focus is dedicated to discuss the NWQD emission purity, $g^2(\tau)$, and FSS. A conclusive paragraph reports on the NWQDs studied in this work.

Surface states in semiconductors can very efficiently act as non-radiative exciton recombination centers. The passivation of the NW surface through the deposition of a semiconductor shell of higher bandgap can largely enhance the intensity of the NW luminescence: the larger-bandgap shell keeps the charge carriers farther from the surface [1, 49]. The semiconductor surface can host carrier traps and adsorbates that induce charge space fluctuations: the charge capture and escape from traps induces a time-dependent variation of the electric field in the surroundings of the trap. Crystal defects, such as rotational twins, can have a similar effect: the twin plane limits the charge movement along the main NW axis, but does not constrain the charges in the NW cross section and the moving charge generates a varying electric field in the surroundings [11]. The electric field affects the position of the energy levels of a nearby NWQD by Stark effect. Integrated over time, this time-dependent Stark effect results in the broadening of the NWQD linewidth. The degradation of the spectral purity of the QD emission is detrimental for the implementation of SP-based qubits. At high excitation power the QD emits at the highest rate and its emission intensity saturates. However, in these conditions the charge fluctuations also increase and the QD emission linewidth undergoes an additional broadening. This effect is known as power broadening. An additional broadening to the Fourier-limited emission linewidth of QDs and NWQDs is the interaction with phonons [119]. This can be suppressed by acting on the phonon population at very low temperatures or by selecting the emission modes in a cavity [120].

The research on NWQDs tackled these challenges. The NWQD emission linewidth has regularly narrowed during the last decade. Initial reports on (Al)GaAs NWQD systems grown by MOVPE show linewidths in the meV range [32]. A reduction to less than 100 μeV was later reported for the MBE-grown (Al)GaAs NWQDs studied in this thesis [14]. Charged states at the interface of the core-shell structure were considered at the origin of the linewidth broadening. Recently, emission linewidths down to 30 μeV were reported for InAsP QD in InP NWs [11]: a thick shell was used to push the surface charges farther from the axial QD in the NW core and the WZ NW was free of crystal defects. InAsP QDs in defect-free InP NWs hold a record emission linewidth of less than 4 μeV [121]. The NW was not coated by a thick shell: in this case, the charge traps were saturated by tuning the excitation power and the exciton-phonon interaction was suppressed by measuring at 300 mK. The state-of-the-art linewidth of NWQDs [121] and bulk QDs [71, 77] are nowadays comparable.

Poor control on the NW crystal phase does not only degrade the purity of the NWQD emission, but also their performance as SP emitters. In III-V binaries, such as InP [122] and GaAs [14, 61], WZ and ZB have a type-II band alignment that favors the localization of electron in ZB segments and holes in WZ segments in polytypic NWs. The energy of the spatially indirect e-h recombination across the ZB-WZ interface ranges between the ZB and WZ bandgaps, as detailed in subsection 2.1.2. These photons are a background source that increases the zero-delay counts of a $g^2(\tau)$ measurement [11]. Zero-delay coincidence counts below 1% were demonstrated in defect-free InP NWs [11]. Polytypism and stacking faults are common in bottom-up NWs, but are naturally absent by the top-down approach. Bulk InAs SKQDs positioned in NWs by post-growth etching of a needle-like NW structure show $g^2(0)$ below 0.8% [92]. Cutting-edge detectors are used to suppress background and false counts in the $g^2(\tau)$ measurements of bulk QDs; together with the implementation of excitation schemes that suppress multi-photon emission, bulk QDs have the best performance as SP emitters (see subsection 2.2.2). However, the state-of-the-art $g^2(0)$ values in bulk QDs [77] and NWQDs [92, 11] are similar if measured in comparable conditions, that is, without schemes of background-emission reduction and with traditional SP detectors.

As a final figure of merit, the FSS of NWQDs is discussed. Axial NWQDs with hexagonal cross-section and positioned in NWs grown along the ⟨111⟩ crystal direction are expected to have a vanishing FSS thanks to the high symmetry of this configuration [76, 123]. The absence of FSS is necessary to emit entangled photons for quantum-information processing [18]. FSS = 8 μeV [11] and below 2 μeV [123] are reported in NWQDs. These FSS values are small enough to obtain highly polarization-entangled X-XX photon pairs with no need of signal post-processing [123, 124]. The measurement of the FSS is performed by analyzing the NWQD emission in two orthogonal linear-polarization bases. Therefore, the influence of the NW dielectric on the emission polarization must be taken into account and the polarization basis should compensate for the asymmetry of the NW cross-section aspect ratio [123, 124]. Considering both entanglement fidelity and source efficiency, NWQDs have a very high performance [124]: the fidelity of entangled states is competitive with other technologies, including bulk QDs and parametric down-conversion, while the efficiency of photon-pair generation is supported by the waveguided photon outcoupling. The improvement of the NWQD emission linewidth, $g^2(0)$, and FSS has been considerable in the last years. This evolution, together with the superior properties offered by the NW acting as a waveguide, show the potential of NWQDs to be a standard for the solid-state generation of SPs on demand.

To conclude, the optical properties of the NWQDs studied in this thesis are summarized hereafter as obtained from measurements performed at 4 or 12 K. These NWQDs show X, CX, and XX emission lines [125]. The XX binding energy is about 4-6 meV, with the CX and XX emissions that are in general at lower energy than the X one (figure 2.7b). Polarization-resolved PL measurements provide cautious evidence of the positive charge of the CX emission [74]. Their SP emission is supported by $g^2(0) < 0.5$ (figure 2.11a), with extrapolated values at zero delay of about 2% [14]. The X emission linewidth is typically below 100 μeV down to 29 μeV [14]. Space charge fluctuations and anisotropic-exchange splitting are responsible for the
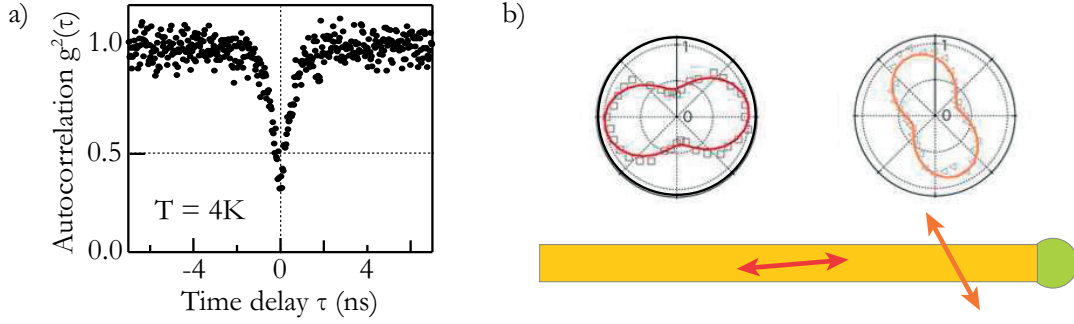
Figure 2.11 – a) Autocorrelation function of one of the NWQDs studied in this thesis that shows a $g^2(0) < 0.5$. b) Polarization plot of two NWQDs at different positions along the NW, as indicated by the NW sketch underneath. Adapted from [14].

linewidth broadening: in particular, the anisotropic exchange interaction was estimated to be also in the order of 100 μeV [125]. These values are comparable with those reported for GaAs QDs grown by droplet epitaxy [126]. In that case, the anisotropic shape of the QDs, with an in-plane aspect ratio between 10% and 25% accounted for FSS between 50 μeV and 250 μeV. Polarization-dependent PL shows that most of the NWQDs studied here are probably elongated with a high aspect ratio, which correlates with their large anisotropic-exchange energy. These quantum emitters emit light that is preferentially polarized along a single direction, although this direction has a random relation with the main axis of the NW and changes from QD to QD [14]. Figure 2.11b reports the polarization plots of two QDs at different positions along the NW. In view of the manipulation of these quantum emitters as a source of photon qubits, it has been proved that these NWQDs can couple with an external magnetic field. The strength of the coupling varies according to the orientation of the external field with respect to the QDs [127].

2.4 Light-emission engineering

The goal of the work in this thesis is to engineer the light emission energy of self-assembled NWQDs in resonance with the absorption energy of a gas of Rb atoms. Rb cells are considered as promising building blocks for fundamental components of future quantum networks, such as quantum memories and repeaters. The NWQDs considered in this thesis emit in an energy range between 1.6 eV and 1.9 eV, while the targeted Rb D2 transition is at 1.589 eV (780 nm). For this reason, we studied different means to redshift the NWQD emission.

Collaborators in Martino Poggio's group at the University of Basel showed the strong coupling of the emission of these radial QDs with the NW mechanical modes under dynamic strain [118]. The QD emission energy was observed to shift by about 10 meV. Given the oscillating nature of the applied field, the QD emission varies over time according to the frequencies of the mechanical resonances of the host NW. Because of the limited and time-dependent energy shift, this strategy is not considered suitable to reach the goal of this thesis: a larger energy

redshift is necessary and a steady energy shift is desired. In a time-dependent scheme the majority of the photons is emitted out of resonance with the Rb absorption.

In the same group at the University of Basel, the effect of an external electric field was tested, too. The static Stark shift due to the external field was accompanied by a Stark shift variable in time, probably as a consequence of space charge fluctuations in the QD surroundings. The overall emission shift was not easily controlled and finer control on the dielectric environment around the QDs is necessary. In addition, an external electric field reduces the overlap of the electron and hole wavefunctions in a QD, which weakens the QD oscillator strength and emission brightness [128]. The effect of an external magnetic field on the studied NWQDs is extensively reported in refs.[125, 127]: these measurements allowed to observe the Zeeman splitting of the QD energy levels, calculate the QD diamagnetic coefficient and collect information on the coupling efficiency with the magnetic field.

As demonstrated in ref. [129], electric and magnetic fields represent excellent ways to finely control the QD emission over few-meV energy ranges and tune it in resonance with the Rb absorption. However, these energy shifts are insufficient to match QD emission and Rb absorption. Temperature has a large impact on semiconductor bandgaps [130], but the emission of the QDs studied here is suppressed above 50 K - 70 K [74].

In this thesis, static strain and composition engineering have been used to tune the bandgap of self-assembled AlGaAs QDs. Both methods are interesting because of the large redshift of the emission energy that can be achieved. GaAs PL redshift of about 300 meV is reported upon the elastic NW deformation: tensile strain values up to 3.5% are reported [131]. NWs are an excellent platform to apply large strain fields: bulk GaAs cannot stand such high values of strain without undergoing plastic relaxation. The composition engineering of the NW semiconductor ideally tunes the NW bandgap and NWQD energy levels over hundreds of meV. In this thesis, the QD emission energy was redshifted by about 300 meV by alloying the AlGaAs-shell matrix with indium. In the following, a description of the effect of strain and composition on the bandgap of a semiconductor alloy is provided from a general and theoretical point of view.

2.4.1 Bandgap engineering by static strain

GaAs phonon modes and Raman spectroscopy

The lattice dynamics in a semiconductor supports a number of modes equivalent to the vibrational degrees of freedom of the unit cell. For ZB GaAs, two different atoms compose the unit cell, which corresponds to six total degrees of freedom. These degrees of freedom are associated with the translation of the center of mass of the unit cell. They correspond to modes of vanishing energy (frequency) for zero k vectors (Γ point) and are usually referred to as acoustic modes. The three remaining degrees of freedom are associated with distortions of the unit cell with no movement of the center of mass. These modes have non-zero energy for
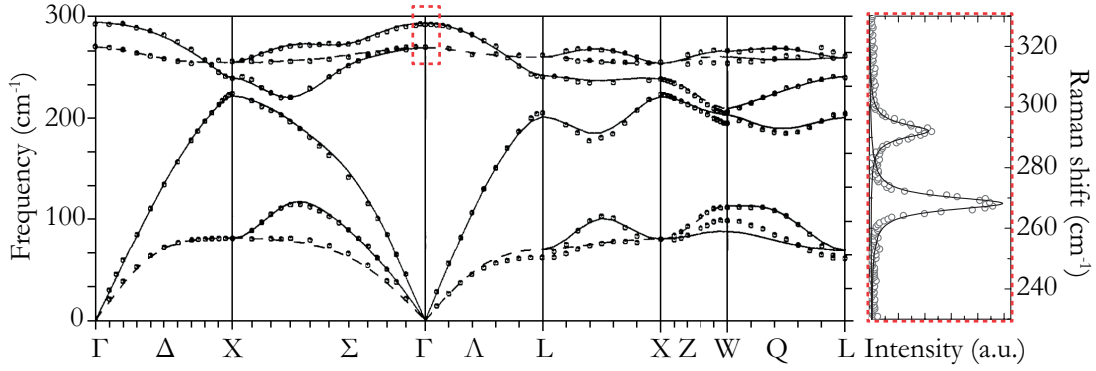
Figure 2.12 – Phonon dispersion in ZB GaAs: the dots are experimental data obtained by neutron scattering and the solid lines a theoretical derivation [133]. The red dashed square highlights the optical phonon modes at the Γ point. A Raman spectrum from a GaAs wafer corresponding to this region of the reciprocal lattice is reported on the right.

k vectors equal to zero: their interaction with photons at the Γ point is visible as a change in the photon energy. These phonon modes are thus referred to as optical modes. Figure 2.12 shows the acoustic and optical phonon branches of GaAs. The atoms involved in the optical modes can oscillate along directions parallel or perpendicular to the k vector of the phonon wave. In the first case the mode is called longitudinal optical (LO), while in the second case it is called transversal optical (TO). Ga and As form a dipole that generates an electric field in the direction on the phonon k. Therefore, the LO modes have additional energy with respect to the TO modes: the TO-LO energy difference is referred to as piezoelectric splitting of the TO-LO modes. In bulk GaAs ZB, the energies of the two modes are $E_{TO} = 268$ cm^{-1} and E_{LO} = 292 cm^{-1} [132, 133], in good agreement with the values reported for GaAs NWs [134, 135]. The WZ unit cell has a four-atom base. The increase in the number of atoms brings additional degrees of freedom to the atom vibrations with respect to ZB. Nine optical phonon modes are possible in WZ GaAs and partially overlap in energy with the ZB modes. No further details on the phonon modes in the WZ phase are provided in the following, since ZB is the phase of interest in the NWs studied here.

The phonon frequencies of any lattice depend on the average distances and relative positions of the atoms. When external stress deforms a semiconductor unit cell, the atom vibrations and phonon energies are modified. The study of the modified phonon modes provides information about the entity and nature of the strain. Raman spectroscopy is a non-destructive technique to study the phonon modes in strained semiconductors. Raman scattering is an inelastic interaction between light and matter. In classical terms, Raman scattering can be described considering the polarization of a material upon the interaction with an incident light wave. In Einstein's tensor notation, the polarization P induced by the external field **E** depends on the material susceptibility χ by:

$$P_\nu = \chi_{\nu\mu} E_\mu, \tag{2.2}$$

χ describes the material response to an external electromagnetic field. This response depends on the position of the atoms in the material and is modulated by their displacement $\mathbf{W}$. It is thus convenient to split the overall material susceptibility into a static contribution X_0 and one that varies with $\mathbf{W}$:

$$\chi_{\nu\mu} = \chi_{\nu\mu}^0 + \frac{\partial \chi_{\nu\mu}}{\partial \mathbf{W}}\mathbf{W}. \tag{2.3}$$

By substituting equation 2.3 into equation 2.2, the elastic and inelastic terms of the polarization are made explicit. These two terms respectively oscillate at the same or at a shifted frequency with respect to the driving field:

$$P_\nu = \chi_{\nu\mu}^0 E_\mu + \frac{\partial \chi_{\nu\mu}}{\partial \mathbf{W}}\mathbf{W}E_\mu = P_\nu^{elastic} + P_\nu^{inelastic}. \tag{2.4}$$

The dipole induced in the material that oscillates at a lower (higher) frequency with respect to the incident light emits at lower (higher) energy: the two energy shifts are respectively known as Stokes and anti-Stokes shifts. The dipole vibration at the same frequency as the incident light is responsible for the appearance of the Rayleigh peak, in between the Stokes and anti-Stokes peaks, in the Raman spectra. In a quantum description of the inelastic nature of Raman scattering, the energy is provided or subtracted to the incident photon by, respectively, annihilation or creation of a quasi-particle excitation in the matter, such as a plasmon or a phonon. The scattered photon undergoes an energy shift to lower or higher frequency (Stokes and anti-Stokes respectively). In typical Raman spectra, only a small portion of the incident photons undergoes inelastic scattering, while most photons generate an elastically scattered peak at the same energy as the incident photons, that is the Rayleigh peak. In the quantum picture of the process, one can observe that the Raman scattering involves a third quasi-particle that is not necessary in the elastic scattering. This difference is at the origin of the low probability of the Raman scattering process and its low brightness.

In both the classic and the quantum description of the Raman scattering, it is possible to compute the intensity of the scattered signal as a function of the polarization of the incident and scattered light and the orientation of the probed crystal. Together with the presence of crystal-phase-dependent modes, this relation can provide structural information on the phase and orientation of the probed crystal. For instance, in the classical picture of light-phonon Raman scattering, it is possible to consider a plane-wave form for both the incident electromagnetic field $\mathbf{E}$ and the atomic displacement $\mathbf{W}$:

$$\begin{aligned} \mathbf{W} &= \mathbf{W}_0 cos(\mathbf{q}\,\mathbf{R}_l - \omega_p t); \\ \mathbf{E} &= e_i E_0 cos(\mathbf{K}_i \mathbf{r} - \omega_i t), \end{aligned} \tag{2.5}$$

where e_i is the polarization of the incident light, E_0 is the amplitude of the electromagnetic field and $\mathbf{W}_0$ is the amplitude of the atomic-displacement wave. Equations (2.4) and (2.5) give a form of $\mathbf{P}^{inelastic}$ from which the intensity of the scattered light is calculated as a function of

the material susceptibility and the polarization of the incident (e_i) and scattered (e_s) light:

$$I^{inelastic} \propto \left| \mathbf{e}_s \cdot \mathbf{P}^{inelastic} \right|^2 = \left| e_{s\nu} \frac{1}{2} \frac{\partial \chi_{\nu\mu}}{\partial \mathbf{W}} \mathbf{W}_0 e_{i\mu} \right|^2 E_0^2. \tag{2.6}$$

By defining a second-order Raman tensor:

$$R_{\nu\mu}^{\mathbf{w}_i} = \frac{1}{2} \frac{\partial \chi_{\nu\mu}}{\partial w_i}, \tag{2.7}$$

the scattering intensity is written in a compact way as:

$$\left| e_s R^{\mathbf{w}_i} e_i \right|^2. \tag{2.8}$$

R describes how the material susceptibility varies upon interaction with a phonon mode. Light is composed of transversal electromagnetic waves. Therefore only some phonon modes can interact with light of a certain polarization and incident direction. In particular, the product of R with some directions of e_i and e_s is zero, meaning that a specific phonon mode has no effect on the light polarized in certain directions. These configurations define a set of selection rules specific for each crystal structure and orientation. In the work presented here, the NWs have always been studied in backscattering configuration: the incident and scattered light propagate along the same direction in opposite senses; this direction is perpendicular to the {110} side facet of a horizontal NW. In the case of a ZB NW, the LO phonon mode is forbidden for any choice of the polarizations e_s and e_i. Since visible photons carry negligible momentum with respect to phonons, Raman spectroscopy provides information about the phonon branches near the Γ point. When the lattice periodicity is interrupted by surfaces, like in nanostructures with high surface-to-volume ratio, the loss of periodicity relaxes the conservation of momentum and phonons farther from the Γ point can contribute to the Raman spectra. This effect results in a broadening and downshift of the Raman peaks [136], but it is negligible in GaAs NW with diameters larger than about 20 nm such as those studied in this work.

Band structure and phonon modes under deformation

In this thesis, Raman spectroscopy is used to determine the strain in NWs through the measurement of the phonon modes. The NW response to strain depends on its crystal phase: here the focus is on ZB NWs [137]. For simplicity, we consider the cube shown in figure 2.13a. The body mechanics can be described by the application of forces to the cube facets. At equilibrium conditions, only the three forces $\mathbf{F}_1$, $\mathbf{F}_2$, and $\mathbf{F}_3$ are necessary; they correspond to the forces applied to the cube faces with normal vectors $\mathbf{n}_1$, $\mathbf{n}_2$, and $\mathbf{n}_3$. Each force $\mathbf{F}_i$ can be decomposed into the three component $\mathbf{F}_{ij}$, with $j = 1, 2, 3$ along the axis system defined by the vectors $\mathbf{n}_i$. Stress is defined as the ratio between a force and the area of the surface to which it is applied. The stress component σ_{ij} is the ratio between the force component F_{ij} and the area of the face normal to n_i. $\sigma_{ij} > 0$ corresponds to tensile stress. Imposing the
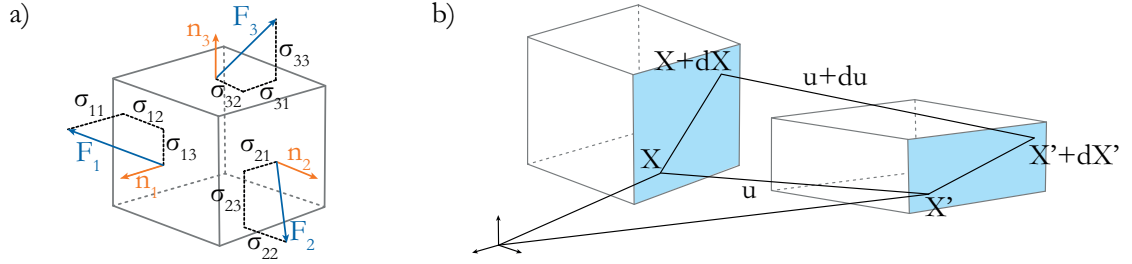
Figure 2.13 – a) Sketch of a cube subject to forces F_1, F_2, and F_3 depicted in blue. In orange the vectors normal to the faces n1, n2, and n3. The *ij* indices correspond to the indices of the stress components σ_{ij}. b) Deformation of the reference cube: illustrative positions X and X+dX as well as the transformed X' and X'+dX' are indicated and linked by the displacement vectors u and u+du, respectively.

mechanical equilibrium, the sum of forces and momenta is zero and $\sigma_{ij} = \sigma_{ji}$. Figure 2.13b helps to analyze the body deformation by means of the component u_i of the displacement vector u that links each component x_i of each point x of the body with its new coordinates x'_j.

$$x'_j = \sum_i (1 + e_{ij}) x_i, \tag{2.9}$$

where e_{ij} are the components of the displacement tensor defined as

$$e_{ij} = \frac{\partial u_i}{\partial x_i}. \tag{2.10}$$

The displacement tensor describes both rigid rotations and deformations of the body, respectively by components $\epsilon_{ij} = \frac{1}{2}(e_{ij} - e_{ji})$ and $\epsilon_{ij} = \frac{1}{2}(e_{ij} + e_{ji})$. The interest here is for the second, whose components constitute the strain tensor. Under small forces, a linear relation exists between stress and strain, which defines the elastic compliance S and stiffness C tensors as follows:

$$\epsilon_{ij} = S_{ijkl}\sigma_k l, \tag{2.11}$$

$$\sigma_k l = C_{ijkl}\epsilon_{ij}. \tag{2.12}$$

Uniform stress in all directions is called isotropic stress: it is also called hydrostatic because a body under a column of liquid is subject to the same pressure and stress in all directions. The strain tensor is diagonal, with components:

$$\epsilon_{ij} = \begin{cases} \epsilon_h = -P/3B & \text{for } i = j \\ 0 & \text{for } i \neq j \end{cases} \tag{2.13}$$

P is the hydrostatic pressure and B the bulk modulus that describes the ratio between the relaxed and stress volumes of the body. Being diagonal, hydrostatic stress changes the volume of the lattice unit cell without deformation of the interatomic-bond angles. The bond length varies by $\Delta r = r_0 \epsilon_h$, where r_0 is the unstrained bond length. The hydrostatic mode Grüneisen

parameter γ_i links the shift in the phonon energy of the i-th mode with the applied strain ϵ_h:

$$\gamma = -\frac{d\ln\omega_i}{d\ln V} = -\frac{\Delta\omega_i}{3\epsilon_h\omega_i}, \tag{2.14}$$

where V is the volume of the unit cell and ω_i is the frequency of the i-th phonon mode. Hydrostatic stress is mathematically the simplest case. It is used in chapter 6 to approximate the strain rising in the GaAs core from the lattice mismatch between the core and the shell materials of the studied NWs.

In more general cases, the applied stress is anisotropic. In chapter 5, uniaxial stress is used as a theoretical frame of the experimental results. Uniaxial stress is applied along a single direction that, in the case of the NW studied here, corresponds to the <111> NW longitudinal axis. Therefore,

$$\sigma_{ij} = \begin{cases} \sigma = & \text{for } i = j = 3, \\ 0 & \text{otherwise.} \end{cases} \tag{2.15}$$

Strain results in the following tensor [131]:

$$\epsilon_{ij} = \begin{bmatrix} \epsilon_\perp & 0 & 0 \\ 0 & \epsilon_\perp & 0 \\ 0 & 0 & \epsilon_\parallel \end{bmatrix}$$

The Poisson ratio ν is the ratio between $\epsilon_\perp$ and $\epsilon_\parallel$:

$$\nu = -\frac{\epsilon_\perp}{\epsilon_\parallel}, \tag{2.16}$$

which can strongly depend on the crystalline direction in which the uniaxial stress is applied. It is always possible to separate a strain tensor into hydrostatic and deviatoric contributions. The hydrostatic term is the average of the ϵ_{ii} components of the strain tensor; it is therefore isotropic and corresponds to the volume variation of the lattice unit cell without deformation of the bond angles between atoms. The term that remains by subtraction of the hydrostatic strain from the total one is called deviatoric strain. It describes the deformation in the bonding angles without changing the overall volume of the unit cell.

Tensile stress is used in this work to lower the bandgap of the studied NWs. Strain alters the periodicity of the lattice potential and the energy position of the edges of the CB and VB. With specific focus on the HH and electron bands at the Γ point, it can be demonstrated that, under uniaxial stress [131]: the CB edge linearly decreases in energy with increasing tensile strain; the HH VB edge linearly increases in energy with increasing tensile strain; uniaxial stress lifts the LH and HH degeneracy; the energy separation between the HH and LH bands increases with strain; the HH band is at higher energy under tensile strain. Overall, the semiconductor bandgap decreases linearly with increasing tensile strain, as a results of the decreasing energy

distance between the CB edge and the HH VB edge:

$$\Delta E^{cb-hh} = \Delta E_{hydro} + \Delta E_{shear} = \left[3ah + \frac{\sqrt{3}}{2}d_v(1-h)\right]\epsilon_{\parallel}, \tag{2.17}$$

where a and d are the hydrostatic and shear deformation potentials and v is the Poisson ratio in the [111] direction. Equation (2.17) is composed of hydrostatic and deviatoric contributions to the energy shift of the bandgap. The factor $h = \frac{1-2v}{3}$ weights these two terms with the portion of elongation that is converted into isotropic volume change or shear deformation, respectively.

The deviatoric component has a different effect on the modes parallel and perpendicular to the axis of strain application. In the case of uniaxial strain along the [111] direction of a ZB crystal, a singlet TO mode (TO_S) is identified in the [111] direction of the applied strain, while the LO and TO modes along the two orthogonal directions perpendicular to [111] compose a doublet (LO_D and TO_D). Therefore the TO modes vibrate at two different energies TO_S and TO_D according to their direction of vibration. Thanks to the Raman selection rules, these two modes can be distinguished by selecting the linear polarization of the collected signal: linear polarizers parallel and perpendicular to the stress direction allow to observe the TO_S and TO_D modes respectively. Without any selection of the polarization of the scattered light, the TOs dominates the Raman spectra [131]. This effect is probably a consequence of the elongated NW geometry that favors the outcoupling of the light polarized along the NW longitudinal axis. It can be demonstrated that all the phonon frequencies undergo a linear decrease with the applied tensile strain, according to the following equations [131]:

$$\frac{\Delta\omega_{TO_S}}{\omega_{TO_S}} = \left[-3\gamma_T h + r'_T(1-h)\right]\epsilon_{\parallel}, \tag{2.18}$$

$$\frac{\Delta\omega_{TO_D}}{\omega_{TO_D}} = \left[-3\gamma_T h - \frac{1}{2}r'_T(1-h)\right]\epsilon_{\parallel}, \tag{2.19}$$

$$\frac{\Delta\omega_{LO_D}}{\omega_{LO_D}} = \left[-3\gamma_L h - \frac{1}{2}r'_L(1-h)\right]\epsilon_{\parallel}. \tag{2.20}$$

γ_T and γ_L are the hydrostatic mode Grüneisen parameters (γ_T = 1.35 and γ_L = 1.07), while r'_T and r'_L are the deviatoric mode Grüneisen parameters (r'_T = -0.88 and r'_L = -0.53) [131]. These two sets of Grüneisen parameters highlight that each equation is composed by a hydrostatic and a deviatoric term.

2.4.2 Bandgap engineering by composition

As a second strategy to redshift the emission energy of the NWQDs studied in this thesis, the AlGaAs NW shell was alloyed with indium. To illustrate the effect we searched, we consider two semiconductors A and B and a property P, such as the bandgap or the lattice constant: A and B are characterized by P_A and P_B, respectively. Mixing A with B results in a new semiconductor AB with an intermediate property P_{AB}. The simplest way to calculate the value of P_{AB} is by
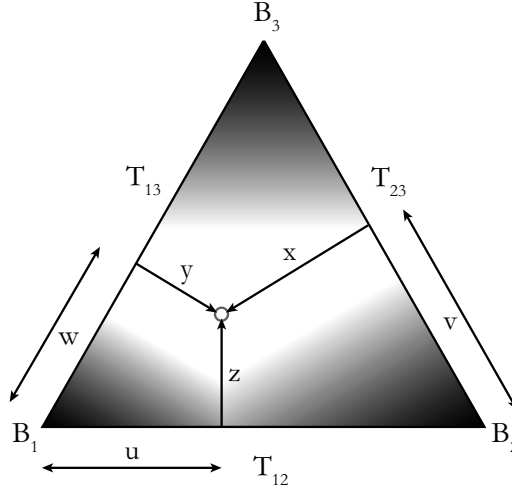
Figure 2.14 – Illustration of the composition variables for ternary (x, y, z) and quaternary (u, v, w) alloys. Based on a scheme similar to the one of ref. [138].

linear interpolation between P_A and P_B in proportion with the relative concentration of A and B in $A_{1-x}B_x$, the so called "Vegard's law". This simple case was used to describe the lattice constant of ternary semiconductors and is known as Vegard's law [139]. It is especially valid when the atomic size of the constituents A and B is similar. A proportionality often exists between the lattice constant of a semiconductor and its energy bandgap. Therefore, if Vegard's law is valid, a linear interpolation between the bandgaps of A and B is also valid to calculate a rough approximation of the bandgap of a compound of intermediate composition.

In real materials, alloy disorder perturbs the perfect linearity of the interpolation [140]. Alloy disorder is present in ternary arsenides, like AlGaAs, because two different group-III atoms can randomly take the same positions in the ZB lattice. For larger lattice mismatch between the extreme components A and B, the deviation from perfect linearity is roughly reported to increase [141]. A quadratic interpolation is often preferred to describe the bandgap of ternary alloys [142]:

$$E_g^{A_{1-x}B_x} = (1-x)E_g^A + xE_g^B - x(1-x)C, \tag{2.21}$$

where the bowing parameter C defines the deviation from the linear behavior. In III-V semiconductors, C is usually positive, that is, the quadratic interpolation gives a smaller bandgap than the linear one. The case studied in this work corresponds to the quaternary alloy AlGaInAs; with respect to a ternary alloy, the addition of a further element provides another degree of freedom to engineer the alloy properties. $Al_vIn_wGa_{1-v-w}As$ is a quaternary alloy of the $B_xC_yD_{1-x-y}A$ type, resulting from the combination of the three ternary arsenides AlGaAs, AlInAs, and GaInAs [138]. Figure 2.14 reports in a visual way the composition-variable space of a quaternary compound of three components B_1, B_2, and B_3 with properties T_{12}, T_{13}, and T_{23}.

Following the same approach as in equation 2.21 , one can derive the following equation for

the bandgap of quaternary $Al_v In_w Ga_{1-v-w} As$ [143]:

$$E_g = \frac{wv E_g^{InAlAs} + v(1-w-v)E_g^{AlGaAs} + w(1-w-v)E_g^{InGaAs}}{wv + v(1-w-v) + w(1-w-v)}, \quad (2.22)$$

with the room- and low-temperature E_g of the constituent ternaries available in ref. [143]. These are the values used in the present work (chapter 6). Although in theory one can consider a mixture of three components in any proportion, often miscibility gaps are observed: different constituents do not mix and segregate in the quaternary alloy forming regions that are predominantly composed of binaries or ternaries. Long-range ordering can also be observed, even in strain-free systems [94]. Strain and surface-energy gradients can further enhance the segregation of different species in different positions of the growth substrate. This topic is further discussed in chapter 6.

2.5 Slow light in gas vapors

The purpose of a photon-based quantum network is (i) to produce a controlled information flux encoded in the properties of the generated photons; (ii) manipulate this information; (iii) distribute it to the receivers. One of the practical barriers to the realization of a quantum network is the increasing error probability with the length of the channel connecting the nodes of the network. The implementation of quantum repeaters in the network is a strategy to overcome this limitation [144]. Atomic vapors are used as coherent slow-light media to implement quantum repeaters [23, 145]. A coherent slow-light medium receives a photon as input in a specific quantum state and releases it in the same state after a certain time delay with respect to its propagation in vacuum. Several slow-light protocols exist [145]. A central concept in slow light is the control of the light propagation by means of its group velocity v_g in a dispersive medium [146]:

$$v_g = \frac{c}{n + \omega(dn/d\omega)}, \quad (2.23)$$

where n is the refractive index and ω the light angular frequency. By controlling the dispersion of light $dn/d\omega$, one controls v_g: the more steeply n increases, the lower the group velocity becomes.

Large light dispersions are observed in proximity of a frequency-resonant gain or light absorption in given media. This property can be artificially obtained by electromagnetically induced transparency (EIT). EIT relies on a control optical field at frequency Ω_C to make a medium transparent to a signal field at frequency Ω_s. The transparency is achieved in a narrow spectral range within an absorption interval. The combination of a spectrally narrow transparency within an opaque region produces a positive refractive index for the signal, with a steep variation as a function of the light frequency in the narrow spectral range around Ω_s. The signal is therefore slowed down when passing through the medium. The light pulse that acts as signal is spatially compressed to a length l smaller than the initial one as a consequence
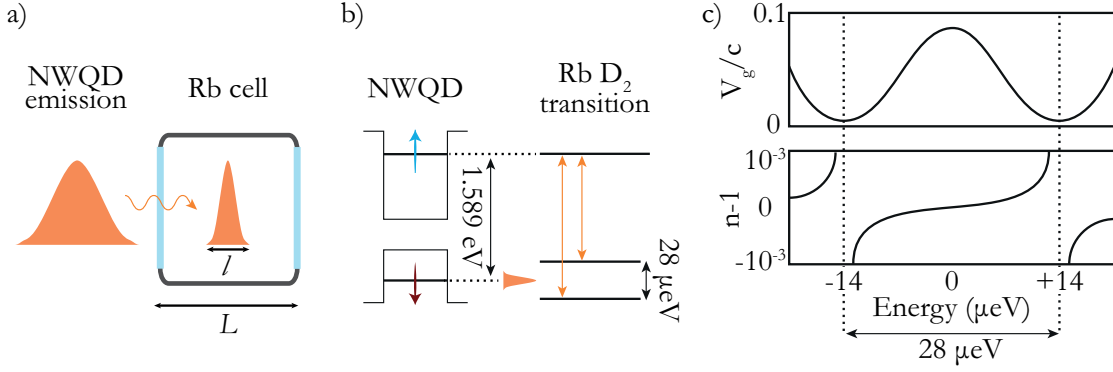
Figure 2.15 – a) Sketch of the contraction of a photon train within the length of a Rb cell. b) Scheme of the electronic levels of a NWQD and of the D_2 transition in a Rb atom. On the right, the refractive index and v_g corresponding to the D_2 resonances are qualitatively sketched.

of slowing down. If the compression is significant, the light pulse is completely contained within a medium of length L, that is $L > l$, as sketched in figure 2.15a. If the control field is turned off in this condition, then the signal is completely trapped inside an opaque medium and, in principle, it can be stopped. By turning off the control field, the input light is then released and collected with a certain time delay with respect to the transmission in vacuum. EIT has been used in the first proofs of slow light that used atomic vapors as a suitable medium [22, 23, 147]. The interesting feature in EIT on atomic vapors is that the signal is stored as atomic excitation in a coherent way: the quantum state of the light and its phase are preserved. The output light has therefore the same characteristic as the input [23, 147]. In the real case, atomic collisions degrade the coherence of the quantum states superimposed to the atoms and limit the storage time to fractions of ms in ultracold atom gases [23, 147].

More recently, atomic gases have been used as slow-light media with no need of EIT. In this case, the rapidly varying refractive index is an intrinsic property of the atomic system within two absorption resonances at a small energy distance from each other. The hyperfine levels of the ground state of alkali atoms represent the ideal case, although a similar configuration of energy levels is offered by any other system, such as QDs or photonic crystals, characterized by two absorption resonances close to each other. The hyperfine splitting of the ground level of an alkali atom generates two Lorentzian absorption resonances. Figure 2.15b is a scheme of the D2 transitions of [87]Rb atoms in resonance with the emission of a NWQD. The complex refractive index in proximity of the resonances is approximated as follows [145, 146]:

$$n(\omega) = 1 - \frac{A}{2}\left(\frac{g_1}{\omega - \omega_1 + i\gamma} + \frac{g_2}{\omega - \omega_2 - i\gamma}\right), \tag{2.24}$$

where ω is the photon angular frequency, ω_1 and ω_2 are the resonant frequencies, 2γ is the full width at half maximum of the resonances, g_1 and g_2 are the respective weights of the possibly different strengths of the two transitions and A is the total strength of the photon-atom coupling. A is proportional to the density of atoms in the gas phase in the cell: since Rb in a sealed cell is in thermodynamic equilibrium with its liquid phase, its gas density is an
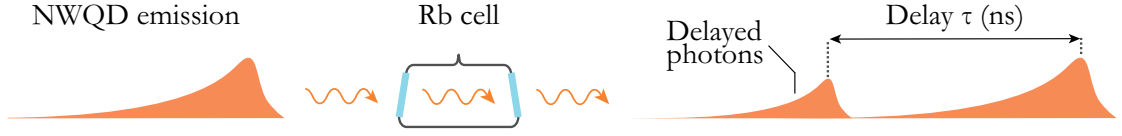
Figure 2.16 – Sketch of the transmission delay of SP through a Rb cell. Based on ref. [146].

exponential function of the cell temperature. Through equation 2.24 the real-part refractive index n and group velocity v_g can be calculated. Their qualitative behavior is shown in the two plots on the right of figure 2.15b: the refractive index n steeply increases between the two resonances, giving minimum v_g in proximity of the resonant frequencies.

Slow light has been reported with this method by using, e.g., Cs atoms [145] and Rb atoms [146]. The case of ref. [146] is very interesting: the signal field was a stream of SPs emitted from GaAs-AlGaAs QDs tuned in resonance with the D2 line of the Rb absorption at 780 nm [129]. The SPs were delayed by 15 times their temporal width, which was limited only by the repetition rate of 12.5 ns of the excitation laser used for the experiment. The delayed signal maintained its SP nature, with only one photon excitation in the Rb vapor at a time. In addition, the polarization of the photons used as input could be retrieved after the delay. This represents a fundamental proof of concept of quantum storage of SPs in a gas of Rb atoms. Interestingly, this demonstration was achieved even though the QD emission linewidth (80 μeV) is broader than the linewidth of the Rb absorption (28 μeV): only the photons within the high-dispersion region underwent the delay, while the off-resonant photons could be spectrally filtered, with no degradation on the maximum delay achieved.

3 Experimental techniques

3.1 Luminescence

Spectroscopy techniques were largely used in this thesis to study the NW and NWQD luminescence. Luminescence is the emission of light by a physical system upon relaxation from an excited state: the photon emission allows the system to transit to a state of lower energy, e.g. its ground state. Luminescence is primarily used in this thesis to determine the emission energy of the engineered NWQDs and NWs. In the following, the experimental aspects of the study of NW luminescence are discussed by distinguishing between laser and electron-beam excitation, that is, PL and CL, respectively.

3.1.1 Photoluminescence

PL is the incoherent and spontaneous emission of radiation from matter excited by an electromagnetic wave. In a semiconductor, an electron is photoexcited to the CB, leaving an empty state in the VB, i.e. a hole; the electron stays in the excited state for an average time interval τ_r, the characteristic lifetime of the transition after which it can release its energy by recombining with the hole and emitting a photon, i.e., by spontaneous photon emission. Electrons and holes can also recombine through non-radiative channels, characterized by decay times τ_{nr}. The characteristic PL decay time τ_{PL} is therefore:

$$\tau_{PL}^{-1} = \tau_r^{-1} + \tau_{nr}^{-1} \tag{3.1}$$

The photon emitted by radiative recombination constitutes the signal studied by PL spectroscopy. The goal is to spectrally study the light emission, that is, to study the light intensity as a function of its wavelength. In this thesis, non-resonant PL was excited by means of laser light: in this process, the laser photons carry energy larger than the one of the observed photon emission. Figure 3.1a sketches the process in the case of the PL emission from the bandgap
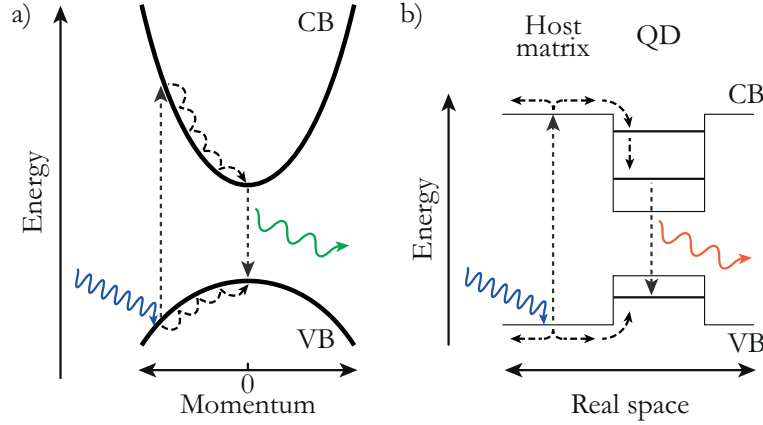
Figure 3.1 – Scheme of non-resonant PL in a) direct-bandgap bulk semiconductors and b) QDs with type-I band alignment with the host matrix.

of a bulk semiconductor with direct bandgap. An incident photon promotes an electron from the VB to the CB at higher energy than the CB edge. The electron releases part of its energy by interaction with the lattice phonons in a quick process of thermalization to the CB edge at the Γ point. From this position in the energy-momentum space, the electron can radiatively recombine with a hole in the VB with conservation of energy and momentum. In indirect-bandgap semiconductors, the radiative electron-hole recombination is assisted by phonons. The need of the phonon as a third particle to complete the transition reduces the recombination rate in this class of semiconductors. On the contrary, direct-bandgap semicon-ductors, such GaAs and AlGaAs up to about 45% Al [132], can show bright luminescence. Yet, non-radiative recombination channels can hinder the PL brightness also in direct-bandgap semiconductors. As an example, surface states may not only generate a local electric field that separates electrons and holes, but they may also introduce intra-bandgap states that provide a preferential path for non-radiative electron-hole recombination. In nanostructures, the high surface-to-volume ratio makes unpassivated surface states detrimental for the PL intensity [148].

In figure 3.1b, the process of non-resonant PL is detailed in the case of a QD: the laser photons excite electron-hole pairs in the continuum of states in the shell matrix; some charge-carriers reach the QD and thermalize to the lowest QD levels. The thermalization process is mediated by phonons on characteristic time scales of several ps. From the ground state, a single electron-hole pair can recombine by releasing energy as one photon. The QD barriers localize the electron and the hole and their wavefunctions usually have a larger overlap in the QD than in the bulk. This effect typically reduces the lifetime of the excited state in the QD with respect to the bulk and increases the brightness of the QD emission. The radiative electron-hole recombination has characteristic time scales of few-hundred ns in the NWQDs studied in this thesis [14].
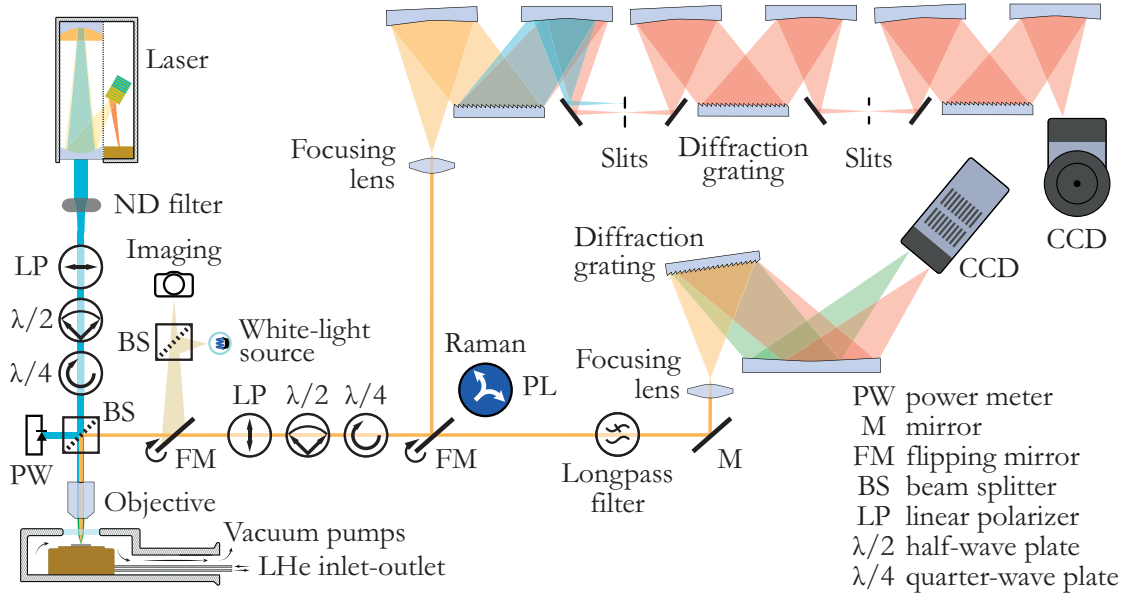
Figure 3.2 – Scheme and main components of setup A (see text) equipped for both PL and Raman spectroscopy.

Time-integrated photoluminescence setups

In the following, the key components of the PL setups used in this thesis are described. Two in-house setups were used for the experimental work of this thesis: they are constituted by the same main components, but slightly differ for the laser, cryostat and detection systems. A simplified sketch is reported in figure 3.2. In the following, the two setups are distinguished as setup A and B, when necessary. The purpose of both setups is to collect the luminescence spectra (photon intensity vs photon energy) of the samples at different temperatures (from LHe to room temperature) without resolving the time-dependence of the light emission: the signal detection happens over integration times (100 ms to 1s) that are longer than the sample recombination lifetime (~ 500 ps) by few orders of magnitude.

The components are described following the light path in figure 3.2, from the source to the detection. Continuous-wave (CW) lasers are used as an excitation source. CW lasers have a constant-power output in time. The laser light path is represented in blue in figure 3.2. The non-resonant excitation process, described in the previous section 3.1, requires the use of lasers at photon energies larger than the bandgap of the studied semiconductors. Setup A features a He-Ne gas laser emitting at a fixed wavelength of 632.8 nm; setup B features two optically-pumped semiconductor lasers emitting at the fixed wavelengths of 532 nm and 488 nm. The maximum output power is less than 5 mW from the He-Ne laser, while it is of 100 mW from both semiconductor lasers. Neutral-density (ND) filters along the optical path reduce the laser intensity to the desired values.

Lasers are optimized for emitting photons at a specific wavelength determined by the res-

onance of the laser cavity and the device design. Nevertheless, the gain medium can emit at different wavelengths and additional modes can resonate in the cavity together with the one chosen by design. Furthermore, in gas lasers, the plasma emits a broad background. In order to improve the spectral purity of the laser emission, narrow-bandpass filters suited for the specific laser line absorb the unwanted wavelengths. The laser light is typically linearly polarized. The control and manipulation of the laser polarization is performed with half-wave plates, quarter-wave plates, and linear polarizers: the first rotate the linear polarization of the light by a chosen angle, the second generate circularly polarized light from a linearly polarized beam and the third select a specific linear polarization.

A beam splitter sends part of the laser beam to a power-meter to monitor its power. The rest of the laser light reaches the sample through an objective. Since the objective focuses the laser light into a spot of less than 1 μm in diameter, the equipment described here is more precisely referred to as a micro-PL setup. An important figure of merit to characterize an objective is its NA. This is defined as:

$$NA = n\sin(\theta), \tag{3.2}$$

where n is the refractive index of the medium that surrounds the objective (either air or vacuum in the setups used in this thesis) and θ is the largest half-angle at which the objective can transmit or collect light. Large-NA objectives increase the brightness of the optical system by increasing its collection solid angle. Setups A and B respectively have objectives with NA equal to 0.85 (about 1 rad of maximum acceptance angle) and 0.75 (about 0.85 rad of maximum acceptance angle).

A crucial advantage of large-NA objectives is the increase in spatial resolution, that is, the minimum distance between two objects at which they are imaged as distinct. The Rayleigh criterion defines d, the spatial resolution of a microscope, as:

$$d = 0.61\frac{\lambda_0}{NA} \tag{3.3}$$

where λ_0 is the wavelength of the considered light in vacuum. From Equation 3.2 and Equation 3.3, $d \sim 0.71\lambda_0$ in setup A and $d \sim 0.81\lambda_0$ in setup B.

To perform low-temperature PL experiments, the samples are mounted in cryostats. Both PL setups are characterized by cold-finger cryostats: in this type of cryostats, LHe or helium vapor cool down the sample stage by direct contact; the sample indirectly cools down by contact with the cold stage. Setup A features a closed-cycle cryostat, while setup B features an open-cycle cryostat. A closed-cycle cryostat recovers the exhausted helium in a closed circuit and, by re-compressing and dissipating the heat, uses it to cool down the sample stage, cycle after cycle. In an open-cycle cryostat, the exhausted gas is dispersed and a constant supply of new LHe from an external Dewar is necessary. The lowest temperatures reached in the cryostats in setup A and B are about 3.7 K and 7 - 10 K, respectively. The objective is positioned outside the open-cycle cryostat of setup B and features a cover-glass correction to compensate for

the image distortion due to the light passage through the cryostat window. The closed-cycle cryostat in setup A hosts the objective inside the cryostat chamber. This design avoids the need to correct the objective focus and reduces the relative drift between the samples and the objective because the two are mounted onto the same hardware frame and kept at the same temperature. For imaging the sample, a white-light source illuminates the sample surface: the objective conveys and collects the light that is captured by a camera to observe a magnified image of the sample surface and to navigate the specimen. Flat substrates predominantly back-reflect the white light and NWs are usually recognized by darker contrast because their faceted surface backscatters only a small amount of light.

The objective collects the sample luminescence, depicted as the orange optical path in figure 3.2. The same type of optics used to manipulate the laser light allows the analysis of the polarization of the PL emission. This signal enters a grating spectrometer with the same focal length of 500 mm in both setups. Diffraction gratings with 300 lines/mm, 600 lines/mm, and 1200 lines/mm are available in each setup to disperse the different photon energies that comprise the PL emission: higher-density gratings have higher spectral resolution, but narrower detection bandwidth and, usually, lower intensity. All gratings feature blazed angles to enhance the signal brightness in the low-energy visible and NIR range. In order to detect the dispersed luminescence, setups A and B rely on silicon charge-coupled-devices (CCDs) cooled by liquid nitrogen and a Peltier cell, respectively.

The spectral resolution of an optical setup depends on several factors, such as the line density of the gratings, the slit width, and the size of the CCD pixels. They affect the best spectral resolution that can be achieved. The spectrometer is characterized by an instrument response function that broadens the linewidth of the peaks measured in PL spectra towards a gaussian profile: the narrower the intrinsic peak linewidth is, the more important the instrumental broadening becomes. Broad peaks may prevent to resolve PL lines closely spaced in energy. A simple way to estimate the instrument linewidth broadening is to measure the linewidth of Dirac-like signals, e.g. stabilized CW lasers. According to the manufacturer, setup A and B respectively mount lasers with linewidths of 2 MHz and less than 1.5 MHz or, equivalently, 0.0083 μeV and 0.0062 μeV. However, the minimal measured linewidth of the laser lines are respectively 118 μeV and 315 μeV. The actual emission linewidth of the lasers are negligible with respect to the measured ones, i.e. the lasers are Dirac-like sources. Therefore, the experimental linewidth are a reasonable approximation of the instrumental linewidth broadening.

A third micro-PL setup (NA = 0.77) was used for the NWQD-Rb coupling experiments, carried in the group of Prof. Richard Warburton, at the University of Basel. The working principle and optical components in this setup are the same as those described for setups A and B. The main difference is the cryostat, of the bath type. In this case, the sample is cooled down by immersion in LHe contained inside a Dewar. An optical fiber guarantees the coupling of the laser and PL light with the sample. For the NWQD-Rb coupling experiments, high spectral resolution around the Rb resonance is required. For this reason, the spectrometer has a grating with higher groove density (1500 lines/mm).

Hanbury-Brown-Twiss interferometer

In this thesis, the study of the photon-emission statistics was necessary to prove the SP nature of the emission from engineered NWQDs (chapter 6). As already mentioned in subsection 2.2.2, the test of SP emission consists in measuring the second-order correlation function $g^2(\tau)$ of the studied emitter: a $g^2(0) < 0.5$ is a signature of SP emission. The $g^2(\tau)$ function correlates light intensities (equation 2.1); its measurement relies on the interference of measured intensities by a Hanbury-Brown-Twiss (HBT) interferometer. On the contrary, in a traditional interferometer (e.g. Michelson and Fabry-Perot interferometers), the amplitudes of overlapping light waves are allowed to interfere: this mechanism measures their correlation that is mathematically described by a first-order correlation function. In both kinds of interferometers, the measured quantity is always the same: light intensity or, equivalently, photon counts. However, in a Michelson or Fabry-Perot interferometer, the intensity fringes result from the constructive and destructive interference of light-wave amplitudes, whereas in a HBT interferometer the characteristic pattern results from the interference of the light intensities measured at two distinct detectors.

A HBT setup counts time-correlated SPs: it detects light down to the SP level, resolve the SP events in time and correlate them with each other as a function of their detection time. By a modification in the detection path, setup A is also equipped for HBT interferometry (figure 3.3). With respect to time-integrated PL, the signal is not sent to the spectrometer but is sent to a home-made monochromator composed of a grating (1200 lines/mm, blazed at 750 nm) mounted on a rotating stage. From the grating, the PL signal reaches a 50:50 beam splitter. Each branch (transmission and reflection) of the beam splitter is coupled with a single-mode optical fiber. The fiber cores accept a narrow energy bandwidth (about 0.8 meV at 680 nm) so that only the chosen emission energy, e.g. the X line of a QD, is coupled to the fiber: all the lines at different angles are discarded. Each optical fiber guides the signal to a silicon SP avalanche diode (SPAD). A timing-correlation card calculates the time difference τ between two events in the two detectors: one detector acts as a start signal when triggered by a photon, while the other detector acts as a stop signal when triggered by a successive photon. For this thesis, the SPADs were operated in the time-binning mode: the time difference between start and stop is binned into a histogram (the available time bins range from 4 ps to 512 ps). Shorter time bins increase the time resolution of the histogram, but reduce the intensity of the collected signal.

Classical light fields emit photons randomly in time: τ equal zero has the same probability as any other time delay. Thermal light emits photons in bursts: the photons are bunched in time and a zero-delay peak forms in the time-delay histogram. For a SP source, only one SPAD is triggered at a time: at the beam splitter, a SP can either couple with the transmission or reflection path, but not both at the same time. Therefore, a SP emitter cannot trigger both SPADs simultaneously: the delay between start and stop signals is always larger than zero. SP light emission is said to be anti-bunched: a dip around zero delay forms in the time-delay histogram. In real measurements, SP emitters still have $g^2(0) > 0$. Reasons for additional counts at zero delay include: unfiltered background emission stemming from the sample,
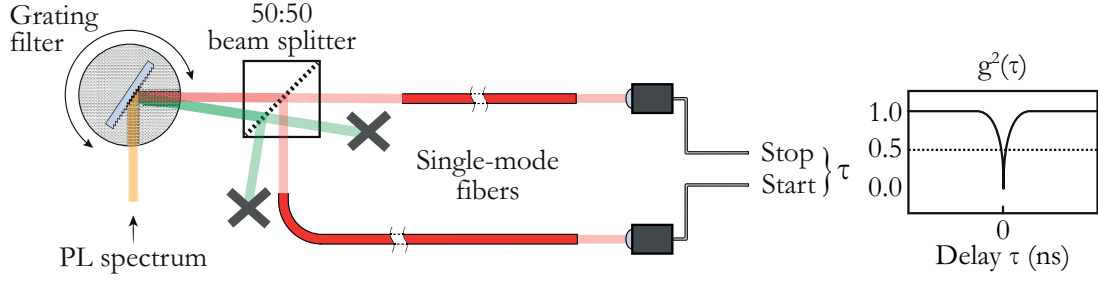
Figure 3.3 – Scheme of the detection branch of setup A equipped for measuring the $g^2(\tau)$ function of a spectrally selected QD emission line.

but not from the studied quantum emitter; dark counts from the SPADs (10 - 50 cps in setup A); and card and SPAD timing jitter (30 - 40 ps for the SPADs of setup A). Figure 3.3 shows an illustrative sketch of a $g^2(\tau)$ in CW mode: the histogram is usually normalized between 0 (at τ = 0) and 1 (for $\tau \to \infty$).

3.1.2 Cathodoluminescence

In excitation, light diffraction limits the spatial resolution of the optical setups used in this thesis to 400 nm - 500 nm in the best conditions (Equation 3.3). In order to map self-assembled NWQDs within the typical lengths of a NW diameter (100 nm - 200 nm), a higher spatial resolution is necessary.

Some purely optical techniques beat the diffraction limit by using diffraction-limited light in appropriate configurations. This category includes super-resolution techniques such as stimulated emission depletion microscopy (STED) and super-resolution optical fluctuation imaging (SOFI). The drawback with these techniques is to work only under specific assumptions on the electronic transitions of the studied system. For instance, STED relies on the selective deactivation of excited fluorophores and SOFI relies on the temporal-dependent fluctuation of fluorophores between two on-off or bright-dim states. Other optical techniques employ light in the near-field: differently from far-field spectroscopy, near-field luminescence is intrinsically not limited by diffraction. Typically based on the detection of the evanescent component of an electromagnetic field in proximity of a metal tip, near-field spectroscopy lacks sensitivity to probe the bulk of the sample, is often affected by weak throughput and only function at short working distances [149].

In this thesis, CL was used to surpass the diffraction-limited resolution of PL. CL is the process of light emission from a sample excited by electrons. Although coherent processes, such as plasmon generation, may contribute to the light emission, the CL signal considered in this thesis originates from the same incoherent electron-hole-pair generation and recombination processes as those discussed for PL [150]. CL is a sub-diffraction imaging method of the sample luminescence with a few advantages with respect to super-resolution techniques and near-field spectroscopy. Like PL, CL is applicable to a wide range of physical systems, without

the restrictions imposed by STED and SOFI. A single CL electron can generate thousands of electron-hole pairs, while a single incident photon only generates one pair. Therefore, with respect to PL, and near-field spectroscopy in particular, CL can benefit from high throughput. Through the control of the acceleration voltage, CL guarantees an easy way to probe a sample at different depths with a freedom that neither far- nor near-field PL can offer. A recognized limitation of CL is the electron-beam-induced damage of organic samples; however, for inorganic-semiconductor samples, such as the NWs studied in this thesis, atom displacement is negligible up to electron energies in the order of 100 keV [151] and sample degradation has not been observed even after prolonged exposure.

Incident electrons interact with a semiconductor through elastic and inelastic scattering. The first generates high-energy backscattered electrons (relativistic Rutherford scattering cross-section); the second comprises a wide range of processes (such as the generation of secondary electrons, X-rays, and electron-hole pairs) that, in a series of scattering events, gradually transfer the electron-beam energy to the specimen. Among these processes, the generation and recombination of electron-hole pairs is the one responsible for the CL emission. A fundamental difference between PL and CL is that a single accelerated electron can generate thousands of electron-hole pairs, while a single photon only generates one pair. The generation factor G gives the amount of electron-hole pairs generated by an incident electron [151]:

$$G = \frac{E_b(1-\gamma)}{E_i},$$
(3.4)

where E_b is the beam energy and γ accounts for the fraction of electron energy dissipated with backscattered electrons. $E_i = 2.8E_g + M$ is the ionization energy required to generate a single electron-hole pair in a material with energy gap E_g; M is a material-dependent parameter, ranging between 0 and 1 eV. For most semiconductors 1 eV $< E_g <$ 2 eV; it is easy to observe that already a low-energy electron (e.g. 1 keV) generates at least hundreds of electron-hole pairs. The intensity of the CL signal scales with G that, in turn, is proportional to E_b; at the same time, at higher probe currents, more electrons interact with the specimen, each with a generation factor G. Therefore, the brightness of the CL signal increases with increasing probe current and acceleration voltage. The details of this relation are beyond the scope of this work and largely vary as a function of parameters such as the quantum yield of radiative recombination in the studied material. The overall CL intensity also depends on the total internal reflection and emission reabsorption in the specimen, modulated by the light collection efficiency of the microscope.

CL can be performed in both SEMs and TEMs. Although single spectra at defined positions may be acquired, the full potential of CL comes from using the electron beam as a scanning probe according to a grid of pixels across the sample and collecting the luminescence from each pixel. If an intensity-wavelength spectrum is collected at each pixel, the technique is usually referred to as hyper-spectral imaging. The CL map is then conveniently compared with the SEM or (S)TEM micrograph of the same region of interest to combine morphological, structural and compositional data with the information on the electronic bands provided by
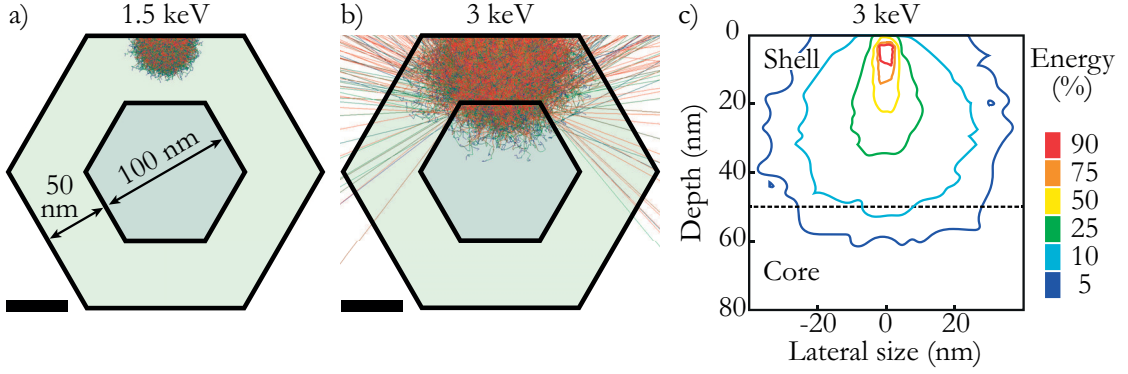
Figure 3.4 – Monte Carlo simulations of the electron-beam interaction with core-shell GaAs-AlGaAs NWs (core diameter 100 nm, shell thickness 50 nm). The beam diameter at the impact point is 5 nm. The simulations are performed with the software CASINO [152] on 5000 electrons in each case (1000 trajectories shown). NW cross section showing the electron trajectories for initial beam energy of a) 1.5 keV and b) 3 keV. c) 2D-projection of released energy relative to the maximum sample excitation in the interaction volume of an electron beam with initial energy of 3 keV. The scale bars in a) and b) correspond to 50 nm.

CL.

The advantage of CL is its shorter electron wavelength in comparison with the wavelength of visible light employed in PL. The electron wavelength is inversely proportional to its energy that, in an electron microscope, depends on the intensity of a controlled electric potential U. Therefore, one can write the relativistic de Broglie electron wavelength λ as:

$$\lambda = \frac{h}{p} = \frac{h}{\sqrt{2m_0 eU}\frac{1}{\sqrt{1+\frac{eU}{2m_0 c^2}}}} \tag{3.5}$$

where h is the Planck constant, c is the speed of light, m_0 is the electron rest mass and e is the electron charge. Normally, a SEM operates between 1 kV and 30 kV, while a TEM operates between 80 kV and 300 kV. The term $\frac{1}{\sqrt{1+\frac{eU}{2m_0 c^2}}}$ highlights the relativistic correction to λ, which gives significantly more accurate results especially in the range of TEM operation voltages. For this thesis, a SEM-CL microscope was operated at 1.5 kV and a TEM at 200 kV; from Equation 3.5, the corresponding electron wavelengths are about 32 pm and 3 pm, respectively. According to Equation 3.3, the related spatial resolutions are better than 2 nm at 1.5 keV and better than 2 Å at 200 keV: in excitation, diffraction does not limit the microscope spatial resolution. Other factors need to be considered: they are discussed hereafter in the case of SEM-CL.

In order of increasing characteristic lengths, the spatial resolution of CL is determined by the electron-beam diameter, the electron interaction volume, and the charge-carrier diffusion length. In a SEM, the electron beam can be focused within very few nanometers at the sample surface. From this position, elastic and inelastic scattering events randomize the electron trajectories deeper in the sample. The Kanaya-Okayama model [151] expresses in μm the

electron penetration R_e as a function of the beam energy E_b in keV:

$$R_e = \frac{0.0276A}{\rho Z^{0.889}} E_b^{1.67},$$ (3.6)

where A is the atomic weight in g/mol, ρ is the material density in g/cm^3, and Z is the atomic number. R_e corresponds to the depth to which the electron-beam energy is dissipated. Equation 3.6 shows that, by controlling E_b, one can tune the electron penetration and gain depth-dependent information on the sample luminescence. The Kanaya-Okayama model agrees well with experimental data for a wide range of atomic numbers and typical SEM acceleration voltages.

The overall shape of the interaction volume depends on Z. For elements of intermediate Z, such as those that compose the semiconductors studied in this thesis, the interaction volume is fairly spherical. This holds for bulk specimens. In thin samples, such as nanostructures and electron-transparent samples prepared for TEM (usually thinner than 80 nm), the interaction volume is much smaller: most electrons undergo only few scattering events before exiting the sample from the side opposite to the incident face. The smaller interaction reduces the spread of the incident beam and keeps the interaction volume closer to the initial diameter of the electron beam. A similar conclusion holds for nanostructures when the theoretical interaction volume exceeds the dimensions of the nanostructures.

Beyond the incident-electron interaction volume (Equation 3.6), the minority-carrier diffusion further extends the region where the CL signal generates. The intensity of the CL signal linearly scales with the number of photons emitted per unit time; in turn, the photon emission rate depends on the radiative recombination rate $\frac{\Delta n}{\tau_r}$, where Δn is the stationary excess carrier density and τ_r is their radiative lifetime. Therefore, by integration over the whole volume of minority-carrier diffusion, the CL intensity I_{CL} is:

$$I_{CL} \propto \int_V \frac{\Delta n}{\tau_r} d^3 r.$$ (3.7)

A reasonable approximation to describe the carrier density is to assume that (i) the carrier generation takes place uniformly at a constant rate g_0 inside a sphere and is zero outside and (ii) the generated carriers can only diffuse or recombine. Under these conditions, it can be demonstrated [151] that the stationary density of excess carriers follows an exponential decay:

$$\Delta n(r) = \frac{C \sinh(r/L)}{r} + \tau g_0$$ (3.8)

where τ is the overall carrier lifetime (including radiative and non-radiative recombination) and L is the minority carrier diffusion length ($L = \sqrt{D\tau}$, with D the carrier diffusivity). The CL intensity is essentially proportional to $\frac{\Delta n}{\tau_r}$ (Equation 3.7). Thus, the actual volume from where the CL signal stems expands beyond the interaction volume of the incident electrons because of the charge-carrier diffusion. However, the carrier density exponentially decays

with the distance from the interaction volume where they are generated and similarly the CL intensity does. For nanoscale emitters, such as QDs, the overlap between the electron and hole wavefunctions shortens the characteristic time of the electron-hole recombination; at the same time, the QD potential limits the charge-carrier diffusion process. These two factors effectively shorten L. Therefore, the CL-intensity contrast inside and outside a QD may be even more pronounced.

The diffusion length L largely varies in different materials and can change within the same material depending on the density of recombination centers, such as defects or surface states. The latter case is particularly important in nanostructures with high-surface-to-volume ratio. For instance, the exciton diffusion length of GaAs QWs is in the μm range at 25 K [153], while it reduces to less than 1μm in GaAs NWs at similar temperatures (7 - 10 K) [154]. In addition, L increases by almost one order of magnitude (from 100 nm to 900 nm) upon the passivation of the recombination centers on the surface of GaAs NWs.

Analytical methods often require to approximate the physical system to derive solution (e.g. the uniform-generation sphere for Equation 3.8). As a complementary approach, Monte Carlo simulations are commonly used to predict stochastically the shape and size of the interaction volume as well as its energy distribution. A Monte Carlo simulation reproduces successive scattering events to calculate an electron trajectory: the electron travels a straight distance between random scattering events. Elastic scattering changes the direction of the electron trajectories; inelastic scattering subtracts energy to the electron. A random number generator defines the probability of a certain type of scattering for each event. The accuracy of the simulation increases with the number of simulated electrons: statistically robust calculations require about 1000 electrons. Figure 3.4 shows illustrative cross sections of simulated electron trajectories in core-shell GaAs-AlGaAs NWs at 1.5 keV and 3 keV.

Figure 3.4c shows the energy isosurfaces in a simulated interaction volume at 3 keV. Together with experiments, this sort of simulations clarifies that the energy distribution of the inter-action volume is not uniform: in particular, a large part of the beam energy is dissipated in proximity of the impact point of the beam with the sample surface. Most of the charge carriers and hence CL intensity originate from this region. To take this effect into account, non uniform generation-rate functions have been proposed, including polynomial [155] and Gaussian distributions [151], with good agreement with experiments and simulations.

In a CL microscope, the electron beam scans the sample surface according to the positions of a pixel grid. The electron beam impacts the sample at each pixel position for a finite integration time (usually ranging from ms to s). During the integration time, the system collects the CL signal and the software associates the acquired signal with the $x - y$ position of the beam in the pixel grid: the CL map is an excitation map (the software owns the information on the position of the beam, that is, the excitation). Because of the extension of the interaction volume and the charge-carrier diffusion process, electron-hole pairs can recombine and generate the CL signal far from the point of impact of the electron beam with the sample surface. In far-

field detection, the luminescence generated at any position during the integration time Δt is collected and associated with the coordinates of the electron beam during Δt. Therefore, the distance travelled by the incident electrons and the generated electron-hole pairs defines the resolution of CL mapping. The characteristic size of a focused electron probe is in general several times or orders of magnitude smaller than the dimensions of the interaction and diffusion volumes; it has negligible influence on the overall spatial resolution. Nevertheless, the probe size may contribute to define the spatial resolution of the CL map at low operation voltages and high currents: on the one hand, the low voltage minimizes the beam size that becomes comparable with the interaction volume (e.g. 20 nm at 1.5 kV in GaAs); on the other hand, the electromagnetic lenses of a SEM are typically less efficient to focus the electron beam in a small surface spot at low acceleration voltage and large probe current.

Overall, when also including the effect of the interaction and diffusion volume, the CL spatial resolution overcomes the diffraction limit associated with PL and allows to map with nanoscale resolution bulk and nanostructured samples. Common to any scanning microscopy technique, the influence of the pixel size on the spatial resolution of the final image is not secondary. Ideally, the pixel size should be comparable with the physically-determined spatial resolution: larger pixels miss details, while smaller pixels are a useless use of resources (acquisition time). However, weak CL emission requires long acquisition times per pixel; the trade-off between acquisition time of the overall map and the desired resolution may result in CL maps at pixels densities insufficient to accurately reproduce all the resolved features.

Cathodoluminescence setup

In this thesis, the CL measurements were performed on a dedicated SEM-CL microscope, equipped with a LHe-cooled sample holder for temperature-dependent measurements down to 5 K - 10 K. Being fully dedicated to CL, this microscope greatly facilitates the alignment of the electron and light optics and features components optimized for the excitation and collection of CL. A scheme of the CL setup is reported in figure 3.5. The microscope head is characterized by a Schottky thermal field-emission gun: in this type of gun, an external voltage (about 5 kV) promotes the electron thermionic emission by lowering the surface barrier of the gun. Schottky thermal field-emission guns guarantee high beam current, which is useful to enhance the CL signal. Depending on the microscope configuration, the probe current can be as high as 10 - 20 nA. In normal conditions, it is kept at about 1 nA. The electron-beam energy ranges from 1 keV to 10 keV. Electromagnetic lenses collect the gun emission, convey it into the microscope column and focus it onto the sample in a spot of less than 10 nm in diameter. The sample is positioned on a cryostat stage equipped with a piezoelectric actuator for moving through the sample. The design of the stage minimizes the sample drift and vibrations over long acquisitions (30 min) and during operation with LHe cooling. An Everhart-Thornley detector collects the secondary electrons for imaging the sample morphology. The light optics is embedded in the microscope column. It is pierced with a hole, in order to transmit the electron beam to the sample. The embedded optics consists of an achromatic (wavelength
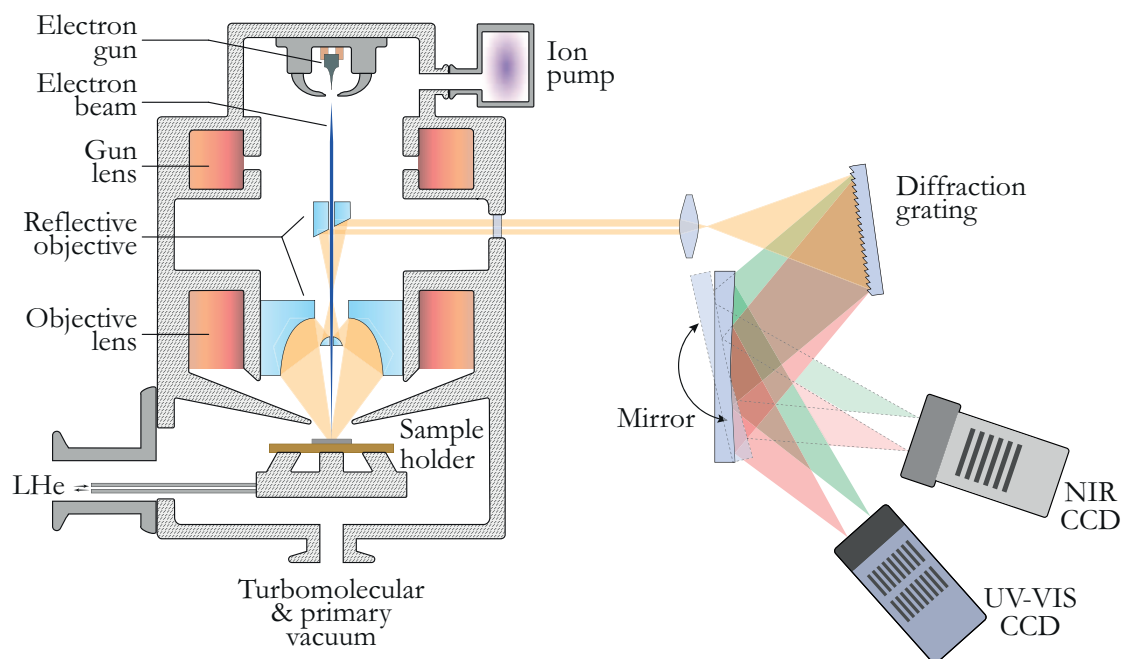
Figure 3.5 – Scheme of the dedicated SEM-CL setup used in this thesis.

between 180 nm and 1.6 μm) reflective objective with NA = 0.71. The objective has a constant collection efficiency over a wide (at least 300 μm) field of view. When the sample is in the objective focal plane, it is also at the optimal working distance (2 mm below the pole piece) for the electron microscope; the microscope design facilitates the optics alignment. Non-dedicated common solutions for CL microscopy consist of add-ons to install on independent SEMs or TEMs. A parabolic mirror is the standard component for the collection of the CL signal. An aperture in the mirror allows the electron beam to reach the sample. With add-on solutions, often the alignment of the optics is technically challenging, especially in the small chamber of a TEM. The point-like focus of the parabolic mirror easily introduces aberrations in the collected images if the alignment is not optimized (off-axis) and limits the field of view to few microns.

The reflective objective collects the CL signal and focuses it at the entrance slit of a spectrometer with focal length of 32 cm. The spectrometer is equipped with several diffraction gratings of different resolution power and optimized for the NIR and the visible and ultraviolet (UV) energies. Two different detectors cover this energy range from about 0.7 eV to 6 eV: a Si CCD for the UV-visible range and an InGaAs photodiode array for the NIR interval. The best spectral resolution achievable in the visible range is about 0.4 nm. Thanks to the diffraction gratings, the CL signal collected at each position of the scan is converted into a spectrum (intensity vs wavelength). Each pixel is associated with its 2D coordinates and a full spectrum (hyperspectral imaging).

The electron-beam releases to the sample a large energy (keV) in a relatively small volume (nm

to μm). The large amount of fluctuating charge carriers and incident electrons are supposed to broaden the CL peaks in comparison with PL. Similarly to the excitation by a laser at high power in PL, charge carriers may pile up in the available states of the semiconductor electronic bands (band filling): electrons and holes also recombine from levels at higher energy than the CB and VB edges: in this conditions, the CL peaks broaden and blueshift. Sample heating is another consequence of the high and localized power of the electron beam [122], but it has not been observed in the samples studied for this thesis. With respect to photons (PL), electrons also bring momentum: this facilitates the electron-hole pair formation at exotic wave-vectors different from the Γ point.

3.2   Raman spectroscopy

In addition to PL measurements, setup A is also equipped for the acquisition of Raman spectra. Figure 3.2 shows a scheme of the setup: the only difference between the PL and Raman configurations of setup A is in the detection segment of the optical path: the position of a flipping mirror allows to send the signal to one of the two segments. PL and Raman spectra can be acquired one after the other on the same sample. Before the flipping mirror, the Raman setup shares the same lasers, cryostat and optics of the PL setup B shown in figure 3.2. In the following, the Raman detection branch is outlined.

In direct-bandgap semiconductors, the PL emission is rather intense: acquisition times ranging from few ms up to few tens of seconds are usually sufficient to reach the desired signal-to-noise ratio. As discussed in subsection 2.4.1, Raman scattering is a three-particle process and has a lower probability to take place than elastic scattering and PL: the Raman signal is weak and requires longer acquisition times to enhance the signal-to-noise ratio. On average, about 30-minute acquisitions were necessary for the spectra reported in this thesis. Long acquisition times benefit from a stable cryostat and sample holder: during low-temperature measurements, the thermal equilibrium between all the cryostat components and the sample was a fundamental prerequisite.

In non-resonant PL, the signal is spectrally distant from the excitation. For instance, in setup B the lasers emit at ~ 2.33 eV (green laser) and ~ 2.54 eV (blue laser). The energy difference between the GaAs PL at LHe temperature (about 1.51 eV) and the two available excitation energies is therefore 820 meV for the green laser and 1030 meV for the blue laser. Thanks to such a large spectral distance between the laser and the PL signal, the laser line is in general outside the energy range projected on the detector already when using diffraction gratings with low density of lines (e.g. 300 lines/mm). The low-energy tail of the intense laser line often still disturbs the acquisition of the PL spectrum, but commercial longpass filters placed before the spectrometer (figure 3.2) usually suffice to clean the PL spectrum from laser contributions. On the contrary, the phonon energies of the GaAs lattice are just slightly more than 32 meV (i.e. about 260 cm^{-1}): this corresponds to the energy distance between the Raman signal and the laser. A common solution to filter the laser line from the Raman spectra is to utilize notch

filters adapted to each of the laser wavelengths used in the setup.

A more versatile solution is represented by the subtractive triple spectrometer used for the Raman measurements of this thesis (figure 3.2). A multiple spectrometer is composed of several monochromators aligned along a common optical path. The entrance slit of each monochromator accepts a finite bandwidth that filters the collected light in a chosen energy range and excludes the laser wavelength. A flipping mirror in setup B redirects the sample emission to the PL or the Raman detection branch. In the Raman branch, the light continues to an achromatic lens that focuses the signal on the entrance slit of the first monochromator. Each monochromator is equipped with diffraction gratings (900 lines/mm and 1800 lines/mm). The horizontal spread of the different wavelengths offsets the laser energy range with respect to the slit of the successive monochromator and only the Raman signal is transmitted. At each step, the width of the slit and the diffraction power of the chosen grating define the bandwidth that is transmitted to the next monochromator. At the last step, the signal is dispersed onto a liquid-nitrogen-cooled silicon CCD to acquire calibrated intensity-vs-wavenumber spectra. The lasers in setup B were chosen with a narrow emission linewidth (< 1.5 MHz) in order to facilitate the filtering of the intense Rayleigh scattering of the laser.

Polarization filters in the excitation and collection paths enable to select the incident and collected polarization of the light with respect to the NW orientation. In the measurements reported in this thesis, the polarization of the incident light is parallel to the NW longitudinal axis in order to take advantage of the antenna effect on the light absorption. In collection, the scattered light is either unfiltered or alternatively filtered in the directions parallel or perpendicular to the NW longitudinal axis (more details are given in chapter 5).

For supplementary material, ref. [156] reports on Raman spectroscopy as an analytical tool for semiconductors. It can be combined with the reading of ref. [157] for further details on the vibrational properties of semiconductors and nanostructures and with the reading of refs. [158, 159] and references therein for an extended study of GaAs NWs by Raman spectroscopy.

3.3   Transmission electron microscopy

Different TEMs were utilized in this thesis: the NW crystal structure was studied by SAED and HRTEM, while the NW composition was analyzed by STEM-based EDX and electron energy-loss spectroscopy (EELS). These results are reported in chapter 4 and chapter 6. NWs are thin enough for TEM imaging with no need for further processing. They easily transfer on TEM grids by gentle friction of the grid on the as-grown substrate: the NWs tend to break towards their bottom and lie on the TEM grid on one of their six {1-10} facets. A few-degree rotation of the TEM grid in the microscope is usually sufficient to align the NW along the <1-10> zone axis. This configuration is ideal to map the NW properties along its longitudinal axis (chapter 4). The incident electrons have the appropriate wavelength to be diffracted by the atomic crystal lattice: the contrast that they produce in bright-field (BF) TEM micrographs provides useful information on the NW crystal structure (phase and defects).

The inner structure of core-shell NWs is studied more easily in transversal cross sections. NW cross sections are electron-transparent (40 - 80 nm) NW segments are cut along planes perpendicular to the NW growth axis. The segments are imaged along the growth direction (<111> zone axis) in either TEM or (S)TEM mode. In this thesis, the goal was to map the composition of the NW cross sections by STEM EDX and EELS. The cross sections for EDX were cut by ultramicrotomy: a piece of hardened epoxy, usually containing hundreds or thousands of NWs, is mounted in an ultramicrotome where a diamond knife cuts thin slices of the epoxy and embedded NWs. Each slice contains hundreds of NW cross sections. As soon as they are cut, the slices fall into a water bath, where they are fished with a loop tool and laid on a TEM grid. The cross sections for EELS were cut by means of focused-ion beam (FIB). The NWs were transferred on silicon wafers and coated with 30 nm of SiO_2 by plasma-enhanced chemical vapor deposition (PECVD). A TEM-lamella is FIB-cut from the coated sample, with few embedded NW cross sections. Compared with ultramicrotomy, this technique produces fewer cross sections per sample and is more expensive. However, it facilitates the alignment of the cutting planes in the direction perpendicular to the NW growth axis, it avoids the use of epoxy and it allows better control on the cut surfaces and on the cross-section thickness.

STEM EDX was chosen as the primary method of compositional analysis of the NWs studied in this thesis. Other techniques were used, such as APT, X-ray fluorescence (XRF), and EELS. They differ for the spatial resolution, sensitivity to trace elements and size of the total volume that they can probe. In the following, STEM compositional analysis is discussed in more details. In STEM, a focused electron beam scans the sample according to a defined pixel grid. For each pixel a wide range of signals can be collected, each by a dedicated detector. In this thesis, HAADF, EDX and EELS detectors provided compositional information on the studied NWs and NW cross sections. HAADF and EDX are discussed in the following.

The HAADF detector collects electrons incoherently scattered at large angles. The intensity of the HAADF signal is proportional to the sample thickness and the atomic number Z of the constituent elements. Therefore, for a specimen of constant thickness, the HAADF contrast provides information on the Z of the elements in the specimen, that is, its composition. As an example, the black stripes observed at the six corners of the hexagonal cross section of a GaAs-AlGaInAs core-shell NW (figure 2.9 and chapter 6) indicate Al segregation at these positions. Al is the lowest-Z element in the shell (Z_{Al} = 13, Z_{Ga} = 31, Z_{As} = 33, Z_{In} = 49): low Z corresponds to a low probability of scattering at large angles. However, the HAADF intensity contrast may not be enough to recognize less important composition fluctuations; also, in ternary and quaternary alloys, different compositions may result in the same average Z and HAADF intensity.

STEM EDX analysis brings essential benefit to the compositional mapping of the specimen. X-ray emission is the process of photon emission due to electronic transitions to ionized inner atomic orbitals. A scheme of the process is presented in figure 3.6. The electron beam interacts with the specimen atoms, to which it delivers enough energy to promote an inner-orbital electron to the continuum of vacuum states. An electron from an outer orbital loses part of its
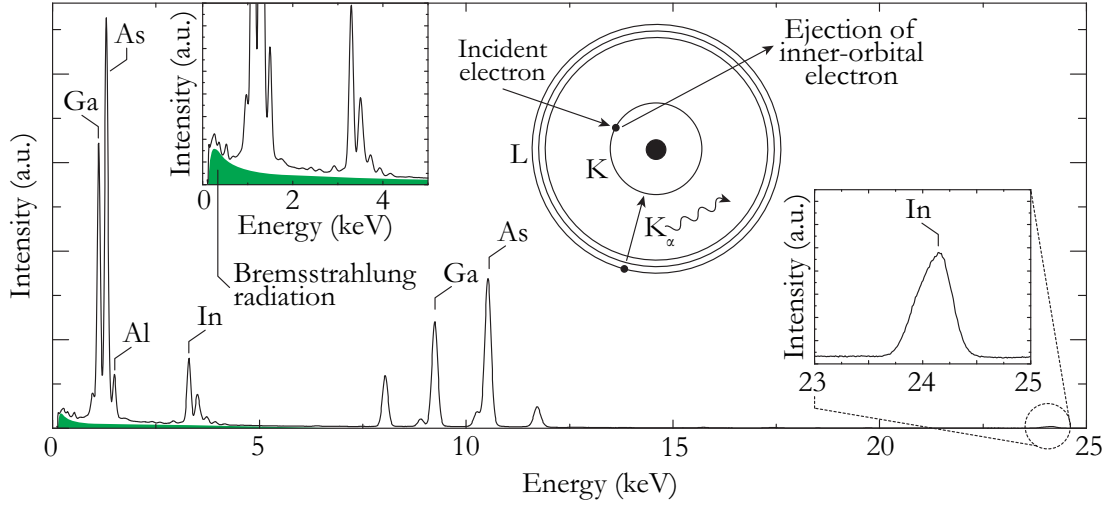
Figure 3.6 – STEM EDX spectrum from a quaternary-alloy (AlGaInAs) NW studied in this thesis. The two insets zoom in the Bremsstrahlung radiation at low energy and the weak K_α line of indium.

energy to occupy the vacant position in the inner orbital. The energy difference between the two orbitals is characteristic for each atom species and for each possible transition between two orbitals in the same atom species. If the energy difference is lost by the emission of a photon, the transitions can be detected. Given the specific correlation between the transition energies and the atomic species, the photon energy is used to identify the atom species that compose the atom.

Typically observed transition energies range from few to few tens of keV, equivalent to X-ray photons. The conventional labelling, assigns a letter (K, L, or M) to the transitions according to the principal quantum number n of the arrival orbital: K for $n = 1$, L for $n = 2$, and M for $n = 3$. Only heavier elements have high-energy outer orbitals and emit L and M lines. A subscript letter from the Greek alphabet is traditionally used to identify the variation of principal quantum number involved in the transition: α denotes $\Delta n = 1$ and β denotes $\Delta n = 2$.

In figure 3.6 an illustrative STEM EDX spectrum of a NW is reported. Several discrete peaks are visible: they correspond to the discrete transition energies between atomic orbitals. For instance, the K_α line of Al is visible at 1.486 keV; Ga, As, and In are heavier elements and show both K and L lines (Ga: K_α = 9.251 keV and L_α = 1.098 keV; As: K_α = 10.543 keV and L_α = 1.282 keV; In: K_α = 24.210 keV and L_α = 3.286 keV). Each peak may be composed of few closely spaced lines corresponding to the possible transitions involving the sub-levels of each orbital. Additional lines correspond to the characteristic X-ray emission of the materials that compose the TEM grid (copper and carbon) and of the oxygen incorporated into the NW as a surface oxide. The typical spectral resolution of EDX spectra is of few tens of eV. The energy difference between successive orbitals decreases from the inner to the outer levels. Consequently, the energy spread among the peaks in the EDX spectrum of figure 3.6 increases with the peak energies: the low-energy L peaks have all similar energies and are more difficult to resolve; the high-energy K lines are more spaced in energy, thus easier to resolve. The deconvolution of

55

overlapping peaks requires advanced algorithms and peak-fitting procedures. An additional deconvolution concerns the low-energy continuum of the Bremsstrahlung emission (inset in figure 3.6): this emission is produced by the deceleration of the electrons interacting with the specimen and does not carry compositional information.

During a sample scan, each pixel is associated with an EDX spectrum. The signal is acquired by dedicated X-ray detectors. For this thesis, the used TEM column is equipped with four silicon drift detectors (SDDs) that form a collection solid angle of 0.9 srad. For the acquisition of a STEM EDX map, the signal is integrated for several minutes until the signal-to-noise ratio of each element allows a significant peak deconvolution. The intensity of the X-ray signal is proportional to the electron-beam current. In this thesis, high current values of about 2 nA were used. The signal intensity also increases with the concentration of an element in the sample. This relation provides quantitative information on the composition of the specimen. The detection efficiency depends on the characteristic energy of the X-ray: the SDD sensitivity decreases at higher energies. Therefore, the low-energy peaks (L lines) may better probe the presence of elements in low concentrations.

In first approximation, the spatial resolution of the STEM map depends on the beam diameter. However, the EDX signal often requires long acquisition times for each pixel. The probability of sample drift increases with the acquisition time and results in the degradation of the spatial resolution of the mapping. In order to maintain the total map acquisition time within reasonable limits, the total number of pixels may be reduced. Therefore the size of each pixel increases beyond the optimal resolution if the size of the region of interest cannot be adapted. The spatial resolution of STEM EDX is a trade-off of these different factors, but nanoscale resolutions were normally achieved for the measurements shown in this thesis.

Further detailed readings about TEM and its application for structural and compositional analysis can be found in ref. [160, 161, 162].

4 Twin-driven emission-energy redshift along single nanowires

In order to control the properties of self-assembled nanostructures, it is essential to control the factors that influence their formation. The self-assembled NWQDs considered in this work form by spontaneous segregation of Al and Ga on the NW sidewalls. Ga and Al segregation is reported for the deposition of AlGaAs on planar (110) GaAs substrates by both MBE and MOCVD [103, 104]. Plate-like Al- and Ga-rich segregates form with a variable thickness, ranging from few nm [103] down to monolayers [104]. They tend to form sheets alternatively enriched in Ga or Al. The presence of a miscibility gap between AlAs and GaAs has been proposed to explain the separation between the two; exchange reactions between Al and Ga at the growth surface represent the mechanism for the adatom reordering [103]. Small deviations from the (110) orientation are observed in the plate-like nanostructures and define the lateral size of the Ga- or Al-rich sheets. The random occurrence of impurities can explain these deviations. Importantly, Al and Ga do not segregate if the deposition is performed on (100)-oriented GaAs or by methods of epitaxial deposition with a higher growth rate (i.e. liquid-phase epitaxy) [103]. The <110> crystal direction of the GaAs substrate is thus fundamental to form Al/Ga segregates. The NW sidewalls are indeed of the {110} type. As observed in subsection 2.3.2, HAADF micrographs of core-shell GaAs-AlGaAs NW cross sections (figure 2.9d) show brightness contrast in laminar features parallel to the NW sidewalls. These segregates may develop into the Ga-rich QD nanoclusters considered in this thesis.

The NW surface further enhances the segregation processes typical of AlGaAs by providing an uneven surface chemical potential μ. This is modulated by the variable curvature of the faceted NW surface, the occurrence of {110}-type facets together with {112}-type polar nanofacets and the alternation of ZB, WZ, and crystal defects along the NW. The influence of {110}- and {112}-type facets on the Al/Ga segregation is well documented in the literature, as well as the role of the polarity of the {112}-type nanofacets. The increased surface curvature at the ridge between two NW sidewalls is commonly taken into account, too [163, 98, 14, 102]. The combined effect of these factors on the adatom surface diffusion explains the formation of Al-rich planes with a 3-fold symmetry along the <112> directions.

In addition to the Al/Ga segregation throughout the NW cross section, Al and Ga can also

segregate along the NW length. The intercalation of crystal defects and different phases along the NW can drive the adatom diffusion. The work exposed hereafter (section 4.2) originates from the need to better understand these phenomena: it links the adatom diffusion along the NW length with the occurrence of crystal defects and the QD properties. The background to this study is found in ref. [96], where the PL emission from large ensembles of the same NWs used in the following (section 4.2) is analyzed. That study showed that the NWQD occurrence and emission energy is tuned by the shell thickness: more QDs can form in the larger volume of a thicker shell; at the same time, if the shell is thicker, some QDs can grow and emit at lower energy. In the same work, complementary PL measurements were conducted along single NWs. The thickness of tapered NWs was measured by SEM and correlated with the local QD occurrence and emission energy extracted from PL spectra. This study on single NWs agrees with the analysis on larger NW ensembles: where the shell is thicker, the QD occurrence increases and the QD emission energy redshifts. A summary of this PL-based correlation between QDs and shell thickness is given in section 4.1. However, the single-NW PL mapping also showed a more abrupt trend together with the smooth thickness-dependent variation of the QD properties. An abrupt increase in the QD occurrence consistently showed few μm below the NW top and was systematically accompanied by a sudden redshift of the average QD emission energy at the same position.

Non-systematic previous observations on the NW crystal structure lead to the formulation of the following hypothesis about the origin of the abrupt variation of the QD properties: the QD formation may be influenced by a sudden increase in the occurrence of crystal defects in the NW few μm below the NW top.

In several core-shell NWs of different materials, stacking faults and alternating ZB and WZ segments in the core are reported to influence the local growth rate and composition of the shell [164, 165, 166, 167, 54, 168, 169]. Stacking faults and different crystal phases modulate the surface energy of the sidewalls of the NW core: the local surface-energy gradients drive the migration of different adatoms and, consequently, the composition of the shell. These reports show that the NW crystal phase is an important factor to tune the composition of the NW shell. With specific focus on GaAs-AlGaAs core-shell NWs, APT measurements recently demonstrated that the core crystal phase drives the segregation of Al and Ga in the shell [62]. This work specifically suggests that Al-rich rings develop around the short ZB segments in NW mainly composed of WZ.

In order to verify the hypothetical correlation between QD formation and crystal-defect occurrence in the AlGaAs shell, a systematic correlation between the structure and the optical properties of identical NWs was required. The SEM-CL and TEM analysis along the same single NWs was chosen as the appropriate methodology to enable this correlative study with high spatial resolution. This work is reported in the following section 4.2. It shows that the sudden redshift of the NWQD emission energy and the abrupt increase in the NWQD occurrence are linked with a swift increase in density of rotational twins along ZB NWs. A model is proposed to account for the experimental observations: the effect of a non-uniform crystal phase on

the surface energy of the NW sidewalls is discussed and linked with the deposition of an AlGaAs shell of heterogeneous composition. Composition fluctuations in the AlGaAs shell may facilitate the formation of the self-assembled NWQDs and account for their increase in occurrence and redshift in emission energy. Furthermore, finite-element simulations of the NWQD electronic band structure show that the presence of rotational twins in the ZB phase decreases the NWQD exciton emission energy. A similar redshift was already reported for the band-edge emission energy in defected GaAs NWs as a function of the density of twins [59]. This effect depends on the type-II band alignment of the CB and VB edges between pure-ZB and twinned NW segments; the assumption is that the band edges of a twin align like WZ to the surrounding ZB. Assuming control on the formation of defects, the twin-driven NWQD formation allows to tune the NWQD-property distributions. For instance, ref. [170], reports on the growth of defect-free as well as defected core-shell NWs similar to those studied here. The emission of the QDs embedded in the NW shell is analyzed by CL and a difference in the emission between the two groups of defect-free and defected NWs is found.

4.1 Preliminary correlation with the shell thickness
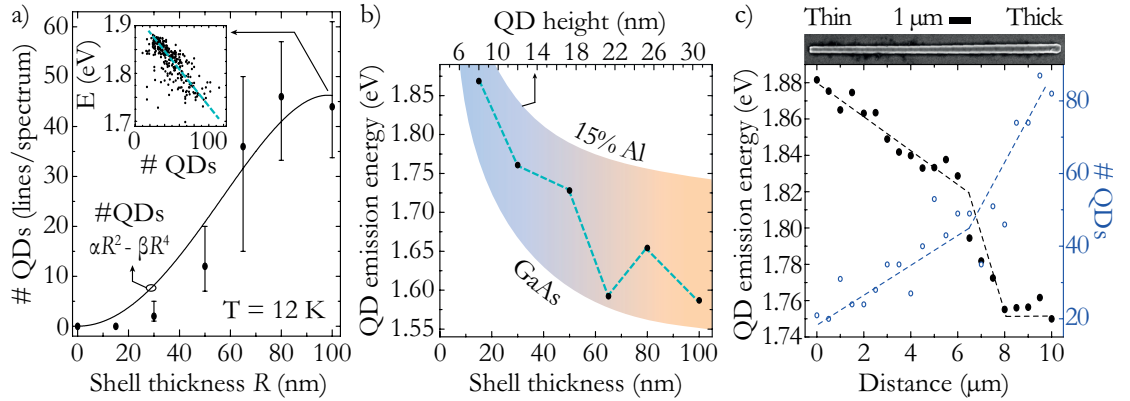
Figure 4.1 – a) Median of NWQD-occurrence distributions (1st and 3rd quartiles as width) vs the nominal shell thickness as in [96]. The solid line is a 4th-order polynomial fit of the data, as justified in the text. The inset is the QD energy-vs-occurrence of the whole set of spectra from the sample with 100-nm shell. The dashed line is a guide to the eye. PL experimental conditions: laser power of ∼ 100 W/cm^2 in a spot of 1 μm in diameter; sample temperature of 12 K. b) Low-energy tail of the NWQD emission-energy distributions vs nominal shell thickness. The shaded area corresponds to simulations of the exciton emission energy for QDs of different dimensions and compositions. c) QD emission energy (left axis, full black dots) and occurrence (right axis, open blue dots) along a single tapered NW (from bottom to top). The dashed lines are guides to the eye. An SEM image of the NW is reported on top of the plot. Thin and thick refer to the NW diameter.

A summary of the work of ref. [96] is presented here. This work links the properties of the NWQDs in the AlGaAs shell with the shell thickness. It is based on the automatized analysis of micro-PL spectra acquired on ensembles of several tens of NWs. The routine described in ref. [96] extracts the number of QD lines/spectrum and records their energy. The number of QD lines/spectrum is a measurement of the QD occurrence: in figure 4.1a, the QD occurrence is plotted as a function of the nominal shell thickness of the NWs. The QD occurrence is plot as

the median of the ensemble distributions; the error corresponds to the 1st and 3rd quartiles of the distributions.

Figure 4.1a shows that the QD occurrence increases for an increasing shell thickness until saturation. In order to interpret this observation, one can assume that QDs form in the NW shell at a constant rate per unit of shell volume. Therefore, the overall amount of QDs increases for an increasing shell volume (i.e. a thicker shell). Concomitantly, the QDs can grow larger in a thicker shell and merge: therefore, the probability for two or more QDs to merge increases with the shell thickness. This process can be modelled by: (i) a constant QD formation rate F per unit of shell volume V, that is $\frac{dF}{dV}$ is a constant; (ii) a QD merging rate M increasing as a function of the shell volume. For simplicity, M can be modelled as a function linearly increasing with the shell volume. Integrating $\frac{dF}{dV} - \frac{dM}{dV}$ in the NW volume, it can be demonstrated that the QD occurrence vs shell thickness has the form of $\alpha R^2 - \beta R^4$ for NWs of both cylindrical or hexagonal cross section (α and β are positive constants). The solid curve in figure 4.1a is a fit of the experimental data according to this polynomial form. Although the specific functional dependence of the QD formation and merging rates is probably more complex, this simple model captures the essence of the trend of QD occurrence vs shell thickness: an initial increase followed by saturation for thicker shells. Importantly, in the PL spectra, physically distinct QDs can spectrally merge because their emission lines overlap in energy: this spectral merging sums to the physical one considered in the model.

The shell of these NWs is tapered: the shell thickness decreases from the top to the bottom of the NW. The tapering is enhanced in nominally thicker NW shells. This shell-thickness gradient is expected to influence the QD properties at a local level. Where the shell is locally thicker, more QDs form and can grow larger; larger QDs emit at lower energy. The inset in figure 4.1a reports on the QD emission energy. It is derived from the whole dataset of the NWs with a shell of nominal thickness of 100 nm. Each data point is the average QD emission energy from a single spectrum vs the QD occurrence (i.e. the number of QD lines) in the same PL spectrum. The plot shows a correlation, indicated by the dashed line as guide to the eye: the spectra where the local QD occurrence increases also tend to emit at lower energies. This trend confirms that when the QD occurrence increases their emission energy redshifts.

Results on the QD emission energy from the whole ensemble of NWs are shown in figure 4.1b. For this analysis, only the 5% of QDs with lower emission energy is considered. The plot in figure 4.1b reports the average emission energy of this low-energy sample as a function of the nominal NW shell thickness. In first approximation, low-energy emitters correspond to larger QDs. From figure 4.1b one can observe that the emission energy of these low-energy QDs redshifts for an increasing shell thickness. This can be interpreted considering that large QDs can grow larger in thicker shells. The emitters at higher energy are excluded from this analysis because small QDs of high emission energy can form at any moment during the shell growth: only the larger ones are indeed observed to correlate with the thickness of the shell [96].

The shaded area in figure 4.1b corresponds to the exciton emission energy simulated (software

Nextnano) in pyramidal QDs based on the Ga-rich pyramidal nanoclusters reported in ref. [14] and shown in figure 2.9a. In the simulations, the QDs are surrounded by an $Al_{0.33}Ga_{0.67}As$ matrix and contain Al between 0% and 15%. Only the QD dimensions and compositions that overlap with the experimental energies are shown. Figure 4.1b indicates that an increase of about 20 nm in the QD size can account for the whole interval of the experimental emission redshift.

Following these findings on large NW ensembles, the combination of SEM images and PL linescans on single identical NWs revealed that the shell thickness controls the NWQD properties also at a local level [96]. SEM images showed that the NWs are significantly tapered: assuming that the core has a constant diameter, the shell thickness increases by about 50 nm from the bottom to the top of the NWs [96]. The NW tapering is only due to the gradient of material supply along the NWs during the shell growth: neighbor NWs close to each other screen the molecular beams. In figure 4.1c, the NWQD emission energy and occurrence are shown for an illustrative PL linescan as a function of the position along the NW . A SEM image of the NW is shown on top of the plot. Moving along the NW, from the thinner bottom towards the thicker top, the QD emission energy gradually decreases, while the QD occurrence gradually increases. These inverted trends correlate well with the increasing shell thickness from the NW bottom to the top [96]. However, at about 7 μm an abrupt upturn of the already increasing QD occurrence is observed; similarly, a sudden drop of the already decreasing QD emission energy is found at the same position. This observation suggested that a further analysis with higher spatial resolution was necessary; it is presented in the following by a direct-correlation study between CL and TEM mapping of identical NWs.

4.2 Tuning adatom mobility and nanoscale segregation by twin formation and polytypism

Luca Francaviglia [1] *, Gözde Tütüncüoglu* [1] *, Federico Matteini* [1] *and Anna Fontcuberta i Morral* [1,2] *.*

[1] *Laboratoire des Matériaux Semiconducteurs, Institut des Matériaux, École Polytechnique Fédérale de Lausanne, 1015 Lausanne, Switzerland.*

[2] *Institut de Physique, École Polytechnique Fédérale de Lausanne, 1015 Lausanne, Switzerland.*

For the work here presented, I conducted the experimental characterization that includes PL, TEM, and STEM EDX measurements and performed or coordinated the acquisition of the CL maps; I performed the Nextnano simulations; I interpreted and modelled the experimental

results. I wrote the draft version of the manuscript.

Abstract

Nanoscale variations in the composition of an $Al_xGa_{1-x}As$ shell around a GaAs nanowire affect the nanowire functionality and can lead to the formation of localized quantum emitters. These composition fluctuations can be the consequence of variations of crystal phase and/or nanoscale adatom mobility. By applying electron-microscopy-related techniques we correlate the optical, compositional and structural properties at the nanoscale on the same object. The results indicate a clear correlation between the twin density in the nanowire and the quantum-emitter density as well as a significant red-shift in the emission. We propose that twinning increases nanoscale segregation effects in ternary alloys. An additional red-shift in the emission can be explained by the staggered band-alignment between wurtzite and zinc-blende phases. This work opens new avenues in the achievement of homogeneous ternary and quaternary alloys in nanowires and in the engineering of the segregation effects at the nanoscale.

Introduction Semiconductor nanowires (NWs) and quantum dots (QDs) provide a suitable platform for photodetection and emission at the single-photon and classical level [171, 15, 109] as well as for classical and quantum computing [172, 173, 174, 175, 176]. In addition, it is well-known that NWs can host crystal phases otherwise unstable in normal conditions in the bulk form. Hexagonal wurtzite (WZ) phase can be achieved both in III-V and group IV semiconductors, which otherwise typically exhibit a cubic zinc-blende (ZB) or diamond phase in the bulk [9, 177, 178]. This unique property has allowed to access the WZ GaAs band gap and the alignment of its band edges with respect to those of the ZB phase [179, 59, 61, 180, 181]. In addition to its value in fundamental studies, the tuning of the NW crystal phase is exploited to define QDs in NWs [10, 55, 57, 58]. On the other hand, uncontrolled variations in the crystal phase, along with the existence of stacking defects (through twins and stacking faults) can be detrimental for the functionality of the NWs. Improved optical and electrical properties are demonstrated in defect-free NWs [11, 182].

In addition to a different electronic band structure, WZ and ZB exhibit slightly different surface properties that impact the adatom mobility during growth. The coexistence of WZ, ZB and twins in the same NW is thus an excellent platform to study how the NW crystal phase impacts the adatom incorporation on the NW sidewalls under the same growth conditions [167, 180, 169, 54]. Adatom mobility and sticking coefficient determine the formation of radial heterostructures, like core-shell NWs [54]. Here, we study GaAs-$Al_{0.33}Ga_{0.67}As$ core-shell NWs grown by molecular beam epitaxy (MBE). It has been shown that AlGaAs exhibits spontaneous segregation of Al and Ga at the nanoscale. Ga-rich clusters can form [14, 95] and act as QD-like single-photon emitters in the 1.72-1.90 eV emission range [14, 96]. While the exact formation mechanism for these QDs is still unknown, the differentiated adatom mobility in the facets and corners of the NW core is one of the key elements in the explanation.

A sketch of the structure of the studied NWs and NW-based QDs is provided in figure 4.2(a). In a previous publication [96], we reported on a correlation between the shell thickness and
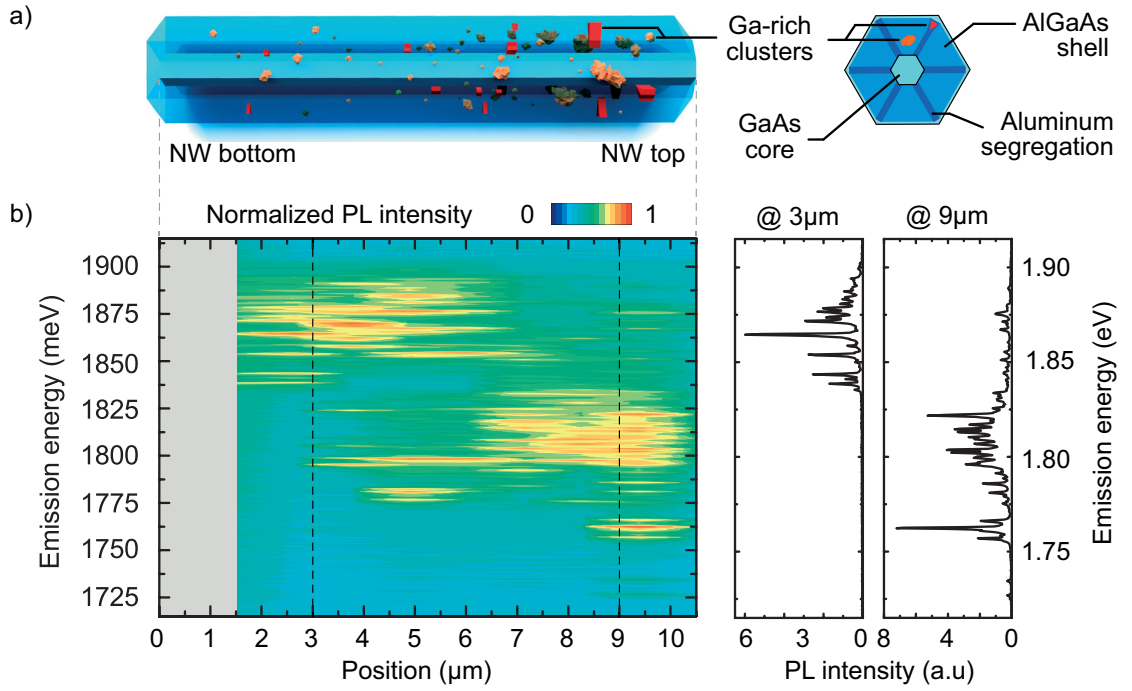
Figure 4.2 – (a) Simplified 3D representation and cross-sectional sketch of the core-shell GaAs-AlGaAs NW structure. The possible Ga-rich emitters are depicted in red and orange in the shell, depicted in blue [14, 95, 96]. (b) On the left: contour plot of normalized PL spectra in the 1.72 eV - 1.90 eV energy range from the bottom to the top of a NW on a TEM grid ($1\mu m$ steps between consequent spectra). The grey band indicates a NW segment covered by the TEM-grid carbon film, as revealed by the SEM image in figure 4.3(c). No emission was detected in this region. On the right: PL spectra (not normalized) from the positions indicated by the dashed vertical lines in the contour plot.

the QD emission energy, which we confirmed also by CL maps (figure S6 in the Supporting Information). Both on large NW ensembles and at the single-NW level, the QDs redshift for an increasing shell thickness, probably because of the occurrence of larger QDs in a thicker shell. However, together with this smooth energy shift related to thickness, a more abrupt decrease of the emission energy was caused by some other factor. In this work, we study the possible role of structural defects in the core to trigger the Ga segregation, providing clues on the QD formation mechanism. In particular, we consider the effect of stacking defects on the electronic band alignment in the QDs and on the self-segregation process that forms the Ga-rich QDs of the shell. We study the optical properties of the QDs on a grid for transmission electron microscopy (TEM) in order to correlate the local emission characteristics at the nanoscale with the information on the structure and the shell composition obtained by electron microscopy. Similarly to the work of Heiss et al. [59], we study identical NWs by photoluminescence (PL), cathodoluminescence (CL), scanning electron microscopy (SEM), TEM and energy-dispersive X-ray spectroscopy (EDX). We then provide a simple model to explain and support the experimental data. We first simulate the QD emission energy as a function of the density of twins, which alters the band edges of the QD potential well. We then discuss how the crystal phase of the GaAs core can perturb the compositional profile of the

(Al)GaAs matrix epitaxially grown around the GaAs core. We recall that the inhomogeneous composition of the NW shell is at the origin of the formation of the NW-based QDs studied in this work. A single factor, the crystal structure of the NW core, has a large impact on the QD optical emission acting on both the semiconductor band gap and the QD composition itself.

Experimental methods A schematic representation of the structure of our NWs is presented in figure 4.2(a). We start by growing GaAs NWs by the Ga-assisted method on a Si (111) substrate covered by native oxide as explained in detail in Refs [43, 5]. The NWs have a hexagonal cross-section. Once the GaAs NWs are about 10-μm long, we stop the NW vertical growth by interrupting the Ga supply and consuming the Ga droplet. We switch then to planar epitaxial conditions for {110} surfaces and grow an AlGaAs shell [183]. For the samples investigated here, the Ga and Al deposition rates were set to 0.6 Å/s and 0.3 Å/s respectively, which results in the stoichiometry $Al_{0.33}Ga_{0.67}As$. Scanning TEM (STEM) EDX measurements indicate an average composition of the NW shell of 27±2% of Al; Raman measurements conduct to a comparable average of 29±8% of Al in the NW shell [134]. The Al shell content has been extensively reported to be spatially non-uniform, with Al-rich planes at the ridge between two NW facets [14, 95, 96, 102]. By changing the deposition time of the AlGaAs shell we grew three different samples with nominal shell thickness of 30 nm, 50 nm, and 100 nm. Here, we report on the samples with a 50-nm thick shell. Data on the 30 nm and 100 nm samples are consistent with the ones on the 50 nm and are shown in figures S5 and S10 in the Supporting Information. We always complete the AlGaAs shell growth with the deposition of 5 nm of GaAs to avoid oxidation. We transfer few NWs from the three samples onto three different carbon-coated TEM grids by gently scrubbing the grid on the as-grown sample. The observed NWs lie horizontally on one of their six side facets, supported by the carbon film. Markers on the TEM grids facilitate the localization of the same NWs for each of the measurements: PL, SEM-CL, TEM and (S)TEM EDX. For the current work, we perform TEM after the optical characterization in order to avoid the deterioration of the NW optical properties by interaction with accelerated electrons of high energy. Nevertheless, we observe that the NW emission is not affected by long CL mappings. No evidence of e-beam-induced heating is found, therefore no preventive measure is implemented to disperse heat [122].

We perform the PL measurements in a close-loop liquid-helium Attocube cryostat cooled down to 4.2 K. We use a continuous-wave HeNe laser as an excitation source with wavelength equal to 632.8 nm. Through an objective with NA = 0.85, we focus the laser light on the sample in a spot of 1 μm in diameter. The power density at the sample is less than 100 W/cm^2. We collect the PL signal through the same objective, disperse it with a 300 l/mm grating and detect it with a nitrogen-cooled charge-coupled device (CCD). The integration time for each spectrum is 1 s. For PL linescans, the Attocube piezo-positioner ensures the movement along a NW in 1μm-long steps. Together with SEM images, the step distance allows to define the absolute position of the PL spectra on the NW.

We perform the CL measurements in an Attolight Rosa SEM-CL microscope. The TEM grids are mounted in the microscope on a stage cooled down to 12 K by liquid helium. We excite

the luminescence with a current in the order of 1 nA and an acceleration voltage of 1.5 kV. This produces a small interaction volume of primary electrons in the NW (figure S1 in the Supporting Information). A reflective objective (NA 0.71) embedded within the electron optics collects the emitted light to a 32-cm focal-length spectrometer, where a 600 l/mm grating disperses the signal onto a Peltier-cooled CCD. For each NW, we acquire several 128 x 128 pixels CL maps and merge them into a unique map after the acquisition. The exposure time of each pixel is 100 ms. In the same setup and right before each CL map, we acquire the SEM images of exactly the same sample regions by means of an Everhart-Thornley detector.

We use an FEI Tecnai OSIRIS TEM operated at 200 kV (point resolution of 0.24 nm) to study the NW crystal structure, both in conventional bright-field (BF) and high-resolution (HR) TEM modes. We tilt the NWs to observe them along the ZB ⟨110⟩ direction or equivalent WZ ⟨11-20⟩, as confirmed by the diffraction patterns. The NW growth direction is ⟨111⟩. Only the edges of the NWs are thin enough for performing HRTEM without further sample preparation. For this reason we solely show HRTEM micrographs of the shell. However, one should note that the shell grows epitaxially around the GaAs core and its crystal phase follows the structure of the core [53, 54]. We acquire EDX maps in STEM mode in the same microscope at a probe current of 2 nA. The TEM image acquisition relies on a Gatan Orius CCD camera, while four silicon drift detectors (SDD) at a 0.9-srad solid angle collect the X-ray signal for the compositional mapping.

We calculate the QD emission energy by 1D simulations of an 8-nm GaAs potential well with $Al_{0.2}Ga_{0.8}As$ barriers. We iteratively solve the Poisson and Schrödinger equations by means of the commercially available software Nextnano [184, 185]. The reported exciton energies include the contribution of the charge-carrier confinement and the exciton binding energy. The QD potential well is simplified as pure GaAs in order to use the experimental values in Ref. [59] and because the exact band structure of WZ AlGaAs is still a matter of debate [60, 186, 187]. The potential barrier is set by $Al_{0.2}Ga_{0.8}As$, in agreement with the experimental Al fluctuations in the shell away from the Al-rich ridges [95, 102]. The QD width is chosen in agreement with previous studies [14, 125, 95]. We use the software material parameters for ZB GaAs and AlGaAs, while we overwrote the software library for the WZ GaAs by upshifting the conduction- and valence-band (CB and VB) edges by respectively 53 meV and 76 meV with respect to ZB [59]. In figure S8 in the Supporting Information we show more simulations for different WZ band offsets available in the literature, which confirm the findings shown here.

Results Figure 4.2(b) shows a contour plot of the PL spectra acquired at 1-μm steps from the bottom to the top (increasing NW position) of a GaAs-$Al_{0.33}Ga_{0.67}As$ core-shell NW. The 3D NW sketch in figure 4.2(a) is aligned with the PL linescan reported in figure 4.2(b). The grey band in figure 4.2(b) indicates a segment with no emission at the very bottom of the NW. This segment is covered by the carbon film of the TEM grid, as later revealed by the SEM image in figure 4.3(c). Two spectra are extracted from the linescan and are reported on the right in figure 4.2(b). They correspond to the positions indicated by the vertical dashed lines in the contour plot. In both the extracted spectra and the contour plot, the reported
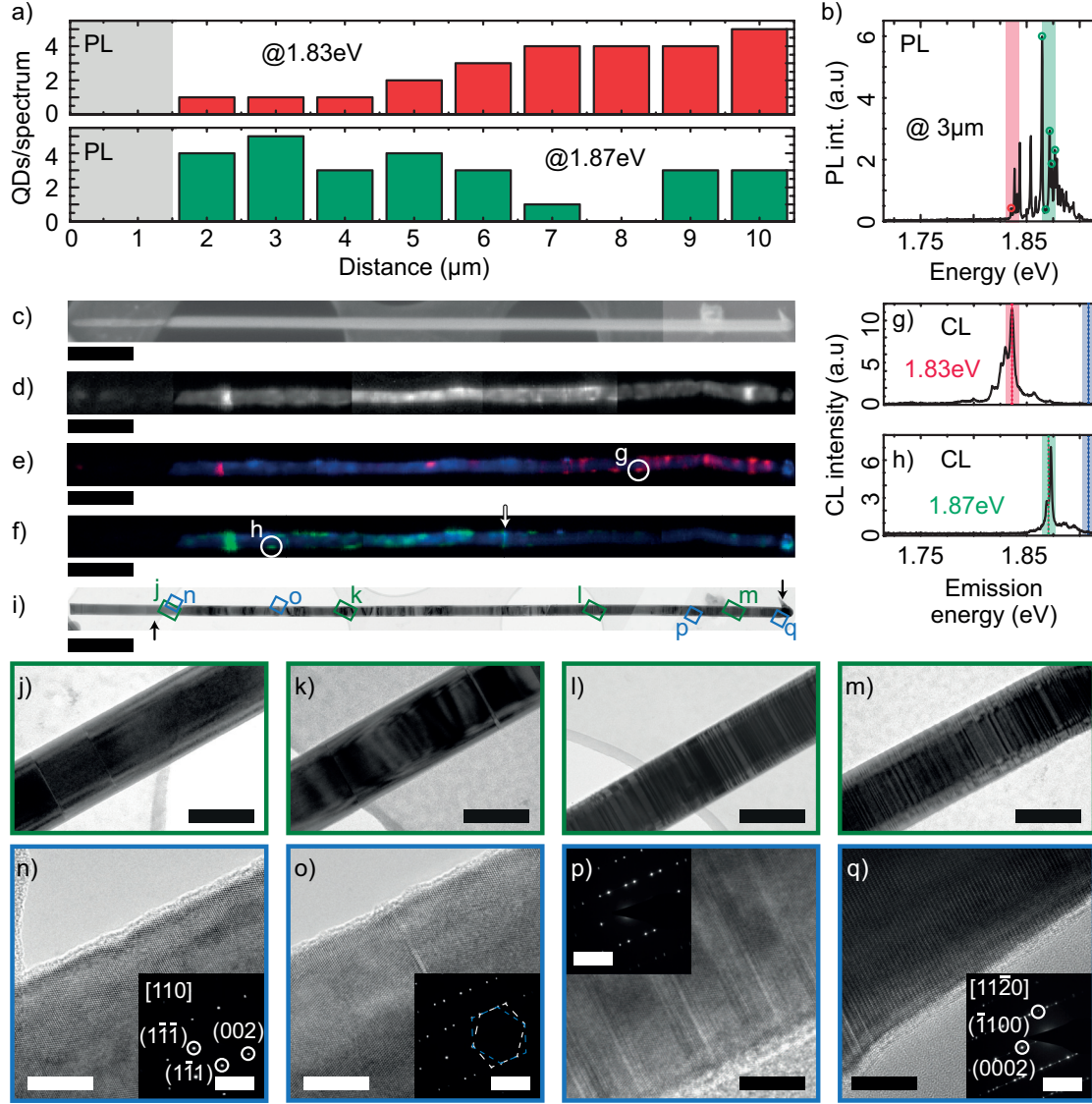
Figure 4.3 – (a) Histograms of the QD occurrence in PL spectra for the two spectral regions centered at 1.83 eV and 1.87 eV. The data are extracted from the PL spectra shown on the right in figure 4.2(b) according to the automatic routine described in Ref. [96]. (b) Illustrative PL spectrum with indicated the peaks found by the routine (same PL spectrum as the one at 3 μm in figure 4.2(b)). The red and green stripes respectively correspond to energy ranges centered at 1.830±0.007 eV and 1.870±0.007 eV. (c) SEM image of the same NW. (d) Panchromatic 12 K SEM-CL map of the same NW. (e - f) Energy-filtered CL maps of the same NW. Color coding: 1.910±0.007 eV in blue in (e) and (f), 1.830±0.007 eV in red in (e) and 1.870±0.007 eV in green in (f). The arrow in (f) indicates an extended emitter that crosses the entire NW diameter. (g - h) Single-pixel CL spectra corresponding to, respectively, the localized emitters circled in (e) and (f). Color-coding like in (e)-(f). The PL spectra on the right of figure 4.2(b) were acquired at the same positions. (i) BF-TEM micrograph of the same NW. (j - m) Zoomed-in TEM micrographs of different regions along the NW as indicated in figure 4.3(i). (n - q) High-resolution TEM micrographs of the NW at the positions indicated in (i). The diffraction patterns are in the insets in each figure from (n) to (q). Scale bars: (c - f, i) 1μm, (j - m) 200 nm, (n - q) 10 nm and 4nm^{-1} in the insets.

range of the emission energy (1.72 eV - 1.90 eV) corresponds to the QD emission. Given the diffraction-limited spatial resolution of PL, the single QDs appear to stretch over few μm in the linescan. Each spectrum in the contour plot is normalized between 0 and 1, in order to primarily appreciate the position in energy of the QD emission. We observe that some lines group together both in space and energy. In particular, one group is visible in the bottom part of the NW at energies between 1.85 eV and 1.90 eV, while a second one can be found at lower energies (between 1.80 eV and 1.85 eV) in the top part of the NW. Therefore, the NW results to be divided into two regions according to two groups of different emission energy. In addition to some isolated lines, the two main groups define a spatially abrupt transition at $7\pm1\mu$m. The uncertainty comes from the 1 μm steps of the linescans and the spatial resolution of micro-PL. The comparison of the two selected spectra on the right confirms a redshift of the groups of QD lines when moving towards the NW top. The two spectra also show that more QD lines appear towards the NW top, which reflects an increased amount of optically active QDs. We turn now to a detailed analysis of the spectral features and statistical occurrence of the QDs along the NW. Figure 4.3(a) illustrates the occurrence of QD lines per PL spectrum in two selected energy intervals centered at 1.830$\pm$0.007 eV (upper red histogram) and 1.870$\pm$0.007 eV (lower green histogram). The number of QD lines per spectrum is indicative of the number of QDs per spectrum. Each histogram column corresponds to one PL spectrum. The selection of the QD lines is performed automatically as described in Ref. [96]. An example of the QD-peak detection procedure is shown in figure 4.3(b). We show the PL spectrum at 3 μm (identical to the one reported on the right of figure 4.2(b)). The red- and green-shaded stripes correspond to the chosen energy intervals and the red and green circles to the selected QD peaks. We note that we chose to monitor the occurrence of the emission at the lower and higher energy range, but that there are other peaks in between these two energies. The plot in figure 4.3(a) indicates that the number of QDs emitting around 1.83 eV increases from 1 QD/spectrum to 5 QDs/spectrum in the direction of the NW tip. Concomitantly, the occurrence of QDs emitting at 1.87 eV decreases from a maximum of 5 QDs/spectrum at 3 μm from the base to no QDs at 8 μm. Surprisingly, 4 QDs/spectrum appear again in this energy range at the tip of the NW. Yet, the overall count of PL QD lines shows that the low-energy (1.83 eV) emitters become more frequent towards the NW top, while the opposite happens with those emitting at high energy (1.87 eV). We now turn to a higher spatial resolution of the luminescence by providing the CL mapping on the same NW. CL measurements can improve the spatial resolution of luminescence mapping beyond the PL limits. The size of the electron beam, the volume of the exciton generation and the minority-carrier diffusion length define the CL spatial resolution (figure S1 in the Supporting Information) [188]. In addition, the CL resolution can be improved by selecting only one emission-energy range at a time, which may rule out the detection of multiple, spatially close emitters. The spectral selection [189] improves the spatial resolution in the energy-filtered CL maps. Figure 4.3(c) shows the SEM image of the NW. Figure 4.3(d) corresponds to the panchromatic (all-wavelength) map of the CL emission, where brighter pixels correspond to more intense CL signal. Figure 4.3(e) and (f) show only selected emission energies from the panchromatic maps. The color coding is the following: 1.910$\pm$0.007 eV in blue in both (e) and (f), 1.830$\pm$0.007 eV in red in (e) and 1.870$\pm$0.007 eV in green in (f). Red
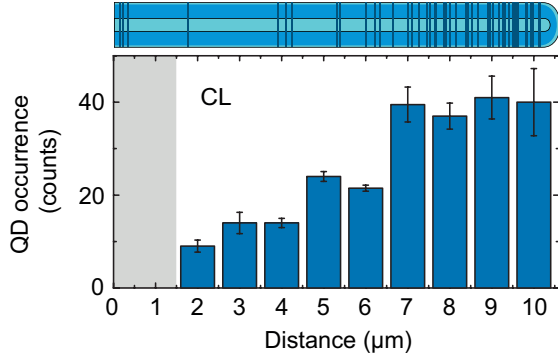
Figure 4.4 – Graph of the QD density (counts per μm) vs NW position. The error bars are the standard deviations of the distributions of QD occurrence in each μm. The gray stripe indicates the NW bottom hidden by the carbon film. A sketch of the twinned NW is aligned above the plot.

and green encode the same energy ranges chosen in figure 4.3(a). The scale bars in figures 4.3(c) to (f) correspond to 1 μm. The histograms in figure 4.3(a) and the CL maps in figures 4.3(c-f) are aligned. The SEM image revealed that the very bottom segment of the NW is covered by a portion of carbon film from the TEM grid. Our measurements indicate that it weakens the signal from this portion of NW with respect to the rest by light absorption and reflection. In all the reported CL maps we can recognize bright emission over the full length of the NW, besides the carbon-covered base. The CL emission at 1.91 eV corresponding to the band-edge emission of AlGaAs (shown in blue) is found through the full NW length. It does not exhibit spatial localization features as for the other emission peaks. On the contrary, the emitters at 1.83 eV and 1.87 eV (figures 4.3(e) and 4.3(f) respectively) are clearly spatially localized. The emission zones exhibit different shapes and dimensions. Some extend over very few pixels (each pixel is about 20 x 20 nm), while others are larger and appear as stripes across the full NW diameter. An example is indicated by the arrow in figure 4.3(f) at about 6 μm from the NW base. Especially in figure 4.3(e) and (f), SEM-CL allows to clearly resolve localized emitters not only along the NW long axis, but also within the 200-nm thick NW diameter. We recognize the bright and localized emitters in the CL maps as the shell QDs revealed by the PL spectra. This correlation is also corroborated by the similar trend in the occurrence of high- and low-energy emitters in the upper and lower portions of the NW as illustrated here below. The CL mappings of figures 4.3(e-f) clearly illustrate that most of the emission at 1.83 eV stems from the upper part of the NW (above about 7 μm in figure 4.3(e)). Reversely, the emission at 1.87 eV mainly stems below 7 μm (figure 4.3(f)), with the exception of a rather large emitter at the very tip of the NW. Interestingly, there are almost no low-energy (1.83 eV) emitters below 7 μm (figure 4.3(e)). Similarly, the upper region of the NW shows almost no emission at high energy (1.87 eV - figure 4.3(f)). The transition between the two spectral regions in the CL maps is quite abrupt and in good spatial agreement with the PL linescan (figure 4.2(b) and 4.3(a)).

Figure 4.3(g) reports a single-pixel CL spectrum acquired at about 7 μm on the NW, while figure 4.3(h) reports a single-pixel CL spectrum acquired at about 3 μm on the NW. These positions are indicated by circles in figures 4.3(e) and (f) respectively. By comparison with the PL spectra acquired at the same positions, one can observe that the CL spectra are consistent with the PL. In particular, the CL spectrum acquired towards the NW top (figure 4.3(g)) emits at lower energy than the one acquired in the lower part of the NW (figure 4.3(h)).

We proceed now to correlate the QD emission characteristics with the local structural proper-
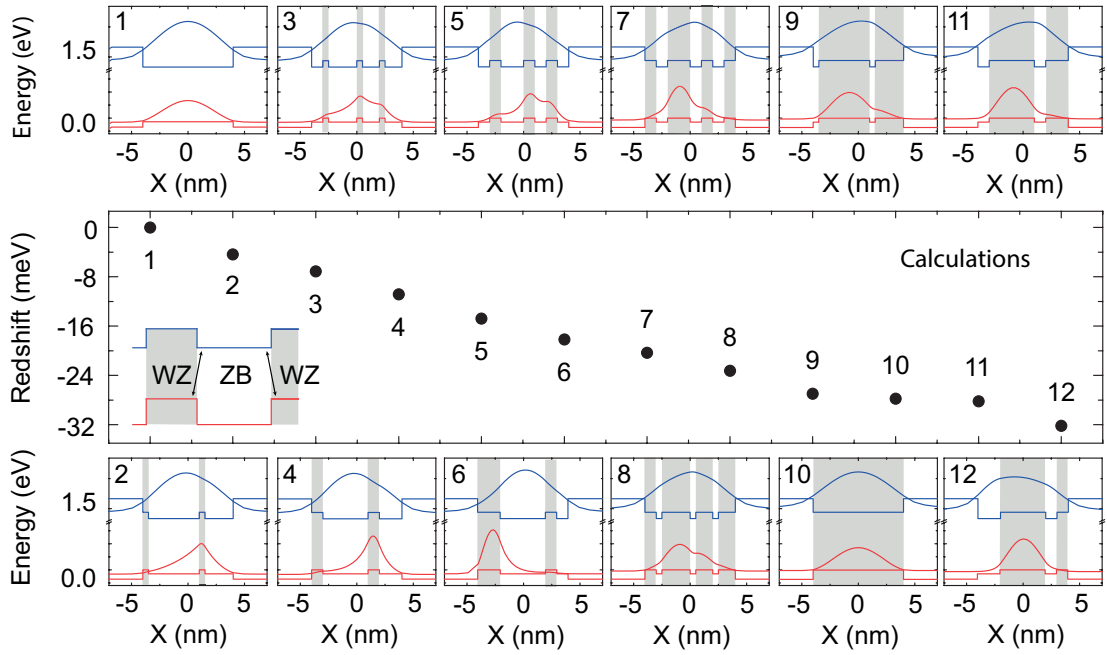
Figure 4.5 – Simulations of the QD exciton emission energy as a function of the WZ-ZB ratio and relative arrangement inside the QD. The zero corresponds to the emission energy from the ZB QD. The twelve energies are reported by decreasing energy and linked by their number with sketch of the simulated QD structure, reported above and below the graph. Each sketch shows the CB and VB edges (upper/blue and lower/red respectively) and the electron and hole density probabilities (upper/blue and lower/red respectively). The gray bands correspond to WZ.

ties of the NW. For this, we show the TEM data from the identical NW. Figure 4.3(i) corresponds to the low-magnification (scale bar 1 μm) BF TEM image of the NW. We use this full-length image to locate the position of the higher-magnification TEM images taken from the NW bottom to the top and reported in figures 4.3(j) to (q), as indicated by the corresponding letters. In particular, figures from 4.3(j) to (m), framed in green, are BF TEM images at the same intermediate magnification (scale bars equal to 200 nm); figures from 4.3(n) to (q), framed in blue, are HRTEM images (scale bar 10 nm). The insets in figure 4.3(n) to (q) are the diffraction patterns (scale bar 4 nm^{-1}) taken at the positions of the corresponding HR micrographs.

In figures 4.3(j) to (m) we observe brightness contrast as radial stripes along the NW. From the HRTEM micrographs in figures 4.3(n) to (q) we recognize that this contrast stems from twins in a ZB crystal. We find only one extended WZ segment at the very top of the NW (figure 4.3(q)). As a general trend valid on few-μm-long NW segments, we quantify less than 20 twins/μm in the lower part of the NW and about 200 twins/μm in the upper NW, with an abrupt increase above 7 μm (figure S2 in the Supporting Information). As an illustrative case, figure 4.3(n) shows a 50-nm NW segment of pure ZB phase at the NW bottom. Moving towards the NW top, more rotational twins are visible: first isolated, like in figure 4.3(o), then with increasing density, like in figure 4.3(p). Such a trend in twin density has already been reported for similar GaAs NWs [59]. Excluding the WZ region at the very top of the NW (figure

69

4.3(q)), each twin-free segment in the rest of the NW follows the ZB atomic stacking. The plane of a twin between two ZB segments results in a WZ-like atomic stacking [190, 122]. In principle, an increase in twin density can be regarded as an increase in the insertion of WZ planes along the NW. In the upper NW, the density of twins is high and the distance between two defect interfaces can reduce to one lattice constant, that is, the thickness of the defect itself [59]. We move now to the correlation between the QD occurrence and density with the crystalline structure of the NW. CL provides indeed enough spatial resolution to count single bright emitters along the NW. The number of bright QDs visible in the CL as a function of the position along the NW is plotted in figure 4.4. On top of the graph we include a sketch of the NW with an illustration of the twin density along the axis, as obtained by HRTEM. The data are grouped in 1-μm steps to smoothen the curve and facilitate the reading. The error bars are the standard deviations of the distributions of QD occurrence in each μm. We observe that the lower part of the NW hosts about 20 QDs/μm. At positions between 7 and 10 μm about 40 QDs/μm are observed. We thus conclude that, also considering the QD density, the NW seems to be split into two differentiated regions. These, in turn, correlate well with the two regions of different density of twins.

Discussion In the following, we discuss the spatial correlation between (1) the increasing twin density and increasing QD density and (2) the increasing twin density and decreasing QD emission energy. First, we discard the presence of an average gradient in the NW composition along its main axis. For this, we provide an analysis of the average chemical composition in the shell by EDX STEM. The two black arrows in figure 4.3(i) indicate the position where we acquired EDX STEM maps (figure S3 in the Supporting Information). Within the experimental error, there is no difference of Al/Ga average concentration in the two positions, which would affect the shell bandgap along the NW at the microscale [191]. Equally important, we do not observe any variation in the NW diameter, which would hint to a gradient in the shell thickness [96]. We consider two hypotheses: i) the ZB-WZ band alignment and ii) the anisotropic deposition of different adatoms on the NW sidewalls. As already mentioned, a rotational twin in ZB can be considered as a WZ plane [192]. Thus, we first address the modification of the band alignment in the QD by the existence of WZ inclusions in a ZB structure, similarly to Ref. [59]. In spite of some disagreement about the exact values, it is widely reported in the literature that GaAs WZ and ZB have very similar band gaps at low temperature and a staggered band alignment [60, 179, 59, 61, 192, 180, 181]. In particular, both the VB and CB edges are upshifted in WZ, which favors the accumulation of holes in the WZ region and electrons in the ZB. When electrons and holes radiatively recombine across the WZ-ZB interface, the emitted photon is redshifted with respect to both the WZ and the ZB band gaps [59, 179, 60]. This transition is sketched in the inset of the main graph of figure 4.5. We can consider a similar band alignment in the AlGaAs shell, where twins are the epitaxial continuation of those of the core. The CL data consist of excitation maps of the NW luminescence and the bright emitting stripes that sometimes we observed across the whole NW diameter (see for example the region indicated by the arrow in the CL map in figure 4.3(f)) can provide evidence of the presence of type-II band alignment in the AlGaAs shell. Their alignment along the NW radial direction suggests a

tight link with twins: the twin-induced staggered band alignment in AlGaAs (similar to the one in GaAs) may account for the electron and hole localization at a ZB-WZ interface [179, 192].

Twins epitaxially propagate from the NW core to the shell [193, 53]. A QD is defined by a nanoscale change in the composition of the AlGaAs matrix. Both pure ZB and twins can propagate through the Ga-rich segregations that act as the observed QDs. Given the high density of twins in the upper part of the NW, the occurrence of twins in the crystal structure of a QD is highly probable in this NW region. An increase in the twin density has been correlated with an increased probability of thicker WZ-like segments [59]. We have calculated the exciton recombination energy for several configurations where an increasing amount of thicker WZ segments is included in a QD. The thicknesses are consistent with the HRTEM observations. The alignment of the VB (red) and CB (blue) of these mixed-phase QDs is sketched in figure 4.5 (the gray bands represent WZ) and overlapped to the calculated hole (red) and electron (blue) density probabilities. We consider configurations ranging from pure ZB to pure WZ. We have ordered them by energy of the exciton (decreasing from left to right). Each configuration is numbered to help the reader to link it with the energies reported in the main graph in figure 4.5. The emission energy of the QD of pure ZB is taken as the reference zero (configuration #1).

We first observe that any inclusion of WZ in the QD results in a decrease of the exciton energy, up to a maximum redshift of about 32 meV. In part, this depends on the fact that the WZ bandgap that we used in our simulations is smaller than the ZB one by 23 meV [59]. Yet, this is not the only contribution to the redshift of the exciton energy. This consideration is confirmed by the fact that the pure-WZ QD (configuration #10) has not the most redshifted emission. In addition, the only extended WZ segment experimentally observed at the NW top (figure 4.3q) is not correlated with a local redshift of the QD emission (figures 4.2 and 4.3). We rather highlight that the staggered WZ-ZB band alignment plays a key role in the emission-energy reduction [61, 59, 179, 60]. Such a band alignment localizes electrons and holes in ZB and WZ segments, respectively, which favors their recombination across the ZB-WZ interface. Such a spatially indirect transition is redshifted with respect to the direct recombination at the ZB and WZ band gaps because of the VB and CB offsets. From the density probabilities in figure 4.5, we qualitatively observe that the carrier localization is more evident in the WZ segments where holes are confined. This is a direct consequence of the larger hole effective mass with respect to electrons. Since the localization of electrons and holes in spatially separated segments is the cause of the redshifted indirect recombination, we conclude the heavy holes take on the main contribution of the emission redshift. We remark that the carrier localization in different regions reduces the exciton binding energy. This results into a blueshift of the emission that is revealed in our simulations (not shown). However, it is limited to 1 meV at most and is minor if compared to the redshift due to the spatially indirect transitions.

Our simulations clearly point to the fact that a mixed phase can induce a large redshift of the exciton recombination energy. Nevertheless, the occurrence of a mixed crystal phase has not only an influence on the QD electronic bands. The formation of our QDs relies on the segregation of Al/Ga [102] in a ternary alloy. It is accepted that this should depend on
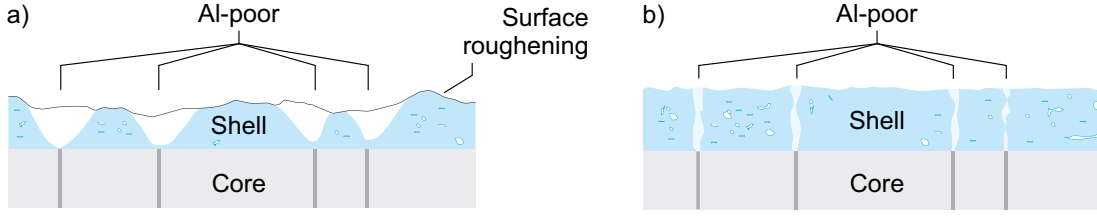
Figure 4.6 – Sketches of the side-view section of core-shell NWs. They illustrate in a cartoon style two scenarios of twin-driven Al-Ga segregation in the NW shell. The core is in gray: darker regions represent twins. The AlGaAs shell is depicted in light-blue: the darker the color, the larger the Al content. (a) Al depletion at the twin positions due to surface roughening. (b) Al depletion at the twin positions driven by different preferential incorporation of Al and Ga on the facets exposed by twin and pure ZB.

the nature of the NW core facets: (110), (112) as well as the polarity of the latter [98, 103]. Therefore, we have to consider that the crystal phase of the core can directly influence the QD formation and composition, and, as a consequence, the QD occurrence and emission energy. For instance, the facilitation of the QD formation at an early stage of the shell deposition allows each QD cluster to grow larger and emit at lower energies [96]. We highlight that Ga-rich clusters should grow to a diameter of at least 4 nm to contribute to the PL spectra [102]. An evidence that the occurrence of twins may facilitate the QD formation is the increase of the QD density in the upper part of the NW (figure 4.4), where the twins are significantly denser (from about 7 μm to the top of the NW). Further support to the correlation between defects and segregation comes from the recent observation that Al is preferentially incorporated on the stacking faults and short ZB segments of WZ GaAs-AlGaAs core-shell NWs [62].

In the following, we elaborate on the twin-induced enhancement of the Al/Ga segregation and propose two mechanisms. In a first case, we base our discussion on the fact that, for several material combinations in core-shell NWs, the growth rates of the shell are reported to depend on the core facets, as well as on the crystal phase and the presence of defects in the NW core [164, 165, 166, 167, 54, 168, 169]. As a result, the shell morphology becomes rough, even in the cases in which the underlying NW facets are originally flat [54]. In particular, the positions of discontinuity in the growth rate correspond to the stacking defects [54, 165]. We adapt this scenario to the ternary alloy in our GaAs-AlGaAs NWs. In figure 4.6(a) we sketch a side view of a NW cross-section: the GaAs core is in gray, with the twins in a darker color; the shell is in blue, with lighter shades corresponding to Al depletion. We depict the shell growth front as irregular: in regularly twinned core-shell NWs with anisotropic shell growth rate, prominent features as high as about 10 nm are observed on the shell surface [54]. A rough shell surface has a variable curvature, which introduces local gradients in the surface chemical potential (μ). We highlight that surface roughness at the atomic scale already defines an uneven μ profile for the adatom diffusion. Therefore, a net flux of different adatoms forms according to the Nernst-Einstein equation and because of the different diffusion lengths of the adatom species involved in the growth (S4 in the Supporting Information) [101]. In the case of AlGaAs, Ga has a longer diffusion length with respect to Al [100]. We expect that Ga concentrates where the shell is concave because these are the positions where the surface curvature lowers μ. We

illustrate this phenomenon in figure 4.6(a) by showing that Ga enriches the concavities formed on top of the twins (white in the light-blue shell matrix).

We also propose a second mechanism of segregation enhancement in which we neglect the roughening of the NW surface. We propose this scenario to highlight that other factors can alter the NW surface energy. For instance, twins are expected to introduce a different configuration of bonding sites at the surface [194, 195]; similarly, simulations and experiments have shown that the surface energy of the GaAs NW sidewalls depends on the NW crystal phase [180, 169, 196, 195]. Therefore, Al and Ga can be incorporated at a different rate in different positions of flat NW facets according to the presence of twins and WZ or ZB segments. To support this consideration, we remind that Al enrichment has been reported on the stacking faults in WZ GaAs-AlGaAs NWs [62]. In the upper part of our NWs we observed high density of twins in ZB. Therefore, in comparison with Ref. [62], we have the opposite phase and we then assume that the formation of Ga-rich clusters is enhanced in the upper part of our NWs. This, in turn, may promote the formation of QD-like emitters. In figure 4.6(b) we represent the side-view section of a core-shell NW with the same color coding as in figure 4.6(a). In agreement with our discussion, we depict a flat shell growth front and illustrate that the Al depletion happens at the twin positions (lighter color in the shell).

It is often observed that the sidewalls of twinned NWs are composed of alternated {111}A- and {111}B-type facets rather than the flat {110} type [194]. In our case, like in Ref. [62], our measurements cannot prove that the NW facets become atomically rougher in presence of twins and stacking faults. For simplicity, we neglected the surface roughness in the discussion of the second mechanism of segregation enhancement. However, the real case is probably a combination of the two mechanisms: the twins induce a roughening of the NW sidewalls, but also have intrinsically a different surface energy with respect to the surrounding phase. Overall, the twins facilitate the Al/Ga segregation.

Figure 4.6(b) also suggests an alternative explanation for the bright emission observed across the whole NW diameter in the CL maps (exemplified by the one indicated by the white arrow in figure 4.3(f)). We already proposed that the WZ-ZB type-II band alignment can propagate into the shell and localize excitons along the NW longitudinal axis. Here, we also consider that Ga-rich rings may form on top of a twinned core and radially grow with the shell. The lower bandgap of Ga-rich rings can confine excitons according to a type-I band alignment. Similar rings were predicted for the Sb segregation on ZB-WZ GaAs NWs [169], while Al-rich rings have been observed in the shell of twinned WZ GaAs-AlGaAs NWs [62].

Conclusion In conclusion, we combined different experimental techniques at high spatial resolution to demonstrate that QD-like Ga-rich clusters in the shell of GaAs-AlGaAs core-shell NWs correlate in occurrence and emission energy with the NW crystal structure. With the support of simulations, we concluded that the band alignment inside a twinned QD redshifts the exciton recombination in agreement with PL and CL observations. We also discussed the further impact of the NW crystal phase on the QD composition and formation during

the MBE growth. Our results can apply to other NW systems, where a ternary alloy is grown around a core and alloy segregation is observed [163]. The control of the crystal structure is then crucial to optimize the optical properties of quantum wells (QWs) and QDs obtained on the NW sidewalls [170], acting on their composition and band alignment. Defect-free NW cores guarantee the highest homogeneity in the composition of a NW shell made of a ternary alloy for, e.g., avoiding exciton localization in a shell QW [197]. Alternatively, by tuning the NW nucleation and growth conditions, several examples in the literature show that it is possible to engineer the insertion of WZ-ZB segments in the NW core [9, 177, 55, 164, 195, 198]. The control of these segments translates into the control of the properties of the shell QDs reported here by promoting their formation and tuning their emission energy. This is in agreement with ref. [62], where segments of alternated crystal phase have been used to locally engineer the shell composition.

5 Redshifting mechanisms: oxide shell as a static straining device

The goal of this thesis is to engineer the emission energy of NWQDs in resonance with the absorption of a gas of Rb atoms. The target energy is the D2 transition of Rb, at 1.589 eV; the natural distribution of the QD emission energies ranges between 1.6 eV and 1.9 eV [96]. A large tuning of the NWQD emission energy is required, approximately between few tens to few hundreds of meV. Electric and magnetic fields are often used for tuning the emission energy of single QDs [128, 129, 125, 127], but usually within an interval of several hundreds of μeV. Preliminary measurements carried in Martino Poggio's group at the University of Basel also showed that a time-dependent Stark shift disturbs the static shift of the NWQD emission energy. On the contrary, strain-tuning is convenient and particularly appealing in NWs. It is common to reach large tuning slopes in the order of several tens of meV per strain % [199, 200, 201]. Furthermore, NWs can sustain large strain before they undergo plastic relaxation, which expands the achievable tuning range with respect to the bulk [6, 200]. Interestingly, the strong coupling between the shell QDs similar to those studied in this thesis and the mechanical modes of the host NWs has been already demonstrated [118].

In the work reported in this chapter, static strain is used to redshift the NWQD emission energy. A technologically simple device is chosen to apply strain: it consists of the conformal deposition of a SiO_2 coating on the NW surface by PECVD. This straining device has been applied for the first time to NW and NWQDs by Bavinck et al. [202]. The dielectric envelope is deposited on bottom-up InP NWs hosting an axial InAsP QD. The device is particularly efficient: ref. [202] reports a redshift of the NWQD emission energy by more than 100 meV. At the same time, no degradation of the optical properties of the embedded NWQDs is observed. Using the same straining methods, a study on the core strain distribution in top-down core-shell NWs followed few years later [201].

Nevertheless, the origin of the stress was still unclear. The work presented here elucidates on this important aspect: only understanding the working principle of the straining device, one can extend the device applications and control its functionalities. Several physical processes generate stress when a thin film is deposited on a substrate and may be considered to explain the presence of stress also in the SiO_2-NW device. Some causes of stress originate from the

difference of the mechanical properties between the materials that constitute the film and the substrate. For instance, stress may arise from the difference in thermal expansion coefficient (TEC) between the oxide and the substrate. A standard temperature for SiO_2 PECVD is 300°C. While cooling down to room or cryogenic temperatures, the NW and the oxide shrink at a different rate. SiO_2 has a smaller TEC [203, 204] than GaAs and AlGaAs [205, 206, 132]. Therefore the oxide is expected to apply tensile strain to the NW.

Other sources of stress directly depend on the stress state in the deposited film. This intrinsic stress tightly depends on the microstructure of SiO_2, that is controlled by the deposition conditions, such as the deposition temperature. In the work reported hereafter, it is clarified that stress related with TEC plays a minor role in the functioning of the NW straining device. The major contribution to the applied stress is related with the intrinsic stress state of the oxide. The mechanisms that induce intrinsic stress in thin films are discussed in section 5.1. They mainly depend on the grain structure of the thin film.

In section 5.2, the experimental work is presented. PL and Raman spectroscopy show clear evidence of the increasing strain in the NWs for an increasing thickness of the applied SiO_2 coating. A maximum redshift of the QD emission-energy distributions of more than 100 meV is achieved. Section 5.2 also reports the TEM analysis of the microstructure of the SiO_2 coating. This is directly controlled by the deposition temperature. By Raman spectroscopy, the oxide microstructure is correlated with the strain in the NWs, which is found to clearly decrease when the oxide is composed of large loosely-connected grains. This grain structure is obtained by a deposition at lower temperature (100°C). On the contrary, a compact oxide is deposited at 400°C, which enhances the strain. By polarization-resolved Raman spectroscopy, the work provides the first experimental evidence of the significant anisotropy of applied strain: the strain component parallel to the NW main axis is larger than the one in the perpendicular direction. The strain anisotropy was predicted theoretically [201], but not demonstrated experimentally. In the work here presented, the structural study of the coating provides an explanation of the pronounced strain anisotropy: the SiO_2 grains are visibly elongated in the direction of impingement of the atoms, in a direction that agrees with the main axis of application of stress. The anisotropy of the applied strain may be exploited to act on the shape and FFS of a NWQD [207].

5.1   Intrinsic stress in thin films

In the experimental work presented in this chapter, SiO_2 is deposited on core-shell GaAs-AlGaAs NWs by PECVD. The oxide is composed by grains oriented in the direction of the impinging atoms. Figure 5.1a reports a sketch of the mechanism of formation of grains in a thin film. The deposition material first gathers into clusters that grow with the supply of impinging atoms; consequently, the clusters increase in size, coalesce and form grain boundaries. With low-diffusivity materials, the structure initially formed is immobile: the further material deposition mainly results into the epitaxial growth on the lower clusters
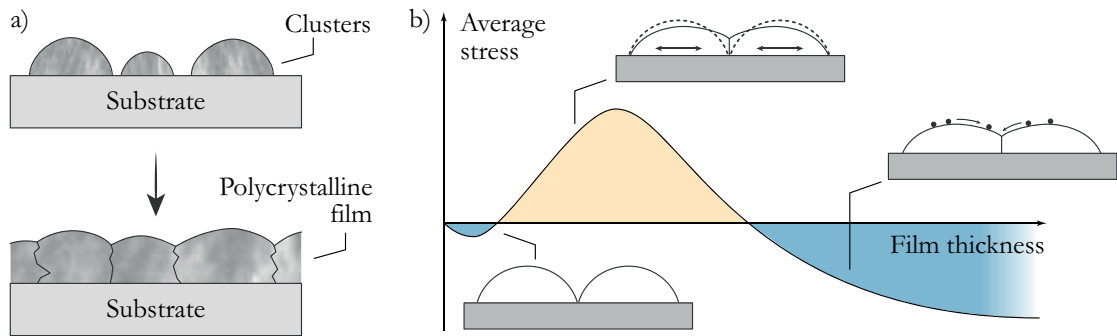
Figure 5.1 – a) Sketch of the formation of grains in a polycrystalline film. b) Schematic stress-vs-thickness curve; the sketches indicate the mechanisms responsible for the observed stress.

and the formation of grains elongated in the direction of impingement of the atoms. For the same material, an increase of the substrate temperature increases the atom diffusivity, which, in turn, enlarges the initial grain size. By further material supply, the gaps between the clusters are filled in a continuous film. The interaction among the grains is responsible for the generation of stress in the deposited film.

In a typical setup for the measurement of stress in thin films, a thin slab of known mechanical properties acts as a deposition substrate and is monitored during the film growth. Because of stress, the film-substrate system bends. From the measurement of the curvature of the bent structure, one can unambiguously derive the stress in the film. Figure 5.1b reports the stress curve in a thin film as a function of the film thickness: the stress is initially slightly compressive, becomes tensile for thicker films and compressive again upon further deposition of material, asymptotically reaching a negative constant value. This trend is valid for a wide range of materials, in spite of small differences in the details [208, 209].

The appearance of compressive stress at an initial deposition stage is ascribed to the smaller lattice spacing in a nanocrystal with respect to the bulk: this would generate interface compressive stress that is applied to the substrate [209]. The onset of tensile stress in thicker films is markedly more relevant. The compressive stress in the film reverses when the clusters become large enough to be in contact with each other (first sketch in figure 5.1b). In order to reduce the energy related with the surface area of the clusters, adjacent islands may elastically deform to close the gaps that separate them: part of the surface energy is converted into elastic energy. A simple analytical framework is to imagine regularly spaced clusters that stretch to bridge the gaps among them and form a continuous and stressed film. In the second sketch in figure 5.1b, the deformation of two crystallites with respect to the initial shape (dashed profiles) reduces the gap in between them and generates tensile stress in the interior. In thicker films, the transition from tensile to compressive strain is indicative that, beyond the simple relaxation of the previously accumulated tensile stress, the generation of compressive stress starts again. Compressive strain may arise from the supply of further atoms that fill in the grain boundaries of the film: although the lack of complete understanding on the driving forces for the incorporation of excess atoms, their presence may account for the onset of compressive

stress in thick films. A sketch of the incorporation of excess surface atoms is presented in figure 5.1b.

Some aspects of the origin of stress in thin films are still unclear. Nevertheless, it is widely shown that thin films comprise a conspicuous amount of intrinsic stress. This characteristic is exploited in the work presented in this chapter to fabricate a simple straining device and apply large tensile strain (up to about 1.6%) to the NWs and embedded NWQDs.

5.2 Anisotropic-strain-induced bandgap engineering in nanowire-based quantum dots

Luca Francaviglia, Andrea Giunto, Wonjong Kim, Pablo Romero-Gomez, Jelena Vukajlovic-Plestina, Martin Friedl, Heidi Potts, Lucas Güniat, Gözde Tütüncüoglu and Anna Fontcuberta i Morral.
Laboratoire des Matériaux Semiconducteurs, Institut des Matériaux, École Polytechnique Fédérale de Lausanne, 1015 Lausanne, Switzerland.

For the work reported here, I performed the Raman, TEM and STEM EDX measurements and part of the PL measurements and PECVDs. I analyzed the Raman, TEM and STEM EDX data and contributed to the analysis of the PL spectra. I modelled the strain and wrote a draft of the manuscript.

Abstract
Tuning light emission in bulk and quantum structures by strain constitutes a complementary method to engineer functional properties of semiconductors. Here, we demonstrate the tuning of light emission of GaAs nanowires and their quantum dots up to 115 meV by applying strain through an oxide envelope. We prove that the strain is highly anisotropic and clearly results in a component along the NW longitudinal axis, showing good agreement with the equations of uni-axial stress. We further demonstrate that the strain strongly depends on the oxide thickness, the oxide intrinsic strain, and the oxide microstructure. We also show that ensemble measurements are fully consistent with characterizations at the single-NW level, further elucidating the general character of the findings. This work provides the basic elements for strain-induced bandgap engineering and opens new avenues in applications where a band-edge shift is necessary.

Semiconductor nanowires (NWs) are very versatile building blocks for optoelectronic devices. As an example, NWs can host material or phase combinations otherwise difficult to obtain
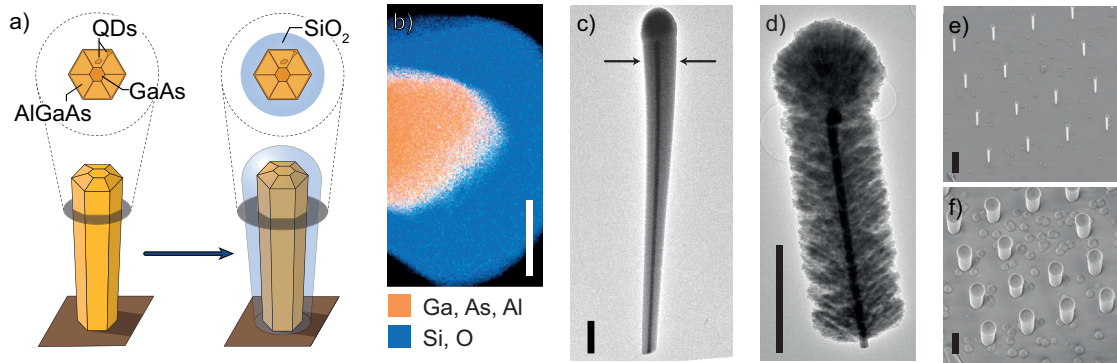
Figure 5.2 – (a) Sketch of the NW on growth substrate, uncoated (left) and coated by SiO_2 (right). The cross sections above show the QDs in the shell of the NW [14, 95]. (b) TEM X-ray energy-dispersive-spectroscopy (EDX) map of the top of a GaAs-AlGaAs NW coated with SiO_2. (c) Low-magnification TEM micrograph of a NW coated with SiO_2 deposited at 300°C. (d) Low-magnification TEM micrograph of a NW coated with SiO_2 deposited at 100°C.(e)-(f) SEM images at 20° tilting of the same NWs in an array, respectively before and after the coating with 180 nm of SiO_2. Scale bars: (b) 100 nm, (c)-(f) 2μm.

in the bulk or in thin films [210, 164]. In this way, a plethora of heterostructures including quantum dots (QDs) can be obtained within NWs. The optical performance of the embedded QDs benefits from the tailored shape and size of a NW, e.g. by an enhanced photon extraction [211, 35, 17, 212] or detection [105, 213] and the potential for an efficient electrical excitation [34]. Several research groups have tried to tune the emission energy of QDs for different purposes. Tuning energy levels involves tuning the absorption/emission which may be used for sensing, for the storage of information, as well as to facilitate the coupling to cavity modes [214, 215, 216, 146]. Strain has shown to be a valuable approach to largely and reversibly tune the emission of QDs [217]. The particular structure and mechanical properties of NWs provide an extended elastic regime in which strain can be applied [6, 118, 7, 200]. The approaches used to apply strain to NW structures include a flexural tensile set-up, the use of nanowires as cantilevers, the application of surface acoustic waves, and the deposition of an oxide envelope [7, 200, 118, 218, 202, 201]. So far, the latest approach has produced the largest tuning of the emission energy, but the origin of the shift is not clear yet.

Here, we report on a NW-oxide system with QDs embedded in the shell of core-shell GaAs-AlGaAs NWs [14, 95]. We provide the first experimental evidence for the presence of strain independently from the redshift of the semiconductor bandgap. To do so, we use non-resonant Raman spectroscopy. We also provide experimental support to the fact that the applied strain mainly results in a uniaxial component along the main axis of the NW, in agreement with previous simulations [202, 201]. We univocally correlate the strain and the redshift on large and variable ensembles of NWs and QDs and at the single nanowire level, in order to prove the reliability and reproducibility of the chosen technique. We provide understanding on the role of the microstructure and deposition temperature of the oxide. This last result, together with the reproducibility of the straining method, opens the possibility to engineer the bandgap and the surface properties of NWs and QDs in NWs. The combination of the two degrees of freedom and the application of different materials suggests the potential of this technique

in photo-electrochemical or optoelectronic applications where a bandgap modulation and surface protection by an oxide is needed.

The NW-oxide straining system We start by explaining how to perform strain engineering in NWs and core-shell QDs by applying an external amorphous shell. Figure 5.2a depicts the schematics of the experiment and the system studied. We can grow NWs both in a self-ordered way [5, 96] and in patterned arrays [47]. In both cases we grow the NWs on silicon to ensure there is no light emission from the substrate. We begin with a GaAs NW obtained by the Ga-assisted method [43, 219, 47] and then follow up with the growth of an AlGaAs shell that intrinsically contains self-assembled QDs [14, 95]. The QD emission is then tuned by applying a static straining device (Figure 5.2a), which is a layer of silicon dioxide obtained by plasma enhanced chemical vapor deposition (PECVD). Figure 5.2b corresponds to the chemical analysis of the III-V/oxide NW-coating structure, indicating a sharp interface between the semiconductor and the oxide.

Figure 5.2c and d correspond to typical transmission electron microscopy (TEM) micrographs of NWs respectively coated with SiO_2 at 300°C (Figure 5.2c) and 100°C (Figure 5.2d) as a substrate temperature. One observes that PECVD is highly conformal and the oxide layer follows the geometry of the NW (more details in Supporting Information). However, a microstructure formed by longitudinal grains is visible in Figure 5.2d and pronounced tapering is also observed in Figure 5.2c: the oxide thickness gradually decreases from the top to the base of the NW. This gradient is due to both electric-field enhancement at the NW tip and the mutual shadowing of the precursors by neighbor NWs during the deposition. The thicker the nominal oxide thickness is, the more important the tapering becomes. For this reason, we have calibrated the real-vs-nominal oxide thickness along the NW length (more details in Supporting Information). In the following, we will refer to the SiO_2 thickness as the average value measured at the top of the NWs, unless differently specified. The arrows in Figure 5.2c indicate what we consider as the NW top. We could recognize and address the single NWs before and after the oxide deposition when core-shell GaAs-AlGaAs NWs [14] were grown on site-selected positions on a silicon substrate [47]. Figures 5.2e-f show scanning electron microscopy (SEM) micrographs, from exactly the same NWs at the corner of an array, before and after the deposition of 180 nm of oxide. It is interesting to notice that the tapering is absent in the array NWs, as demonstrated by the one in Figure 5.2d. This is most probably due to the fact that the length of these NWs is shorter (4 μm) than in the case of the self-assembled NWs (10 μm), like the one shown in Figure 5.2c. For a given inter-NW distance, a smaller NW length causes less mutual shadowing and the resulting tapering is reduced or even eliminated.

We characterized the light emission from the QDs by micro-photoluminescence (μ-PL) spectroscopy performed on each individual NW, while we studied the oxide-induced strain by means of Raman spectroscopy. Unless differently stated, both PL and Raman spectra were always taken at the same top position indicated in Figure 5.2c in order to discard any spread in the results related to the variation of the oxide thickness along the NW axis. This choice equally allows to discard any variations of the QD emission energy along the NW axis [96].

Impact of strain on NWs and QDs First, we elucidate the controlled strain by Raman spectroscopy. In particular, we demonstrate that the SiO_2 provides a tensile strain along the NW

direction. It is well known that an applied stress field results in a change of the phonon energies of an (Al)GaAs crystal, which can be assessed by Raman spectroscopy [220, 158, 159, 7, 200]. The Raman measurements shown in Figure 5.3a, c and e were performed at 12 K, on NWs transferred on a Si substrate in the same backscattering configuration as in ref. [7]. We consider the Lorentzian fit of the peaks in the spectrum of the uncoated NW as a reference. The spectra are composed of two groups of peaks. At high wavenumbers we find the AlAs-like peaks from the AlGaAs shell (TO 359.5 ± 0.3 cm^{-1} and LO 376.7 ± 0.2 cm^{-1}). At lower wavenumbers, we find the GaAs TO mode at 266.4 ± 0.1 cm^{-1} [158] and the GaAs-like modes from the AlGaAs-shell (TO 260.3 ± 0.5 cm^{-1} and LO 277.9 ± 0.1 cm^{-1}) [157, 221]. The GaAs LO mode is not present, due to the selection rules [158, 157]. The position of the AlAs and GaAs-like LO modes of 5 NWs is consistent with an average Al composition of $29\pm8\%$ [132].

All the Raman modes downshift upon both the oxide depositions shown in Figure 5.3a. In particular, the GaAs TO mode downshifts by 2.31 ± 0.21 cm^{-1} after the deposition of 180 nm of SiO_2 and by 4.41 ± 0.14 cm^{-1} after the deposition of 360 nm of SiO_2. This trend follows a linear correlation between downshift and oxide thickness. We thus deduce that the oxide has a clear impact on the strain and that it can be assessed by Raman spectroscopy.

Previous works suggested that the oxide provides anisotropic response along the longitudinal axis of the NW, even under
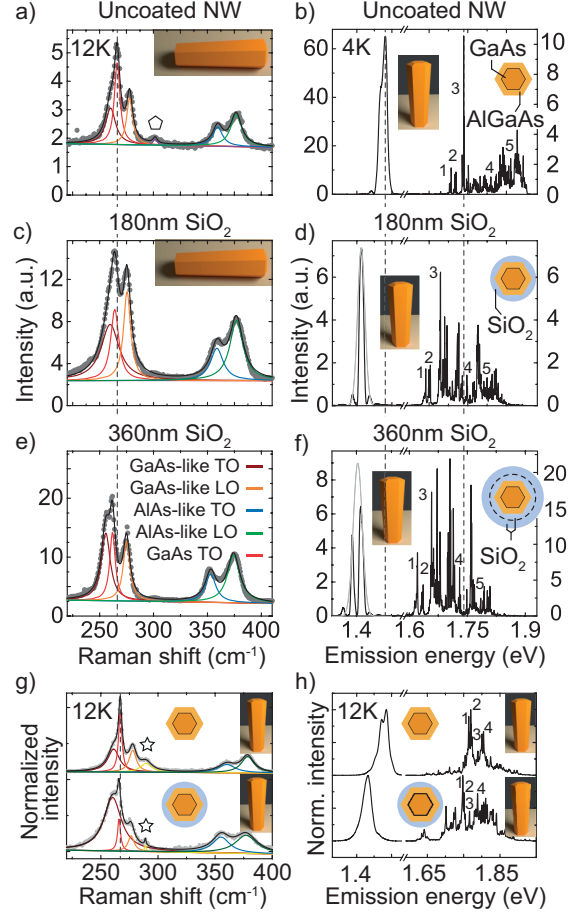
Figure 5.3 – From top to bottom: optical measurements on single NWs respectively uncoated (a, b), coated with 180 nm of SiO_2 (c, d) and with additional 180 nm of SiO_2 (e, f), as represented in the sketches in the right corners of (b, d, f). (a, c, e) Micro-Raman at 12 K of single NWs. The peaks are fitted by Lorentzian curves. Color-coding legend in (e). The pentagon in (a) labels the 2nd-order Raman scattering of the Si substrate. The dashed vertical line corresponds to the position of the GaAs TO peak in the uncoated NW as a reference. (b, d, f) μ-PL spectra at 4.2 K of exactly the same array NW. The dashed vertical lines correspond to the emission from the core and the QD line 3 in the uncoated NW. Raman (g) and PL (h) spectra of the very same vertical array NW before and after SiO_2 coating. The star in (g) indicates the GaAs LO mode. The color coding is the same as in (e). The dashed vertical line corresponds to the GaAs TO mode in the uncoated NW (g). Four QD PL lines are labelled in (h).

the assumption of isotropic properties of the oxide [202, 201]. Here, we provide additional arguments of why the strain should be uniaxial. The TEM micrograph of the NW coated with SiO_2 shown in Figure 5.2d provides some insight. The micrograph clearly shows a granular structure, with oriented grains tilted towards the NW axis. The TEM micrographs of all the NWs show this feature, even when the grains are less pronounced. We believe that this structure results from the impingement direction of atoms and ions during the oxide deposition (Figure 5.2d and more details in Supporting Information). Similar structures have been observed before on NWs coated with permalloy by sputtering [222]. Given this structural anisotropy of the oxide shell, we deduce that the exerted strain is probably anisotropic, as well. In particular, a net longitudinal contribution should be considered along the NW growth axis.

We proceed now with the quantification of the strain by evaluating the Raman shifts. For this we use the model from ref. [7]. In this work, Signorello et al. applied a controlled uniaxial stress along the longitudinal axis of GaAs NWs, which corresponds to the (111) direction of the zinc-blende (ZB) crystal. This direction is the same as in our case. Eq. 5.1 relates the shift of the GaAs TO mode ($\Delta\omega_{TO}$) with the strain along the NW longitudinal axis (ϵ_{zz}):

$$\epsilon_{zz} = \frac{\Delta\omega_{TO}}{\omega_{TO}} \frac{1}{[-3\gamma_T H + r'_T(1-H)]} \qquad \text{with} \qquad H = \frac{1-2\nu}{3} \qquad (5.1)$$

ω_{TO} is the relaxed phonon frequency in cm^{-1} for the GaAs TO mode, $\gamma_T = 1.35$ and $r'_T = -0.88$ are respectively the hydrostatic and deviatoric mode Grüneisen parameters [7] and $\nu = 0.16$ is the Poisson ratio for GaAs (111). We use the same Grüneisen parameters as for bulk GaAs because a minor difference was reported [7, 159], while we utilize the Poisson ratio found for GaAs NWs in the (111) direction [7]. We use the same parameters for all temperatures, as no substantial difference has been reported for measurements at lower temperatures [7]. The shift of the GaAs TO mode is consistent with a tensile strain of 0.54±0.06% and 1.04±0.08% upon, respectively, the first and second deposition of 180 nm and 360 nm of SiO_2. Given the brittle behavior of GaAs at low temperature, it is remarkable that the NWs do not break under such a high strain [223]. Probably, the high surface-to-volume ratio and the absence of bulk and surface defects increase the fracture stress in the NWs [6]. Further support to the calculation of strain by means of Equation 5.1 will be provided in the following by the measurements on NW ensembles.

We address now the impact of strain on the optical properties of the NWs and QDs. Figures 5.3b, d anf f report the μ-PL spectra performed exactly on the same NW upon successive coatings with SiO_2. The top spectrum (Figure 5.3b) corresponds to the NW-QD structure before any oxide deposition. The two spectra below (Figures 5.3d and f) were taken after depositions of 180 nm each time, for comparison with the same oxide thickness as in the Raman spectra in Figures 5.3a, c and e. The PL spectra were acquired at 4.2 K, with the laser incident on the top of vertical NWs.

In each μ-PL spectrum, we distinguish emission of two different origins. The broader emission around 1.5 eV corresponds to the free exciton emission from the GaAs NW core. It mainly

originates from GaAs in the ZB phase. In the top spectrum of the uncoated NW, the peak exhibits a small shoulder at lower energies, which may be due to the presence of few crystal twins and few wurtzite (WZ) segments. The intensity modulation is attributed to Fabry-Perot resonances [224] and it is particularly visible in the samples coated with SiO_2. The emission clearly redshifts for an increasing oxide thickness. We have fitted the peaks with a Gaussian curve to assess the energy shift upon SiO_2 deposition. In particular, we fitted the two peaks in the PL of the uncoated NW with two Gaussian curves, while in the other PL spectra the Gaussian curves fit the maxima of the Fabry-Perot resonances. The first deposition results in a redshift of about 68 meV, while the second deposition brings an additional redshift of about 9 meV. One should note that the second deposition results in the oxide completely filling the space between the NWs. We think that this changes the straining conditions with respect to the case in which the single NWs are enveloped by independent oxide shells. In turn, we think that this can explain the smaller redshift of the core emission after the second deposition.

The group of narrow lines at higher energy in the spectra in Figure 5.3b, d and e originates from the QD emission in the NW AlGaAs shell. Due to the excitation depth of the laser we excite several QDs simultaneously [14, 95]. One advantage of measuring the same single NW is that we can follow the evolution of individual emission lines. Some illustrative peaks at different energies are labelled as 1, 2, 3, 4 and 5. Also in this case a redshift is qualitatively visible. As quantitative examples, the peak fits of the lines 1, 2, 3, 4 and 5 all give a redshift between about 60 and 73 meV upon the first deposition. The second deposition brings an additional redshift between about 7 and 21 meV. There is no apparent correlation between the redshift and the initial QD emission energy. On the contrary, both the core and all the measured QD lines, redshift more after the first deposition. As already mentioned, the second deposition is less effective probably because the oxide completely fills the space between the NWs.

Interestingly, we notice an overall increase in both the Raman and PL intensity after coating the NWs, which is already visible in the spectra in Figures 5.3a to f. (more details in Supporting Information). We believe that this positive effect depends on the smoother transition in refractive index between the vacuum and the NW in presence of SiO_2 [225].

Figures 5.3a to f show the cumulative effect of the SiO_2 deposition on the Raman and PL spectra of the NWs. In order to corroborate the link between the Raman downshift and the PL redshift, Figures 5.3g and h correspond to the same vertical NW. We acquired Raman and PL spectra at the same temperature (12 K) before and after the deposition of 110 nm of SiO_2. We observe that the GaAs TO peak downshifts by slightly more than 1 cm^{-1} and the GaAs LO by about 0.6 cm^{-1}; the PL emission of QD 3 in Figure 5.3h redshifts by 23 meV and the core PL by about 37 meV. The PL redshift is in reasonable agreement with the Raman downshift measured on the same NW. As expected for 110 nm of SiO_2, these shifts are lower than those obtained for 180 nm of SiO_2 and shown in Figures 5.3c and d. No relevant difference is present between the PL spectra acquired at 4 K (Figure 5.3b, d, f) and those acquired at 12 K (Figure 5.3g, h).
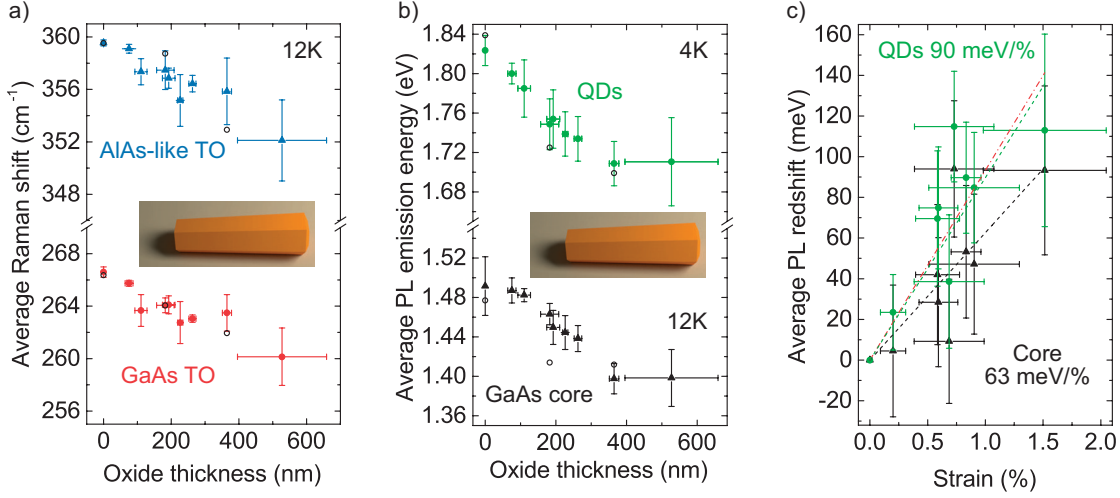
Figure 5.4 – (a) Average GaAs TO (red circles) and AlAs-like TO (blue triangles) Raman shift of horizontal NWs at 12 K vs oxide thickness. All the error bars are the standard deviations of the distributions. (b) QD emission energy acquired by PL on ensembles of horizontal NWs at 4.2 K vs oxide thickness. The horizontal error bars are the standard deviations of the oxide thickness distributions. Average of the emission energy of the QDs (green circles) and GaAs core (black triangles) distributions with the standard deviation as a vertical error bar. The open black circles in a and b are the values of the corresponding quantities derived from the single-NW spectra in Figures 5.3a and b. (c) Average QD (green circles) and core (black triangles) PL redshift vs strain. The dashed green and black lines are a linear fit of, respectively, the QD and the core PL redshift. The dash-dotted red line corresponds to the theoretical redshift of the heavy-hole bandgap recombination in GaAs NWs [7].

Nature of strain In order to provide more precise evidence of the nature of strain we turn to the systematic study of larger ensembles of NWs. Measurements on large NW ensembles provide a statistically robust support to the results obtained on single NWs and confirm the reproducibility of the results. For this, the NW structures were grown in a self-organized manner on the Si substrates as in Ref. [5, 95, 96]. A large-area sample was divided into nine pieces. Each piece underwent the deposition of a SiO_2 coating of different thickness, excluding one kept as an uncoated reference. The oxide thickness ranged between 75 nm and 527 nm, as characterized by TEM. For these Raman and PL measurements on large ensembles, we dispersed the NWs onto silicon substrates.

We chose 5 NWs for each oxide thickness to perform Raman measurements at 12 K. Figure 5.4a shows the average peak position of two TO modes as a function of the thickness of the oxide in each subsample. The peak position was derived from Lorentzian fits, like in Figure 5.3a (more details in Supporting Information). The error bars represent the standard deviations. Here, we show only the evolution of the GaAs TO and AlAs-like TO modes for clarity. The GaAs TO mode is independent from the percentage of Al in the shell. Similarly, the AlAs-like TO mode has an almost flat dependence on the Al content in the AlGaAs alloy [132]. Therefore, we expect that the peak position of these modes depends only on the strain in the NW and we use the GaAs TO mode as a gauge of the applied strain. Figure 5.4a shows that the Raman peaks downshift for increasing oxide thickness in a linear way. The Raman downshift confirms the increase in tensile stress applied by an increasing thickness of the oxide, which, in turn, redshifts the

PL emission energy. We notice a broadening of the vertical error bar in the graph of Figure 5.4a. This broadening is a consequence of the larger variability in the oxide properties for thicker depositions, like local changes in thickness and density. Indeed, it actually highlights the large impact of the oxide shell against minor variations in the properties of the oxide and the NW. Considering the average GaAs TO peak, we measure a maximum downshift of 6.45 $\pm$ 2.22 cm^{-1} between the uncoated NWs and those coated with the thickest oxide (measured thickness of 527 nm on average).

We performed μ-PL measurements at 4.2 K on 25 NWs from the same ensembles prepared for Raman spectroscopy. Figure 5.4b shows the average emission energy of the NW GaAs core and shell QDs as a function of the measured oxide thickness. The error bars are the standard deviations of the emission distributions. Both the QD and the core PL redshifts are clearly visible and maximized by the second-to-last deposition with respect to the uncoated NWs (measured oxide thickness of 365 nm). The average QD position shifts by $\sim$ 115 meV, while the GaAs core by only $\sim$ 94 meV. The shifts are significantly larger than the dispersion given by the error bars. Both the horizontal and vertical error bars in Figure 5.4b increase for thicker oxides. This observation reflects the increase in the variability of the oxide properties in thicker depositions. Yet, the overall trend of the graph is clear, and it supports the fact that the applied strain is large enough to overcome minor variations in the properties of the oxide and the NWQDs [226, 227, 228]. Theoretical predictions and experiments show that the pressure coefficient of AlGaAs at the Γ point increases with the Al content in the composition range of our interest [132, 229]. As a consequence, one can deduce that, for a given strain, the AlGaAs bandgap redshifts more than the one of pure GaAs. This fact can account at least in part for the difference in the overall redshift of the core and the QDs, which is visible in Figure 5.4b. Moreover, one should take into account that, in the case of the QDs, strain does not only redshift the AlGaAs band gap in which the QD potential well is set. Strain can also decrease the confinement by changing the QD shape and decreasing the QD potential barrier. This second consideration is supported by the aforementioned increase in pressure coefficient in presence of Al [132, 229]. The QD barriers redshift more than the Al-poor QD well. Therefore the confinement on the excitons trapped in the QDs is smaller, which provides an additional redshift.

It is also interesting to focus on the onset of the PL redshift of the QDs and the core. The core PL shows a first slope that seems to get steeper after the first two depositions. According to Ref. [7], uniaxial stress along [111] lifts the GaAs crystal symmetry and light- and heavy-hole bands split; in particular, the heavy-hole band redshifts more than the light-hole one. Under small strain, the two bands are still close enough in energy to contribute to the PL emission [7]. Under larger strain, only the heavy holes contribute. This transition may be visible as the initial change in slope in the core redshift in Figure 5.4b. On the contrary, because of confinement, we can assume that QDs only emit by recombination of electron and heavy-hole excitons, that is with a unique slope.

We turn now to the validation of the strain as mostly uniaxial. For each oxide thickness of the

NW ensembles, we calculate the corresponding average strain from the shift of the Raman peaks. Eq. 5.1 is valid for the GaAs TO mode.

In Figure 5.4c we plot the redshift of the median of the QD and core PL as a function of the corresponding strain. We use eq. 5.1 to calculate the strain from the Raman GaAs TO shifts in Figure 5.4a. In Ref. [201], the nature and value of the strain is uniform along the NW radial direction. In our case, the data do not seem to indicate otherwise. Therefore, we assume that the strain calculated from the downshift of the GaAs TO peaks corresponds to the strain applied to the QDs as well as to the core. We can calculate a linear fit of the redshift as a function of the strain (the dash-dotted green and black lines in Figure 5.4c respectively for the QDs and the core). We obtain that the QD PL shifts by 90 meV/%, while the core by 63 meV/%. The QD redshift is consistent with those already reported for a very similar NW-oxide system [201]. It also agrees with theoretical calculations [7] and with the value found in Ref. [7], by experiments with a straining system that guarantees the uniaxial nature of the applied stress. Our QD redshift is slightly more pronounced than the experimental one for GaAs [7]. This difference may further support our previous considerations on the loss of confinement in strained QDs and on the increase in pressure coefficient in the AlGaAs matrix [132, 229]. Calculations only based on hydrostatic stress [159] lead to inconsistently larger slopes. This comparison discards purely hydrostatic strain in our case and, together with the agreement with the work of Signorello et al., further validates the conclusion that, effectively, also in our system the stress is mainly applied as a component along the NW longitudinal axis.

On the other hand, the core PL redshifts less than the theoretical expected value (red dash-dotted line in Figure 5.4c). We mainly ascribe this discrepancy to the large influence (more details in the Supporting Information) that few twins and WZ segments have on the PL emission energy [59]. In particular, they are responsible for uncontrolled shifts of the PL emission energy from the NW core. Together with the PL shift that may be induced by surface charges trapped at the NW-oxide interface during PECVD, we prefer to rely on Raman spectroscopy to estimate the applied strain.

We provide now further support to the highly anisotropic nature of the strain by polarization-dependent Raman measurements. In Figures 5.5a and b we respectively show the Raman spectra of an uncoated and a coated NW lying horizontally. We excite the NWs with light linearly polarized along the longitudinal NW axis and alternatively collect the scattered light with a linear-polarization filter aligned parallel or perpendicular to this axis, as sketched in each panel in Figures 5.5a and b. With this method it is possible to distinguish the different contributions of the two GaAs TO modes, because their degeneracy is lifted under anisotropic stress. The two modes are usually named TO_S and TO_D [230, 231], respectively detected for scattered light with parallel and perpendicular polarization with respect to the NW axis [7]. No splitting is observed between the two configurations for the uncoated NW in Figure 5.5a. In the case of the coated NWs, the spectrum collected in the perpendicular configuration is clearly shifted with respect to the one collected in the parallel configuration (Figure 5.5b): the GaAs TO mode in the parallel configuration is at 260.6 cm^{-1}, while it is at 264.4 cm^{-1}

under perpendicular collection. The difference (3.8 cm^{-1}) indicates a smaller strain in the perpendicular direction. One can therefore state that the applied stress is highly anisotropic and it is mainly applied as uniaxial tension in the direction parallel to the NW longitudinal axis (see the Supporting Information for more measurements).

The TO splitting is manifested as broadening in non-polarized Raman spectra. The GaAs TO peak is thus the convolution of the two contributions. The splitting, and thus the full width at half maximum (FWHM) of the convoluted spectra, increases with increasing strain. In Figure 5.5c, we plot the average FWHM of the GaAs TO modes from non-polarized Raman spectra at 12 K as a function of the sample oxide thickness. The linewidth broadens with the oxide thickness, in agreement with an increase in anisotropy.

In Figure 5.5d, we plot the Raman shift of all modes from spectra acquired at 12 K on horizontal NWs. We use the position of the modes in the uncoated NWs as zero, in order to compare the downshift of the different modes in the same plot. As expected, one can observe that in the thickest depositions, the downshift of the LO modes is less and less pronounced with respect to the one of the TO modes.

In Ref. [7], the authors estimate the Poisson ratio for GaAs NWs, under the assumption that the deformation potentials are the same as in the bulk. They report a slightly smaller value for NWs (0.16 ± 0.04) with respect to the bulk (0.186), although their result is affected by a large experimental error. We use the results from the

Figure 5.5 – (a) - (b) Polarization-dependent Raman spectra of uncoated (a) and coated (b) horizontal NWs at 12 K. In each panel, the upper curve (red) corresponds to a spectrum taken with both collection and excitation with linear polarization parallel to the NW longitudinal axis, while in the lower curve (black) only the excitation polarization is parallel to the NW longitudinal axis and the collection is perpendicular. The vertical dashed lines correspond to the position of the TO peak in the case of parallel collection. (c) Average full width at half maximum (FWHM) of the GaAs TO mode in the Raman spectra taken at 12 K on horizontal NWs vs oxide thickness. The linear polarization of these spectra was not selected. The sketch shows that the mode linewidth broadens as a consequence of the convolution of the two peaks revealed by polarization-dependent Raman spectroscopy. (d) Average Raman shift with respect to the uncoated NWs for all the modes at 12 K vs oxide thickness. The color coding follows the one introduced in Figure 5.3e. The Raman shift of each mode is referred to those of the uncoated NWs as zero.

polarization-dependent Raman spectra to deduce the Poisson ratio of GaAs and analyze if it changes with the envelope-induced strain or the nanoscale size of the NWs. We obtain an average value of $\nu = 0.19\pm0.02$, which highlights no major differences with the bulk (more details on the derivation in the Supporting Information).
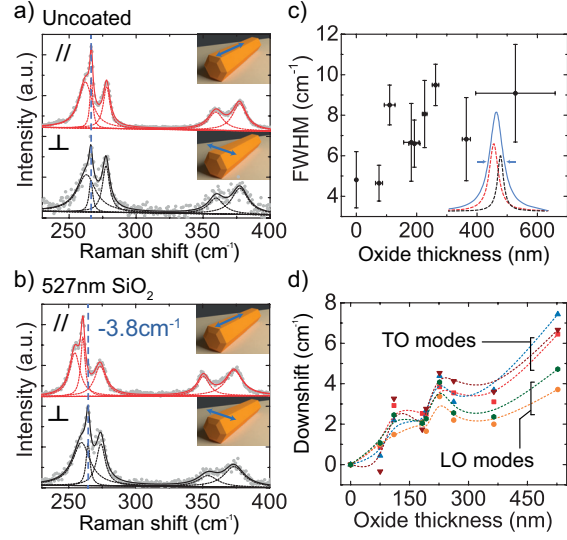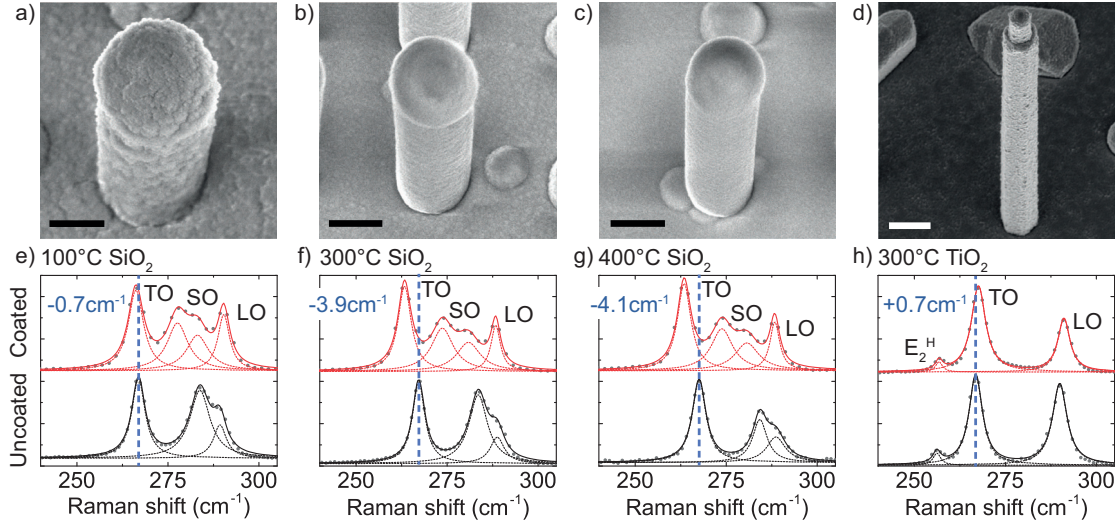
Figure 5.6 – (a) - (d) From left to right: SEM images of GaAs array NWs respectively coated with SiO_2 at 100°C, 300°C and 400°C and TiO_2 at 300°C. Scale bars are 500 nm. (e) - (h) Raman spectra of the NWs from (a) to (d) in the same order. Black: uncoated NWs. Red: coated NWs. The dashed curves are Lorentzian fits. The TO, LO, E_2^H [158] and surface optical (SO) [232] modes are labelled. The dashed vertical lines in blue correspond to the TO GaAs mode of the uncoated NWs. In blue in the upper left of each plot is the shift of the Raman TO upon coating.

Importance of oxide nature At the origin of strain, the literature [209] typically distinguishes between intrinsic and extrinsic contributions. Among several cases, the first category includes the structure of the deposited film, while a typical example of the second category is the thermal strain that results from the difference between the thermal expansion coefficient (TEC) of the oxide and the NW.

We now provide considerations on the structure of the oxide and its correlation with strain. In Figure 5.6, we present the data about four different depositions as illustrative examples out of ten NWs for each case. In particular, Figures 5.6a-c show SEM images of array NWs of purely GaAs coated with SiO_2 at different substrate temperatures during the PECVD: 100°C in Figure 5.6a, 300°C in Figure 5.6b and 400°C in Figure 5.6c. By increasing the substrate temperature, the surface morphology of the SiO_2 becomes smoother; as expected [209], the grain structure is less pronounced and the size of the grains decreases. The TEM micrographs in Figure 5.2c and d of, respectively, a NW coated at 300°C and 100°C, confirm this observation. Figures 5.6e-h report the Raman spectra of the corresponding vertical NWs in Figures 5.6a-d. For each case we acquired the Raman spectra at room temperature (RT) before and after the SiO_2 PECVD. In this scattering configuration, both the GaAs TO and LO are allowed. In addition, a surface optical (SO) mode appears [233, 234, 235, 232] and splits after the SiO_2 deposition. In general, the SO mode shifts because of a change in the dielectric constant at the NW surface [233, 234, 235, 232]. Once coated, in our NWs both the strain and the change in dielectric constant control the SO position. However, there is a unique and continuous NW-oxide interface. Therefore, there is also a unique dielectric constant at the NW surface after coating and the SO split may rather depend on the anisotropic nature of the applied strain. Moving to

the analysis of the TO and LO modes, we observe that they all downshift in all the three SiO_2 depositions. We report the downshifts of the TO modes in blue in the graphs. The downshifts increase from left (+0.7 cm^{-1} in Figure 5.6e) to right (+4.1 cm^{-1} in Figure 5.6g). Therefore the tensile strain increases together with the deposition temperature. The downshifts are coherent for all the ten NWs measured in each sample, except for the deposition at 100°C. In this case, we observed fluctuations and even upshifts of the Raman modes. We highlight that this effect is not related with the oxide thickness. On purpose, the SiO_2 thickness of the depositions at 300°C and 400°C are both about 300 nm and the corresponding Raman shifts similar. The deposition at 100°C shows the smallest shift in spite of a larger oxide thickness of about 480 nm.

The evolution of the tensile strain with the SiO_2 structure indicates a correlation between the two. In particular, the stiffness of the SiO_2 deposited at lower temperature reduces. As one can infer from the low-density gaps between two grains in Figure 5.2d, the large grains obtained at lower temperature are loosely connected to each other. In this case, the oxide is easily damaged, for instance during the transfer of the NWs on TEM grids (more details in the Supporting Information). On the contrary, the SiO_2 deposited at higher temperatures is more robust. In other words, the SiO_2 deposited at 100°C lacks the necessary solidity to transfer any significant strain to the NWs. Through the grain structure, one can therefore control the stiffness of the oxide and, in turn, the application of the tensile strain. This possibility demonstrates a further degree of freedom in SiO_2 PECVD: high-temperature depositions can maximize the applied strain, while a low-temperature deposition may be useful for protecting NWs from the environment without changing their optical properties.

At the atomic level, the importance of the oxide structure for the application of strain gets further support in Ref. [201]. Here the authors consider the atom and ion impingement during PECVD and how it forces the atomic bonds of SiO_2 in a non-equilibrium configuration. This builds up strain in the oxide itself, that is eventually transferred to the NW. We found in the literature that this can be controlled through the deposition parameters, such as the plasma frequency during PECVD [236], but we have not further investigated this technical aspect. The authors of Ref. [201] find that the built-in strain is as important as the strain derived from the thermal dilation. In particular, the TEC of SiO_2 [204, 203] is smaller than the one of GaAs and AlGaAs [205, 206, 132] and this agrees with the application of tensile strain to the NW. However, also in our case the thermal strain cannot account for all the strain we observe. For instance, there is an almost linear correlation between the thermal strain and the temperature gradient from the deposition temperature to RT, but this is not the trend that we observe from the Raman data in Figure 5.6. Furthermore, we do not record a larger downshift of the Raman peaks when we further decrease the measurement temperature down to 12 K (more details in the Supporting Information).

Therefore, we conclude that the main working principle of our straining device is the atomic-scale internal strain of the oxide, modulated by the oxide stiffness at the level of its microstructure. Yet, when the internal strain is set to a smaller contribution by adjusting the parameters

of the deposition, the thermal strain may play a major role.

We also deposited TiO_2 by sputtering in order to further demonstrate the versatility of the same device concept for another deposition technique and another material. We studied an ensemble of 10 NWs before and after the sputtering. As an example, in Figure 5.6d we show the SEM image of an array NW that we sputtered with TiO_2 at 300°C and in Figure 5.6h we compare the Raman spectra acquired at RT before and after the deposition. The Raman modes upshift as a consequence of the deposition, which corresponds to compressive strain. In the Supporting Information, we show the μ-PL response of the NW at RT before and after the TiO_2 deposition: the blueshift of the GaAs PL signal further supports the compression of the NW by means of the TiO_2 coating. Therefore, we can change the strain from tensile to compressive and we demonstrate this change with a more general approach than in Ref. [202].

In conclusion, we presented an efficient and yet simple system to shift the emission of QDs embedded in NWs. The strain can be quantitatively tuned by the thickness of the deposited oxide. We give robust evidence of the reproducibility of the system in spite of the variability of the emission of the NWs and the QDs. By means of Raman spectroscopy, we provide the first experimental proof of the presence of tensile strain independently from the measurements of the redshift of the NW bandgap. Raman spectroscopy provides quantitative evidence to evaluate the amount and nature of the applied strain. This would not be possible only with PL measurements, because the PL emission energy is sensitive to many more effects, such as surface states and polytypism [59]. We give an experimental estimation of the applied strain in agreement with its uniaxial nature, that we further support by the analysis of the polarization-dependent Raman spectra. We have validated this method for different materials and techniques. Concomitantly, the temperature of the deposition brings a further degree of freedom to the functionalization of the NW-oxide system. This opens the possibility to functionalize the properties of the NWs at the surface while tuning their bandgap. This could open new avenues for instance, in photo-electrochemical applications in which the bandgap of the semiconductor is related to the light absorption but also to the overpotential. Here, the oxide shell would protect the semiconductor from corrosion and at the same time it would enable the tuning of the overpotential of the device by strain.

Experimental methods

Nanowire growth We grew the NWs in a DCA P600 MBE machine through the Ga-assisted method [43, 47] on Si (111) substrates. More details on the growth of the self-assembled NWs are available in Ref. [43, 96], while the detailed growth process of the arrays NWs is available in Ref. [47].

Oxide deposition We coated the NWs with SiO_2 by PECVD in a PlasmaLab system 100 PECVD by Oxford Instruments. We used 400 sccm of N_2 98% - SiH_4 and 710 sccm of N_2O at a radio frequency power of 20 W. We deposited the TiO_2 coating in a Pfeiffer SPIDER 600 sputtering machine.

Morphology and structure We acquired the SEM images in Zeiss MERLIN and Zeiss GEMINI 300

microscopes operated at 3 kV to study the morphology of the NW on their growth substrates. We used FEI Tecnai OSIRIS and FEI Talos microscopes operated at 200 kV on NWs transferred on carbon-coated TEM grids for studying the structure and measuring the thickness of the oxide. By switching to the STEM mode on the FEI Tecnai OSIRIS microscope, we acquired the EDX maps.

Photoluminescence For the low-temperature μ-PL spectra, we put the NWs in a close-cycle liquid-helium cooled cryostat at 4.2 K. We used a continuous-wave HeNe laser (emission wavelength = 632.8 nm) as an excitation source. We focused the laser light in a 1 μm-large spot on the sample by means of an objective with NA = 0.85. The power density on the samples was in the order of 100 W/cm^2. We collected the PL signal through the same objective, dispersed it with a 300 l/mm grating and detected it by means of a nitrogen-cooled charge-coupled device (CCD). For the QD PL spectra at RT and the NW-core PL spectra at 12 K we used a single-frequency optically-pumped semiconductor laser at 532 nm wavelength (continuous wave) as an excitation source. We used a microscope objective (NA = 0.75) to focus the laser on the NWs in a spot with a diameter of 1 μm and a power density of about 10^3 W/cm^2. We collected the PL signal through the same objective and dispersed it with a 300 l/mm grating onto a Peltier-cooled CCD.

We analyzed the PL signal from the NW ensembles by means of an automatized code. We acquired the spectra from 25 NWs for each oxide thickness. From each PL spectrum, we calculated through the code the median of the emission energy weighted on the intensity of the signal at the different energies. We plotted the average of the medians of the 25 spectra. The standard deviation of the average gave the error bars.

Raman spectroscopy We collected the low-temperature Raman spectra by putting the NW on the cold finger of a helium-cooled cryostat at 12 K. We used the same setup as the one for the RT PL, with the difference that we used a power density of about 10^4 W/cm^2 and a triple spectrometer in order to separate the Raman emission from the Rayleigh scattering. A final 1800 l/mm grating dispersed the light on a nitrogen-cooled CCD. We realized the measurements in backscattering configuration with the NWs transferred in horizontal position on a Si wafer. For the polarization-dependent Raman spectra, we filtered the laser light with a linear polarizer and aligned the selected polarization to the NW main axis by means of a rotator. We used a second polarizer to filter the scattered light.

We collected the RT Raman spectra by means of a commercial Renishaw inVia Raman microscope using the same excitation source as in the low-temperature measurements. We used a grating with 1800 l/mm to disperse the light, a notch filter to discard the Rayleigh scattering of the laser and a Peltier-cooled CCD to detect the signal.

Author contributions
PL spectroscopy on single NWs was performed by AG and LF. PL spectroscopy on NW ensembles along with the statistical analysis was realized by AG. Raman spectroscopy on NW ensembles and single NWs along with the analysis was realized by LF. TEM measurements

and analysis were performed by LF. PRG performed the deposition by sputtering, while AG and LF by PECVD. Strain analysis and modelling was performed by LF. NW ordered arrays were obtained by WK, JVP MF, HP and LG, while the ensembles by GT. AFiM conceived and designed the experiments and supervised the project. AG and LF made the figures. AG, LF and AFiM wrote the manuscript. All authors discussed the results and commented on the manuscript.

Supplementary Information

The Supporting Information is available free of charge on the ACS Publications website. It contains the TEM micrographs of several depositions in different conditions, the calibration of the measured-vs-nominal oxide thickness and additional Raman and PL data.

6 Redshifting mechanisms: Indium incorporation in the AlGaAs shell

The bandgap of a compound semiconductor is controlled by the relative proportion of its constituents. Alloying different elements into a single compound can be a powerful strategy to reach significant bandgap-energy shifts. Ideally, other semiconductor properties, such as the lattice constant, can be widely tuned by changing the relative amount of the different atomic species present in the alloy. With this regard, quaternary alloys are very attractive for engineering different properties of a semiconductor simultaneously: for instance, the bandgap can be tuned to shift the semiconductor emission energy, while its lattice constant can be independently controlled to match the lattice parameter of the growth substrate.

In the work presented in this chapter, indium is incorporated at different concentrations in the AlGaAs alloy that constitutes the NW shell. The resulting compound is a quaternary AlGaInAs alloy. Self-assembled QDs are observed in these GaAs-AlGaInAs core-shell NWs: they are optically active and the signature of SP emission has been detected by autocorrelation measurements. The goal of the indium incorporation is to redshift the emission energy of the NWQDs embedded in the shell. The distributions of the QD emission energies redshift by about 300 meV. By this large energy shift, in the samples with 15% to 25% of indium in the alloy, the emission energy of several QDs approaches the absorption energy of the D2 transition of Rb at 1.589 eV.

The exact understanding of the incorporation of indium in AlGaAs is more complex. Indium interacts with the other elements present in the shell. At low concentrations, indium may act as a surfactant: without being significantly incorporated, it may influence the diffusion of the other adatoms. At higher concentrations, the incorporation of indium is influenced by local gradients in the chemical potential at the NW surface. The shape, polarity, crystal phase and direction of the NW facets tune the surface chemical potential and thus drive the diffusion of Ga, Al, and indium. In addition, In-based compounds are lattice-mismatched with GaAs/AlGaAs. Therefore, strain is expected to be present in GaAs-AlGaInAs core-shell NWs and drive the adatom diffusion. These factors may act on the composition of the self-assembled QDs in the AlGaInAs shell. Different schemes of the effect of indium on the NWQD emission energy are discussed in section 6.1. A comparison with the experimental results is provided, in

order to define what scheme is most probably responsible for the observed redshift.

In section 6.2 the study of the NWQD emission-energy redshift and the spatially resolved analysis of the NW composition are addressed in details. Different methods of compositional analysis are combined together. APT, STEM EELS and EDX are used to map the composition of few NWs. They reveal a rich pattern of depletion and enrichment of the quaternary shell at different positions. Al-rich planes form at the ridge between two facets of the hexagonal NW cross section. At the same position, the shell is markedly depleted in gallium and indium. These compositional fluctuations have a 3-fold symmetry ascribed to the polarity of the {112}-type nanofacets comprised between two {110}-type NW sidewalls. Interestingly, wedge-shaped In-rich regions surround the Al-rich planes only in the (112)B directions. These segregates have not been reported before and may be a specific characteristic of the quaternary alloy. A model is provided in the conclusion of this chapter to explain the experimental observations. The indium segregation is related with a miscibility gap with Al and the distribution of strain in the shell. Strain builds up because of the difference in lattice constant between GaAs and AlGaInAs. The distribution of strain in the NWs is found by means of simulations, supported by the experimental measurement of strain by PL and Raman spectroscopy.

6.1   Schemes of quantum-dot emission redshift with indium

Schemes of the QD emission-energy redshift induced by indium are proposed in the following. As already observed in subsection 2.3.2, the studied NWQDs form by Al/Ga segregation in the AlGaAs alloy. Ordered Al-rich and Ga-rich layers are observed in the bulk [103] and in NWs [94] along the same (110) direction (figure 2.9) as a consequence of a miscibility gap between GaAs and AlAs. Exchange reactions between Al and Ga are proposed to account for the Al/Ga (re)ordering [103]. Atoms diffuse at the growth surface and segregate into Ga- and Al-rich clusters.

If indium is also considered, multiple scenarios are possible. Indium has a higher surface mobility and a lower sticking coefficient with respect to Al and Ga [70]. Therefore, at low vapor pressure, indium may not incorporate significantly in the quaternary alloy because of the competition with Al and Ga; it may rather interact with the other species as a surfactant, that is, it may change the diffusion kinetics and surface energy for the other species without mixing with the alloy. As an example in a different III-V system, Sb at low concentrations acts as a surfactant during the formation of InAs-GaAs QDs; it alters the QD growth and shifts their emission energy [237].

In the experimental work presented in this chapter (section 6.2), different NWs are grown with increasing indium fractions in the shell alloy, ranging from 0% to 25%. Indium is added to redshift the emission energy of the QDs embedded in the shell. If indium acts as a surfactant during the growth of the shells with low indium fractions (four samples ranging from 1% to 4% indium), the emission redshift may derive from the enhancement of the Al/Ga segregation and lead to QD nanoclusters even richer in Ga. In first approximation, this Ga enrichment
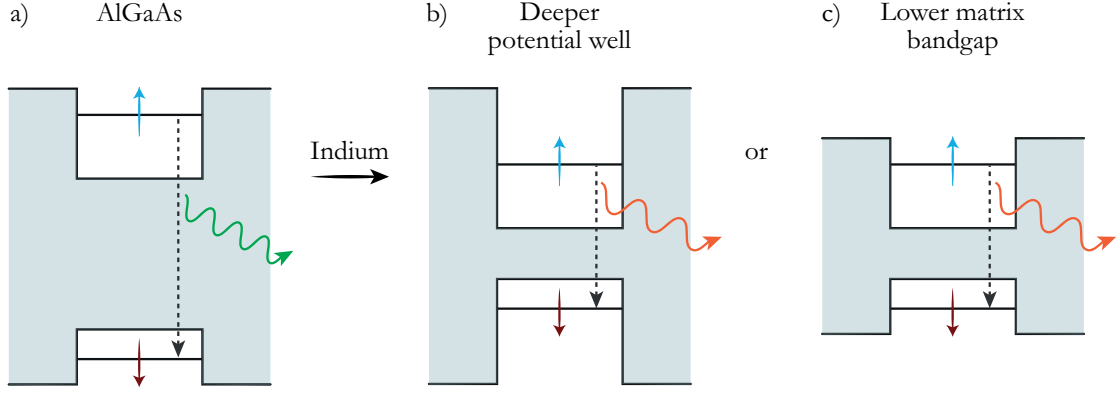
Figure 6.1 – a) Band-alignment scheme of a 2-level (Al)GaAs QD in an (Al)GaAs matrix of higher bandgap. b) Band-alignment of the same QD as in (a) further enriched in gallium or indium that lower the QD potential well with unchanged barriers; c) QD band-alignment for non-selective indium incorporation: the overall matrix bandgap is lowered. In both (b) and (c) the QD emission energy redshifts with respect to (a).

would lower the QD emission energy without changing the AlGaAs matrix barrier. Figure 6.1a and b respectively sketch the QD potential well in the original AlGaAs alloy and for a deeper potential well, richer in Ga. The scenario sketched in figure 6.1b may also occur if indium is incorporated only in the Ga-rich nanoclusters to form In-rich QDs. In both scenarios (In-assisted Ga-enrichment or direct In-enrichment) the QD emission energy would redshift. Indium incorporation is confirmed at any concentration in the whole range considered in this work (from 1% to 25%): a gradual redshift of the QD emission lines is observed for an increasing amount of indium added to the shell. Also assuming no preferential clustering of indium at the nanoscale, the observed redshift is described by the lowering of the overall shell bandgap. This scenario is depicted in figure 6.1c.

6.2 Segregation scheme of indium in InAlGaAs nanowire shells

Luca Francaviglia [1], *Gözde Tütüncüoglu* [1], *Sara Martí Sánchez* [2], *Enrico di Russo* [3], *Simon Escobar Steinvall* [1], *Jaime Segura Ruiz* [4], *Heidi Potts* [1], *Martin Friedl* [1], *Lorenzo Rigutti* [3], *Jordi Arbiol* [2,5], *Anna Fontcuberta i Morral* [1,6].

[1] *Laboratoire des Matériaux Semiconducteurs, Institut des Matériaux, École Polytechnique Fédérale de Lausanne, 1015 Lausanne, Switzerland.*

[2] *Catalan Institute of Nanoscience and Nanotechnology (ICN2), CSIC and BIST, Campus UAB, Bellaterra, 08193 Barcelona, Catalonia, Spain.*

[3] *Groupe de Physique des Matériaux, Université de Rouen, Saint Etienne du Rouvray, 76801, France.*

[4] *European Synchrotron Radiation Facility, Grenoble, 38043, France.*

[5] *ICREA, Pg. Lluís Companys 23, 08010 Barcelona, Catalonia, Spain.*

[6] *Institut de Physique, École Polytechnique Fédérale de Lausanne, 1015 Lausanne, Switzerland.*

At the moment of the submission of this thesis, the following article is undergoing peer-review for publication as a Rapid Communication paper in Physical Review Materials. With

unchanged content, the layout and the bibliography of this article are integrated with the rest of this thesis.

In the work reported in this chapter, I performed the PL, Raman, TEM and STEM EDX measurements. I analyzed the Raman, TEM and STEM EDX data and contributed to the analysis of the XRF maps. I simulated the strain in the core-shell NWs and drafted the model of the indium segregation. I wrote a draft of the manuscript.

Abstract
Quaternary alloys enable the independent optimization of different semiconductor properties, such as the separate tuning of the bandgap and the lattice constant. Nanowire core-shell structures should allow a larger range of compositional tuning as strain can be accommodated in a more effective manner than in thin films. Still, the faceted structure of the nanowire may lead to local segregation effects. Here, we explore the incorporation of indium in AlGaAs shells up to 25%. In particular, we show the effect of In incorporation on the energy shift of the AlGaInAs single-photon emitters present in the shell. We observe a redshift up to 300 meV as a function of the group-III site fraction of In. We correlate the shift with segregation at the nanoscale. We find evidence of the segregation of the group-III elements at different positions in the nanowire, not observed before. We propose a model that takes into account the strain distribution in the nanowire shell and the adatom diffusion on the nanowire facets to explain the observations. This work provides novel insights on the segregation phenomena necessary to engineer the composition of multidinary alloys.

Introduction Quaternary alloys enable to independently tune the semiconductor lattice constant and bandgap by careful composition engineering. However, the controlled deposition of quaternary alloys with randomly distributed composition can be challenging. On one hand, miscibility gaps and diffusion may induce the segregation of the different species that compose the alloy, and limit the possible compositions [238, 239]. On the other hand, strain may build up when quaternary semiconductors epitaxially grow on substrates of different lattice constant. To avoid plastic relaxation [240, 241], the theoretical range of available compositions is significantly narrowed in real applications. Due to their reduced diameter, semiconductor nanowires (NWs) provide a suitable growth platform to minimize plastic relaxation, [25, 242, 243, 244, 245, 246] permitting lattice-mismatched material combinations not achievable by planar schemes [247, 248, 249, 250].

In this work, we explore the range in which In can be incorporated in AlGaAs shells of core-shell GaAs-AlGaAs NWs. The goal is to understand how much the emission energy of single-photon emitters, spontaneously forming in the shell, can be redshifted [14, 95, 97]. In particular, we want to dissociate the bandgap engineering from additional segregation effects that may occur due to the presence of In. Consequently, we characterize the optical emission and correlate it with the incorporation of In using several techniques at different length scales. We find that group-III elements in the shell segregate to different positions and generate regions of different bandgaps. In particular, we find consistent evidence of the In segregation in novel

a)

Core-shell NW

QDs   GaAs

AlGa(In)As

Al-rich plane

b)

10x laser power

250x10⁻⁹ Torr

12K

86x10⁻⁹ Torr

25x10⁻⁹ Torr

Indium increase

0 Torr

PL intensity (a.u.)

Emission energy (eV)

1.4   1.5   1.6   1.7   1.8   1.9

c)

Indium fraction (%)

0   5   10   15   20   25

PL emission energy (eV)

E_g^{Shell}

$g^2(\tau)$

X-X   4K

Delay τ (ns)

-4 -2   0   2   4

E_g^{GaAs}

Indium flux (10⁻⁹ torr)
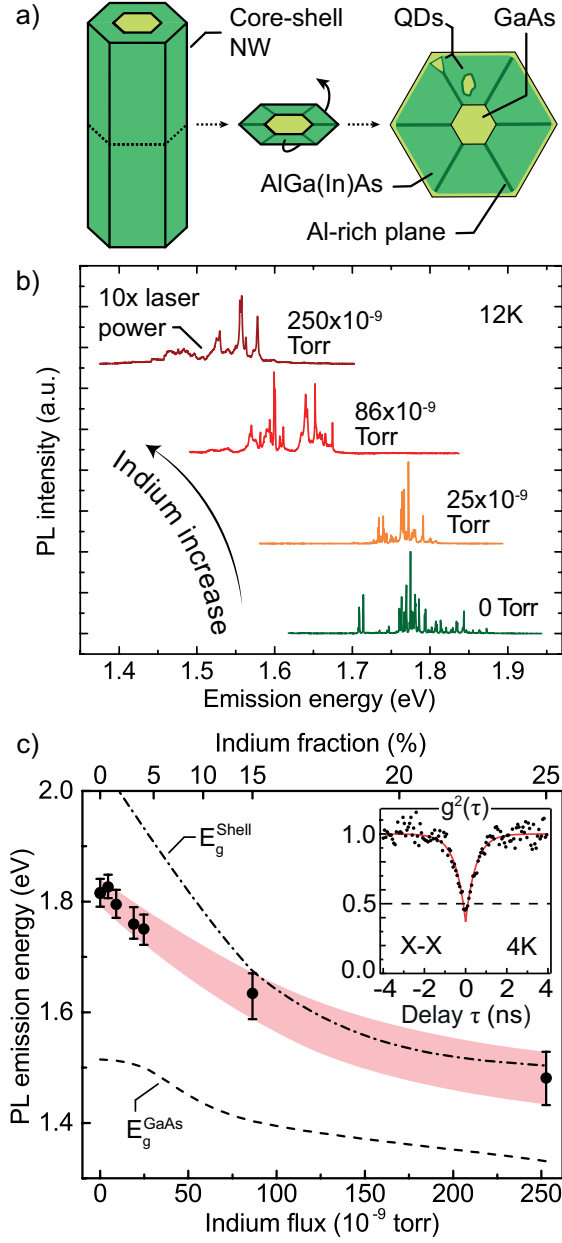
0   50   100 150 200 250

Figure 6.2 – (a) Sketch of a core-shell NW and shell QDs. (b) Micro-PL spectra of shell QDs grown at increasing In pressures. (c) Ensemble medians of the PL QD emission energy vs the In MBE pressure (bottom abscissa) or shell fraction (top abscissa) given by APT, XRF, STEM EDX and growth-rate calibrations. 1st and 3rd quartile as error bars, highlighted, as a guide to the eye, by the shaded area. The dashed and the dashed-dotted lines are the strained core and shell bandgaps, respectively [143, 140]. Inset: single-photon g^2 of a QD exciton (3% In).

wedge-shaped In-rich features. We correlate these observations with the 3-fold polarity of the NW cross section and the migration of the adatoms on the NW sidewalls. In addition to the role of the crystal directions of the NW facets [98, 163, 94], we consider strain to cause the peculiar In segregation; the presence and distribution of strain are further analyzed by finite-element simulations as well as Raman and photoluminescence (PL) spectroscopy.

The material system: core-shell NWs
The GaAs-AlGa(In)As core-shell NWs are grown in a high-mobility molecular-beam-epitaxy system (MBE, DCA P600). We use Si(111) substrates and self-catalyzed growth [43, 251] at a substrate temperature of 640°C. When the NWs are about 10 μm long, we stop the axial growth by interrupting the Ga supply and consuming the catalyst. We then lower the substrate temperature to 460°C to promote radial growth of an AlGa(In)As shell on the NW sidewalls [183, 252]. We start with an $Al_{33}Ga_{67}As$ shell and then incorporate In without modifying the Ga or Al rates. For this, we varied the In partial pressure from 4.5 x 10^{-9} Torr to 2.5 x 10^{-7} Torr, while the Al and Ga pressures were kept constant. Unless stated, the samples are identified by the group-III site fraction of In measured through various techniques and expressed as percentage in the notation $Al_xGa_yIn_{1-x-y}$As (Al, Ga, and In sum to 100%) : 0%, 1%, 2%, 3%, 4%, 15%, and 25%. An outer GaAs shell of 5 nm prevents the oxidation of the inner AlGa(In)As.

Previous reports show that the composition of an AlGaAs shell deposited around a GaAs NW exhibits nanoscale fluctuations [14, 95, 96, 253, 102, 62]. This phe-

nomenon depends on the different surface mobility of Ga and Al during growth and the presence of surface-potential gradients (μ) on the NW sidewalls. The formation of Al-rich planes at the ridge between two NW facets was reported [163]. Furthermore, Ga-rich clusters can form quantum-dots (QDs) that behave as single-photon emitters in the NW shell [14, 95, 102]. A sketch of a core-shell GaAs-AlGaAs NW and its cross section is presented in figure 6.2a, illustrating the distribution of Al-rich planes and QDs made from Ga-rich nanoclusters.

Light-emission properties First we address the optical functionality of the core-shell NWs and embedded QDs. We used a single-frequency optically pumped semiconductor laser, with a wavelength of 532 nm, focused in a spot of less than 1μm in diameter (100 W/cm^2) to measure NW samples at 12 K using a helium cryostat. The PL signal is collected into a spectrometer and dispersed by a 300 l/mm grating onto a Peltier-cooled CCD. The QDs in the AlGaAs shell emit bright and narrow PL lines (linewidth below 100 μeV) [14] between 1.7 eV and 1.9 eV [96]. The green spectrum at the bottom of figure 6.2b illustrates the PL emission of these structures; the sharp peaks are attributed to the presence of QD single-photon emitters [14, 125]. Figure 6.2b also contains PL spectra of the shell-QD emission for increasing In fraction, revealing several sharp peaks at different energies. The emission-energy range redshifts with increasing In fraction in the shell. One can also qualitatively determine that the QD emission linewidth broadens in samples of higher In fraction. The sample with the highest In fraction showed a decreased PL intensity, compensated for by increasing the laser power (see figure 6.2b).

For a statistical analysis on large ensembles of NWs and QDs, figure 6.2c shows the median emission energy of the QDs as a function of the measured In pressure in the MBE chamber (bottom axis) or as a function of the In fraction (top axis) measured in the shell by X-ray fluorescence (XRF) combined with atom probe tomography (APT) for 1% to 4% of In and scanning transmission electron microscopy energy-dispersive X-ray spectroscopy (STEM EDX) for 15% and 25% In (supplementary information). We measured 25 NWs from each sample. The QD emission lines were identified by an automatic routine [96]. The dashed-dotted line indicates the expected shell bandgap as a function of shell composition [143]. The dashed line corresponds to the GaAs bandgap. Both lines are corrected for the simulated strain [140] that arises from the core-shell lattice mismatch, as further discussed in the manuscript.

The inset in figure 6.2c shows a Hanbury-Brown-Twiss autocorrelation measurement ($g^2(\tau)$) of the exciton line of a QD from a sample with 3% In. The power-dependent PL showing the exciton nature of the emission line is reported in the supporting information. The sample is measured at 4.2 K in an Attodry 700 closed-cycle cryostat and is excited in continuous wave by a HeNe laser at 632.8 nm through an objective with NA = 0.81, which also collects the QD signal from the cryostat. A 1200 l/mm grating is used to select the QD line of interest that is sent to a 50:50 beam splitter. The two paths of the beam splitter are coupled to single-mode optical fibers that send the signal to two single-photon avalanche diodes, one for each path. The dip in the autocorrelation function in the inset of figure 6.2c is below 0.5, which is the signature of the single-photon emission. Several factors increase the count at zero delay, including

background counts from QD lines spectrally close to the chosen one.

The effect of the shell-composition engineering on the QD emission energy is significant. From figure 6.2c, the median QD emission redshift is visible as a function of the increasing In incorporation, by up to about 300 meV. In a random-distribution alloy, the addition of In to AlGaAs lowers the shell bandgap and the QD emission energy. Since lower-bandgap nanoscale clusters in the AlGa(In)As matrix form the studied QDs, their emission is always expected to be redshifted with respect to the bandgap of the host shell matrix (dashed-dotted line in figure 6.2c). In figure 6.2c, we observe that the energy difference between the QD emission and the shell bandgap is gradually reduced for higher In fractions. This calls for a different segregation effect at low and high In fractions, whose mechanisms and details may be investigated in a further study.

Compositional analysis at the nanoscale In NWs the composition can vary significantly at the nanometer scale due to their faceted nature. The hexagonal cross-section of a GaAs NW exhibits six {110} facets. The ridges between two of these facets are {112} nanofacets with alternating A- and B-polar (Ga- and As-terminated) surfaces [163, 98, 62]. {110} and {112} facets have different and species-dependent sticking coefficients [62]. In addition, the increased surface curvature at the ridges increases the local surface energy and affects the adatom mobility. Here we provide compositional measurements with spatial resolution down to the nanometer scale: APT and STEM-based electron energy loss spectroscopy (EELS) and EDX.

We performed laser-assisted APT measurements on the sample with 2% In. The specimen is cooled to 80 K and irradiated with UV laser light (343 nm wavelength) in 2-nJ pulses; the detection rate is 0.0025 events/pulse. The evaporated NW volume is a cylinder with diameter of 64 nm and length of 90 nm; in figures 6.3a - c, it is shown as a 2D projection on a plane perpendicular to the NW growth axis. Figures 6.3a - c show respectively the In, Al and Ga fractions. It is possible to distinguish the GaAs core by the absence of In and Al. In the shell, radial segregation of Al along the ridges between two facets of the hexagonal NW core is visible as the three Al-rich stripes in the reconstructed NW volume, in agreement with previous works [163, 98, 14, 95, 102, 62]. In addition to the Al-rich planes, APT reveals that the shell distribution of the other group-III atoms is not perfectly random throughout the NW shell. A slightly higher In fraction (up to 3%) is visible in proximity of two of the Al rich planes indicated as 1 and 3 in figure 6.3a. Farther from these positions, the average In fraction decreases to about 1.6%. In figure 6.3b and c we can also observe that the shell in proximity of the Al-rich planes is slightly depleted in Al and enriched in Ga. At shorter length scales, APT-based distributions [95] of the distances between first-neighbor atoms in the shell do not evidence short-range reordering of the quaternary alloy (figure S13 in the supporting information).

To study the segregation of Al, Ga, and In in more extended regions, we studied the NW cross-sections by high angular annular dark field (HAADF) STEM and EELS in an aberration-corrected (AC) TEM microscope (FEI Titan) operated at 300 keV. We used the sample with

15% In. We prepared NW cross sections to directly map the shell composition: the NWs were
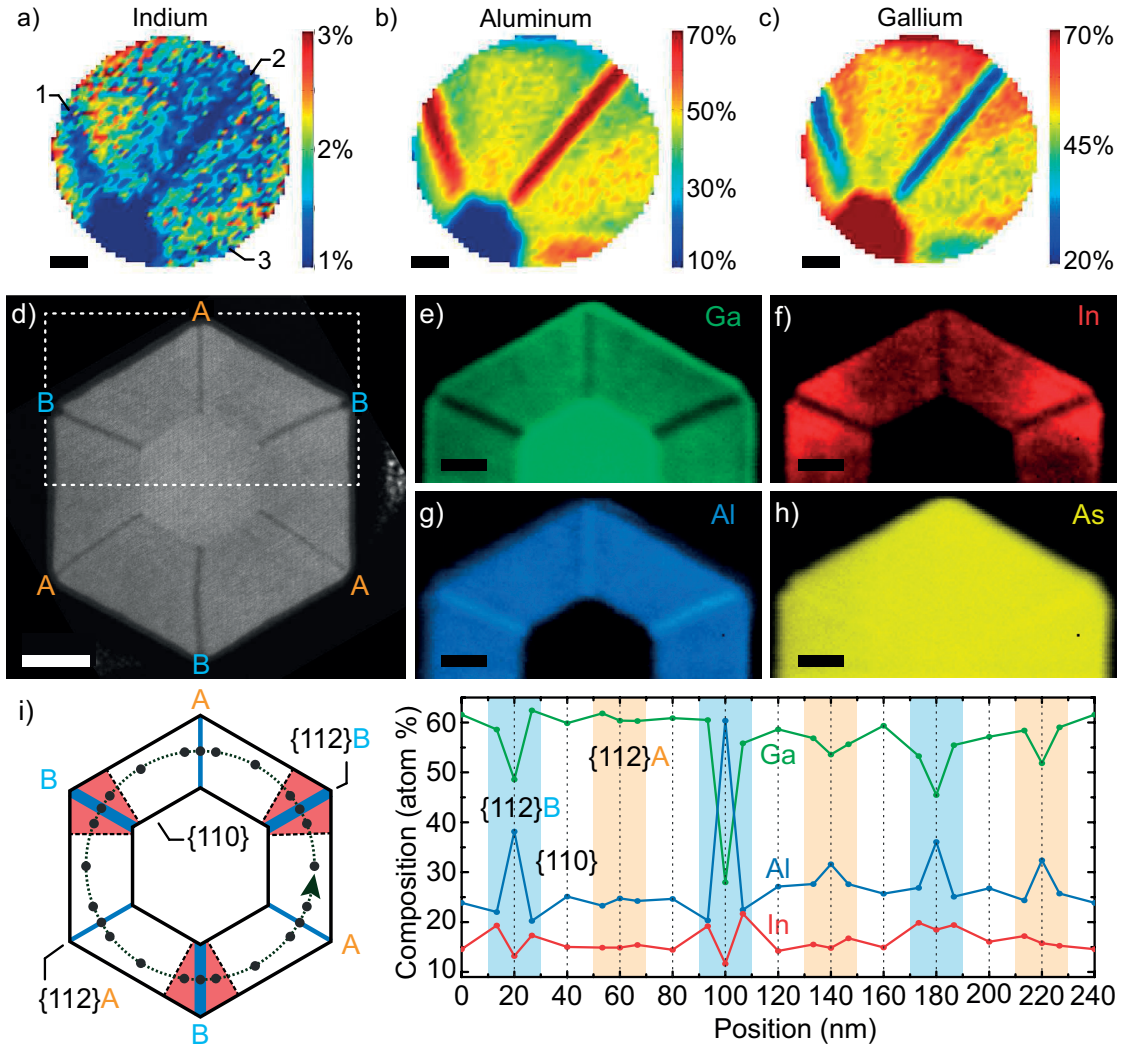

Figure 6.3 – (a), (b), and (c) APT of In, Al, and Ga fractions (2% In). (d) HAADF STEM micrograph of a NW cross section (15% In) with A and B polarity indicated. (e-h) EELS Ga, In, Al, and As maps of the dashed rectangle in (d). (i) Left: sketch of shell segregation. Right: shell Ga (green), Al (blue), and In (red) atomic group-III percentages vs position along the circumference in the sketch. Scale bars: (a-c) and (e-h) 10 nm, (d) 20 nm.

spread on a Si substrate and the cross sections were FIB-cut perpendicularly to the NW growth direction ($\langle 111 \rangle$). The cross-section HAADF micrographs are acquired along the $\langle 111 \rangle$ zone axis, with the NW sidewalls corresponding to the {110} family (figure S4 in the supporting information). Figure 6.3d reports the HAADF micrograph of one NW cross section. The HAADF contrast depends on the sample thickness and composition: the higher the atomic number (Z) of the species in the sample, the brighter the HAADF signal. Through high-precision FIB cut, the NW cross sections have negligible thickness variations: the contrast in figure 6.3d depends on the average Z at different positions across the sample. In this figure, the hexagonal shape of the NW cross section is clearly visible and the core is distinguishable from the shell. The

dark stripes that form in the shell along the ridges between two NW facets ($\langle 112 \rangle$ crystalline directions) are due to local enrichment with a light element, such as Al, as already observed by APT and in agreement with the literature [98, 14, 94]. It is possible to observe that the thickness of the Al-rich planes follows a 3-fold symmetry as observed by Zheng et al. [98]. We obtain a thickness of 3 nm and 1.7 nm for the thick and thin planes, respectively (more details in figure S4 in the supporting information). Similarly, the HAADF contrast shows that the thick planes are richer in Al than the thin ones. Comparing our observations with the literature [98], we assign the thin planes to the A polarity and the thick ones to the B polarity. Accordingly, we labelled the two polarities in figure 6.3d as A (orange) and B (blue). We highlight that, without the alternation of the A- and B-polarity of the {112} nanofacets, all the corners of the hexagonal NW cross-section would be equivalent.

With the exception of the Al-rich planes, the HAADF micrograph in figure 6.3d shows little compositional contrast in the shell. By carefully inspecting figure 6.3d and figure S4 in the supporting information, a slightly brighter contrast is visible in proximity of the Al-rich planes: it corresponds to a local increase in the fraction of elements with higher Z, such as Ga and In. To clarify this observation, in figures 6.3e - h we report the EELS maps of the upper half of the NW cross section shown in figure 6.3d: the selected region, indicated by the dashed rectangle in figure 6.3d, includes an A-polar and two B-polar ridges as well as part of the {110} NW sidewalls. The Ga, In, Al, and As distributions are shown in figure 6.3e, f, g, and h respectively. Principal component analysis (PCA) was used to enhance the signal-to-noise ratio in these maps [254, 255]. The NW core is clearly distinguished from the shell by the absence of Al and In and a thin Ga-rich layer, corresponding to the GaAs capping, surrounds the shell (figure 6.3e). As is randomly distributed throughout (figure 6.3f), as opposed to the distributions of the group-III elements: the presence of Al-rich planes along the hexagon ridges is confirmed (figure 6.3g), together with the Ga and In depletion at the same positions (figure 6.3e and f). Reports on GaAs-InGaAs and GaAs-InAlAs core-shell NWs [256] also show Ga and In depletion along the $\langle 112 \rangle$ direction. The brightness and thickness of the Al-rich planes agree with the 3-fold polarity-driven segregation previously discussed.

In agreement with the localized In enrichment shown by APT (figure 6.3a), STEM EELS shows in figure 6.3f In-rich features surrounding the Al-rich planes at the $\langle 112 \rangle$B directions: interestingly, moving from the core to the outer shell, the In-rich regions become broader with a wedge-like shape on each side of the Al-rich B-polar planes. Ga has a more random distribution in the shell, although a slight increase is visible around the A-polar {112} nanofacet in figure 6.3e. This Ga-rich feature is not as pronounced as the In-rich ones surrounding the B-polar planes; it also has a relatively constant thickness around the A-polar planes, while the In-rich features develop an unusual wedge-shaped profile. One may also observe that, in proximity of the Al-rich planes aligned in the $\langle 112 \rangle$ directions of both polarities, the Al fraction slightly decreases (figure 6.3g). Although the contrast is not sharp, this would agree with the local increase in the Ga and In fractions at the same positions. EELS maps on whole NW cross sections confirm the 3-fold symmetry of the shell segregation and the In enrichment only around the three $\langle 112 \rangle$B directions (see the supporting information). On the left of figure 6.3i, a scheme summarizes

the main compositional segregations observed in the NW cross sections (the scheme is aligned with figures 6.3d - h): the red-shaded areas indicate the wedge-shaped In-rich segregation and blue stripes indicate the alternatively thicker and thinner Al-rich planes. The polarity of the {112} nanofacets is labelled.

We acquired STEM-EDX maps of NW cross sections from the same samples as the one used for EELS. We use a FEI Tecnai Osiris TEM operated in STEM mode at 200 kV with a probe current exceeding 1 nA. The X-ray signal is collected by four silicon drift detectors under a solid angle of 0.9 srad. The NW cross sections are prepared by embedding the as-grown sample into epoxy. After hardening, the epoxy with embedded NWs is detached from the growth substrate and is mounted into an ultramicrotome and cut into 80-nm-thick slices transferred on a TEM grid. The EDX maps (figure S3 in the supplementary information) for the Ga, Al, and In distributions in the core-shell cross sections confirm the presence of the same features observed in the EELS maps. Our observations are particularly robust: three independent techniques (APT, EELS and EDX) confirm the formation of novel 3-fold wedge-shaped In-rich segregates in NWs with different average In fractions; together with the clear symmetry of these features, the agreement of the three techniques excludes artifacts due to sample preparation.

We now turn to a quantitative analysis of the distribution of the different species in the NW cross section: the EDX-based quantification is more accurate than the one based on EELS [1]. Figure 6.3i shows on the right a plot of the Ga (green curve), Al (blue curve), and In (red curve) atomic percentage extracted from a STEM EDX map as a function of the position along the dashed circumference shown in the sketch on the left (i.e. a circular linescan of 240 nm in length). The data points at 0 nm and 240 nm correspond to the same position on the circumference (arrow in the sketch). The shaded areas in the plot are colored in orange and blue with the same coding as in figure 6.3d to distinguish the A- and B-polarity of the {112} nanofacets respectively. The data points acquired in the middle of the flat {110} facets have a white background.

We focus on the most prominent fluctuation around the ⟨112⟩B facet at position 100 nm. Moving from the {110} plane to the {112}B nanofacet, the Al fraction first decreases (from 25% to 20%), then rises to 60% at the corner. In smaller proportions, the In distribution is opposed to the Al trend: for the same positions, In first increases (from 14% to 19%) and then decreases to 12% at the corner. Ga is almost constant at 61% and 60% and then decreases to 28% at the corner. Very similar trends in Al/Ga/In fractions are reproduced at the six corners of the hexagonal NW cross section and are modulated according to a 3-fold symmetry: the compositional variations are consistently more pronounced in proximity of the B-polar facets.

Strain analysis and growth model We turn now to the understanding of the element distribution in the shell by taking strain into account. Figure 6.4a shows the PL spectra of the GaAs core at 12 K for core-shell NWs of increasing In fraction. The band-edge GaAs PL redshifts

---

[1]For the elements here considered, the EELS peaks overlap with an important background that is absent in the EDS spectra. The EELS background does not prevent the localization of the elements in the maps, but may reduce the accuracy of the quantification.
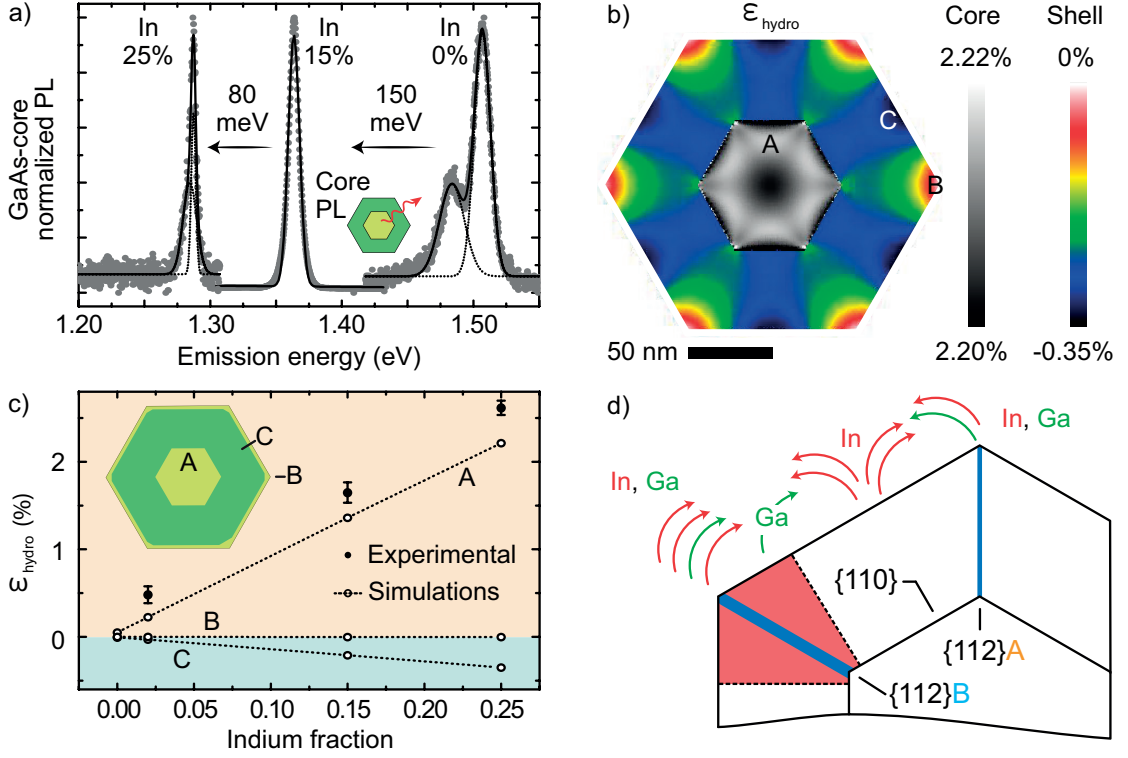
Figure 6.4 – (a) GaAs PL of NWs with In shell fraction of 0%, 15%, and 25%, acquired at 12 K with excitation laser of wavelength of 532 nm and power density of 100 W/cm^2. (b) Hydrostatic strain simulation in core-shell NWs (25% In) as in ref. [257]. (c) Simulated and average experimental (1σ error bar) hydrostatic strain vs In fraction. (d) Sketch of the Ga and In diffusion on the NW sidewalls.

from 1.51 eV down to 1.37 eV and 1.29 eV for shells containing 15% and 25% In, which we attribute to the tensile strain imposed by the shell. Tensile strain in the core is also confirmed by Raman spectroscopy (supplementary information).

To gain insight in the strain distribution imposed by the lattice-mismatched core-shell NW, we simulated the strain given the lattice mismatch, dimensions and geometry of the structure. We use the methodology of Boxberg et al. [257], adapted to hexagonal GaAs-AlGaInAs NWs at low temperature [143] in the software Nextnano [184, 185]. The strain magnitude and distributions in the core and shell are claculated by minimizing the elastic energy due to the lattice mismatch between the two. Figure 6.4b shows a map of the hydrostatic strain ϵ_{hydro} in NWs with 25% In in the shell. ϵ_{hydro} is dominated by the principal component along the NW longitudinal axis, as reported elsewhere [258]. Shear strain components are one order of magnitude smaller than ϵ_{hydro}, in agreement with previous reports [258]. As expected from the core-shell lattice mismatch, ϵ_{hydro} is on average negative in the shell (compressive) and positive in the core (tensile). We find about 2.2% of tensile strain (position "A" in figure 6.4b), softly modulated following a 6-fold symmetry. The shell is subject to a maximum compression of -0.35% in the middle of the NW facet (position "C" of figure 6.4b). The shell strain intensity is modulated by a 6-fold symmetry in a more pronounced way. The outer corners are relaxed

(minimum strain of 0% at position "B" in figure 6.4b). Importantly, the regions of smaller strain in the shell expand around the NW sidewall ridges, becoming larger the farther they are from the core. The experimental (PL) [199] and simulated strain values are plotted in figure 6.4c: the simulated compressive strain in the shell (position C) and the the experimental and simulated tensile strain in the core increase linearly with the In fraction. The theoretical and experimental values agree within 15%.

A growth model that explains the non-random distribution of In and Al in the shell is presented. The expected behavior of Ga and In adatoms at the NW facets is sketched in figure 6.4d. We start by addressing the Al distribution. Al tends to incorporate more efficiently at the vertices of the hexagonal cross section ({112} nanofacets) [163, 98, 14]. This is the consequence of a larger sticking coefficient on those facets [100, 259]. For a similar reason, it has been shown that the incorporation is higher on B- than A-polar facets [98]. This results in a three-fold symmetry of the Al distribution.

We now turn to the incorporation of In. According to our simulations, there is a compressive strain in the middle of the facets (position C in the drawings). Since AlGaInAs exhibits a larger lattice constant than AlGaAs, we expect In to be favorably incorporated in the relaxed corners. In adatoms exhibit high mobilities, allowing diffusion to occur at the scale of the NW facets. Strain relaxation should support an In flux towards the more relaxed {112} corner nanofacets, while the {110} facets exhibit a significantly lower In fraction in the center (arrows leaving this position in figure 6.4d). Qualitatively, there is good match between the wedge-shaped In segregation and the simulated strain distributions that show increasing strain relaxation towards the outer NW shell. This correlation suggests that strain has an important role in shaping the In segregation. It is also known that moving steps in step-flow or 2D-island growth may drive the atom segregation [260]. Here, it is difficult to assess how atomic steps affect the In diffusion without performing in-situ experiments. However, the steps may enhance, but definitely do not significantly prevent, the strain-driven segregation of In at the NW ridges. In highly lattice-mismatched GaAs-InGaAs core-shell NWs [25], the coherent shell deposition on the {110} sidewalls occurs simultaneously with the strain-driven migration of In-rich material towards protrusions at the NW ridges. Therefore nanoscale strain gradients are the major force driving the In segregation at the ridges of lattice-mismatched NW heterostructures.

We also observe that In is poorly incorporated at the highly Al-rich stripes. We attribute this to the low miscibility of In with Al-containing alloys [261]. At the {112} nanofacets In competes with Al for the available binding sites. This is particularly relevant for the B-polar nanofacets because Al tends to accumulate more in these positions. Throughout the shell, the In segregation strongly correlates with polarity: regions with a markedly higher In fraction coincide with the B-polar vertices. We note that the polarity-driven incorporation of In has not been demonstrated in the past. The competition between In and Al to stick on the {112} nanofacets strongly favors Al on the B-polar surfaces: this mechanism may generate a net flux of In atoms towards the surroundings of the {112}B Al-rich planes. The literature on GaAs-AlGaAs core-shell NWs also reports that the {112}B nanofacets are systematically wider

than the {112}A ones [98, 62]; concomitantly, the surface-curvature gradient from the {110} to the {112} facets, depends on the polarity of the {112} nanofacet [62]. The polarity-dependent width and curvature of the NW surface may facilitate the In incorporation in proximity of the B-polar directions by directly acting of the local NW surface energy or by influencing the strain relaxation.

Conclusion In conclusion, we have demonstrated a significant (300 meV) redshift of the emission energy of single-photon emitters embedded in the shell of core-shell GaAs-AlGaInAs NWs. The redshifting mechanism is based on the In incorporation in the AlGaAs shell alloy to form a quaternary semiconductor of lower bandgap. The spatial distribution of different species in the shell is determined by several high-resolution techniques of compositional analysis. In addition to the well-known Al and Ga segregation, we find evidence of novel wedge-shaped In-rich segregation. We explain the distribution of the different species in the quaternary alloy with their diffusion on the NW sidewalls driven by crystal-phase, polarity and strain. Finite-element simulations provide insight in the role of strain to drive the segregation of In. These findings advance the understating of the segregation phenomena in quaternary alloys, as required to take full advantage of the additional degrees of freedom that they offer.

7 Optical coupling with Rb

This chapter is a brief report on the experiments conducted in the group of Prof. Richard Warburton at the University of Basel. The goal of the experiments was to observe (i) the absorption of the NWQD emission by a gas of Rb atoms and (ii) the consequent delay of the SPs. Preliminary results related with (i) are shown in the following and experimentally confirm the achieved overlap between the NWQD emission energy and the target Rb absorption thanks to the engineering of the composition and strain state of the NWQDs. An outlook on improvements for future measurements is proposed at the end of the chapter, with particular attention to point (ii).

7.1 Preliminary results

In chapter 5 and chapter 6, it is shown how the engineering of the strain state and composition of self-assembled NWQDs allows to redshift the NWQD emission energy by few hundreds of meV. Under appropriate conditions (enough strain or indium incorporation), the distributions of the NWQD emission energy overlap with the Rb D2 line (1.589 eV). However, the single NWQD emission lines are usually offset from the exact resonance. The fine tuning of the emission energy of each NWQD requires the dynamic control on the NWQD electronic levels. The most common implementations include the application of external electric or magnetic fields [129, 146] and strain [262, 207].

With respect to magnetic and electric fields, in general strain is particularly advantageous because of a steeper tuning slope of several tens of meV/% [201, 7, 134]. By choosing between compressive and tensile strain, the switch between blueshift and redshift is straightforward. Interestingly, the application of uniaxial stress along three independent directions by means of a piezoelectric transducer allows to tune both the emission energy and FSS splitting of planar QDs [207]. Although limited in range by the breakdown of the piezoelectric material, the strain tuning of the QD emission energy by piezoelectric actuators is nowadays common: a bulk sample with buried QDs is glued on a piezoelectric transducer to directly transmit stress to the QDs through the surrounding bulk matrix. In order to reproduce a similar design,
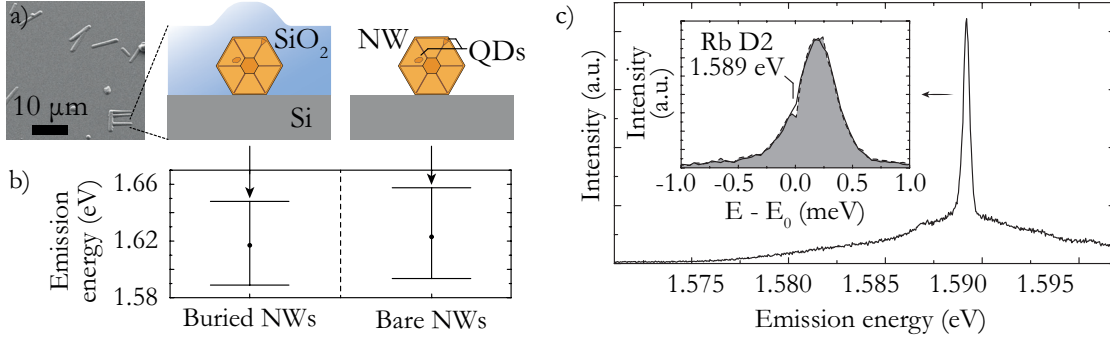
Figure 7.1 – a) SEM (on the left) and sketch (on the right) of the NWs buried in SiO$_2$ (nominal thickness 1 μm) for strain tuning. A sketch without SiO$_2$ is also reported for clarity. b) PL emission energy distributions of the QD lines of about 20 NWs for each group; the NWs nominally contain 10% of indium in the shell. The two data sets correspond to the emission from the NWs before (right) and after being buried in SiO$_2$. The dots are the medians of the distributions, while the width is given by the 1st and 3rd quartiles. The emission energy is extracted from the spectra by means of the routine described in chapter 5. c) Illustrative spectrum of the PL emission of a QD close to resonance with the D2 transition of Rb. In the inset, the PL of the same peak is transmitted through a Rb cell at room temperature (black solid curve) or heated at higher temperature (black dashed curve). The shaded area under the second curve highlights the missing counts at the emission energy that correspond to the Rb transition. The energy axis is rescaled with respect to the Rb resonance (E_0).

the core-shell NWs are dispersed on Si wafers (300 μm thick) and covered by 1 μm of SiO$_2$ by PECVD at 300°C: the NWs are buried in the SiO$_2$ slab, solidly sandwiched between Si and SiO$_2$. A cross-sectional sketch, with a buried NW, is reproduced in figure 7.1a, together with a top-view SEM image of the sample: the conformal SiO$_2$ deposition allows to localize the buried NWs from the oxide morphology. The so-prepared sample is epoxy-glued on a piezoelectric transducer to transmit uniaxial strain to the Si-SiO$_2$ matrix and the embedded NWs.

The buried NWs are core-shell GaAs-AlGaInAs NWs with a nominal 10% of indium content in the shell (chapter 6). Figure 7.1b reports the emission-energy distributions of the NWQDs before (left) and after (right) the SiO$_2$ deposition. The data points are the median of the distributions acquired on 20 NWs for each group and the widths correspond to the 1st and 3rd quartiles: the remaining 25% of the NWQD emission lines emits beyond these limits, at higher and lower energies. The oxide deposition further redshifts the NWQD emission energy: this sample preparation corresponds to the combination of the two redshifting mechanisms discussed in the previous chapters: alloying the shell with indium and coating the NW with SiO$_2$. In particular, around the low-energy end of the energy distribution of the buried NWs, several NWQDs spectrally overlap with the Rb absorption energy.

The measurement of the optical coupling between NWQDs and Rb consists in an absorption measurement: the buried NWs are cooled down to LHe temperatures in a bath cryostat (subsection 3.1.1); a Rb cell is positioned along the optical path of the PL signal to the spectrometer; Rb absorbs the photons in resonance with the D2 transition and the spectrometer detects a lower intensity for the photons at this specific energy. In particular, the used Rb cell contains a mixture of Rb isotopes according to their natural abundance (72.2% ^{85}Rb and 27.8% ^{87}Rb [262]). ^{87}Rb has a broader split between the hyperfine levels (28 μeV); at intermediate energies

within them, the hyperfine levels of ^{85}Rb defines two additional absorption resonances [262]. Overall, the two isotopes should increment the light absorption in the 28-μeV bandwidth.

Ideally, the NWQDs should be spectrally isolated from the emission lines of other emitters: the latter may add background counts that deteriorate the signature of SP emission from a single NWQD. Figure 7.1c shows the PL spectrum stemming from a QD in a buried NW: its emission is spectrally isolated, although overlapped with a broad background that may also degrade the quality of its SP emission. The peak position is very close to 1.589 eV. This is a strict requirement: even assuming flawless transmission of the strain to the Si-SiO$_2$ matrix and the NWs, the used piezoelectric transducer can shift the NWQD emission by only few tens of μeV. This limited tuning range significantly restricts the number of NWQDs suitable for coupling.

All the studied NWQDs have linewidths broader than the energy difference between the Rb hyperfine states: only the photons within the 28-μeV-wide bandwidth are delayed and absorbed. One can take advantage of the broad linewidth of the NWQD emission and demonstrate the light absorption only at the energy of the Rb D2 transition. In the inset of figure 7.1c, the solid black curve is the same spectrum as in the main graph of the same figure: it is blown up around the energy of the Rb resonance energy E_0, with respect to which the emission-energy axis is rescaled for clarity. During the acquisition of this spectrum, a Rb cell was positioned between the emitter and the spectrometer and kept at room temperature: no evidence of Rb absorption is revealed. In the same inset of figure 7.1c, the dashed black curve is the spectrum acquired after transmission through a heated Rb cell. The shaded area below this curve highlights a small dip in the intensity at E_0: it confirms the light absorption by the Rb atoms. Although the studied NWQD is subject to strain to tune its emission, the peak position is still partially offset from the resonance with Rb; however, the broad linewidth allows to observe the absorption on the low-energy side of the peak. In order to appreciate the weak spectral feature of Rb absorption, the acquisition time of the spectra in figure 7.1c is 100 s.

This measurement proves experimentally that the redshifting mechanisms discussed in this thesis can bring the emission of NWQDs close enough to the resonance with Rb to observe light absorption in the transmitted light. Considering the narrow linewidth of the Rb D2 lines, the experimental proof of absorption is meaningful: a slight miscalibration in the measurement setup corresponds to missing the target energy. Indeed, the Rb absorption is used as a spectral reference: the resonance energy is known with better precision than the spectral resolution in the reported PL spectra. In figures 7.1 (and in the following figure 7.2), the Rb absorption is used to calibrate the spectrometer and shift the abscissa ($E - E_0$) of the spectra.

The signature of the Rb absorption is observed only if the Rb cell is heated above room temperature. In the cell, the Rb vapor is at equilibrium with the solid and liquid phase (the melting point of Rb is at about 40°C). As already observed for Equation 2.24, the vapor density exponentially increases with temperature: a denser vapor enhances the light absorption. The cell is heated by Joule effect by means of a hot filament that generates about 5 W. The temperature
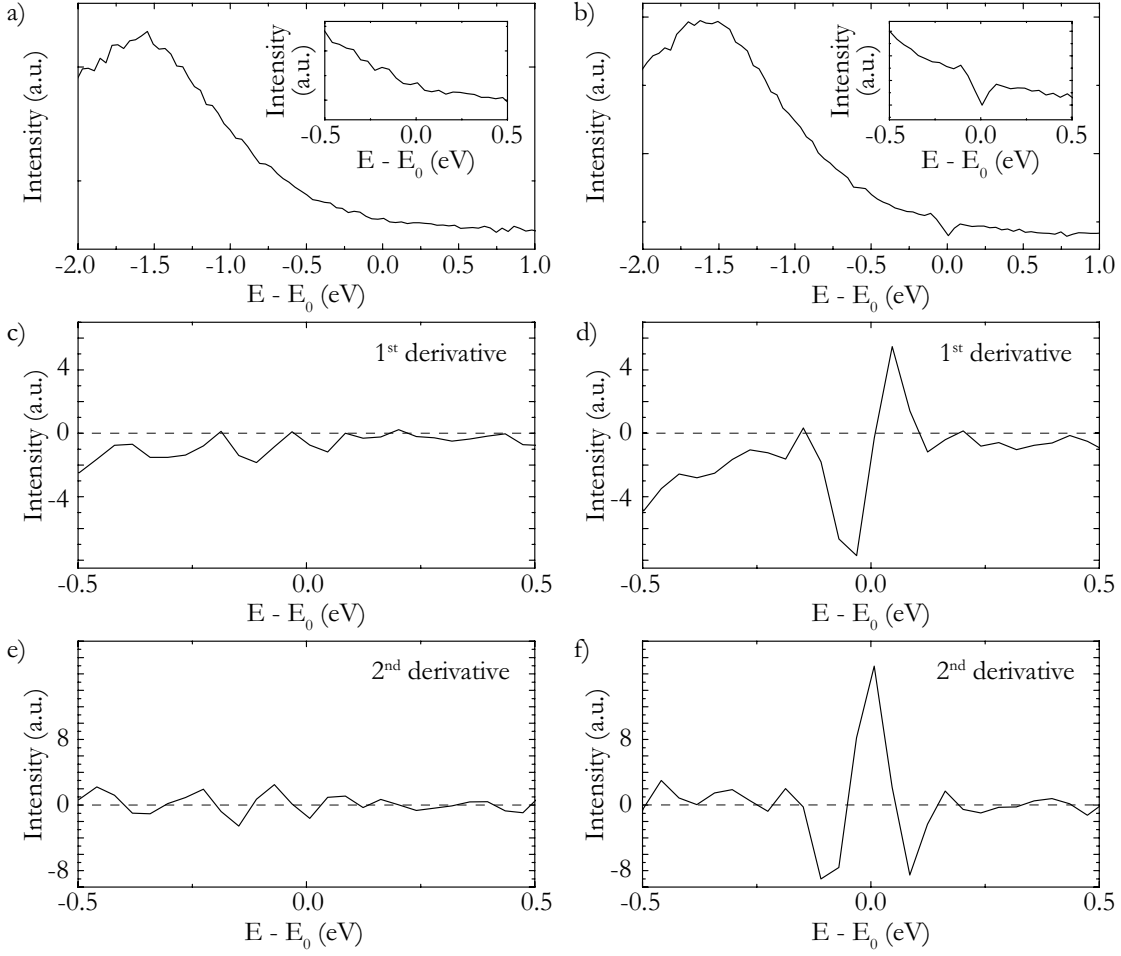
Figure 7.2 – Rb absorption experiments on a broad emitter: the figures on the left (a, c, e) report on the acquisition with a Rb cell at room temperature; the figures on the right (b, d, f) report on the acquisition of the same emitter with a Rb cell heated at higher temperature. a-b) Transmitted PL signal; the insets zoom in the spectral region of the Rb resonance. c - d) First derivative of the spectra in the insets in a) and b), respectively. e - f) Second derivative of the spectra in the insets in a) and b), respectively.

of the cell is not known, but the optical density of the cell is observed to increase during the heating: the effect is measured by the drop of the light transmission form a tunable laser set in resonance with the Rb absorption. Doppler broadening dominates the Rb transitions already at room temperature [262]. Higher temperatures enhance the Doppler broadening, that may facilitate the observation of the light absorption as a broader feature.

Figure 7.2 reports further evidence of the Rb absorption. The chosen emitter has a broad spectrum: it may stem from a In- or Ga-rich cluster of irregular shape in the quaternary AlGaInAs alloy. In general, the measurements of QD-atom optical coupling consist in tuning the emission energy of a narrow-linewidth emitter across the Rb resonance, where a dip in light transmission is recorded [129, 62]. The broad emitter shown in figure 7.2 allows to directly observe the effect of the transmission through Rb for different emission wavelengths.

In figure 7.2, the left-hand side panels correspond to the transmission of the NWQD PL without a Rb cell; the right-hand side panels correspond to the transmission through a Rb cell heated by a hot filament. The PL spectra corresponding to the two configurations are reported in figures 7.2a and b respectively. The emission energy is rescaled with respect to the Rb resonance energy E_0. The insets zoom in the spectral region around E_0. A dip at E_0 in the spectrum in figure 7.2b confirms the light absorption by the heated Rb cell.

Derivative spectroscopy enhances small spectral features. It is commonly used in absorption spectroscopy to reveal the presence of chemicals in traces. Figures 7.2c and d report, with the same $x - y$ dimensions, the 1st derivative of the spectra in figures 7.2a and b respectively. The influence of the background is reduced and the position of a weak peak is more easily distinguished: the peak position corresponds to the abscissa at which the 1st derivative is zero. While in figure 7.2c the curve is flat, in figure 7.2d the presence of the negative peak of the Rb absorption at E_0 is clear. Figures 7.2e and f report, with the same x-y dimensions, the 2nd derivative of the spectra in figures 7.2a and b respectively. Higher-order derivatives assume higher values and further enhance weak absorption features: the 2nd derivative further supports the Rb absorption at E_0 for transmission through a heated Rb cell.

7.2 Outlook

The ultimate goal of the optical coupling between NWQD emission and Rb absorption is to demonstrate that light is delayed at the SP level while maintaining unaltered the photon properties, e.g. its polarization [146]. While some reports demonstrate the optical coupling and SP delay between planar QDs and gas vapors [146, 207], only very recently the coupling has been demonstrated with QDs embedded in NWs [12]: the emission energy of narrow-linewidth GaAs QDs embedded in AlGaAs NWs is tuned in resonance with the Rb D2 line by means of an external magnetic field. The AlGaAs NW hosts a single on-axis GaAs QD; the controlled length of the GaAs segments defines the QD emission energy only at tens of μeV from the Rb resonance; an external magnetic field of less than 1T is sufficient to bring the QD in resonance with Rb, as demonstrated by the dip of the QD PL transmission through the Rb cell.

On the other hand, the delay of the SPs emitted by a NWQD has never been demonstrated. With regard to the experimental setup described in the previous section 7.1, some modifications would help the observation of SP delay. It would be beneficial to implement an efficient cell heater to increase the optical density of the Rb cell. Although a mixed-isotope vapor enhances the light absorption with four different available transitions, the demonstration of SP delay is preferred if the cell contains only one single species. Cells with up to 98% of ^{87}Rb content are commercially available: the spectral region between the resonances would be ideal to enhance the SP delay thanks to the steep increase of the refractive index [146].

In order to increase the occurrence of useful QDs, larger tuning of the QD emission energy is necessary. Strain is a powerful tuning mechanism, because NWs stand very large strain

and the emission of the embedded QDs can shift significantly upon the application of large strain. However, piezoelectric actuators provide a limited straining range. In addition, in the experiments presented here, the PECVD oxide may lack enough cohesion to efficiently transmit the strain to the NWQDs. If the grains that compose SiO_2 do not coalesce, their reciprocal movement dissipates most of the strain-field energy. A possible solution would be to deposit materials with a lower melting point or, equivalently, SiO_2 at higher temperatures to obtain a unique solid slab of Si and SiO_2 with embedded NWs. On the other hand, magnetic fields up to 9 T are relatively common in PL setups equipped for magnetic measurements. A magnet with this capability is now available in Richard Warburton's group and mounted on a cryostat for magnetic PL measurements. Considering that tuning slopes of about 100 $\mu eV/T$ are demonstrated on GaAs QDs [129], an overall blueshift of about 1 meV may be achievable.

Although a narrow emission linewidth is necessary for quantum applications, the demonstration of SP delay does not strictly depend on it: in the first demonstration of QD SP delay with Rb, the QD emission linewidth is about 80 μeV, that is, few times larger than the 28 μeV of the Rb hyperfine splitting. The photons outside this energy interval are neither delayed nor absorbed. Nevertheless, the majority of the photons emitted by narrow-linewidth emitters centered at 1.589 eV undergo strong delay in the region of steep variation of the refractive index and, being slightly off the hyperfine resonances, they are affected by low absorption (section 2.5). Overall, the increased transmission of highly delayed photons facilitates the demonstration of SP delay. Low-power resonant excitation (the incident laser wavelength matches the QD emission wavelength) generally narrows the QD emission linewidth, concomitantly increasing the emission brightness. Being at the same energy, the laser excitation and PL signal are distinguished by means of another optical property, such as their polarization. However, in the used setup, this strategy proved challenging: it requires a flat surface that is not immediate to achieve by burying the NWs in SiO_2.

8 Conclusions and outlook

This thesis focused on engineering the optical properties of self-assembled QDs embedded in the shell of core-shell GaAs-AlGaAs NWs. The main goal was the redshift of the QD emission energy into resonance with the Rb D2 absorption line. The results here presented contribute to the understanding of the segregation dynamics of different atom species on the NW sidewalls. Specific emphasis was given to clarify the correlation with crystal defects in the NW core, a point under debate [74] since the first evidence of the NWQD occurrence. The redshift of the NWQD emission energy by strain and composition engineering allowed to achieve the target energy of the Rb absorption and highlighted that NWs are a versatile and flexible platform for engineering semiconductors beyond the limits of a planar design.

In chapter 4, single NWs are analyzed by a comprehensive combination of microscopy techniques at high spatial resolution. By TEM and HRTEM, the density of crystal defects along the NWs is mapped; by micro-PL and SEM-CL, the occurrence and emission energy of the NWQDs is recorded on the same NWs. The correlation between structural and optical data is apparent: when the density of rotational defects increases, the occurrence of NWQDs rises, while their emission energy redshifts. The twin-driven segregation of Al and Ga on the NW sidewalls accounts for these findings and is supported by the APT observation of the crystal-phase-induced composition modulation of AlGaAs along GaAs-AlGaAs NWs [62]. Furthermore, finite-element calculations connect the redshift of the QD emission energy with the twin-ZB band alignment inside the QD. This work proves that the engineering of the NW crystal structure represents a form of control on the NWQD properties; at the same time, it highlights the importance of mastering the NW crystal phase to obtain homogeneous heterostructures on the NW sidewalls.

Chapter 5 focuses on a post-growth strategy to redshift the NWQD emission. A static straining device is presented in the form of a PECVD oxide coating on the core-shell GaAs-AlGaAs NWs. In spite of the simplicity of fabrication, this device allows to redshift the NWQD emission by more than 100 meV without affecting their optical properties. Thanks to the intrinsic strain in the oxide, the coating applies tensile strain to the NWs and the embedded NWQDs. In turn, the strain tightly depends on the oxide microstructure that is controlled by the deposition
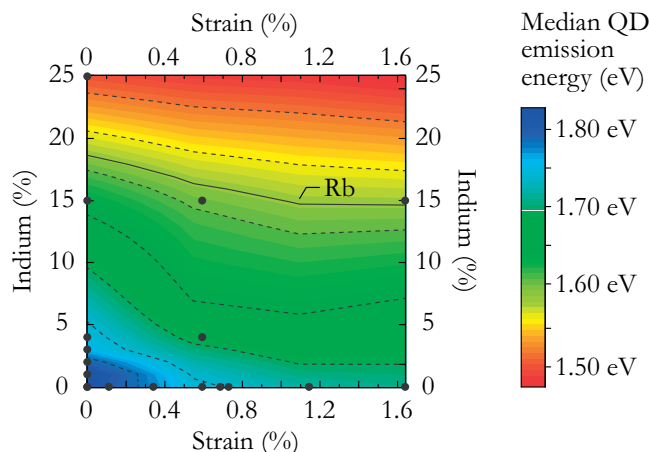
Figure 8.1 – Contour plot of the median emission energy (grey dots) of NWQD ensembles from different samples: GaAs-AlGaAs NWs coated with PECVD SiO$_2$ (strain varying from 0% to about 1.6%), GaAs-AlGaInAs NWs with indium in the shell (nominally from 0% to about 25%), and GaAs-AlGaInAs NWs coated with PECVD SiO$_2$ and with indium in the shell. The contour values results from a thin-plate-spline interpolation-extrapolation of the experimental data.

temperature. The strain analysis indicates a pronounced anisotropy, with the largest strain component parallel to the NW longitudinal axis. This relates with the directionality of the grains in the oxide coating. Further materials and deposition techniques are finally explored: they expand the application range of the straining technique by applying straining coatings with further functionalities. These findings provide a base to the understanding of the working principle of this simple and effective device and point to the NW geometry as a probable factor of strain enhancement. The demonstrated control on the deposition material and conditions opens a multitude of opportunities to functionalize NWs; for instance, the coated NWs may act as catalysts for electrochemical reactions: while strain-tuning the semiconductor bandgap to a target value, an electron-conductive coating enables the reduction of the reactants on the large NW surface.

In chapter 6, the NWQD emission is redshifted by alloying the AlGaAs shell with indium. Several techniques of compositional analysis are combined to study the indium incorporation in the NW shell (XRF, APT, STEM EDX and EELS, further supported by PL and Raman spectroscopy). Novel wedge-shaped In-rich features are observed for the first time at the corners of hexagonal NW cross sections. The presence of these In-rich segregates is supported by both STEM EDX and EELS compositional maps. Since In-based compounds are lattice-mismatched with (Al)GaAs, strain is also considered to explain the formation of the In-rich features. PL and Raman measurements of the strain in the NW core as well as calculations of the strain distributions in the NW cross sections are used to support the role of strain in the formation of the In-rich segregates. The NWQDs embedded in the shell are still functional also with the addition of indium and maintain a SP emission. With increasing indium content in the shell, the NWQD emission energy increasingly redshifts up to about 300 meV.

For the thickest depositions, the oxide straining device places the NWQD emission energy in

resonance with the target value. By indium alloying, the QD emission-energy distributions significantly redshift and can even reach energies lower than the Rb resonance. A summary of the achieved redshift for both mechanisms is proposed in figure 8.1. The grey dots represent the medians of the NWQD emission energy distributions obtained from PL spectra: the results for NWs subject only to strain by an oxide coating are reported on the abscissa, while those only due to indium alloying are reported on the ordinate. The combination of the two strategies (oxide coating of NWs alloyed with indium) is fruitful; the corresponding experimental data are in the area between the two Cartesian axes in figure 8.1. Since the incorporation of indium in large amounts (about 25%) has been associated with brightness reduction in the PL spectra (section 6.2), the combination of the two redshifting mechanisms allows to limit the indium incorporation to preserve the brightness of the NWQD emission and extend their energy redshift by the deposition of the oxide.

As shown in chapter 7, the samples used for the Rb-absorption measurements were prepared by a similar approach: NWs with a known percentage of indium in the AlGaAs shell were buried into SiO_2 to ensure the overlap of the NWQD distributions with the energy of the Rb absorption (section 7.1). In chapter 7, the evidence of the absorption of the NWQD PL emission by a gas of Rb atoms is reported: it constitutes a proof of principle of the first essential step towards the implementation into a quantum network based on interfacing these NWQDs with Rb-based quantum memories. The second step would be the demonstration of SP delay and the conservation of the polarization of the delayed SPs, as outlined in chapter 7.

An important figure of merit of the NWQD emission is the linewidth. For the self-assembled NWQDs studied here, this is in the range of 100 μeV or less, in general much wider than the state of the art of very few μeV of both QDs and NWQDs [11, 12]. Space charge fluctuations in the QD surroundings probably represent an important source of broadening of the NWQD emission linewidth. On this research path, some insights on the self-assembled NWQDs studied in this thesis come from core-shell GaAs-AlGaAs NWs grown along the <111>A crystal direction, in which the density of defects is strongly suppressed. Although NWs usually grow in the <111>B direction, one can optimize the yield of NWs grown along the <111>A direction by tuning the MBE growth conditions [170]. Furthermore, the shell structure can be easily engineered to separate the NWQDs from the surface states [11]. The study of these strategies to narrow the linewidth of the self-assembled NWQDs is still at an initial stage and would provide an interesting subject for future research. Together with this and like any other self-assembled system, a sharper impact on the width of the distributions of the NWQD occurrence and emission energy is desirable. First steps in this direction are demonstrated by the reduction of the spread among the NWQD emission energies when the AlGaAs shell is grown at lower temperature (430°C) [74].

Overall, the AlGaAs NWQDs represent a robust system of quantum emitters that form within a wide range of growth conditions [74] and emit bright emission lines also after extended exposure to electron-beam irradiation [253]. Furthermore, some specificities of the GaAs-AlGaAs system, such as the longer coherence time of the trapped charge carriers, are regarded

as highly appealing for quantum emitters in comparison with other materials, such as the more common In-based SK QDs [207]. At the same time, NWs offer additional freedom to engineer the optical properties of QDs embedded in their structure. In this thesis, the wide flexibility to tune the NWQD emission energy was demonstrated by strain and composition engineering. The incorporation of GaAs-AlGaAs QDs with long coherence times into NWs may thus benefit from the freedom offered by the NW host. A hint of these possibilities is given in Appendix A that shows preliminary experiments about the incorporation of axial QDs in recently achieved quantum-thin NWs [48]. By this design, both the longitudinal and lateral confinement of the QD would be ideally controlled and the symmetry of the heterostructure would suppress the QD FSS.

A Towards axial quantum dots in quantum-thin nanowires

During this PhD, a different kind of NW-based QDs has been considered in addition to the self-assembled QDs in core-shell GaAs-AlGaAs NWs. This second type of NWQDs consists in a heterostructure defined along the main axis of a quantum-thin NW, named nano-needle (NN) [48]. The NNs are grown on top of GaAs NWs that have a diameter of several tens of nm, while the NN can be as thin as 10 nm. The NN growth mechanism is known to depend on the distance between the NWs. Therefore, NWs grown in regular patterns with controlled and constant inter-NW distance are preferred [48]. The NW-NN system is grown vertically on (111)Si substrates. The NNs are obtained on top of GaAs NWs according to the three-step protocol described in ref. [48]. The key parameter to thin the NWs into NNs is the As pressure. During the NW growth, the As beam equivalent pressure is about 2×10^{-6} torr (step 1). The shrinkage of the Ga droplet is obtained by increasing the As pressure by about one order of magnitude (8.9×10^{-5} torr - step 2). Ga is still supplied. Under these conditions, the NW keeps growing axially, but the high As pressure reduces the NW diameter. After 5 minutes of growth at high As pressure, conical tips are obtained: they are limited in length (~ 2 μm) and their diameter gradually decreases. In order to obtain long NNs of fixed diameter, the step at high As pressure should not last longer than 2 minutes and a third step must be introduced. In the third growth step, the As pressure is reduced to an intermediate value (5.5×10^{-6} torr - step 3). This sequence of growth steps leads to NNs with constant and small diameter and arbitrary lengths of few μm. A TEM micrograph of a GaAs NN on top of a GaAs NW is shown in figure A.1a.

A QD can be placed in the NN as a segment of lower energy gap with respect to the rest of the NN semiconductor. An axial heterostructure can be defined on the NN axis following the growth scheme of axial NWQDs presented in subsection 2.3.1: during the VLS growth of the NN, a foreign element is supplied; by diffusion into the droplet, it is incorporated into the solid precipitate that forms the NN. This approach is affected by the same limitations of a traditional axial NWQD, namely shallow interfaces due to the reservoir effect. Some expedients can limit the reservoir effect, as mentioned in subsection 2.3.1. For instance, slow growth rates, down to the interruption of the axial growth, sharpen the transition between different materials [29, 36].

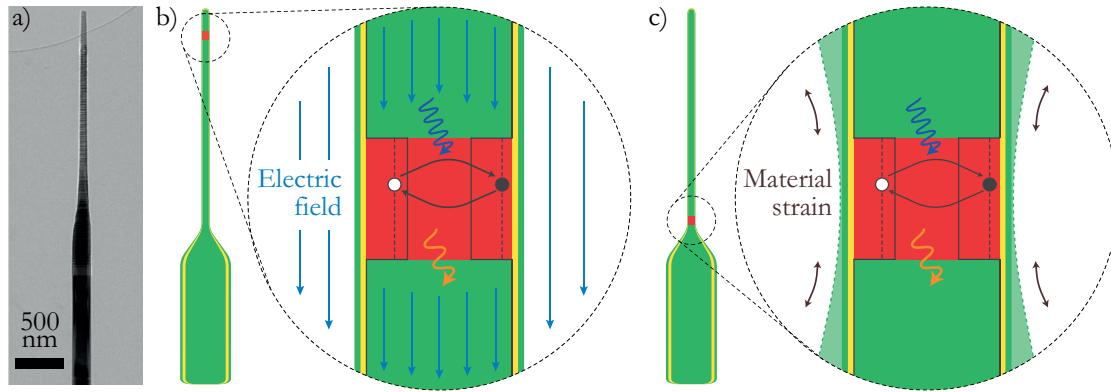## Appendix A. Towards axial quantum dots in quantum-thin nanowires

Figure A.1 – a) TEM micrograph of a GaAs NN on top of a GaAs NW. Schemes of the NN-based electric-field (b) and strain (c) sensors.

Also the presence of a miscibility gaps between the atomic species A and B in the catalyst has been proposed to tackle the reservoir effect: for a wide range of A/B ratios in droplet, the miscibility gap keeps the presence of one of the two (e.g. A) at very low concentrations in the solid; by continuous supply of A, the A/B ratio increases in the droplet, but not in the solid; as soon as the A/B ratio in droplet exceeds a threshold value, a large amount of A is incorporated in the solid [91].

Assuming fine control on the sharpness of the QD interfaces in the longitudinal direction, the length of the QD is directly tuned by the growth time of the QD segment. This dimension defines the longitudinal quantum confinement of the charge carriers trapped into the QD. In (Al)GaAs NWs of few tens of nanometers in diameter, there is no important contribution to quantum confinement by the lateral size of the QD. On the contrary, the thickness of the NN is small enough to contribute to the overall confinement of the trapped charges. In turn, the NN diameter is a function of the droplet size, that depends on the As pressure and duration of the step 2 previously described. The possibility to act on both the longitudinal and lateral confinement of the QD increases the degrees of freedom available to control the QD energy levels.

The main interest of defining axial QDs in NNs is related with the accurate sensing of external perturbations. A scheme of the NNQD design for this application is presented in figure A.1b for the sensing of an external electric field. The QD is positioned at the top of the NN. This design is ideal for probing an external field: the QD is close to the surface; the long thin NN can penetrate in the field without significantly perturbing it. The readout of the amplitude of the Stark shift of the QD emission energy would allow to retrieve the amplitude of the electric field. As scanning probes, the NNs enable high spatial resolution due to their very thin diameter. Interacting with the surface of a sample, the NN bends proportionally to the strength of the tip-surface interaction, that is, to the NN-surface distance or surface composition. The NN is very flexible, thus sensitive to small forces. Figure A.1c sketches the ideal configuration in this case: the QD is placed at the base of the NN. The objective is to enhance the opto-

mechanical coupling between QD and NN. The read-out of the QD state provides a way to retrieve the strain field in the QD, which depends on the bending of the NN and the strength of the interaction.

With regard to the topic of this thesis, achieving these QDs represents an appealing alternative route towards the optical coupling with Rb. The freedom in tailoring the composition of such a NN-based QD and the control on both its lateral and longitudinal size facilitates the tuning of its emission energy. Furthermore, the axial design is particularly interesting for SP applications: its high symmetry should suppress the FSS of the QD energy levels [76, 18]. Two material systems are considered: (Al,Ga)As and (In,Ga)As. The emission energy of a single (Al,Ga)As NN-based QD could be tuned close to the resonance with Rb by controlling the NN diameter and the QD length and composition. The interest is to obtain a SP emitter whose emission energy is very close to the D2 line of Rb: the target could be less than 100 μeV from the energy of the Rb transition. This is necessary to enable the fine tuning in resonance by, e.g., external magnetic fields. A capping shell of higher bandgap would passivate the surface and enhance the QD brightness. Another interesting material candidate is In(Ga)As. For this material combination, the QD can emit at telecommunication wavelengths. This characteristic would facilitate its integration with the current technologies, e.g. coupling with optical fibers. In this case, Rb should be replaced by Cs (D1 transition at 1.386 eV) if the optical coupling with an atomic gas is aimed [263].

A.1 Growth and composition

In the following, the strategies considered to grow a segment of lower bandgap inside a NW or a NN are outlined and preliminary growth results are presented. They are all based on the incorporation of indium along GaAs NWs. In the majority of the experiments, the second segment of a A/B/A axial heterostructure has not been grown. This strategy enabled to focus on the optimization of the A/B interface first. At the end of some growths, a GaAs capping layer is deposited to passivate the NW surface and enhance the brightness of the luminescence stemming from the nanostructure. The absence of the GaAs capping layer in the rest of the growths was chosen to facilitate the compositional analysis of the nanostructure by STEM EDX.

The first approach to the indium incorporation is sketched in figure A.2a. It consists in supplying indium during the growth of a GaAs NW while the catalyst Ga droplet is still present. Indium has a high surface mobility and it is expected to diffuse on the NW sidewalls. Once at the top of the NW, indium can be dissolved into the droplet. At supersaturation, indium can then precipitate with Ga and As to from an (In)GaAs crystal. Different growths were conducted with this strategy for different indium pressures in order to vary the droplet composition.

Figure A.2b shows the STEM EDX map of a heterostructure obtained in this way. The droplet was filled with indium for 75 s (indium pressure equal to 9 x 10^{-8} torr) at a substrate temperature of 460°C. As was then supplied to form an In-rich crystallite. The incorporation of indium
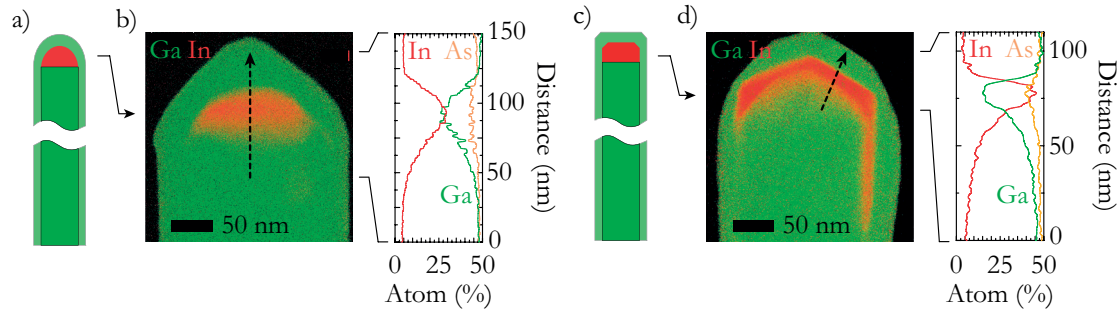
Figure A.2 – a) Sketch of a GaAs (green) NW with indium (red) incorporated into the catalytic droplet. b) STEM EDX map of the tip of a GaAs NW with indium in the droplet. The linescan on the right follows the dashed arrow: the GaAs-InGaAs transition has shallow profiles. The maximum indium concentration in the droplet corresponds to $In_{0.5}Ga_{0.5}As$. In order to passivate the surface, a GaAs capping layer covers the heterostructure. It may affect the Ga/In ratio of the linescan. c) Sketch of a GaAs (green) NW and an In(Ga)As (red) segment epitaxially grown on its tip. d) STEM EDX map of the tip of a GaAs NW with an In(Ga)As alloy epitaxially grown on the top facet. The linescan on the right follows the dashed arrow: the GaAs-InGaAs transition is still shallow on the internal side, but it is much steeper with the GaAs capping. The maximum indium concentration increased and approximately corresponds to $In_{0.85}Ga_{0.15}As$.

(red in the map) at the tip is evident; the In-rich area is not faceted, suggesting that the In/Ga droplet was not completely consumed into a crystallite when the growth of the GaAs capping started. On the right, figure A.2b shows a linescan along the dashed arrow shown on the EDX map. The indium enrichment and Ga depletion at the position of the droplet is evident with a maximum indium content corresponding to $In_{0.5}Ga_{0.5}As$. This value is probably affected by the presence of the outer GaAs capping that biases the compositional mapping in favor of Ga. The transition from GaAs to InGaAs is very shallow, with a smooth increase in the indium content over almost 100 nm. This corresponds to the gradual incorporation of indium into the liquid droplet while the NW keeps growing in the axial direction. As a result, the transition region extends over a long distance. The second transition (from InGaAs to GaAs) is sharper. This interface results from the epitaxial deposition of a solid GaAs capping, which limits the adatom diffusion.

The increased sharpness of the second interface suggested to take advantage of the reduced In/Ga intermixing in the solid phase to sharpen the GaAs/In(Ga)As transition. Therefore, in a second strategy, InAs was directly deposited on GaAs NWs, that is, without the mediation of the droplet. The goal is still to define a small In-rich crystallite at the top of the NW. This mechanism is based on the large lattice mismatch between GaAs and InAs. The small area of the NW tip should facilitate the relaxation of the strain and enhance the incorporation of indium at this position. This strategy has been successfully applied to grow InAs on top of GaAs nano-membranes [264]. Although the GaAs nano-membranes described in ref. [264] have a different orientation of the crystal facets with respect to the NWs, the strain gradient is still expected to favor the indium deposition at the NW tip. A sketch of this configuration is reported in figure A.2c.

Figure A.2d is the STEM EDX map of a heterostructure grown in this way. The indium pressure

and substrate temperature were the same as in the previous growth, but indium was supplied for 200 s after the complete consumption of the droplet. An In-rich region at the top of the NW is clearly visible; it has a faceted surface, indicative of the epitaxial growth as a solid crystal. The linescan along the dashed arrow is reported on the right and shows that the maximum indium content corresponds to $In_{0.85}Ga_{0.15}As$. As before, the presence of the GaAs capping probably biases the quantification in favor of Ga. Nevertheless, the indium content is larger than in the previous case (figure A.2b) because its incorporation is not mediated by the Ga droplet.

The NW tip imaged in figure A.2d is probably surrounded by an In(Ga)As layer on all the facets and has a decreasing thickness moving away from the top. Since the EDX map shows a 2D projection of a 3D volume, the variation of the thickness of the In(Ga)As layer appears as a smooth transition from GaAs to InGaAs. On the contrary, the transition from In(Ga)As to the GaAs capping appears much sharper, within about 10 nm - 20 nm. At this position, the facet is probably perpendicular to the projection plane: therefore, the real length of the transition is observed and the structure geometry does not affect the measurement of the sharpness of the transition. Yet, the In/Ga intermixing is not fully suppressed. As already observed in ref. [264], the strain due to the lattice mismatch between GaAs and InAs causes the intermixing between the two adatoms.

The incorporation of indium through a catalyst droplet is commonly used to define In-based axial heterostructures [89]. On the contrary, the strategy sketched in figure A.2c is less common; the experimental result shown in figure A.2d shows that indium can be preferentially incorporated at the NW tip with no need to use a catalyst droplet. This strategy allows to sharpen the interfaces of a heterostructure grown at this position. The growth conditions can be further optimized to limit the In/Ga intermixing, for instance by decreasing the growth temperature. In figure A.2d a protrusion of the In(Ga)As layer on the NW sidewall is evident on the right of the EDX map. This is probably due to the diffusion of indium along the NW facets. A lower growth temperature and a higher As pressure should reduce the diffusion length of indium and limit the occurrence of this phenomenon. Indeed, it was common to observe several In-rich clusters or patches along the sidewalls of NWs grown in this way. If the growth time of the InAs layer is increased, these In-rich regions would probably merge into a continuous In(Ga)As shell [52].

The first attempts to apply to NNs the strategy presented in figure A.2c were not successful. Indium was not observed to deposit at the tip of the NN, as opposed to what happens at the tip of a NW. The mediation of the catalytic droplet was thus considered to drive the incorporation of indium. Preliminary results on the formation of (In,Ga)As heterostructures in NNs are reported in figure A.3. The NNs were defined according to the three-step protocol already presented. In addition, indium was supplied for 200 s at the same pressure and substrate temperature as in the NW growths previously shown. Figure A.3a sketches an In-rich segment incorporated in the NN. Ideally, this structure can be obtained by starting the indium supply during the NN growth. During the third step of the NN formation, the indium pressure can
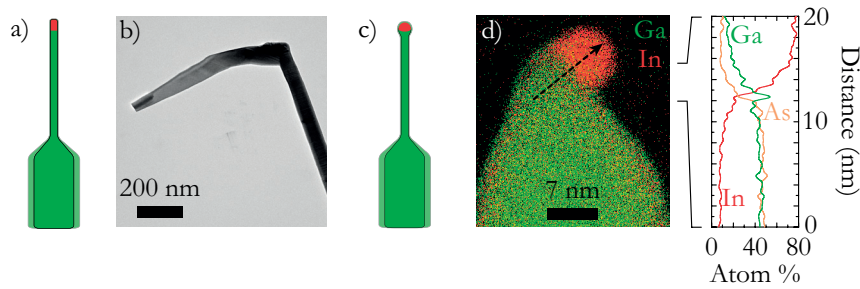
Figure A.3 – a) Sketch of a GaAs (green) NW and NN: an indium segment (red) is incorporated at the top of the NN. b) BF TEM micrograph of a NNs: towards the end of the NN growth, indium was also supplied. In most NNs, this caused the growth direction to abruptly change and form irregular structures such the one shown here. c) Sketch of a GaAs (green) NW and NN where the catalytic droplet is inflated with indium. d) STEM EDX map of the tip of a GaAs NN with indium in the droplet. The linescan on the right follows the dashed arrow: the GaAs-InGaAs transition is rather sharp. Interestingly, both Ga and As decreases in the droplet, while indium increases: liquid indium may have replaced liquid Ga in the droplet in the MBE. The In/Ga ratio is about 8. This NN is not passivated with a GaAs capping, in order to facilitate the compositional analysis.

be increased in order to dissolve some indium into the catalytic droplet. By continuing the axial growth of the NN, the last portion of the NN would be composed of InGaAs. Figure A.3b shows the TEM micrograph of a NN that underwent this sequence of growth steps (without GaAs capping). The last part of the NN shows the irregular growth of a structure in a direction apparently uncorrelated with the NN growth direction. The abrupt change in the NN growth direction was systematically observed on several NNs. Clear signature of the incorporation of indium into these irregular structures was not detected.

On a different approach, figure A.3c sketches the incorporation of indium in the small catalyst droplet on top of a NN; the axial growth of the NN is not continued. This strategy would avoid the formation of irregular nanostructures while still forming an In-rich crystallite at the tip of the NN. This design corresponds to transferring to the NNs the strategy proposed for NWs in figure A.2a. Figure A.3c reports the STEM EDX map of the tip of an irregular NN. It was not covered by a GaAs capping layer to facilitate the compositional mapping of the small structure. An In-rich nano-droplet is visible at the tip. The nano-droplet is less than 10 nm in diameter. It contains mainly indium, as shown by the linescan on the right, taken along the dashed arrow in figure A.3e. This structure formed at the end of a NN like the one shown in figure A.3b: the NN formed an irregular crystal, but maintained a droplet at the top. Indium was preferentially incorporated at this position. This suggests that the strategy described in figure A.3c may be a viable method to incorporate indium at the tip of a NN. Interestingly, the interface between GaAs and In(Ga)As is very sharp. According to theoretical studies [265, 266], the precipitation of a material A dissolved into a liquid droplet of material B may decrease with the decreasing size of the droplet. This predicts a limited indium incorporation in an InGaAs segment during the Ga-assisted VLS growth of a NN of very thin diameter. However, it is an excellent expedient to help obtaining an In-rich crystallite at the tip of a NN with a sharp material transition.
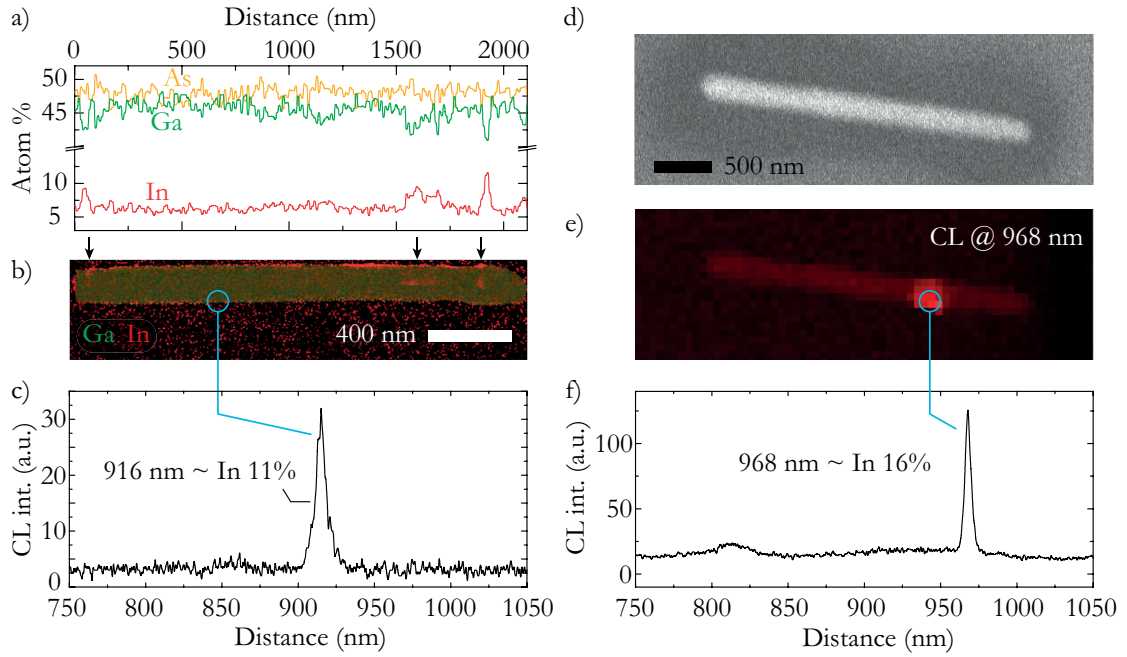
Figure A.4 – STEM EDX linescan (a) and map (b) of the same NW. Indium has been incorporated through the catalyst droplet (strategy of figure A.2a). The droplet size was decreased before the indium supply in order to reduce the size of the In-rich region. The arrows indicate the positions where the indium concentration increases. The one closer to the NW tip, on the right, may be due to indium into the droplet. c) CL spectrum, acquired at 12 K, at the position indicated by the blue circle. The bright CL emission probably stems from an In-rich nanocluster formed in the NW sidewalls. d) SEM image of a NW from the same growth as in figure A.2b. e) CL map of the NW shown in (d). The CL signal if filtered around 968 nm. f) CL spectrum corresponding to the localized emission in e) indicated by the blue circle. At about 820 nm a weaker peak probably stems from the GaAs core.

A.2 Light emission

A fundamental requirement of the NN-based QDs is to be optically active. This is clearly necessary for the SP emission; in this case the optical properties of the emitters should be further analyzed to confirm the SP nature of the emission by measuring the second-order autocorrelation function. Optical activity is also required for using the QD-NN system as a sensor: the optical readout of the QD state enables the measurement of the external field.

Preliminary optical measurements on GaAs-InGaAs heterostructures are reported in the following. Figure A.4a to c report compositional and optical measurements on the same NW. Figure A.4b shows the STEM EDX map of the NW; a linescan extracted from this map is reported in figure A.4a. In this NW indium has been deposited by the method sketched in figure A.2a. In addition, the droplet size was decreased before the indium supply in order to reduce the size of the region enriched in indium. A systematic calibration was not performed, but the shrinkage of the Ga droplet before the indium supply should enable to enhance the quantum confinement in the In-rich crystallite. From the map and the linescan, small fluctuations in the indium concentration along the NW are found. Three In-rich cluster are found along the NW at the positions indicated by the arrows. The one closer to the NW tip,

on the right, may be due to the indium incorporation into the droplet. HAADF images of the same NW at long camera length (770 mm) can show diffraction contrast and allow to distinguish crystal defects in the NW structure (not shown). Although evidence of an increased density of crystal defects is found at the NW top and bottom, a clear correlation between their position and the segregation of indium is not found. Figure A.2c shows a single CL spectrum acquired at the position indicated on the EDX map by the blue circle. It consists of a single peak centered around 916 nm, with a linewidth of few meV. The CL spectrum was acquired with an integration time of 100 ms, at an electron beam acceleration voltage of 3 kV. The bright CL emission probably stems from an In-rich nanocluster formed on the NW sidewalls. In bulk InGaAs, the emission energy of the CL peak (about 916 nm, i.e. 1.35 eV) would correspond to $In_{0.11}Ga_{0.89}As$. None of the In-rich clusters detected in the EDX maps had bright and sharp emission in the CL spectra ascribable to QD-like optical properties.

Figure A.4d, c, and f report on a NW from the same growth of the one shown in figure A.2b. In these NWs, indium was incorporated in the catalyst droplet; the droplet was not shrunk before introducing indium. Figure A.4d reports the SEM image of the NW and figure A.4e is the CL map of the same NW. The CL signal is filtered around the emission wavelength at 968 nm. The CL spectra were acquired with an integration time of 500 ms, at an electron-beam acceleration voltage of 10 kV; these relatively long integration time and high acceleration voltage were required to compensate for the weak emission of the sample. The NW brightness would benefit from an AlGaAs capping that was not possible to grow for this batch of samples. The CL map highlights the presence of a bright and localized emitter at 500 nm from the top. The emission stems from the NW sidewall: it cannot be ascribed to the intentional incorporation of indium in the droplet. The CL spectrum of the emitter highlighted in figure A.2c is reported in figure A.2f. It consists of a bright peak at 968 nm (about 1.28 eV) with a relatively narrow emission of few meV. In the bulk, this energy would correspond to the emission from $In_{0.16}Ga_{0.84}As$. A second peak at higher energy (820 nm) can be assigned to the GaAs bandgap emission. Like in the previous case, none of the emission peaks from this NW stems from the InGaAs heterostructure intentionally grown. The parasitic In-rich clusters on the NW sidewalls seem to have brighter emission (at least in the detectable energy range).

A.3   Outlook

The work presented in this chapter is an initial benchmark for the growth of a fully functional and controlled quantum emitter in a NN. These experiments show that indium incorporates at the tip of GaAs NWs by two methods: incorporation in the Ga droplet (figure A.2a) and through a mechanism that is probably related with the relaxation of strain at the NW tip (figure A.2c). The first mechanism is relatively mainstream, while the second one is particularly appealing: it allows to obtain sharp In(Ga)As-GaAs interfaces and almost pure InAs crystals. The application of this strategy to the NNs proved to be challenging. However, the experiments showed that indium incorporation into the nanodroplet at the top of NNs is promising: it should be studied in a systematic way in order to achieve full control on the droplet size and composition.

The optical characterization of these heterostructures should follow. The emission energy, linewidth and SP behavior should be the first characteristics to address.

The suppression or the control of the parasitic clustering of indium on the NW side facets must be addressed as well. With this regard, the role of crystal defects and surface roughness in clustering indium along the NWs should be further analyzed. The work and the literature presented in chapter 4 and chapter 6 provide a useful theoretical background for this study. The methodology of direct correlation between structural analysis and luminescence mapping at high resolution presented in chapter 4 may prove particularly useful to elucidate this point also in the GaAs-InGaAs system. The growth of a QD on the tip of a NW or NN is useful for sensing external fields and for light emission. Yet, the optimal design for a scanning probe requires to embed the quantum emitter at the bottom of the NN (figure A.1c). This involves the growth of a second segment to cap the QD and continue the axial growth of the NN. This has not been addressed in the preliminary experiments shown here. It will demand for a systematic study to control the growth of the capping segment and prevent the tilting of the NN along irregular directions, as observed for (In,Ga)As (figure A.3b).

Not all the findings valid for the (In,Ga)As system may be valid for AlGaAs-based QDs in NNs. Strain is not expected to play any significant role in lattice-matched GaAs-AlGaAs heterostructures. On the contrary, the dynamics of the Al/Ga incorporation as an axial QDs may show common aspects with (In,Ga)As. The use of (Al,Ga)As NN-based QDs is probably preferable and required in order to compete with the existing technology in planar and NW-based QDs. The state of the art in QD-emission properties in both configurations (bulk and NWs) is based on (Al,Ga)As. This material combination enables longer coherence times [207] and, in highly symmetric QDs, holds record values of $g^2(0)$, SP indistinguishability and entanglement [77, 81]. In addition, optical coupling with a gas of Rb has already been demonstrated with axial (Al,Ga)As NWQDs [12].

B Supporting information of articles

The following pages report the Supporting Information material attached to the articles that compose chapter 4, chapter 5, and chapter 6.

The Supporting Information to chapter 4 comprises Monte Carlo simulations of the electron-beam interaction volume, additional TEM micrographs of NW defects (also in other NWs), compositional mapping along single NWs by STEM EDX, QD occurrence by CL in function of the NW-shell thickness, exciton recombination energy for different material parameters, a comparison between PL and CL linescans on the same NW, and the whole set of NW CL maps.

The Supporting Information to chapter 5 comprises additional TEM micrographs of the oxide structure, the calibration curves of the oxide thickness, the downshift of all the Raman modes, Raman spectra for the PECVD SiO_2 deposited at low temperature, PL spectra of the NW coated in TiO_2, temperature-dependent Raman-spectroscopy data, and further polarization-dependent Raman spectra.

The Supporting Information to chapter 6 comprises the plot of the QD emission-energy range vs indium, polarization-dependent Raman spectra, STEM EDX maps on NW cross sections, AC HAADF micrograph of a NW cross section, XRF maps, further EDX and EELS maps, power-dependent PL of the QD line used for the g^2 measurement, illustrative CL maps, and the data on strain derived from the Raman spectra according to ref. [159].

Supporting Information to chapter 4

Tuning adatom mobility and nanoscale segregation
by twin formation and polytypism

Luca Francaviglia[1], Gözde Tütüncüoglu[1], Federico Matteini[1], Anna Fontcuberta i Morral[*1]

[1]*Laboratory of Semiconductor Materials, Institute of Materials, École Polytechnique Fédérale de Lausanne, 1015 Lausanne, Switzerland*

S1 Interaction volume

We used the software CASINO[1], to simulate the interaction volume of the primary e-beam in the core-shell NWs. At the experimental voltage of 1.5 KV, the interaction volume is within very few tens of nm from the top NW facet (red-yellow trajectories in figure S1), where the electrons impinge. The further diffusion of excitons from the interaction volume sets the limit of the spatial resolution of CL mapping. However, the diffusion follows an exponential law. Therefore, the luminescence intensity rapidly decreases moving away from the excitation volume. A small interaction volume is guaranteed by a low acceleration of the primary electrons and a few-nm probe. The exciton diffusion lengths range between 500 nm and 2µm[2] and decrease the shorter the exciton lifetime is, like in direct-bandgap AlGaAs and QDs. In fact, we can distinguish few-tens-of-nm large emitters from the CL maps. The filtering of different emission wavelengths provides an additional degree of freedom to differentiate the emitters in space. The overall intensity map is diffusion limited, but the energy-filtered signal can ideally overcome this limit[3].
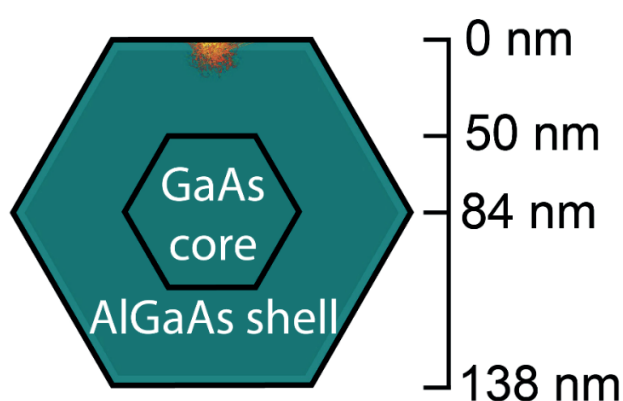

Figure S1. Cross-section of a simulated core-shell NW (green). The scattering event of the primary electrons are highlighted in red-yellow at the top facets.

[1] http://www.gel.usherbrooke.ca/casino/What.html
[2] Zarem et al., APL, **55** 2622 (1989)
[3] Balla et al., ACS Photonics, **4** 292 (2017)

Supporting Information to chapter 4

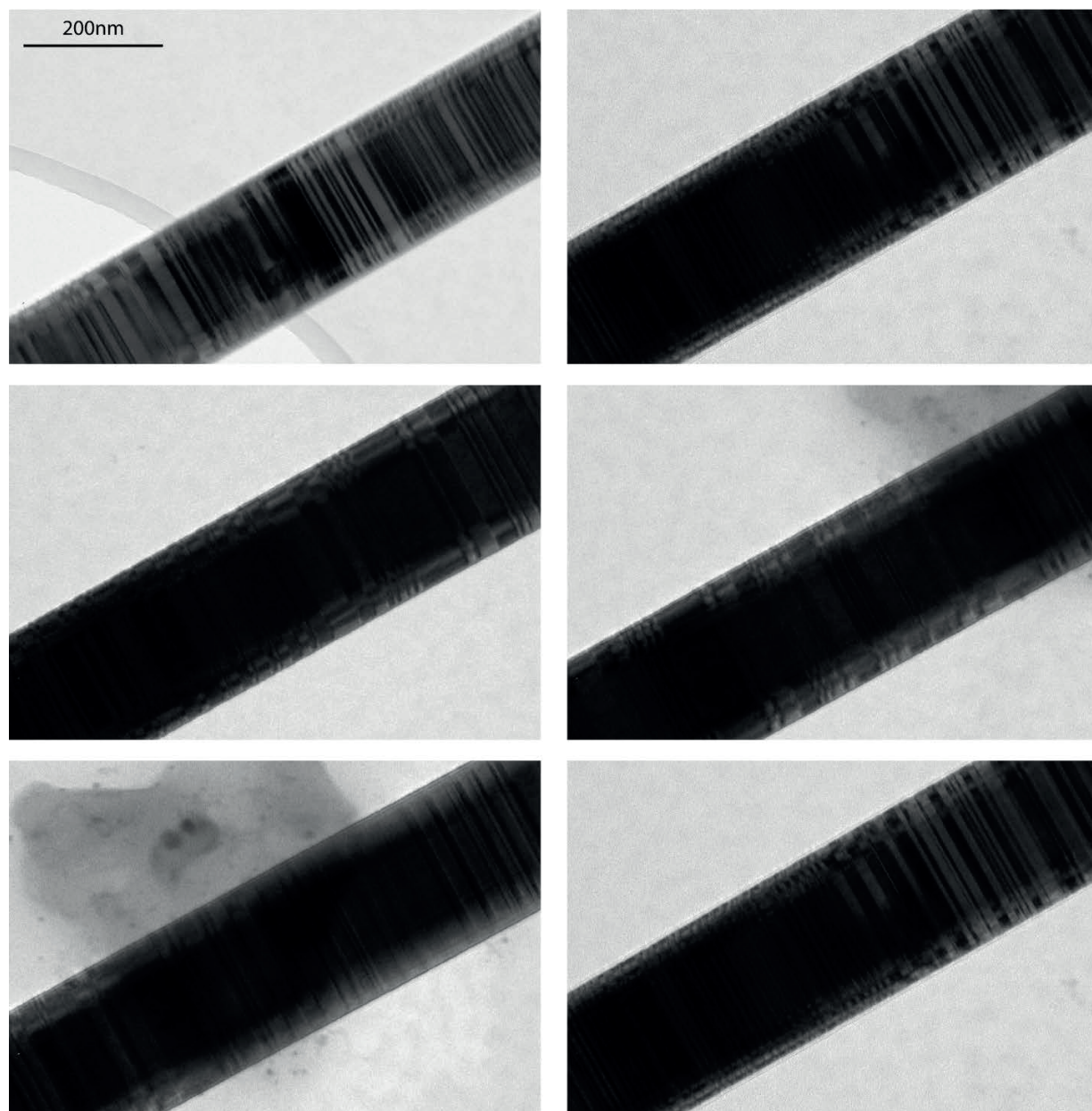## S2 Planar defects at intermediate magnification

Figure S2A. BF TEM micrographs of several positions in the upper part of the NW shown in the manuscript. All images share the same scale bar as the one of the first one at the top left. The contrast reveals a high density of planar defects.
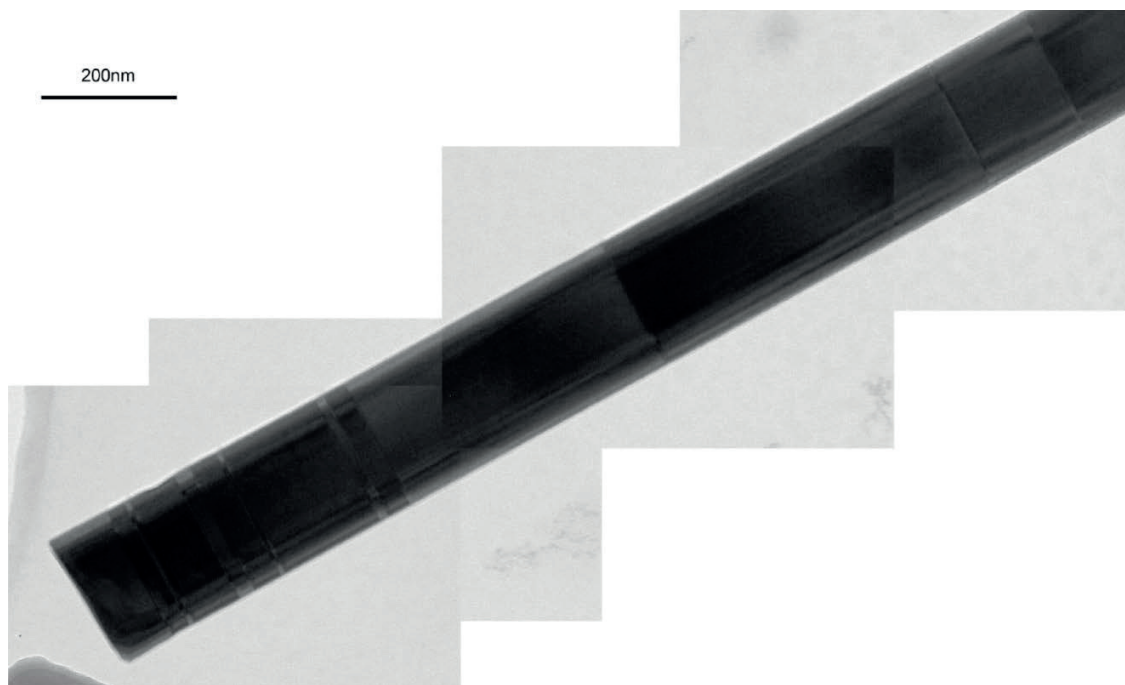
Supporting Information to chapter 4

Figure S2B. Merged BF TEM micrographs of the bottom of the NW shown in the manuscript. The contrast shows almost no defects, except at the very bottom end.

Supporting Information to chapter 4

S3 EDX STEM mapping

We performed X-EDS at the top and bottom of few NWs to check if the Al/Ga ratio changes along the NW. The observed variations (1% less Al from bottom to top) are within the technique accuracy and do not contrast with the hypothesis of the deposition of a constant-composition shell, as further discussed in the manuscript. Yet, we mention that a 1% gradient in the Al content would correspond to a 28 meV redshift.
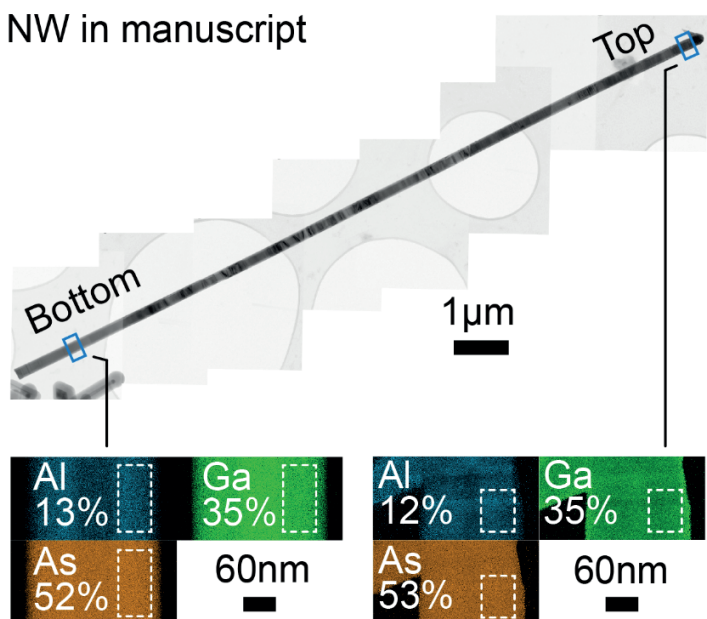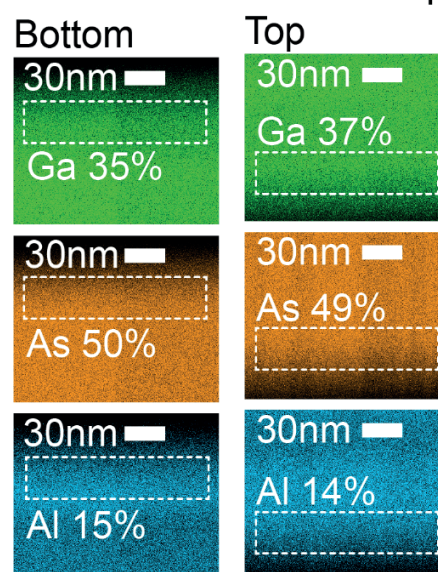

Figure S3. XEDS STEM maps of As, Ga, and Al atomic percentages acquired at the top and bottom of the NW shown in the manuscript and for an additional NW from the same sample. The white dashed rectangles define the regions over which the quantification was performed, in order to exclude counts from the GaAs core.

Supporting Information to chapter 4

S4 Adatom segregation in the AlGaAs shell

The presence of the planar defects perturbs and roughens the chemical potential on the lateral surface of the NWs. The adatoms diffuse along the NW sidewalls during the shell growth following gradients in chemical potential. In particular, in our system the surface chemical potential μ depends on two relevant parameters: the surface energy γ and the surface curvature κ, as summarized by the following equation[4]:

$$\mu = \mu_0 + \Delta\mu_{capillarity} = \Omega(\gamma(\vartheta)+\gamma''(\vartheta))\kappa(z)$$

where Ω is the atomic volume and θ the angle between the facets.
A gradient in chemical potential is responsible for the instauration of net currents of adatoms away from the regions of higher chemical potential, a phenomenon described by the Nernst-Einstein equation:

$$j = -\frac{nD}{kT}\nabla\mu$$

where n is the surface density of atoms, D is the surface diffusion coefficient, k the Boltzmann constant, and T the temperature.

---

[4] Supporting information in M. Heiss et al., Nature Mater. **12**, 439–444 (2013)

Supporting Information to chapter 4

S5 Examples of varying defect density in more NWs

We report TEM images of two more NWs (named A and B) to show that the same increase in defect density is visible while moving from the NW bottom to the top. Like for the NW shown in the manuscript, a defect-free WZ segment forms only at the NW tip.
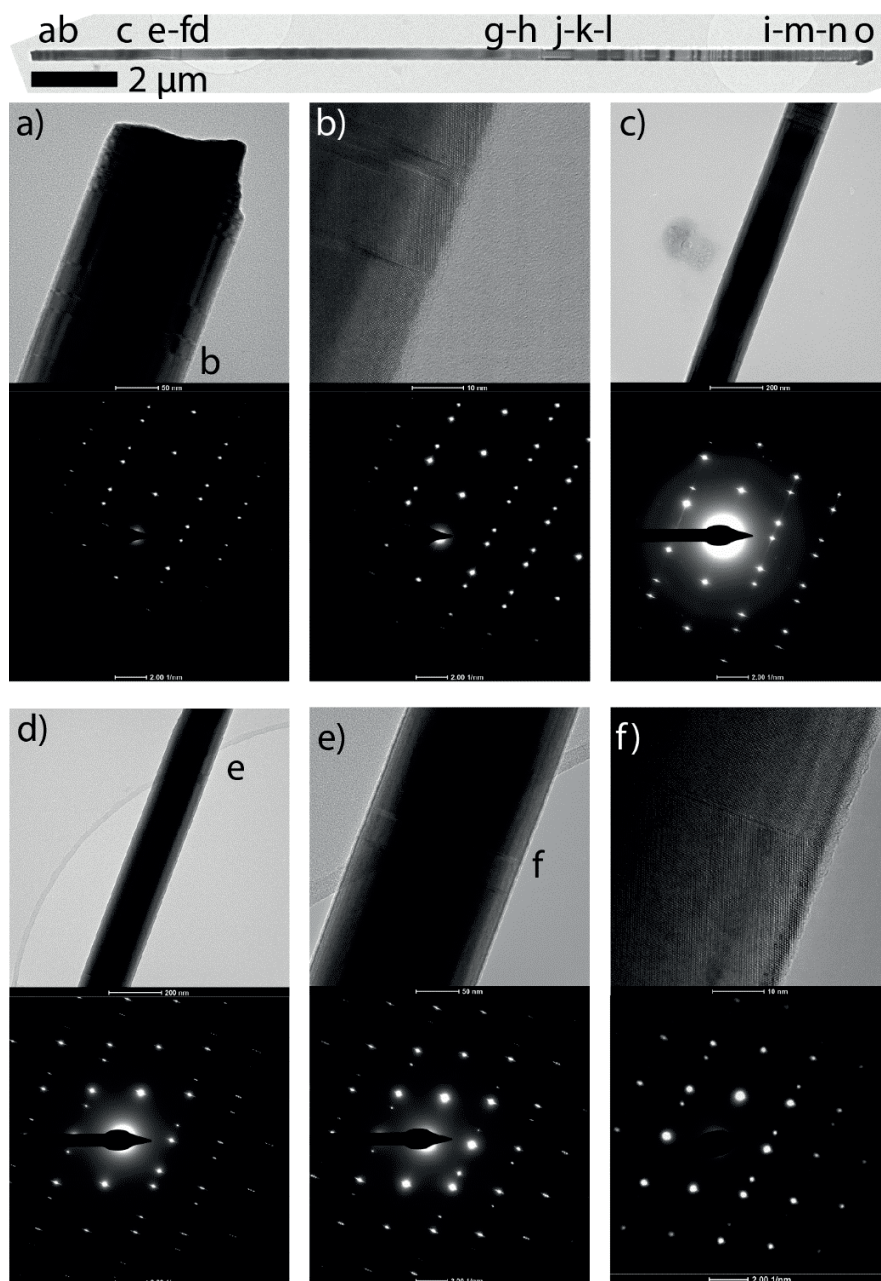

Figure S5A. TEM images and diffraction patterns of NW A.
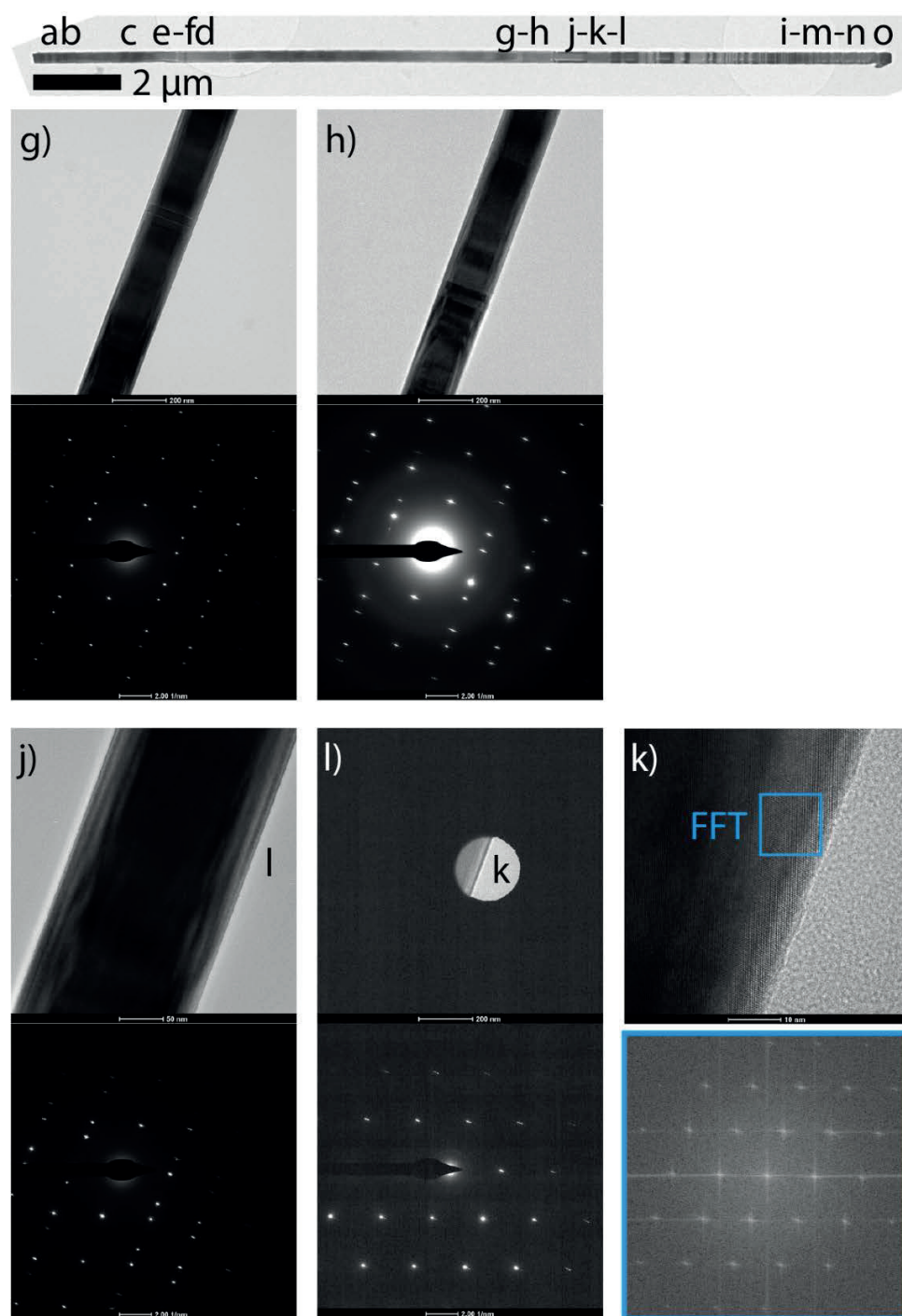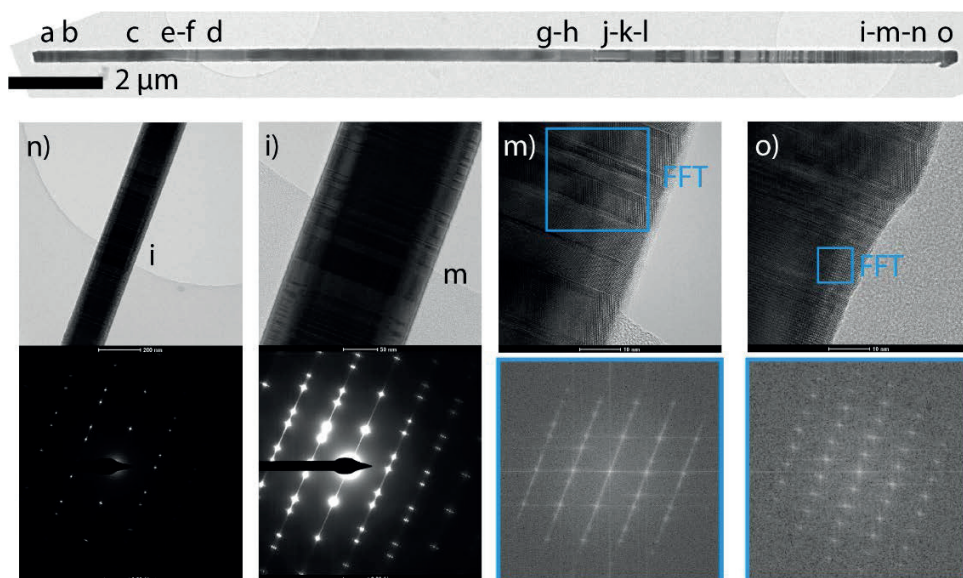
Supporting Information to chapter 4

Figure S5B. TEM images and diffraction patterns of NW A.

Supporting Information to chapter 4

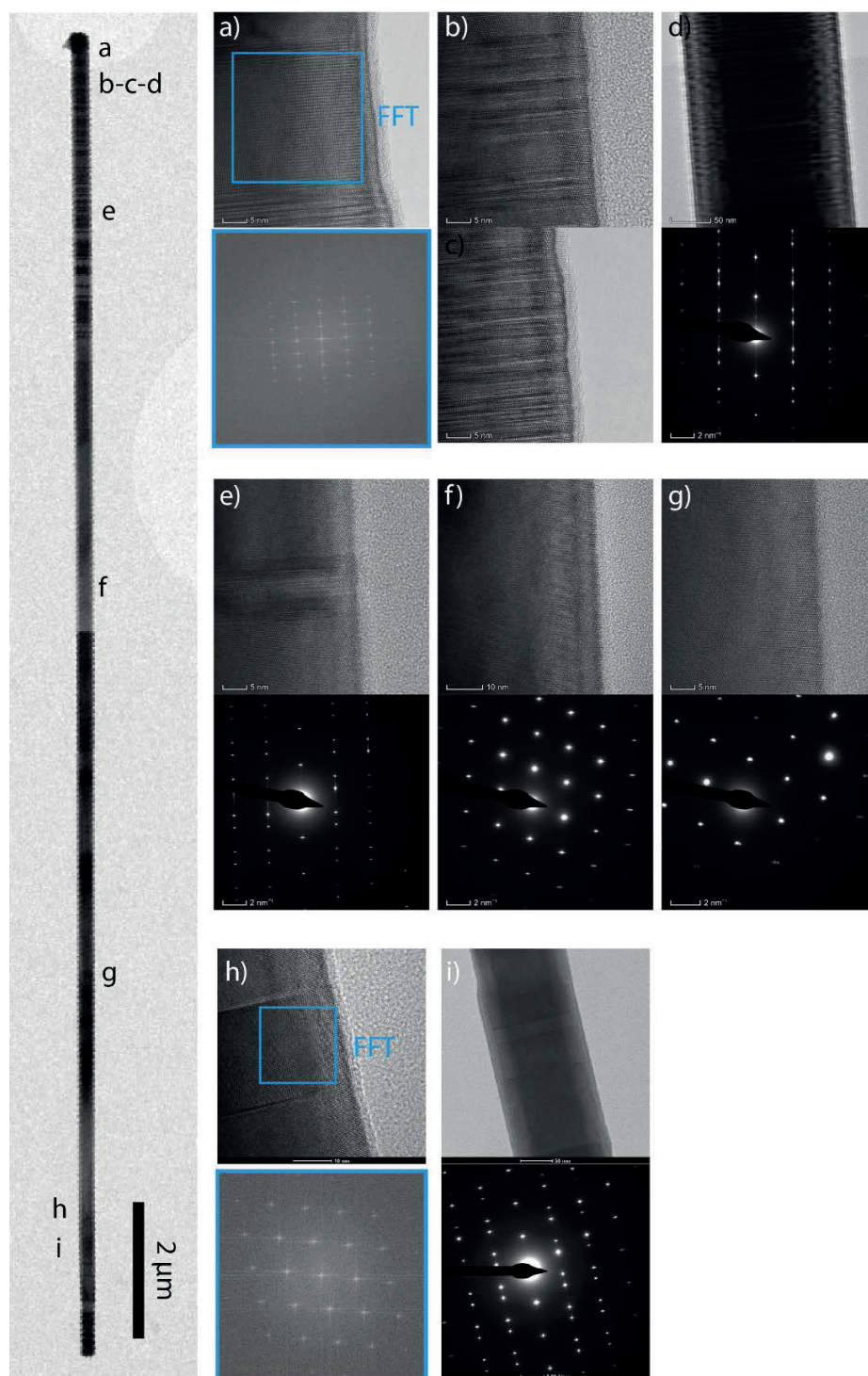*Figure S5C. TEM images and diffraction patterns of NW A.*

Figure S5D. TEM images and diffraction patterns of NW B.

Supporting Information to chapter 4

S6 QD occurrence and energy vs shell thickness

CL maps on NWs with increasing nominal shell thickness reveal an expected increase in QD occurrence. This observation agrees with the same correlation previously obtained by PL[5]. Here, the advantage is that single emitters can be spatially distinguished by using CL. Therefore, the QD count is more accurate.
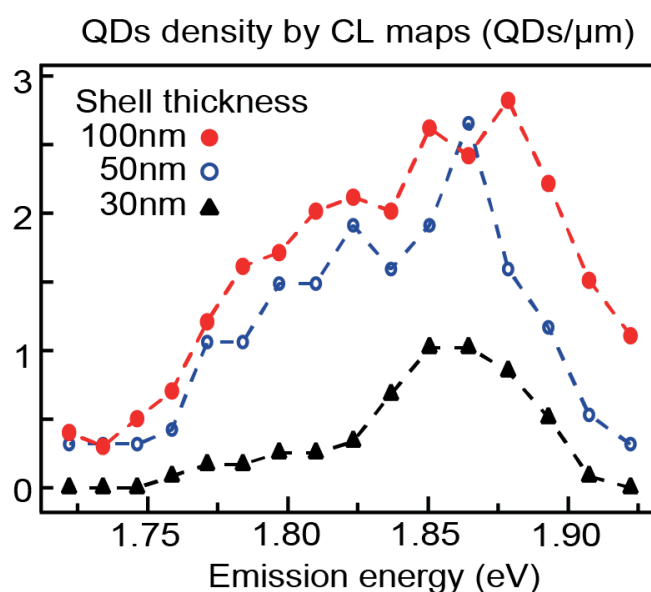

Figure S6. QD occurrence vs emission energy for three NWs of increasing nominal shell thickness (50 nm shell is the same NW shown in the manuscript). The QDs are counted as the single bright spots visible in the acquired maps, while by PL the QDs were counted as peaks appearing in the spectra. This increases the accuracy of the QD count: in addition to the distinction of different emitters by their emission energy, in the CL maps different emitters can be spatially distinguished with higher resolution.

---

[5] Francaviglia et al., APL **107**, 033106 (2015)

Supporting Information to chapter 4

S7 Oblique defects in the NW shell

Interestingly, in more than one NW we found defects not aligned along the radial direction, like those discussed in the manuscript. It was not possible to directly correlate the CL signal with the presence of these defects, but they do not visibly weaken the brightness in the surroundings. The origin of these defects is unknown.
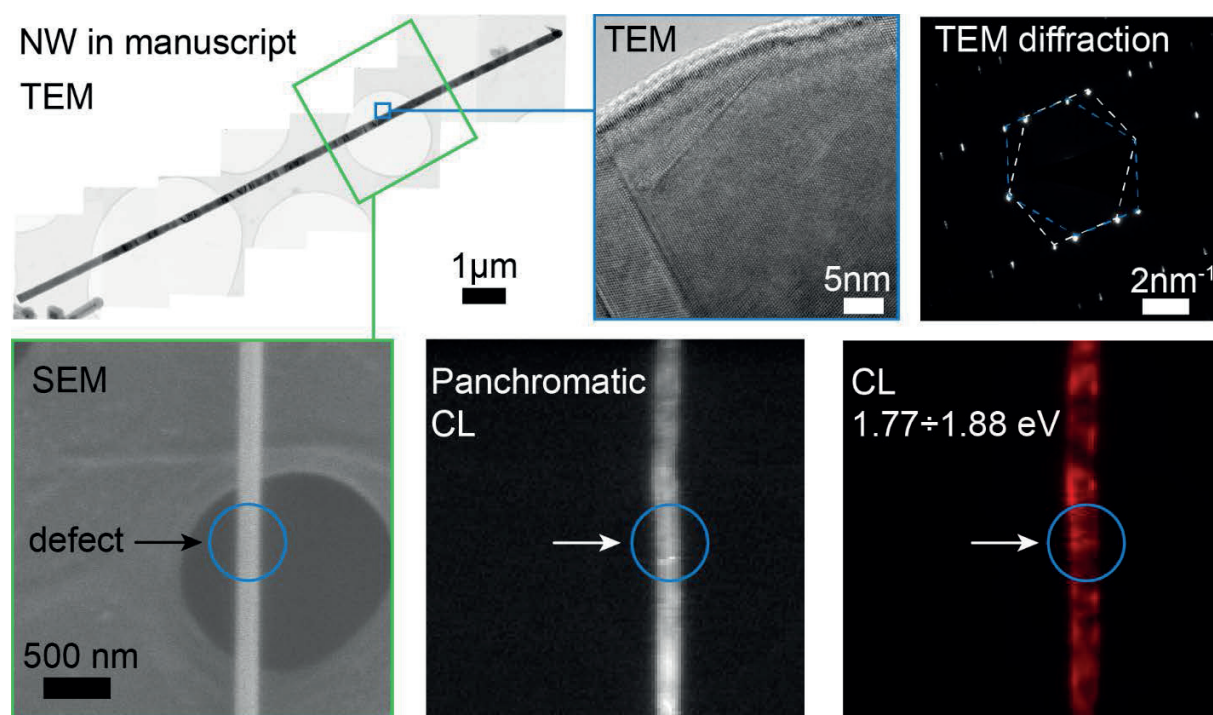

Figure S7-1. TEM images of the same NW as in the manuscript. The zoomed-in region shows an oblique defect. The SEM and SEM CL maps of the corresponding regions of interest on the NWs are reported (panchromatic and for a large bandwidth of 11 meV centered at 1.82 eV). No direct influence of the oblique defect on the CL intensity is visible.
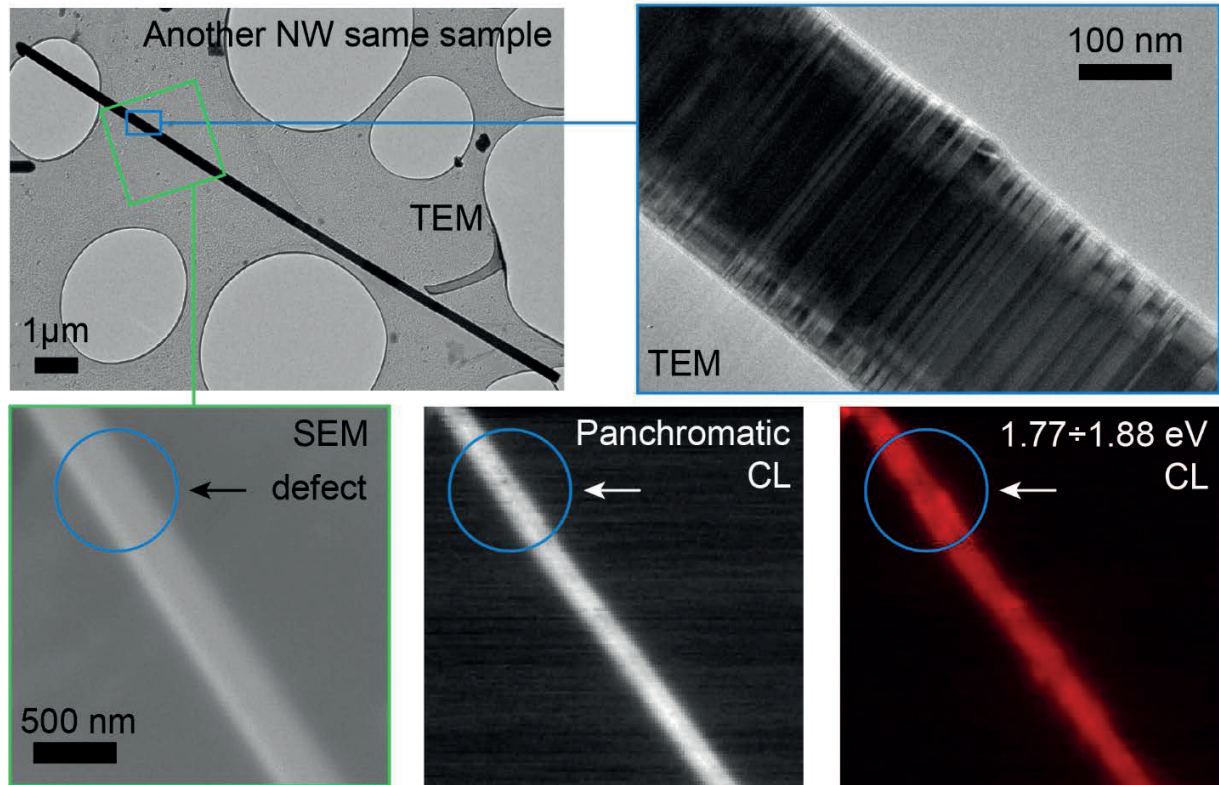
Supporting Information to chapter 4

Figure S7-2. TEM images of another NW from the same sample. The zoomed-in TEM images show an oblique defect. The SEM and SEM CL maps of the corresponding regions of interest on the NWs are reported (panchromatic and for a large bandwidth of 11 meV centered at 1.82 eV). No direct influence of the oblique defect on the CL intensity is visible.

Supporting Information to chapter 4

S8 Nextnano simulations

We ran Nextnano simulations for the same QD configurations as in the manuscript. Here we report the results for different WZ band offsets available in the literature[6]. They show the same trend of decreasing emission energy for an increasing WZ content and electron-hole separation. The red squares corresponds to the results for the largest band offset. In this case, the contribution of the electron-hole separation to the overall energy reduction is more important.
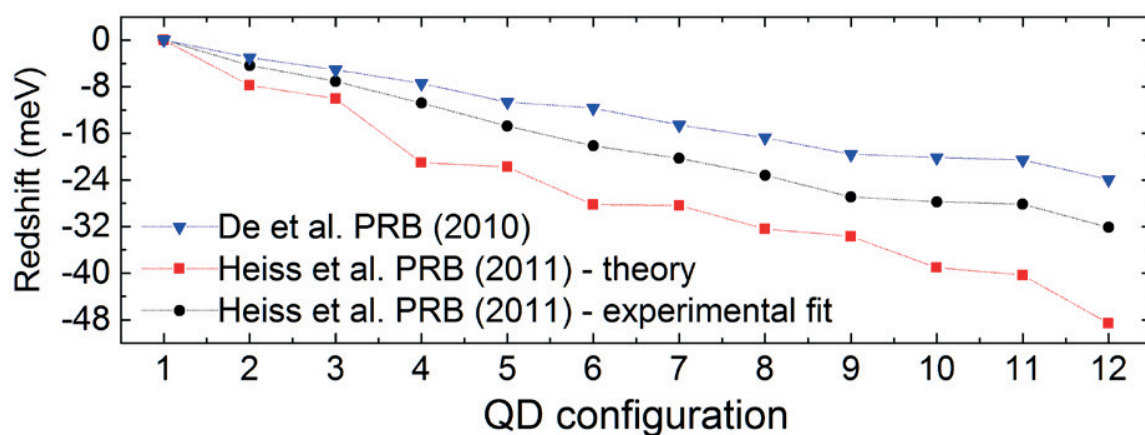

Figure S8. Exciton recombination energy according to the Nextnano simulations. The WZ band offset is set according to the values available in the literature, as indicated in the legend.

---

[6] De at al., PRB **81**, 155210 (2010) and Heiss et al., PRB **83**, 045303 (2011)

Supporting Information to chapter 4

S9 NW linescans: PL vs CL

CL and PL agree about the counting of the QD occurrence and the average QD emission energy. The peak count in PL spectra with many peaks tend to saturate because of the spectral overlap between peaks next to each other. This may explain the higher QD occurrence observed by CL at the NW top, where the QD density is at the maximum: in the CL maps, different peaks at similar energies can be distinguished in space. On the contrary, the QD occurrence observed by CL is lower at the NW bottom, where the QD density is at the minimum: because of lower spatial resolution, PL may count the same emitters more times in few spectra.
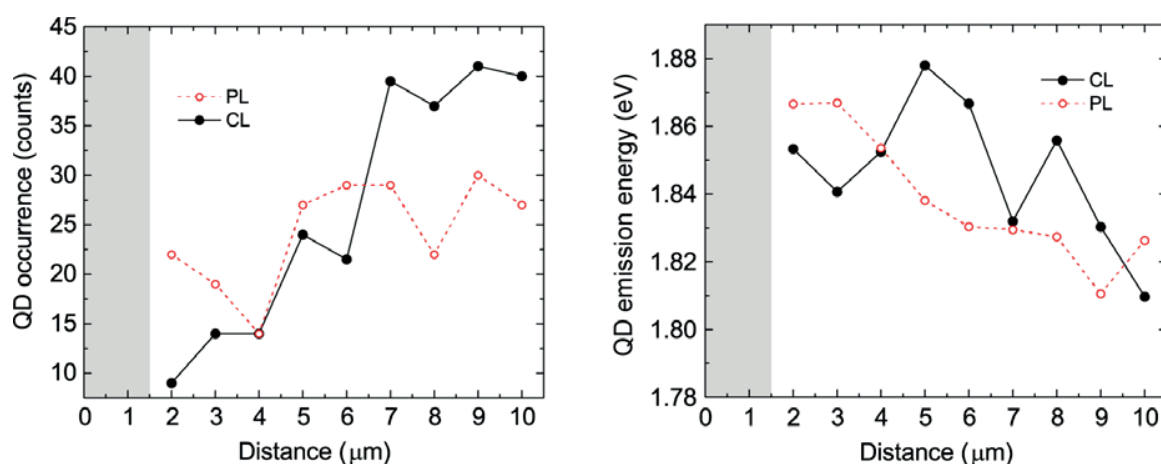

Figure S9. CL (black, full circles) and PL (red, open circles) linescans along the same NW as the one shown in the manuscript. On the left, we report the QD occurrence vs NW position; on the right, we report the QD emission energy vs NW position. The data are taken (PL) or averaged (CL) over 1µm steps. The gray band corresponds to the NW bottom hidden by the carbon film.

Supporting Information to chapter 4

S10 CL maps of additional NWs

In the following we report the CL maps for three NWs of increasing nominal shell thickness (30 nm, 50 nm and 100 nm), including the full set of maps of the NW shown in the manuscript (50 nm shell). In all the samples we observed and increase in the twin density towards the NW top. The most evident correlation between twins density and QD redshift stems from the 50 nm shell NWs.
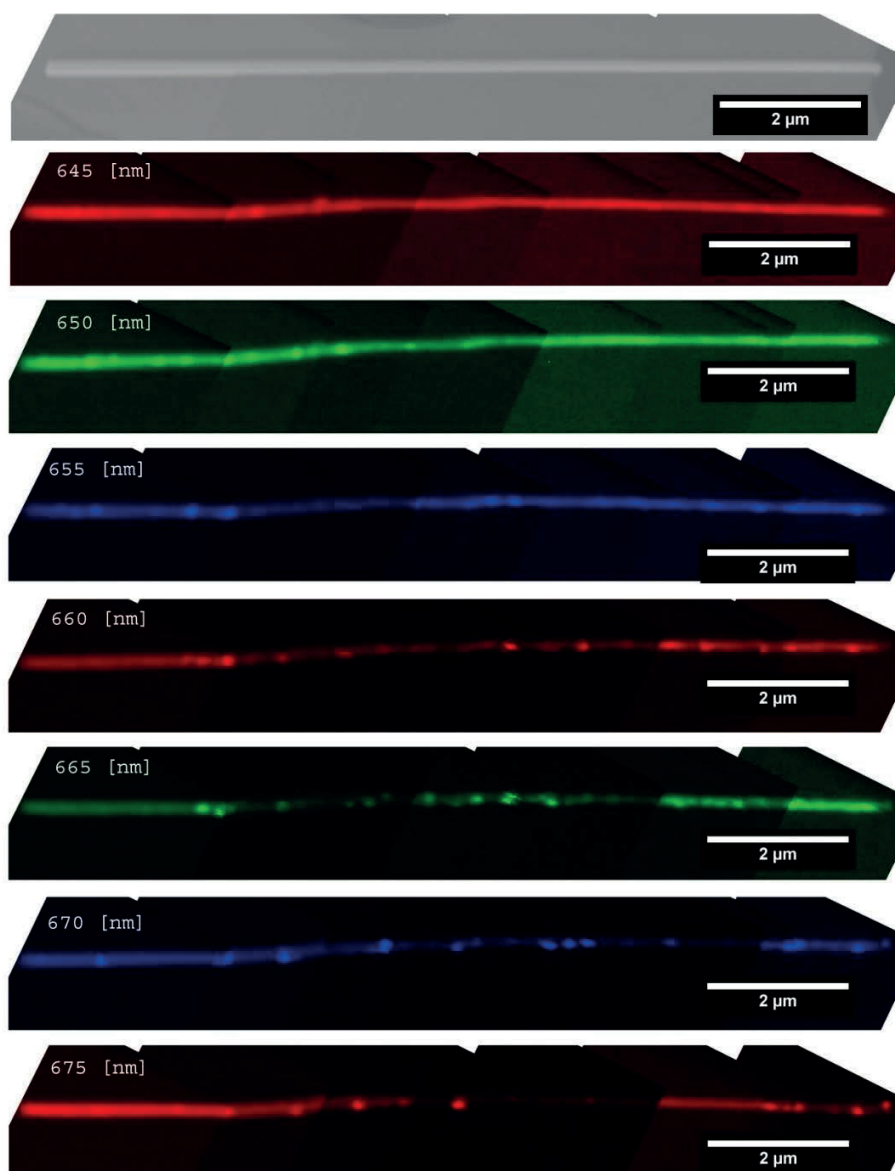
Supporting Information to chapter 4

Figure S10A. CL maps of a 30 nm shell NW. The different wavelengths are highlighted in 5 nm intervals. The first image of the series is the SEM image of the NW.

645 [nm]

650 [nm]

655 [nm]

660 [nm]

665 [nm]

670 [nm]

675 [nm]

Supporting Information to chapter 4

Figure S10B. CL maps of a 50 nm shell NW. The different wavelengths are highlighted in 5 nm intervals. The first image of the series is the SEM image of the NW.

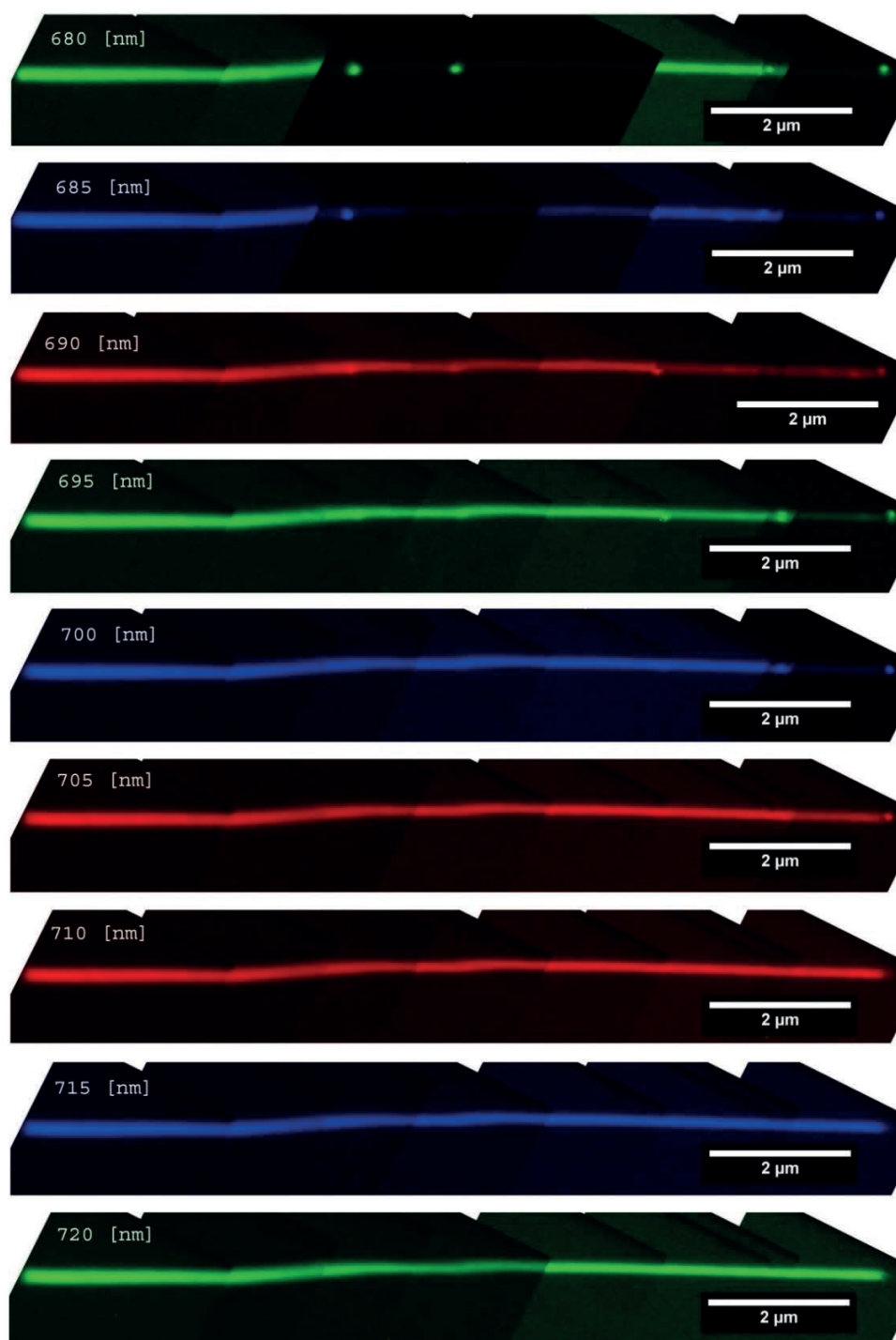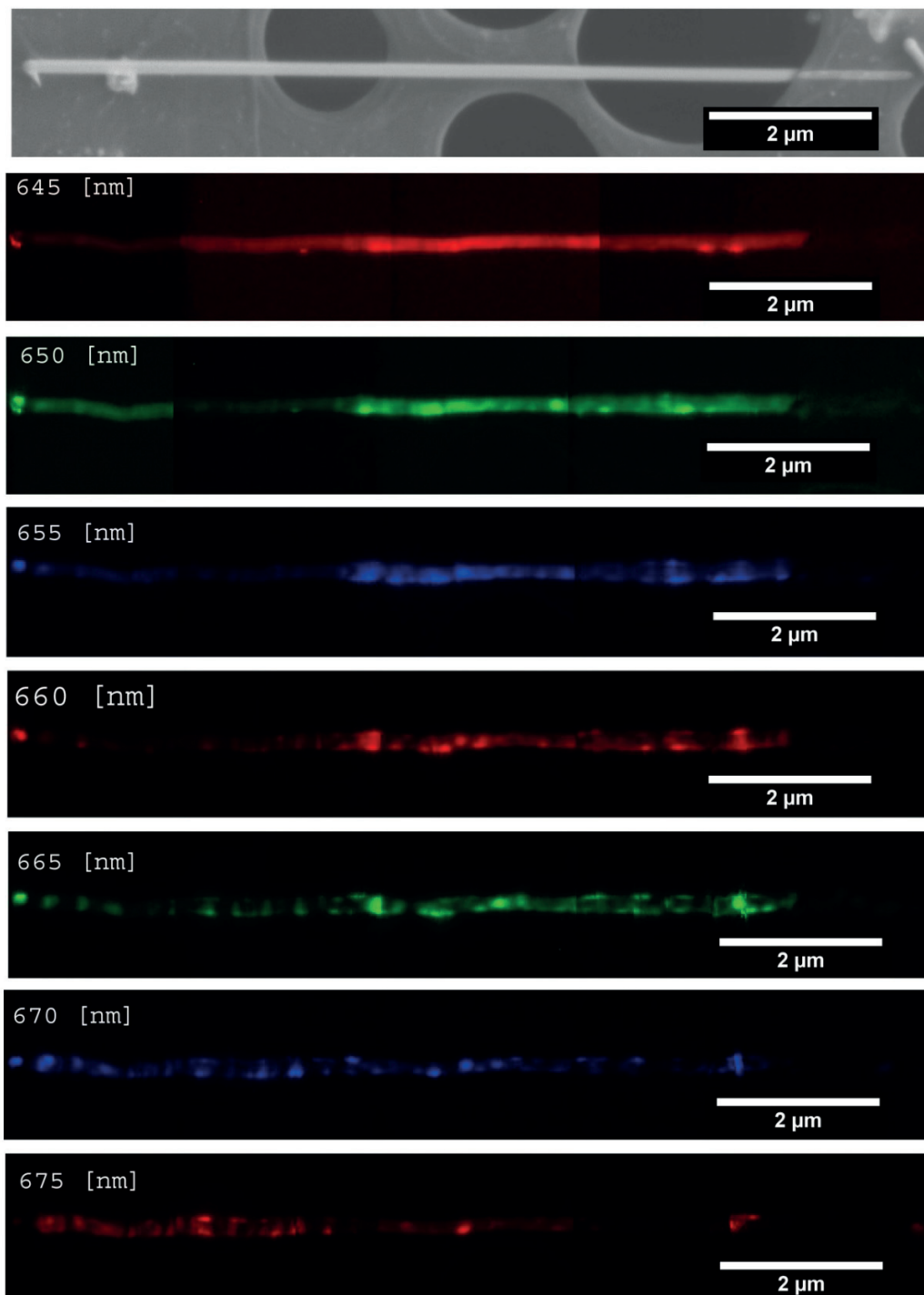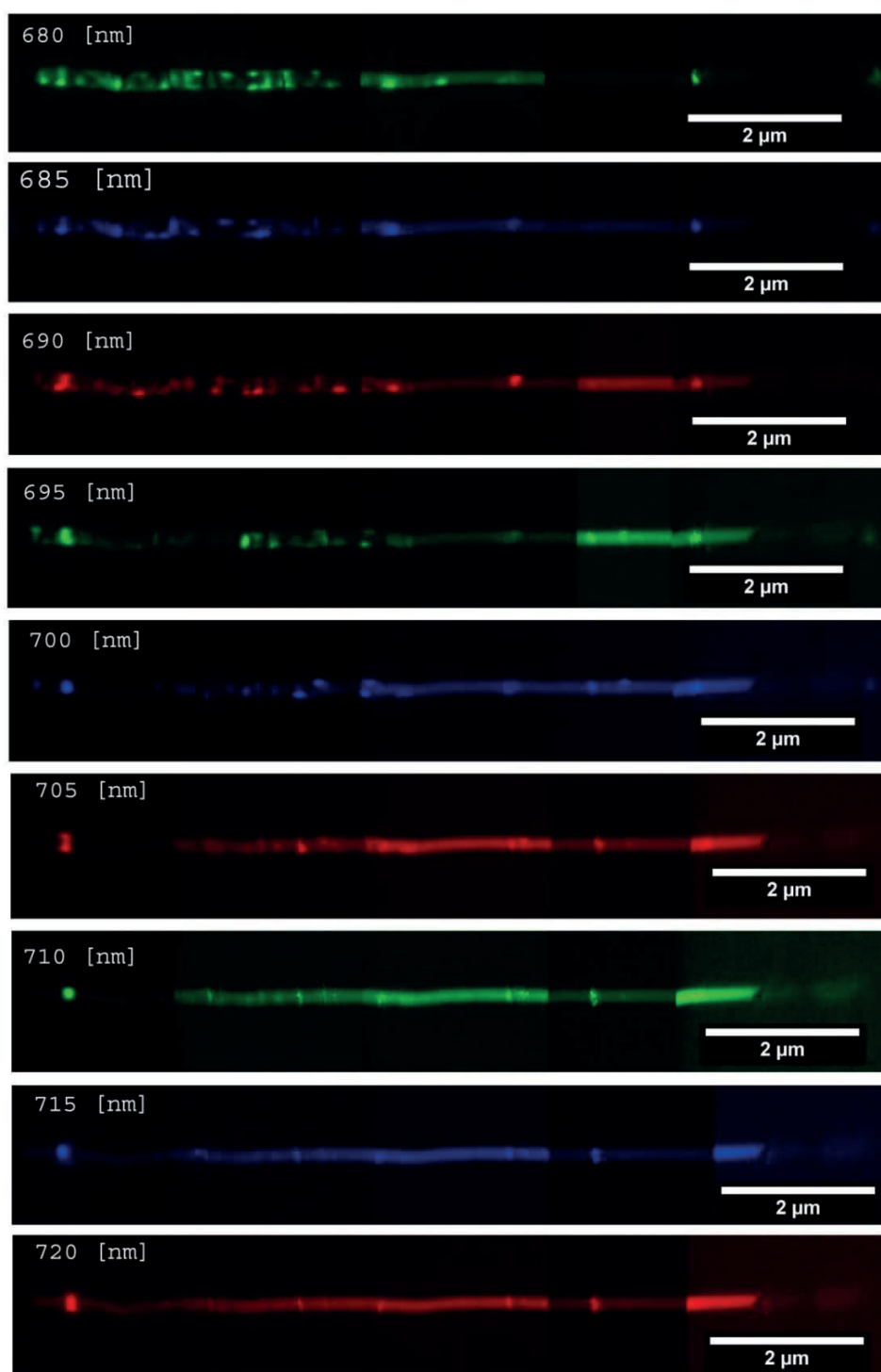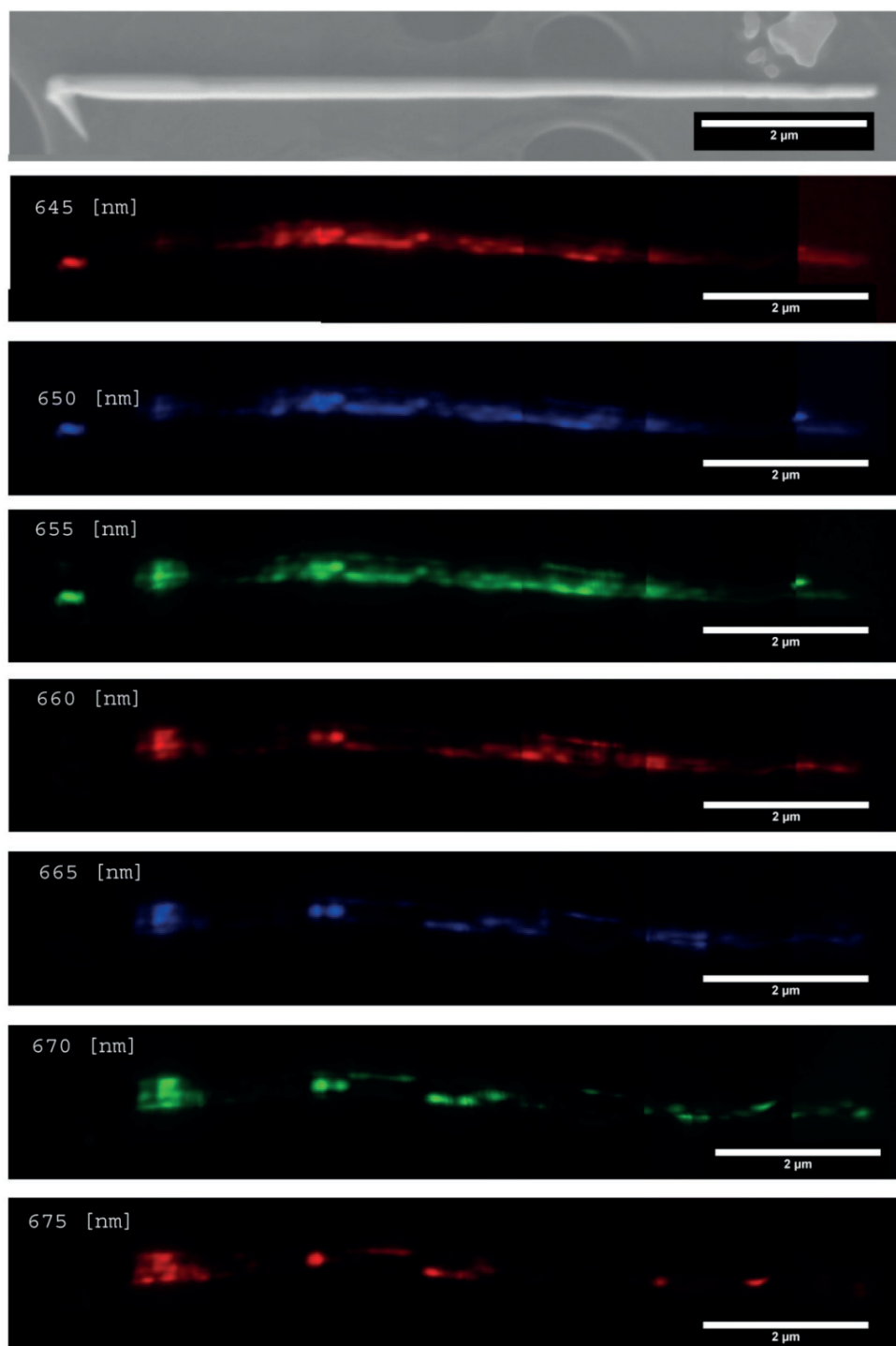# Supporting Information to chapter 4
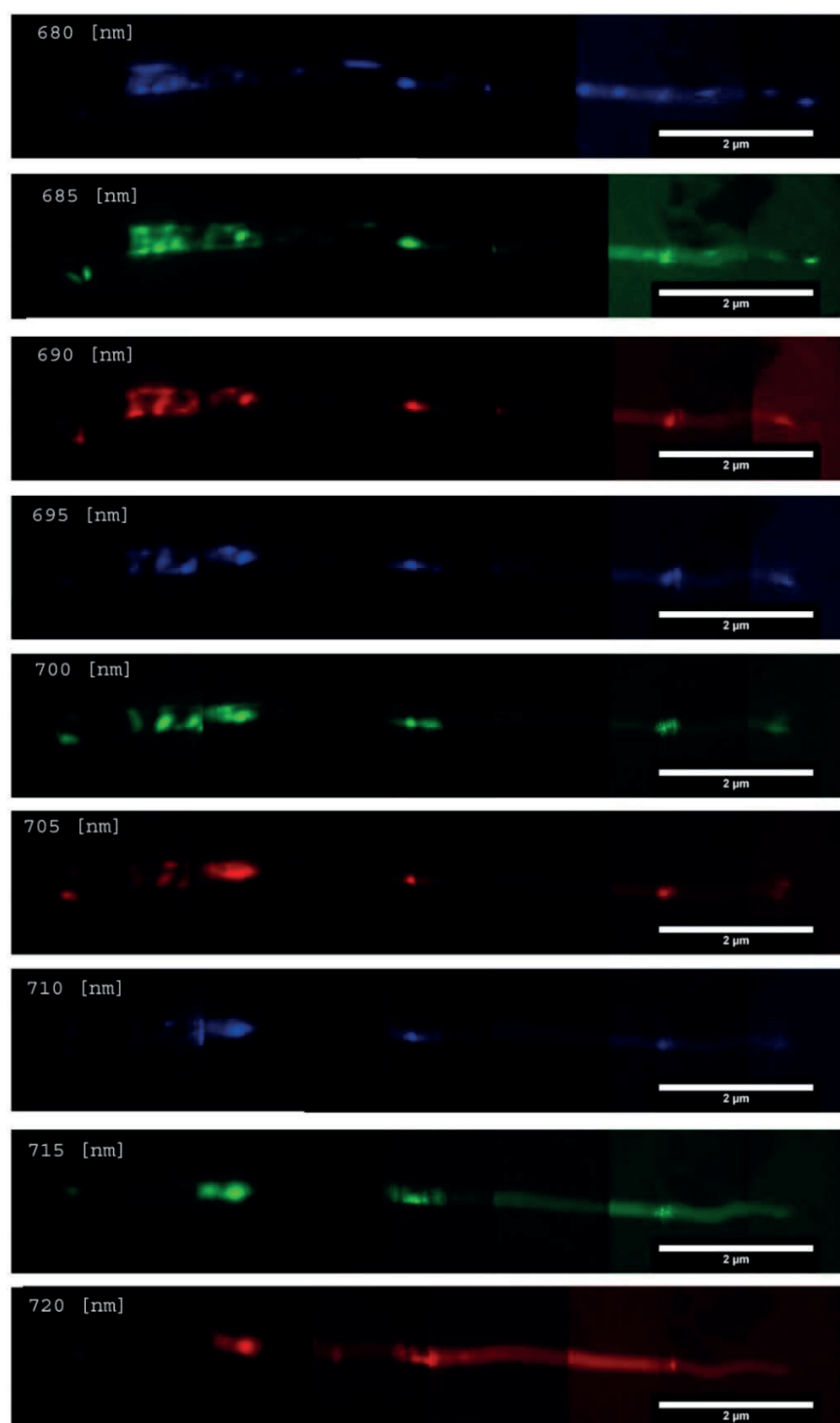
Figure S10C. CL maps of a 100 nm shell NW. The different wavelengths are highlighted in 5 nm intervals. The first image of the series is the SEM image of the NW.

Supporting Information to chapter 5

Anisotropic-strain-induced bandgap engineering
in nanowire-based quantum dots

Luca Francaviglia[1*], Andrea Giunto[1*], Wonjong Kim[1], Pablo Romero[1], Jelena Vukajlovic-Plestina[1],
Martin Friedl[1], Heidi Potts[1], Lucas Güniat[1], Gözde Tütüncüoglu[1], Anna Fontcuberta i Morral[1]

[1]*Laboratory of Semiconductor Materials, Institute of Materials, École Polytechnique Fédérale de
Lausanne, 1015 Lausanne, Switzerland*
*Equal contribution

SI1 Conformal SiO$_2$ PECVD

The PECVD of SiO$_2$ follows precisely the shape of the underlying NW. The oxide thickness is not
constant.
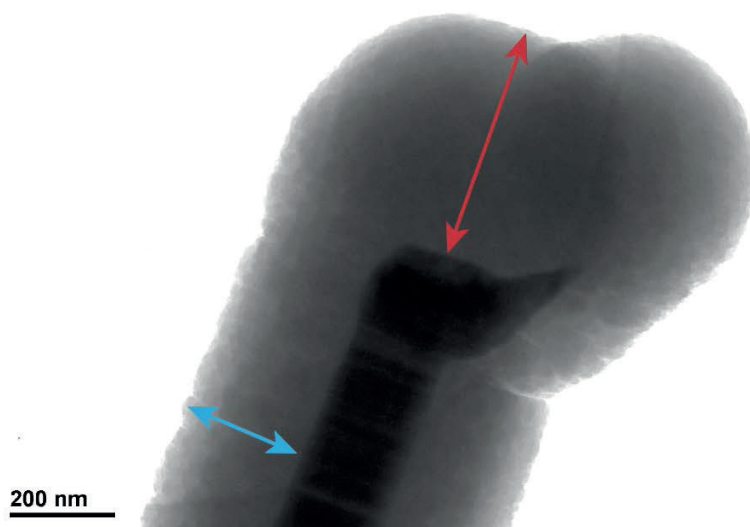
*Figure 1. TEM micrograph of the top of a core-shell GaAs-AlGaAs NW coated with SiO$_2$ by PECVD. The
average oxide thickness on the sidewalls is 226 nm (blue arrow) and on the "head" is 434nm (red arrow).*

Supporting Information to chapter 5

SI2 Calibration of the nominal-vs-real oxide thickness

We acquired TEM images of 6 NWs for each SiO_2 deposition, like in SI1, from different positions along each single NW: top sidewalls and head (like in SI1) and at the sidewalls in the middle and at the bottom of the NW. From the images we calculated the average oxide thickness. At the head and top positions the nominal-vs-measured curve of the oxide thickness follows a linear trend. Shadowing among neighbor NWs saturates the trend for thicker oxides at the middle and bottom positions along the NWs.
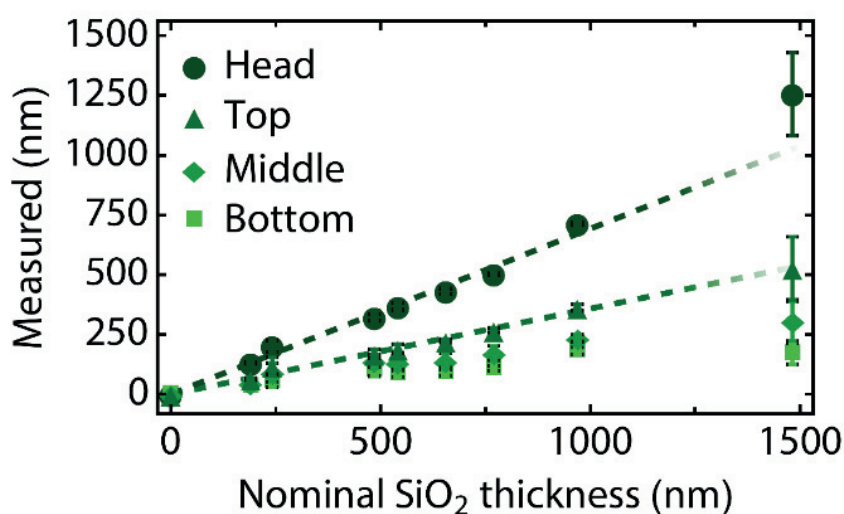
Figure 2. Graph of the average oxide thickness as measured from TEM micrographs vs the nominal one for four different positions along the NWs.

Supporting Information to chapter 5

SI3 Oxide structure

TEM images reveal the grain structure of the oxide. At any temperature the grains align along the direction of impingement of the atoms and ions. This effect is more evident in the depositions at lower temperature (100°C) because of the enhanced visibility of the grains with respect to the reference deposition at 300°C. The tilted alignment of the grains may enhance the anisotropy of the applied stress. The deposition at low temperature produces a less coherent oxide than the one obtained at 300°C.
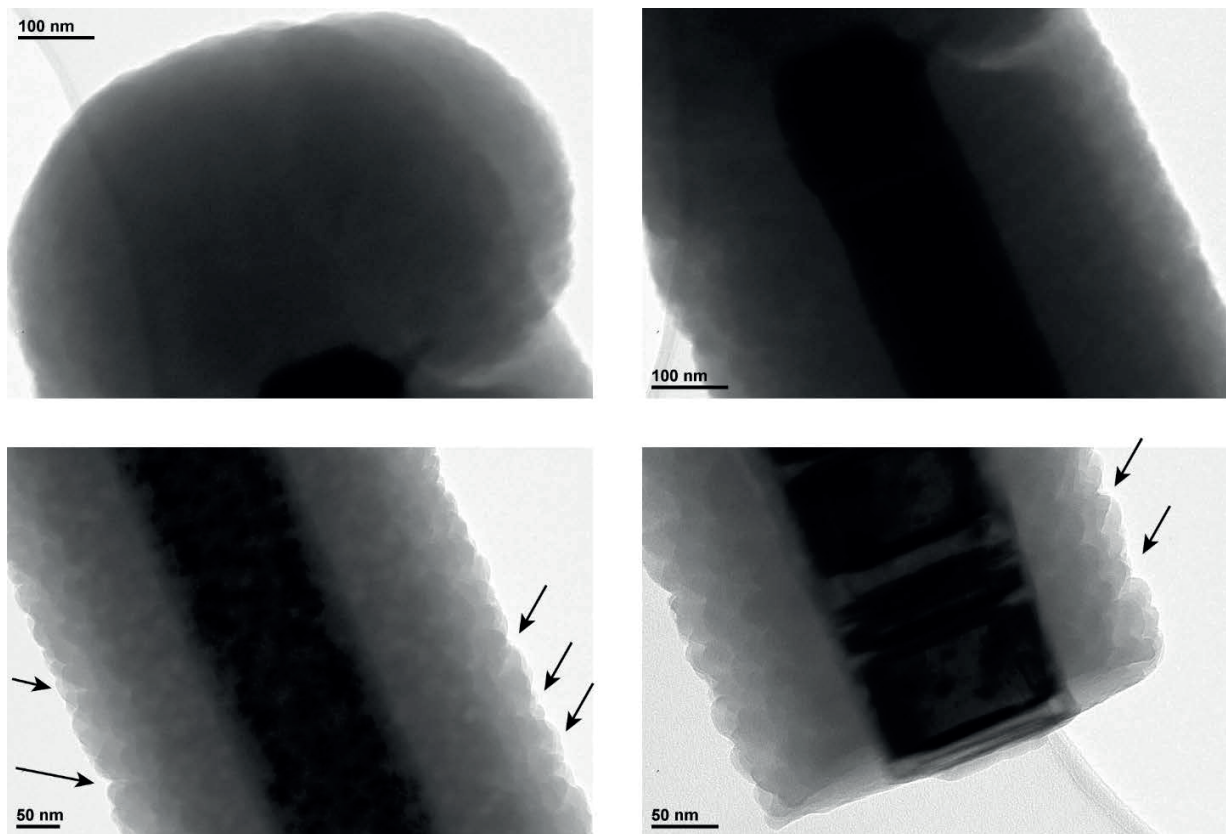
Figure 3. TEM micrographs of different positions along a NW coated with SiO$_2$ at 300°C. The oxide structure is grainy and the grains are aligned along the probable direction of impingement of the atoms and ions during the PECVD. The arrows hint this tilted direction.

Supporting Information to chapter 5
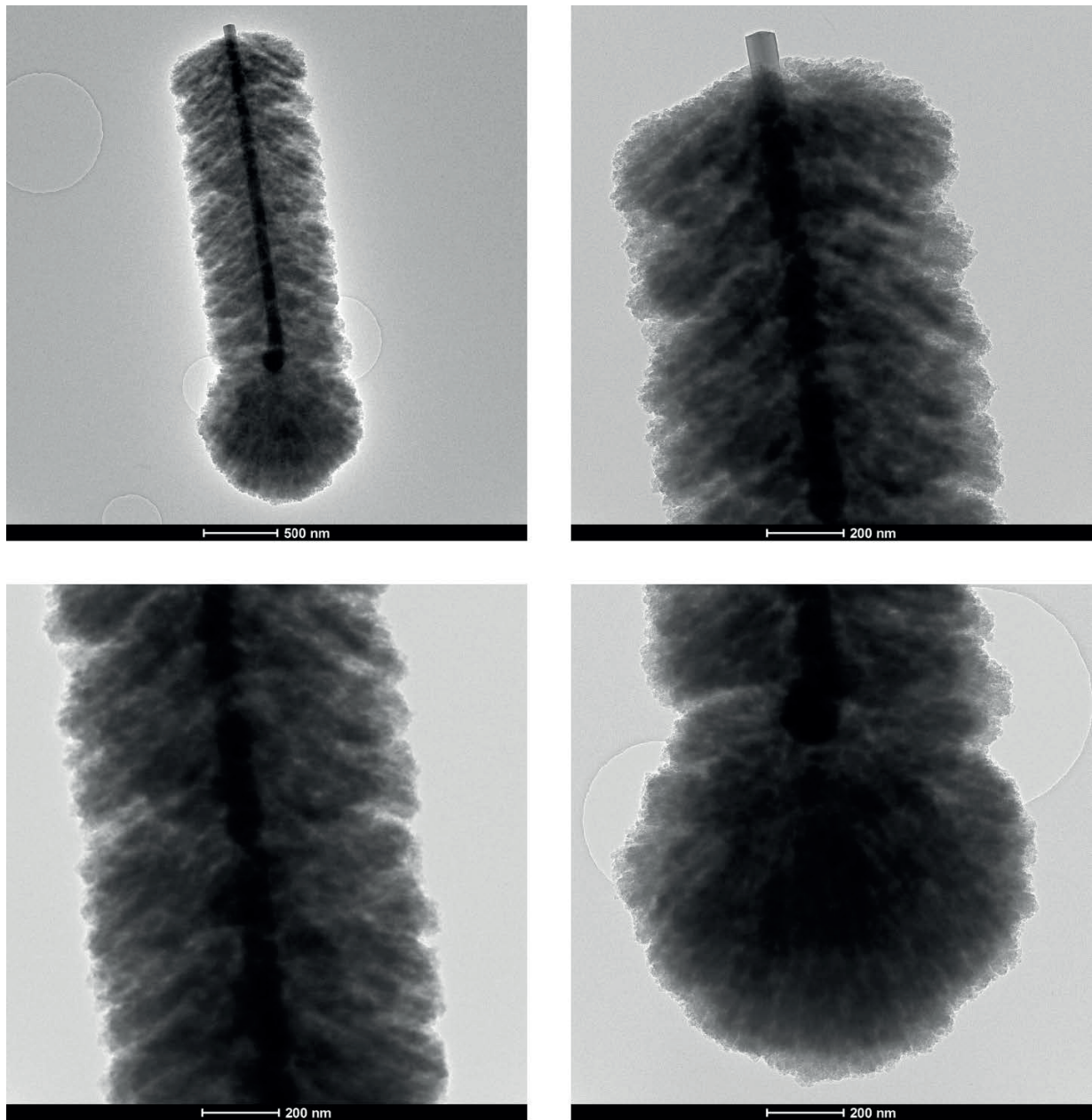
Figure 4. TEM micrographs of different positions along a NW coated with SiO_2 at 100°C. The oxide structure is grainy and the grains are aligned along the probable direction of impingement of the atoms and ions during the PECVD.

Supporting Information to chapter 5

SI4 Raman vs oxide on NW ensembles: all the peaks

We report the Raman shift vs the oxide thickness for all the visible modes. They all downshift for an increasing thickness of the oxide.
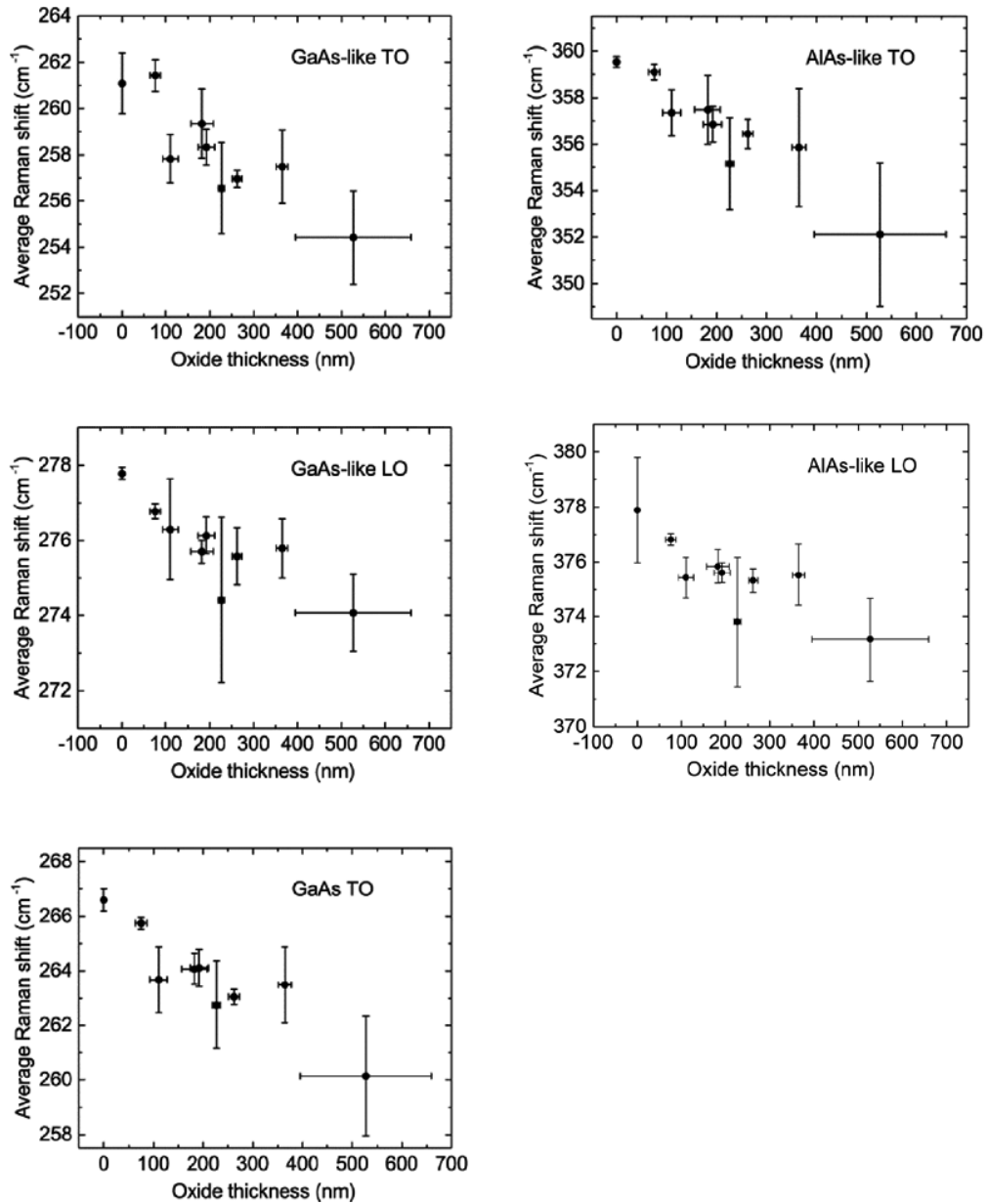
Figure 5. Average Raman shift vs oxide thickness for all the visible modes.

Supporting Information to chapter 5

SI5 Raman 100°C SiO$_2$ PECVD

These Raman spectra illustrate that for this NW the strain is compressive for both TO and LO peaks (upshift) by SiO2 PECVD coating at 100°C. The SO peaks show a downshift due to the increase in dielectric constant of the surrounding medium. Compressive strain is never observed after coating at higher temperatures.
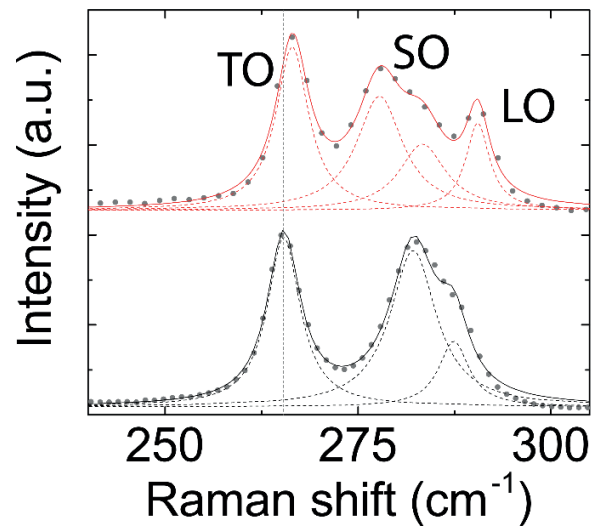
Figure 6. Raman spectra of an uncoated vertical NW and the same NW coated with SiO$_2$. We performed the PECVD at 100°C

Supporting Information to chapter 5

SI6 PL blueshift by TiO2 sputtering

The TiO$_2$ sputtering blueshifts the PL emission of the GaAs NW.
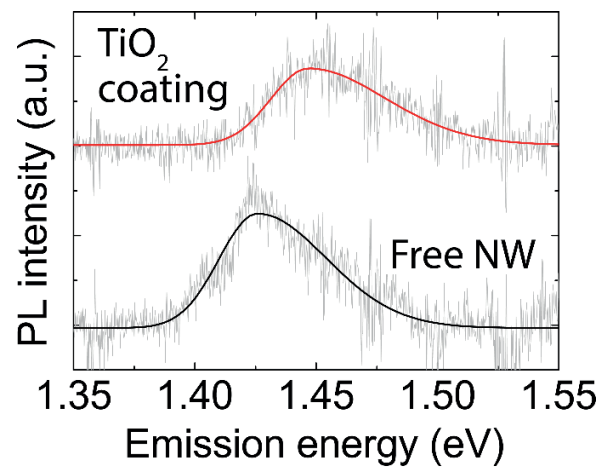
Figure 7. Room-temperature PL spectra of the same vertical array NW before and after coating with TiO$_2$ by sputtering.

Supporting Information to chapter 5

SI7 SiO$_2$ debris

The grains of the SiO$_2$ deposited at 100°C are loosely connected with each other, as demonstrated by gaps among them and by the pieces of oxide found around the NWs on the TEM grid.
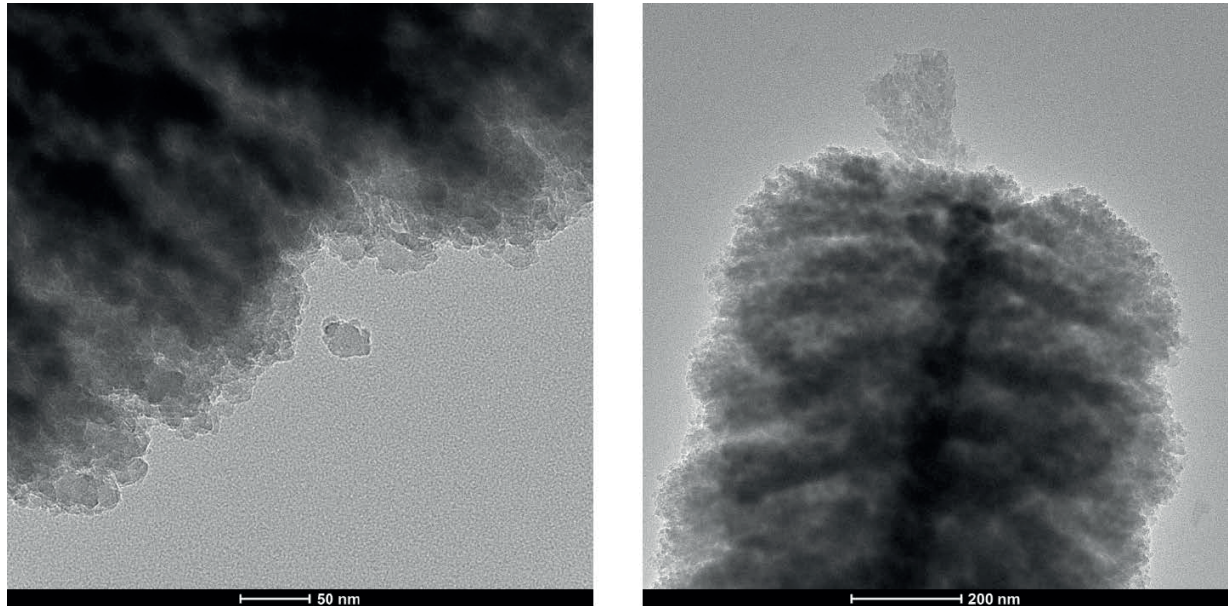
Figure 8. TEM micrographs of array NWs coated with SiO$_2$ at 100°C. Exfoliation and damage of the oxide is visible on the carbon film of the TEM grid as a consequence of the transfer of the NW for the TEM observation.

Supporting Information to chapter 5

SI8 Temperature-dependent Raman spectroscopy

Average difference in the position of the Raman modes of three uncoated NWs and three NWs coated with 365 nm of SiO$_2$. The positive values correspond with the fact that at all temperatures the coated NWs are under tensile strain. By increasing the temperature of the measurements, the spread between the coated and uncoated NWs increase. This agrees with the fact that the difference in TEC has not a pronounced contribution to strain the NWs.
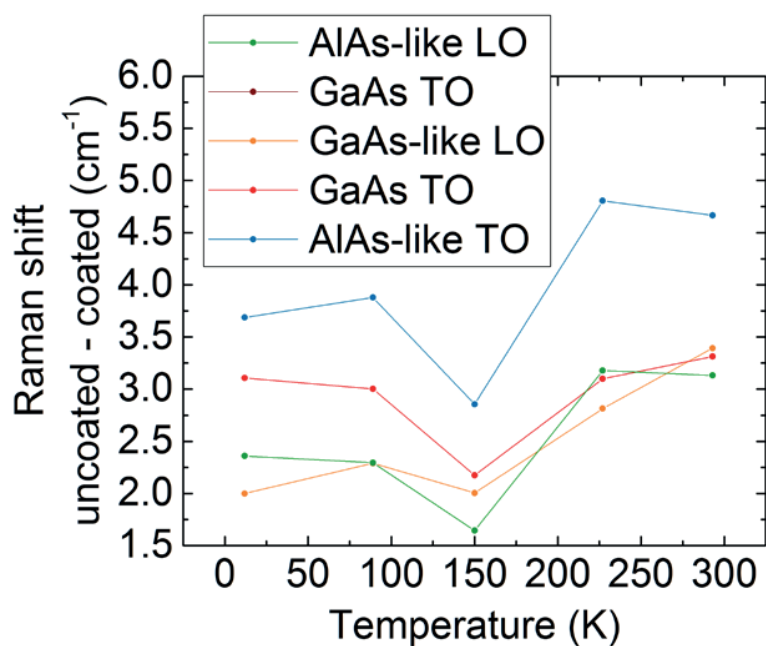
Figure 9. Differential Raman modes vs the measurement temperature. The differential Raman modes are calculated by difference between the average Raman mode of three uncoated NWs – the average Raman mode of three NWs coated with 365 nm of oxide.

Supporting Information to chapter 5

SI9 Raman intensity

The brightness of the micro-PL and micro-Raman signals increases for an increasing thickness of the deposited oxide. This positive trend is useful and may deserve further study in future. We believe that the SiO_2 coating smoothens the gradient in refractive index between the vacuum and the semiconductor NW. For very thick depositions, it is easier to miss the NW with the laser spot. The thick oxide may be misleading by hiding the real position of the NW: the laser is focused on the oxide-NW structure, but outside the NW itself. We take this explanation into account for the reduction of the brightness in the thickest sample. In this last case, the signal is still brighter than in the case of the uncoated NWs.
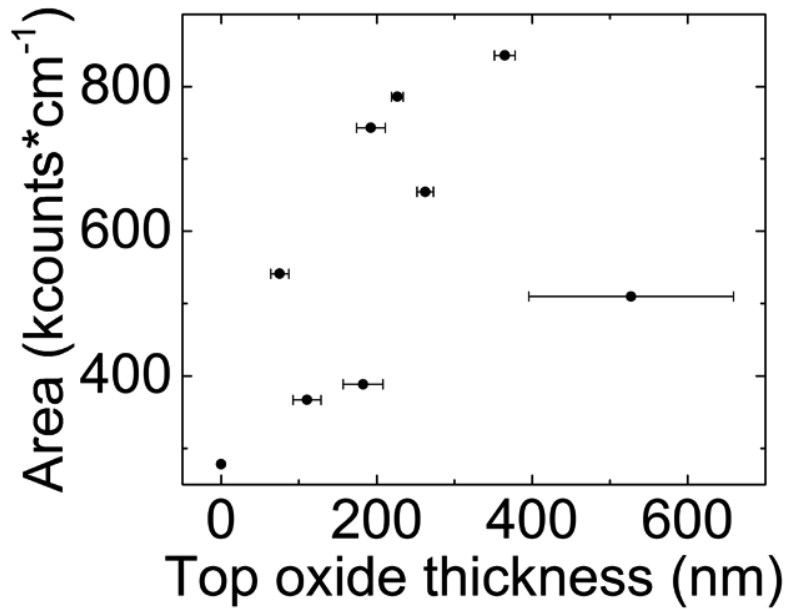
Figure 10. Sum of the area below all the Lorentzian fits of the Raman modes vs oxide thickness. All the spectra were acquired with the same integration time of 30 minutes.

Supporting Information to chapter 5

SI10 Polarization-dependent Raman spectroscopy

We acquired polarization-dependent Raman spectra of few NWs to demonstrate the consistent shift between the parallel and perpendicular configurations in the case of the coated NWs. On the contrary, the uncoated NWs do not show any consistent shift.
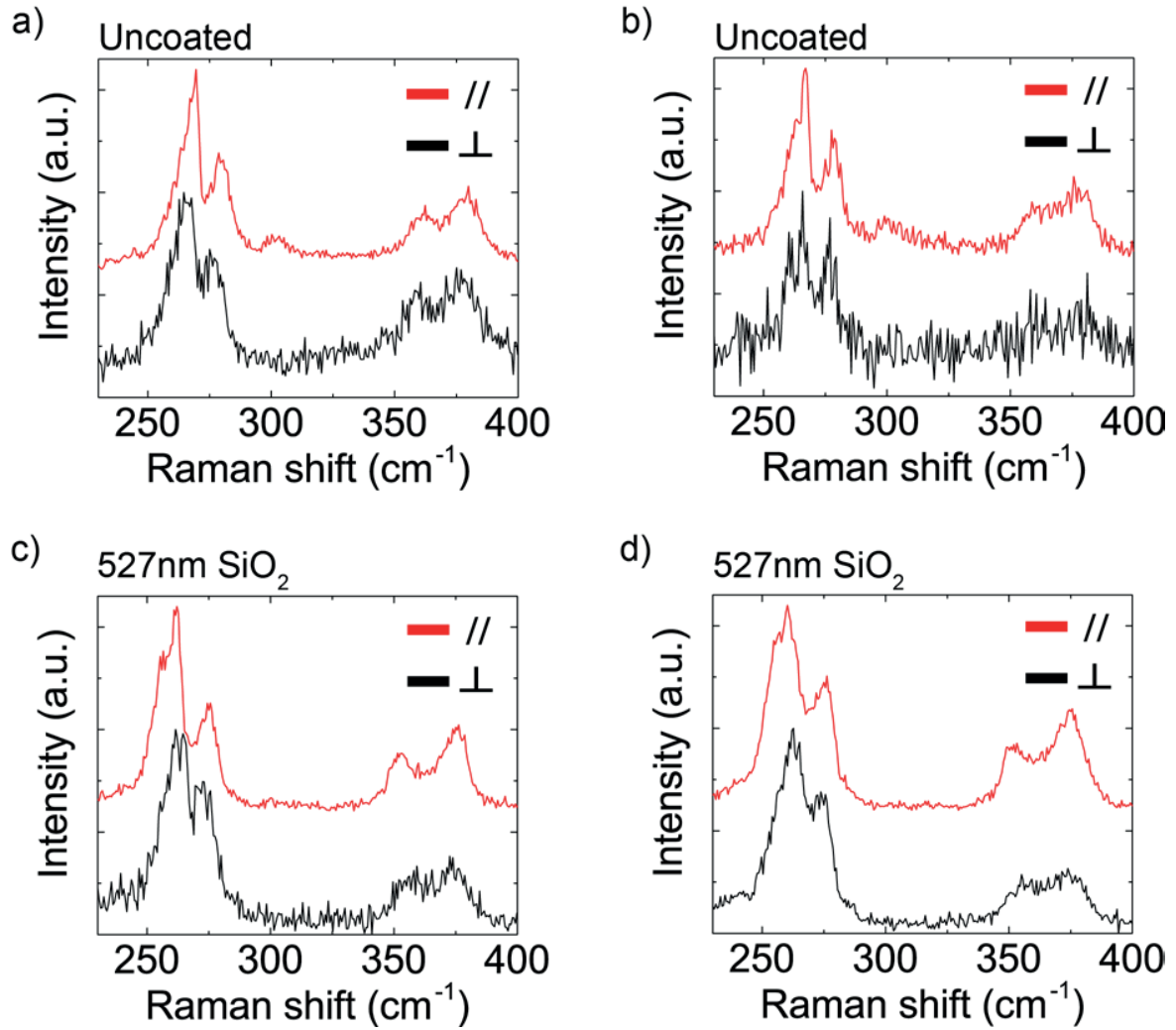
Figure 11. Polarization-dependent Raman spectra of uncoated (a, b) and coated (c, d) NWs.

Supporting Information to chapter 5

SI11 PL from twin- and polytypism-based transitions

The PL spectrum exemplifies the importance that twins and short WZ segments can have on the PL signal of the GaAs core.
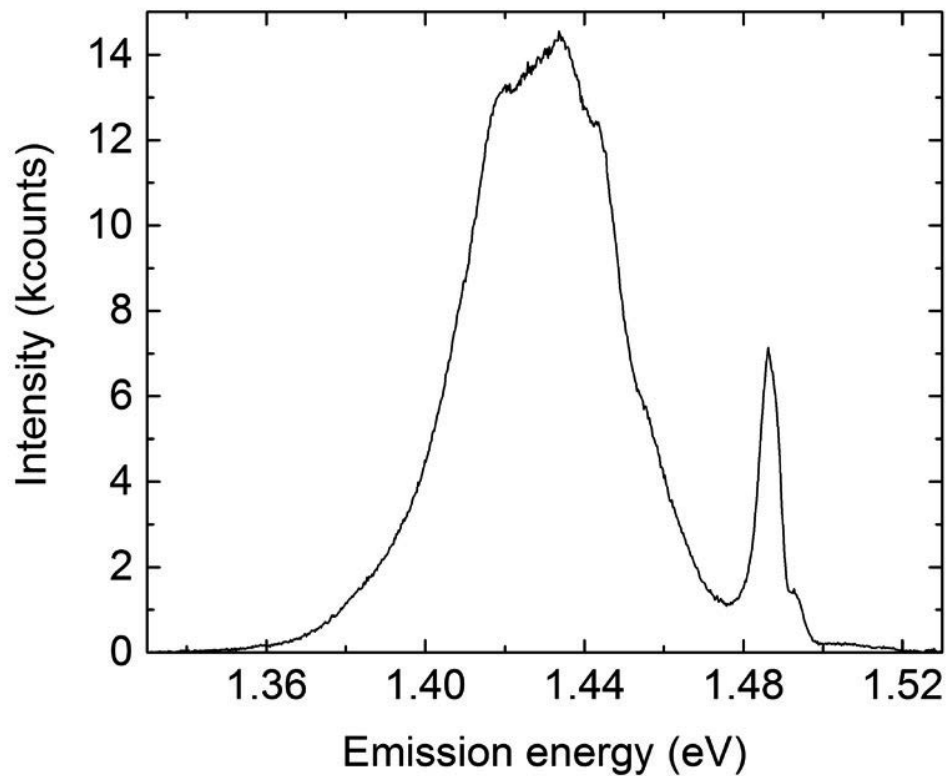
Figure 12. PL spectrum from a horizontal NW at 12 K in the GaAs spectral range. Only the emission at higher energy than 1.48 eV comes from the exciton recombination at the ZB bandgap (occasionally mediated by intra-bandgap states).

Supporting Information to chapter 5

SI12 Derivation of the Poisson ratio

We use the following equation, valid for the GaAs TO$_D$ mode in case of uniaxial stress along the [111] direction:

$$\frac{\Delta\omega_D}{\omega_D} = [-3\gamma_D H - \frac{1}{2}r'_D(1 - H)]\epsilon_{zz}$$

ω_D is the frequency of the relaxed mode and $\Delta\omega_D$ is its shift under stress, while all the other values are the same as in Eq. 1, reported in the manuscript. By combining the equation above with Eq. 5.1 and applying them respectively to the TO$_D$ and the TO$_S$ peaks visible in the polarization-dependent Raman spectra, we can eliminate the dependence on strain and estimate the value of the Poisson ratio ν at 12 K. The reported value ν = 0.19 ± 0.02 derives from the spectra in Figure 4b and in the Supplementary Information.

Supporting Information to chapter 6

Segregation scheme of indium in AlGaInAs nanowire shells

Luca Francaviglia[1], Gözde Tütüncüoglu[1], Sara Martí-Sánchez[2], Enrico Di Russo[3], Simon, Escobar Steinvall[1], Jaime Segura Ruiz[4], Heidi Potts[1], Martin Friedl[1], Lorenzo Rigutti[3], Jordi Arbiol[2,5], Anna Fontcuberta i Morral*[1,6]

[1]*Laboratory of Semiconductor Materials, Institute of Materials, École Polytechnique Fédérale de Lausanne, CH-1015, Switzerland*
[2]*Catalan Institute of Nanoscience and Nanotechnology (ICN2), CSIC and BIST, Campus UAB, Bellaterra, 08193 Barcelona, Catalonia, Spain*
[3]*Groupe de Physique des Matériaux, Université de Rouen, Saint Etienne du Rouvray, 76801, France*
[4]*European Synchrotron Radiation Facility, Grenoble, 38043, France*
[5]*ICREA, Pg. Lluís Companys 23, 08010 Barcelona, Catalonia, Spain*
[6]*Institute of Physics, École Polytechnique Fédérale de Lausanne, CH-1015, Switzerland*

S1 QD emission range vs indium

The width of the QD PL distributions increases with In.
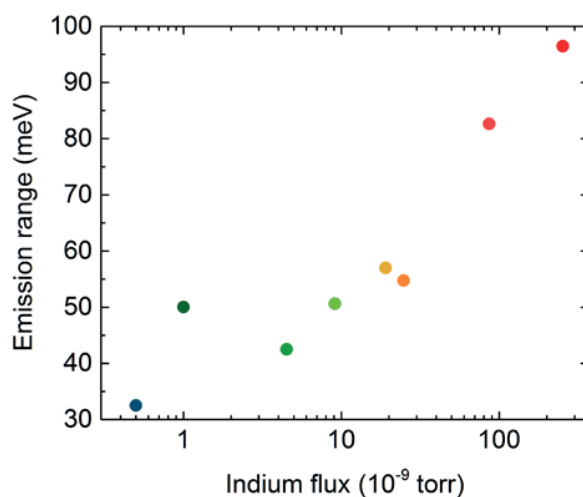
Figure S1. Energy difference between the 3rd and 1st quartiles of the QD emission-energy distributions vs indium flux. The data with abscissa less to equal to 1 are reference GaAs-AlGaAs NWs (no indium). The blue spot corresponds to a sample whose shell was grown at lower temperature (430°C) (similarly to Jeon et al. 2018).

Supporting Information to chapter 6

S2 Polarization-dependent Raman spectroscopy

The position of the GaAs TO peak is constant and independent from the direction of the polarization of the collected light.
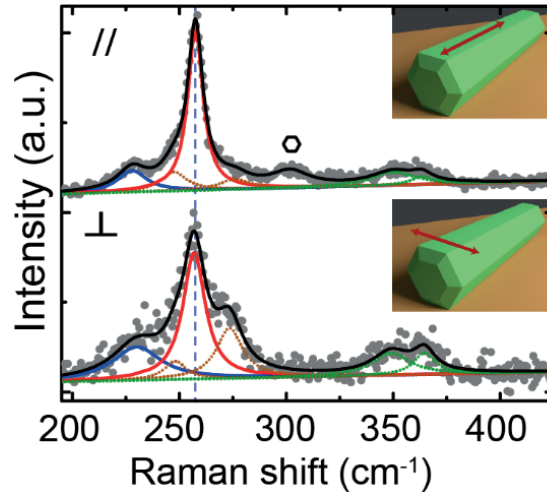
Figure S2-1 Polarization-dependent Raman spectra in backscattering configuration on a GaAs-AlGaInAs NW with 25% indium. The upper panel is for polarization parallel to the NW axis; the lower panel is for polarization collected perpendicular to the NW axis. The color coding is the same as in the main manuscript. The vertical dashed line indicates the GaAs TO position: within the resolution of the spectrometer, the GaAs TO peaks are at the same positions in the parallel and in the perpendicular configurations.
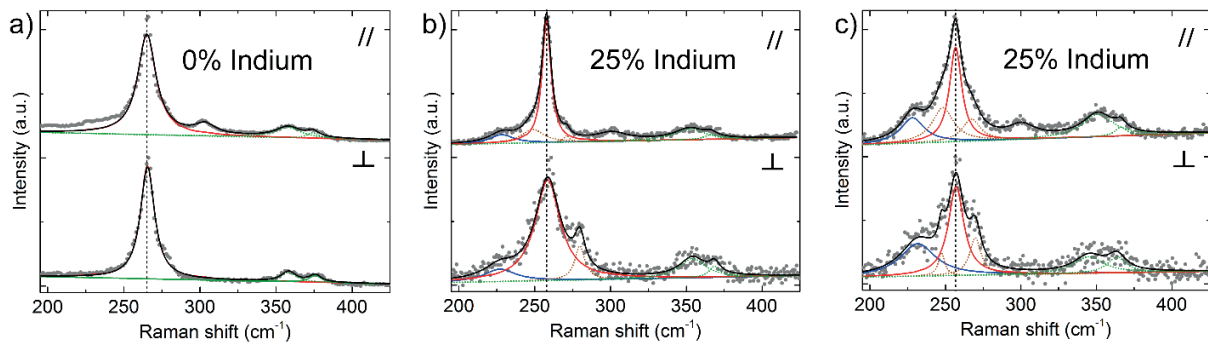
Figure S2-2. Further polarization-dependent Raman spectra as in S2-1. (a) a reference core-shell GaAs-AlGaAs NW without indium in the shell and (b - c) two GaAs-AlGaInAs NWs with 25% of indium in the shell. The GaAs TO peaks are at the same positions in the parallel and in the perpendicular configurations.

Supporting Information to chapter 6

S3 STEM EDS maps on NW cross sections

The STEM EDS maps used to derive the Ga, In, and Al concentrations in the manuscript.
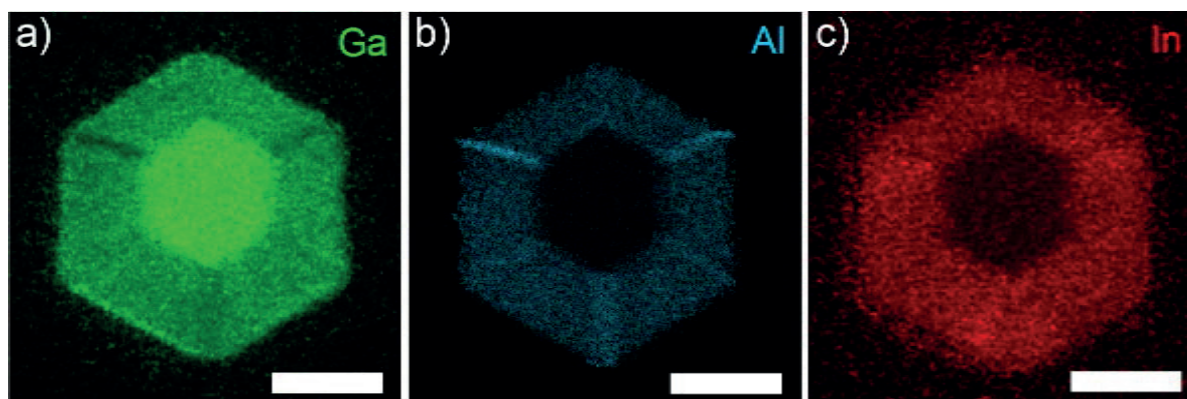
Figure S3-1. (a-c) EDS STEM maps of the NW cross-section (15% indium) used to derive the plot in the manuscript (figure 2). (a), (b), and (c) show the spatial distributions of Ga, Al, and In respectively (As is evenly distributed in the cross section. The scale bars correspond to 30 nm.

Further signatures of the wedge-shaped In-rich regions by STEM EDS.
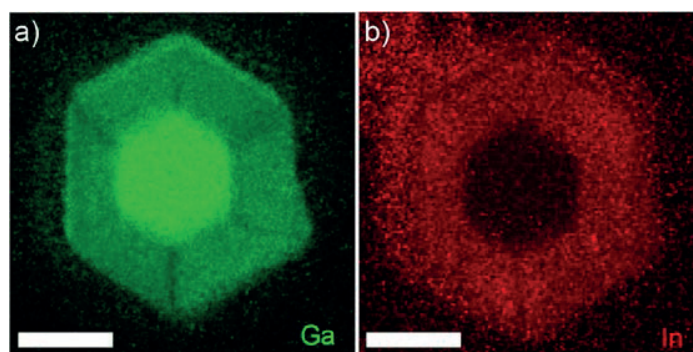
Figure S3-2. STEM EDS maps of another NW cross section from the same growth (15% indium). (a) Ga and (b) Indium distributions. The Ga and In depletions along the {112} direction is visible as well as the 3-fold wedge-shaped In-rich regions at the ridges. The scale bars correspond to 30 nm.

Supporting Information to chapter 6

S4 AC HAADF STEM micrographs

From the AC HAADF micrographs we measured the thickness of the Al-rich planes and, by FFT, we confirm that the NW sidewalls belong to the {110} family.
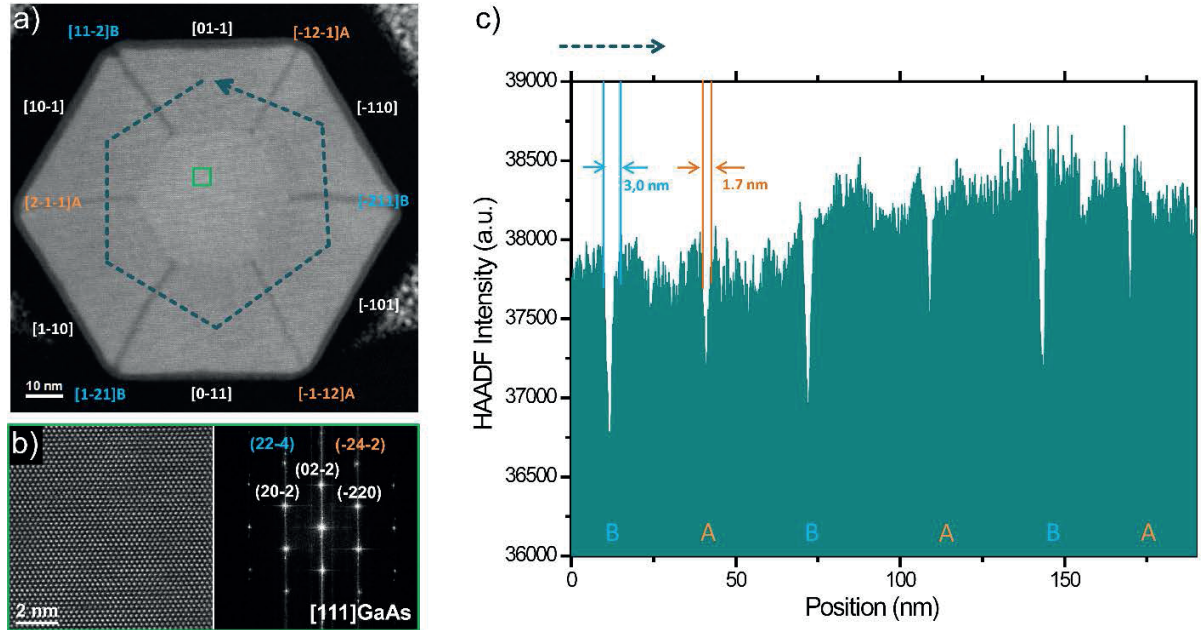
Figure S4. (a) AC HAADF STEM micrograph of a FIB-cut NW cross section. The crystalline direction of the {110} NW sidewalls and {112}A and {121}B ridges are labelled. (b) Left: HR micrograph of the core region highlighted by the green square; right: FFT of the image on the left. The diffraction spots corresponding to the crystalline directions indicated in (a) are labelled. (c) Intensity profile of the HAADF micrograph along the hexagonal linescan indicated by the dashed arrow in (a). The scan direction is indicated by the arrow in (c). The A- and B-polarity tags label the intensity dips corresponding to the Al-rich planes. The thickness of the planes is given, too.

Supporting Information to chapter 6

S5 XRF maps

The X-ray fluorescence (XRF) mapping performed at the beamline ID16B of the ESRF, offers a very low detection limit, allowing the detection of indium even at very low concentrations. The XRF maps were collected using a 29.8 keV pink beam ($\Delta E/E = 10^{-2}$, with a flux of 2×10^{10} photons/s). The beam full width at half maximum was 52 nm x 56 nm, which defines the spatial resolution of the XRF scan. Before scanning, the NWs are dispersed horizontally on SiN windows, 200 nm thick, to reduce the background contribution in the XRF maps. The figures S5 show the XRF maps of NWs with In fractions of 1% (fig. S5-1), 4% (fig. S5-2) and 15% (fig. S5-3). In each figure, (a), (b), and (c) correspond to the Ga, As, and In maps, respectively. XRF confirms that indium has been incorporated in the shell of all samples. With respect to the sample with the minimum indium fraction (1%), the XRF maps show that the average indium concentrations approximately have a 2-fold, 3-fold, 4-fold, 10-fold, and 20-fold increase, which shows the gradual increase of indium also in the NWs with a low indium fraction.
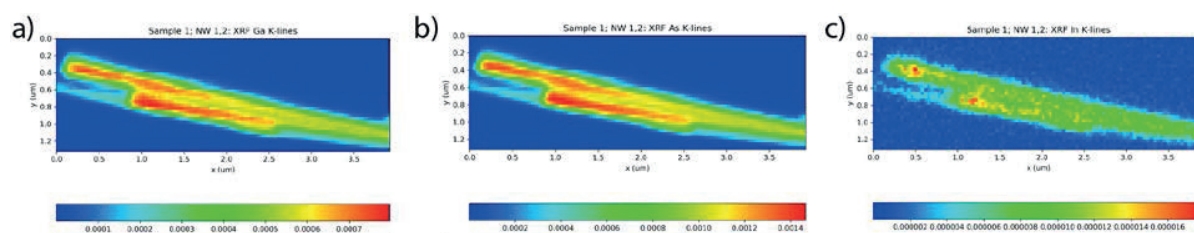
Figure S5-1. XRF scan of a NW with 1% of indium.
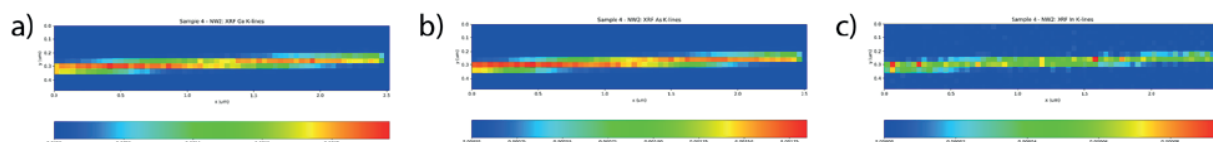
Figure S5-2. XRF scan of a NW with 4% of indium.
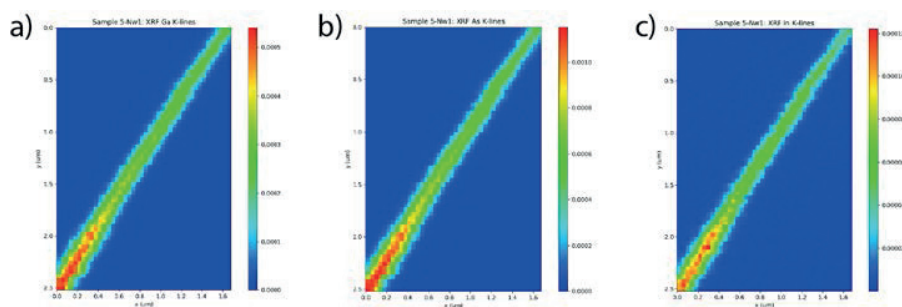
Figure S5-3. XRF scan of a NW with 10% of indium

Supporting Information to chapter 6

S6 STEM EDS maps of horizontal NWs

a)

b)

XEDS NW sample nominal 20%				
Position in NW	Ga	Al	In	Sum
	at %	at %	at %	at %
NW3 shell left	53.3	20.19	26.52	100.01
NW3 shell right	55.11	19.89	25	100
NW2 shell left	54.13	20.14	25.73	100
NW2 shell right	55.51	19.75	24.74	100
Average	54.5125	19.9925	25.4975	100.0025
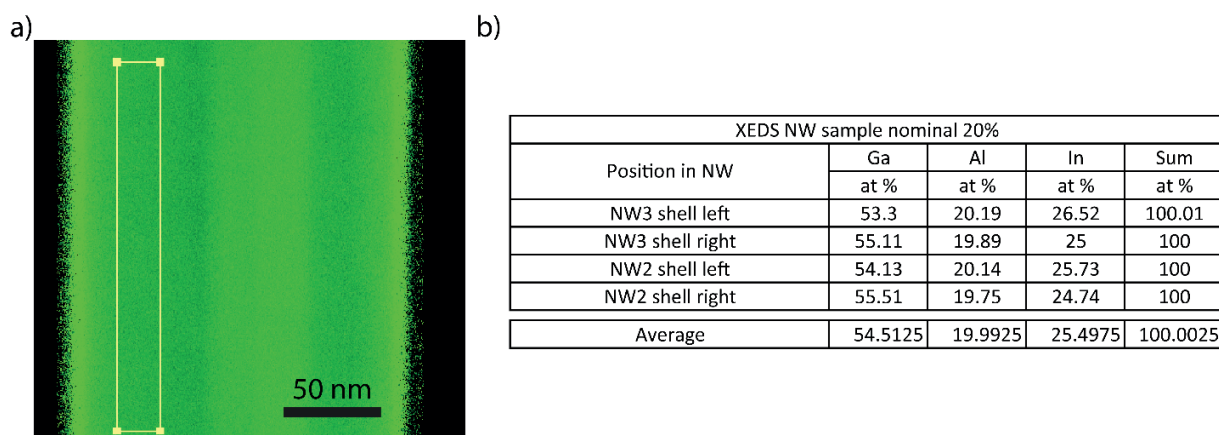
Figure S6. (a) Illustrative STEM EDS map of a horizontal NW with 25% of indium in the shell. (b) Average shell compositions for two NWs extracted from regions like the one indicated by the yellow rectangle in (a). The GaAs capping is expected to slightly affect the In and Al concentration in favor of Ga. The NW cross sections are unaffected by the GaAs capping and were used for quantification, away from the In-rich segregates, for the sample with In 15%. The comparison with longitudinal maps like in (a) show that the GaAs capping affects marginally the EDS quantification.

S7 EELS map of a whole NW cross section

EELS maps of whole NW cross sections show the 3-fold symmetry of the group-III segregation.
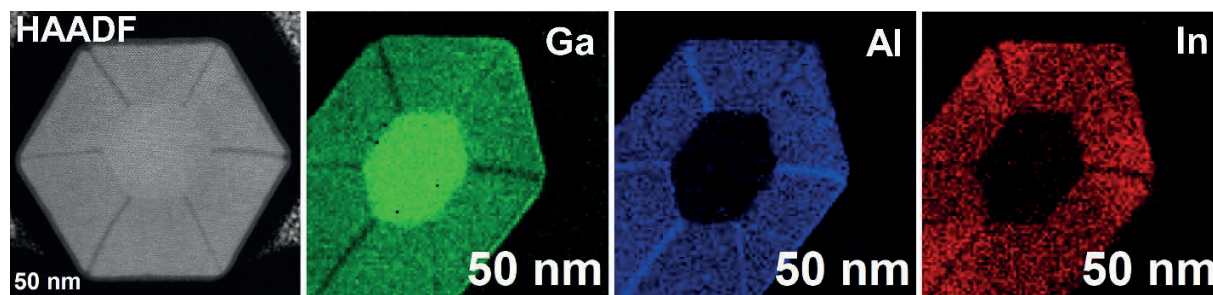
Figure S7. (a) HAADF STEM micrograph and (b) STEM EELS scans of a full NW cross sections (15% indium). Notice that the deformation observed on the NW cross-section in the EELS maps is due to the sample drift occurred during the acquisition.

Supporting Information to chapter 6

S8 Peak area vs input power

The studied QDs typically emit exciton, biexciton and charged-exciton lines[1][2]. The g2(τ) reported in the manuscript was measured on a QD exciton line, as demonstrated by the plot here below.
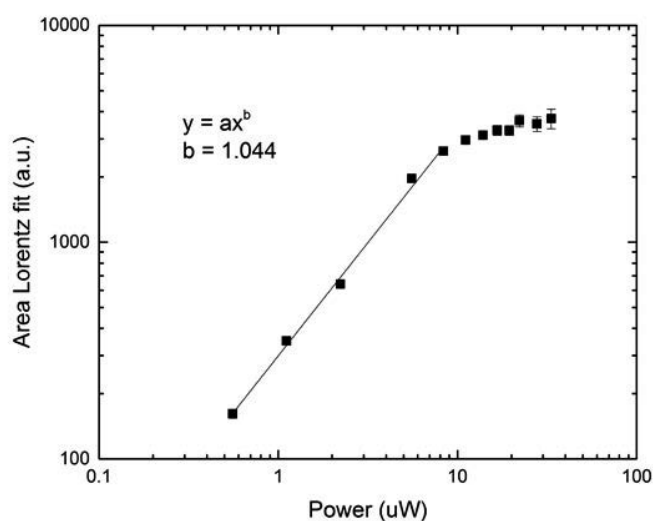
Figure S8. Lorentzian-fit area vs input power with power fit (exponent ~1, i.e. exciton peak) for the QD line whose $g^2(\tau)$ is reported in the manuscript.

[1] M. Heiss et al., Nat. Mater, 12, 490 (2013)

[2] Y. Fontana, *Optically active quantum dots in bottom-up nanowires*. PhD thesis, École Polytechnique Fédérale de Lausanne (2015).

Supporting Information to chapter 6

S9 Illustrative CL map

The CL maps show experimental evidence of the inhomogeneous composition of the shell along a NW, which associated with the QD-like emission.
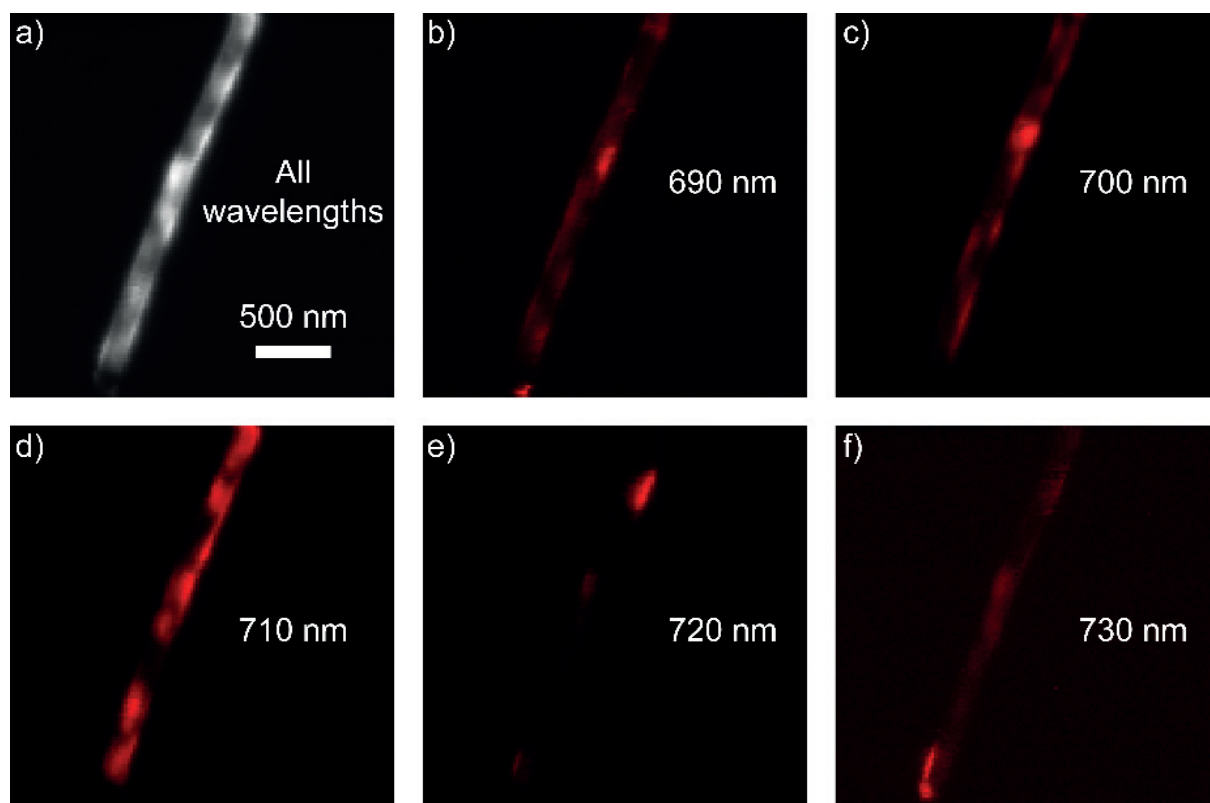
Figure S9. Illustrative SEM-CL maps of the top portion of a NW with 4% of indium in the shell. a) shows the whole CL signal, while in b) to f) the CL signal is filtered for the different indicated wavelengths (bandwidth of 8 meV). 710 nm is about the median of the QD emission-energy distribution of this sample. Electron-beam energy: 1.5 keV.

Supporting Information to chapter 6

S10 Experimental strain: Raman spectroscopy

The increasing downshift of the GaAs TO mode from the core of NWs with increasing In fraction in the shell is indicative of the increasing tensile stress applied by the shell to the core.
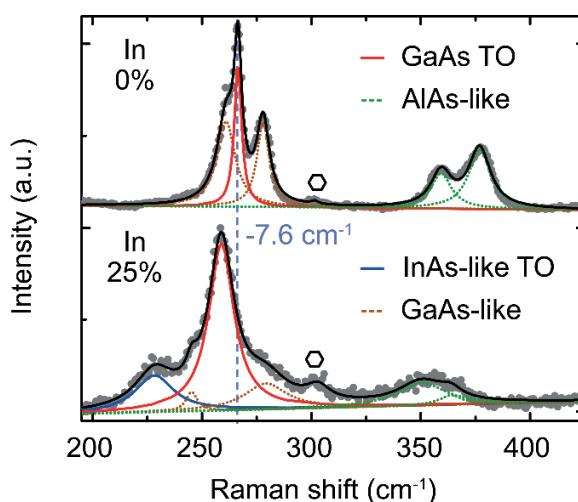
Figure S10. Micro-Raman spectra of core-shell NWs with 0% (top) and 25% (bottom) of In. The vertical line indicates the position of the relaxed GaAs TO mode in the top panel. Starting with the pure AlGaAs/GaAs system, we identify peaks from both the AlAs- and GaAs-related modes (TO and LO). The hexagon indicates the 2nd-order Raman peak of the Si substrate. The sample with 25% In exhibits significantly shifted and broader peaks with respect to the reference. This is consistent with both the disorder and strain introduced by In.

Supporting Information to chapter 6

S11 Experimental vs simulated strain

Additional derivation of strain from the Raman spectra according to NW-based calibrations (Zardo et al., 2012) do not significantly differ from the derivation from the spectra according to bulk parameters (Trommer et al., 1980).
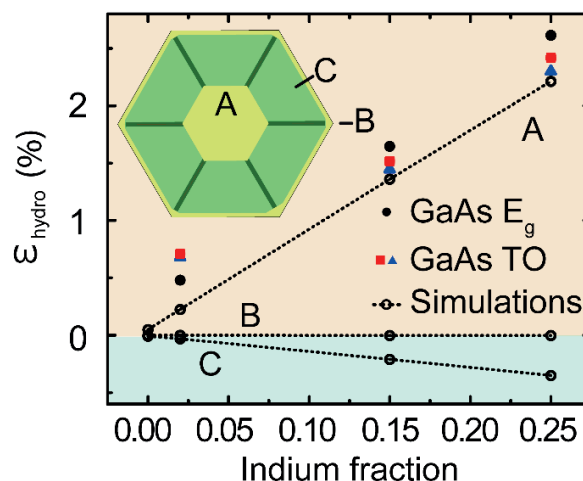
Figure S11. Hydrostatic strain vs indium fraction. Like in figure 4c in the manuscript, the open circles, the red squares and the blue triangles correspond to the values derived from simulations, Raman spectra and PL spectra. In addition, the blue triangles show the results derived from the same Raman measurements according to the NW-based calibrations in Zardo et al., 2012.

S12 APT mass spectrum
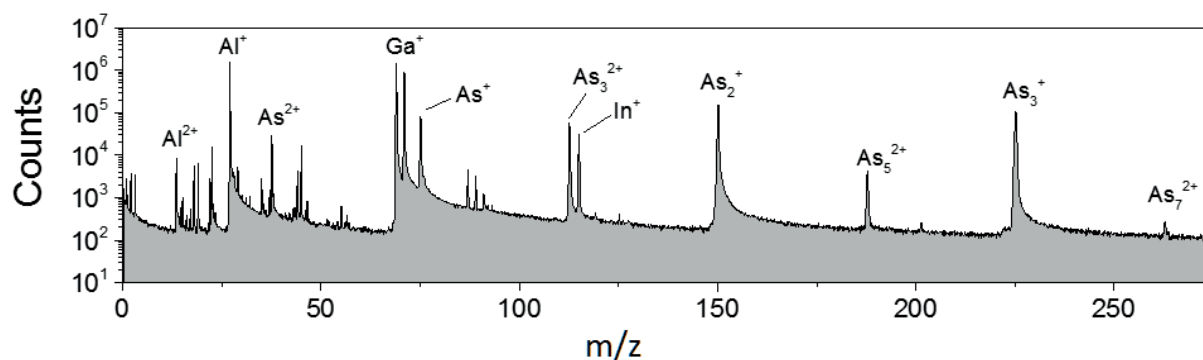
Figure S12. Mass spectrum of the entire volume evaporated from the tip of the NW (2% In) shown in the manuscript: Al, Ga, In, and As are all detected.

Supporting Information to chapter 6

S13 Distribution of first-neighbor atoms

Monoatomic-layer segregation is observed and predicted in compound semiconductor[345] and is expected to alter the average distribution of the distances between two atoms of the same species. APT is a sensitive technique to derive the distributions of the first-neighbor atomic distances. The good agreement between the measured and the theoretical random-alloy distributions highlights that there is no significant difference between the two: APT shows no evidence of segregation at atomic length-scales.
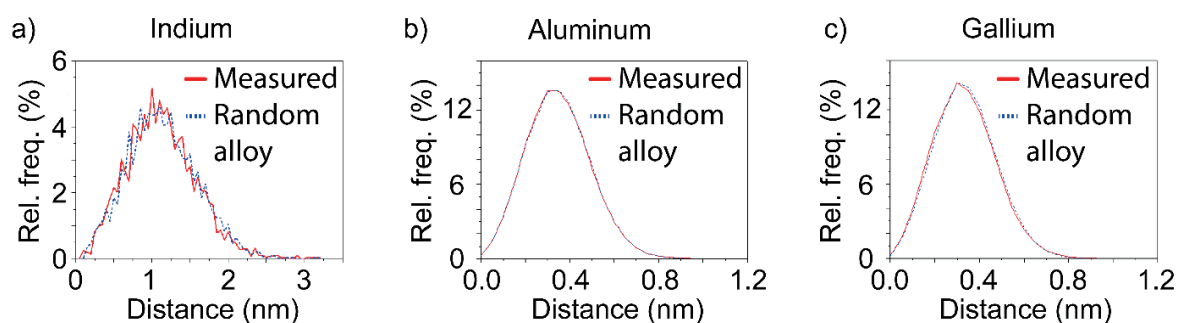
Figure S13. Experimental (solid red) and theoretical (dotted blue) first-neighbor (a) In-, (b) Ga, and (c) Al atomic-distance distributions. Experimental and theoretical curves overlap, showing no evidence of reordering or clustering at length scales in the atomic range. On average, the In-In distance is longer because it is diluted in the alloy.

---

[3] P. M. Petroff et al., *PRL*, **48**, 3, 1982.
[4] P. C. Kelires et al., *PRL* **63**, 1164, 1989
[5] G. Vantarakis et al., *PRL* **108**, 176102, 2012

Bibliography

[1] K. Tomioka, Y. Kobayashi, J. Motohisa, S. Hara, and T. Fukui, "Selective-area growth of vertically aligned GaAs and GaAs/AlGaAs core-shell nanowires on Si(111) substrate," *Nanotechnology*, vol. 20, no. 14, 2009.

[2] X. Yan, X. Zhang, X. Ren, X. Lv, J. Li, Q. Wang, S. Cai, and Y. Huang, "Formation Mechanism and Optical Properties of InAs Quantum Dots on the Surface of GaAs Nanowires," *Nano Letters*, vol. 12, no. 4, pp. 1851–1856, 2012.

[3] C. Somaschini, S. Bietti, A. Trampert, U. Jahn, C. Hauswald, H. Riechert, S. Sanguinetti, and L. Geelhaar, "Control over the number density and diameter of GaAs nanowires on Si(111) mediated by droplet epitaxy," *Nano Letters*, vol. 13, no. 8, pp. 3607–3613, 2013.

[4] E. Russo-Averchi, J. Vukajlovic Plestina, G. Tütüncüoglu, F. Matteini, A. Dalmau-Mallorquí, M. De La Mata, D. Rüffer, H. A. Potts, J. Arbiol, S. Conesa-Boj, and A. Fontcuberta i Morral, "High yield of GaAs nanowire arrays on si mediated by the pinning and contact angle of Ga," *Nano Letters*, vol. 15, no. 5, pp. 2869–2874, 2015.

[5] F. Matteini, G. Tütüncüoglu, H. Potts, F. Jabeen, and A. Fontcuberta i Morral, "Wetting of Ga on SiO_x and Its Impact on GaAs Nanowire Growth," *Crystal Growth & Design*, vol. 15, no. 7, pp. 3105–3109, 2015.

[6] Y.-B. Wang, L.-F. Wang, H. J. Joyce, Q. Gao, X.-Z. Liao, Y.-W. Mai, H. H. Tan, J. Zou, S. P. Ringer, H.-J. Gao, and C. Jagadish, "Super Deformability and Young's Modulus of GaAs Nanowires," *Adv. Mater.*, vol. 23, no. 11, pp. 1356–1360, 2011.

[7] G. Signorello, S. Karg, M. T. Björk, B. Gotsmann, and H. Riel, "Tuning the Light Emission from GaAs Nanowires over 290 meV with Uniaxial Strain," *Nano Lett.*, vol. 13, no. 3, pp. 917–924, 2013.

[8] R. B. Lewis, P. Corfdir, H. Küpers, T. Flissikowski, O. Brandt, and L. Geelhaar, "Nanowires Bending over Backward from Strain Partitioning in Asymmetric Core-Shell Heterostructures," *Nano Letters*, vol. 18, no. 4, pp. 2343–2350, 2018.

[9] F. Glas, J. C. Harmand, and G. Patriarche, "Why does wurtzite form in nanowires of III-V zinc blende semiconductors?," *Physical Review Letters*, vol. 99, no. 14, pp. 3–6, 2007.

Bibliography

[10] N. Akopian, G. Patriarche, L. Liu, J.-C. Harmand, and V. Zwiller, "Crystal Phase Quantum Dots," *Nano Lett.*, vol. 10, no. 4, pp. 1198–1201, 2010.

[11] D. Dalacu, K. Mnaymneh, J. Lapointe, X. Wu, P. J. Poole, G. Bulgarini, V. Zwiller, and M. E. Reimer, "Ultraclean Emission from InAsP Quantum Dots in Defect-Free Wurtzite InP Nanowires," *Nano Lett.*, vol. 12, no. 11, pp. 5919–5923, 2012.

[12] L. Leandro, C. P. Gunnarsson, R. Reznik, K. D. Jöns, I. Shtrom, A. Khrebtov, T. Kasama, V. Zwiller, G. Cirlin, and N. Akopian, "Nanowire Quantum Dots Tuned to Atomic Resonances," *Nano Lett.*, vol. 18, no. 11, pp. 7217–7221, 2018.

[13] E. Uccelli, J. Arbiol, J. R. Morante, and A. i Morral, "InAs Quantum Dot Arrays Decorating the Facets of GaAs Nanowires," *ACS Nano*, vol. 4, no. 10, pp. 5985–5993, 2010.

[14] M. Heiss, Y. Fontana, A. Gustafsson, G. Wüst, C. Magen, D. D. O'Regan, J. W. Luo, B. Ketterer, S. Conesa-Boj, A. V. Kuhlmann, J. Houel, E. Russo-Averchi, J. R. Morante, M. Cantoni, N. Marzari, J. Arbiol, A. Zunger, R. J. Warburton, and A. Fontcuberta i Morral, "Self-assembled Quantum Dots in a Nanowire System For Quantum Photonics," *Nature Mater.*, vol. 12, pp. 439–444, 2013.

[15] I. Friedler, C. Sauvan, J. P. Hugonin, P. Lalanne, J. Claudon, and J. M. Gérard, "Solid-state single photon sources: the nanowire antenna," *Opt. Express*, vol. 17, no. 4, pp. 2095–2110, 2009.

[16] G. Bulgarini, M. E. Reimer, T. Zehender, M. Hocevar, E. P. A. M. Bakkers, L. P. Kouwenhoven, and V. Zwiller, "Spontaneous emission control of single quantum dots in bottom-up nanowire waveguides," *Appl. Phys. Lett.*, vol. 100, no. 12, pp. –, 2012.

[17] J. Claudon, N. Gregersen, P. Lalanne, and J.-M. Gérard, "Harnessing Light with Photonic Nanowires: Fundamentals and Applications to Quantum Optics," *ChemPhysChem*, vol. 14, no. 11, pp. 2393–2402, 2013.

[18] O. Benson, C. Santori, M. Pelton, and Y. Yamamoto, "Regulated and Entangled Photons from a Single Quantum Dot," *Phys. Rev. Lett.*, vol. 84, pp. 2513–2516, mar 2000.

[19] "IBM Q - quantum devices and simulators." www.research.ibm.com/ibm-q/technology/devices/. Accessed: 2018-10-28.

[20] "Quantum flagship final report." www.ec.europa.eu/digital-single-market/en/news/quantum-flagship-high-level-expert-group-publishes-final-report. Accessed: 2018-11-20.

[21] "Quantum manifesto." www.qt.eu/app/uploads/2018/04/93056_Quantum-Manifesto_WEB.pdf. Accessed: 2018-10-30.

[22] L. V. Hau, S. E. Harris, Z. Dutton, and C. H. Behroozi, "Light speed reduction to 17 metres per second in an ultracold atomic gas," *Nature*, vol. 397, no. 6720, pp. 594–598, 1999.

[23] D. F. Phillips, A. Fleischhauer, A. Mair, R. L. Walsworth, and M. D. Lukin, "Storage of Light in Atomic Vapor," *Phys. Rev. Lett.*, vol. 86, pp. 783–786, jan 2001.

[24] R. S. Wagner and W. C. Ellis, "Vapor-liquid-solid mechanism of single crystal growth," *Applied Physics Letters*, vol. 4, no. 5, pp. 89–90, 1964.

[25] R. B. Lewis, L. Nicolai, H. Küpers, M. Ramsteiner, A. Trampert, and L. Geelhaar, "Anomalous Strain Relaxation in Core–Shell Nanowire Heterostructures via Simultaneous Coherent and Incoherent Growth," *Nano Letters*, vol. 17, no. 1, pp. 136–142, 2017.

[26] M. de la Mata, X. Zhou, F. Furtmayr, J. Teubert, S. Gradečak, M. Eickhoff, A. Fontcuberta i Morral, and J. Arbiol, "A review of MBE grown 0D, 1D and 2D quantum structures in a nanowire," *Journal of Materials Chemistry C*, vol. 1, no. 28, p. 4300, 2013.

[27] J. Tatebayashi, Y. Ota, S. Ishida, M. Nishioka, S. Iwamoto, and Y. Arakawa, "Site-controlled formation of InAs/GaAs quantum-dot-in-nanowires for single photon emitters," *Applied Physics Letters*, vol. 100, no. 26, p. 263101, 2012.

[28] B. J. Ohlsson, M. T. Björk, A. I. Persson, C. Thelander, L. R. Wallenberg, M. H. Magnusson, K. Deppert, and L. Samuelson, "Growth and characterization of GaAs and InAs nanowhiskers and InAs/GaAs heterostructures," *Phys. E*, vol. 13, no. 2–4, pp. 1126–1130, 2002.

[29] M. T. Björk, C. Thelander, A. E. Hansen, L. E. Jensen, M. W. Larsson, L. R. Wallenberg, and L. Samuelson, "Few-Electron Quantum Dots in Nanowires," *Nano Lett.*, vol. 4, no. 9, pp. 1621–1625, 2004.

[30] M. T. Björk, B. J. Ohlsson, T. Sass, A. I. Persson, C. Thelander, M. H. Magnusson, K. Deppert, L. R. Wallenberg, and L. Samuelson, "One-dimensional heterostructures in semiconductor nanowhiskers," *Appl. Phys. Lett.*, vol. 80, no. 6, pp. 1058–1060, 2002.

[31] J. Heinrich, A. Huggenberger, T. Heindel, S. Reitzenstein, S. Höfling, L. Worschech, and A. Forchel, "Single photon emission from positioned GaAs/AlGaAs photonic nanowires," *Appl. Phys. Lett.*, vol. 96, no. 21, 2010.

[32] H. Sanada, H. Gotoh, K. Tateno, and H. Nakano, "Exciton and Biexciton Emissions from Single GaAs Quantum Dots in (Al,Ga)As Nanowires," *Jpn. J. Appl. Phys.*, vol. 46, no. 4S, p. 2578, 2007.

[33] M. P. V. Kouwen, M. E. Reimer, A. W. Hidma, M. H. M. Van Weert, R. E. Algra, E. P. A. M. Bakkers, L. P. Kouwenhoven, and V. Zwiller, "Single electron charging in optically active nanowire quantum dots," *Nano Letters*, vol. 10, no. 5, pp. 1817–1822, 2010.

[34] E. D. Minot, F. Kelkensberg, M. van Kouwen, J. A. van Dam, L. P. Kouwenhoven, V. Zwiller, M. T. Borgström, O. Wunnicke, M. A. Verheijen, and E. P. A. M. Bakkers, "Single Quantum Dot Nanowire LEDs," *Nano Lett.*, vol. 7, pp. 367–371, 2007.

[35] M. E. Reimer, G. Bulgarini, N. Akopian, M. Hocevar, M. B. Bavinck, M. A. Verheijen, E. P. A. M. Bakkers, L. P. Kouwenhoven, and V. Zwiller, "Bright Single-photon Sources in Bottom-Up Tailored Nanowires," *Nat. Commun.*, vol. 3, p. 737, 2012.

[36] J. Tatebayashi, Y. Ota, S. Ishida, M. Nishioka, S. Iwamoto, and Y. Arakawa, "Highly uniform, multi-stacked InGaAs/GaAs quantum dots embedded in a GaAs nanowire," *Applied Physics Letters*, vol. 105, no. 10, p. 103104, 2014.

[37] X. Yan, X. Zhang, J. Li, J. Cui, Q. Wang, Y. Huang, and X. Ren, "Growth of InAs quantum dots on Si-based GaAs nanowires by controlling the surface adatom diffusion," *J. Cryst. Growth*, vol. 384, no. 0, pp. 82–87, 2013.

[38] X. Yan, X. Zhang, J. Li, J. Cui, and X. Ren, "Controllable growth and optical properties of InP and InP/InAs nanostructures on the sidewalls of GaAs nanowires," *Journal of Applied Physics*, vol. 116, no. 21, pp. 0–6, 2014.

[39] J. Y. Tsao, *Materials fundamentals of molecular beam epitaxy*. Elsevier San Diego, 1993.

[40] M. Hetzl, M. Kraut, J. Winnerl, L. Francaviglia, M. Döblinger, S. Matich, A. Fontcuberta i Morral, and M. Stutzmann, "Strain-Induced Band Gap Engineering in Selectively Grown GaN-(Al,Ga)N Core-Shell Nanowire Heterostructures," *Nano Letters*, vol. 16, no. 11, pp. 7098–7106, 2016.

[41] F. Martelli, M. Piccin, G. Bais, F. Jabeen, S. Ambrosini, S. Rubini, and A. Franciosi, "Photoluminescence of Mn-catalyzed GaAs nanowires grown by molecular beam epitaxy," *Nanotechnology*, vol. 18, no. 12, 2007.

[42] R. Perumal, Z. Cui, P. Gille, J. C. Harmand, and K. Yoh, "Palladium assisted hetroepitaxial growth of an InAs nanowire by molecular beam epitaxy," *Semiconductor Science and Technology*, vol. 29, no. 11, 2014.

[43] C. Colombo, D. Spirkoska, M. Frimmer, G. Abstreiter, and A. Fontcuberta i Morral, "Ga-assisted Catalyst-free Growth Mechanism of GaAs Nanowires by Molecular Beam Epitaxy," *Phys. Rev. B*, vol. 77, p. 155326, 2008.

[44] A. Fontcuberta i Morral, C. Colombo, G. Abstreiter, J. Arbiol, and J. R. Morante, "Nucleation Mechanism of Gallium-assisted Molecular Beam Epitaxy Growth of Gallium Arsenide Nanowires," *Appl. Phys. Lett.*, vol. 92, p. 63112, 2008.

[45] F. Matteini, V. G. Dubrovskii, D. Rüffer, G. Tütüncüoglu, Y. Fontana, and A. F. i Morral, "Tailoring the diameter and density of self-catalyzed GaAs nanowires on silicon," *Nanotechnology*, vol. 26, no. 10, p. 105603, 2015.

[46] S. Plissard, G. Larrieu, X. Wallart, and P. Caroff, "High yield of self-catalyzed GaAs nanowire arrays grown on silicon via gallium droplet positioning," *Nanotechnology*, vol. 22, no. 27, 2011.

[47] J. Vukajlovic-Plestina, W. Kim, V. G. Dubrovski, G. Tütüncüoglu, M. Lagier, H. Potts, M. Friedl, and A. Fontcuberta i Morral, "Engineering the Size Distributions of Ordered GaAs Nanowires on Silicon," *Nano Letters*, vol. 17, no. 7, pp. 4101–4108, 2017.

[48] W. Kim, V. Dubrovskii, J. Vukajlovic-Plestina, G. Tütüncüoglu, L. Francaviglia, L. Güniat, H. Potts, M. Friedl, J.-B. Leran, and A. Fontcuberta i Morral, "Bistability of Contact Angle and Its Role in Achieving Quantum-Thin Self-Assisted GaAs nanowires," *Nano Letters*, vol. 18, no. 1, 2018.

[49] O. Demichel, M. Heiss, J. Bleuse, H. Mariette, and A. Fontcuberta i Morral, "Impact of surfaces on the optical properties of GaAs nanowires," *Appl. Phys. Lett.*, vol. 97, no. 20, 2010.

[50] F. Qian, Y. Li, S. Gradečak, H. G. Park, Y. Dong, Y. Ding, Z. L. Wang, and C. M. Lieber, "Multi-Quantum-Well Nanowire Heterostructures for Wavelength-Controlled Lasers," *Nature Mater.*, vol. 7, pp. 701–706, 2008.

[51] J. Treu, M. Bormann, H. Schmeiduch, M. Döblinger, S. Morkötter, S. Matich, P. Wiecha, K. Saller, B. Mayer, M. Bichler, M. C. Amann, J. J. Finley, G. Abstreiter, and G. Koblmüller, "Enhanced luminescence properties of InAs-InAsP core-shell nanowires," *Nano Letters*, vol. 13, no. 12, pp. 6070–6077, 2013.

[52] M. Hetzl, J. Winnerl, L. Francaviglia, M. Kraut, M. Döblinger, S. Matich, A. Fontcuberta i Morral, and M. Stutzmann, "Surface passivation and self-regulated shell growth in selective area-grown GaN-(Al,Ga)N core-shell nanowires," *Nanoscale*, vol. 9, no. 21, pp. 7179–7188, 2017.

[53] R. E. Algra, M. Hocevar, M. A. Verheijen, I. Zardo, G. G. W. Immink, W. J. P. Van Enckevort, G. Abstreiter, L. P. Kouwenhoven, E. Vlieg, and E. P. A. M. Bakkers, "Crystal structure transfer in core/shell nanowires," *Nano Letters*, vol. 11, no. 4, pp. 1690–1694, 2011.

[54] S. Gorji Ghalamestani, M. Heurlin, L. E. Wernersson, S. Lehmann, and K. A. Dick, "Growth of InAs/InP core-shell nanowires with various pure crystal structures," *Nanotechnology*, vol. 23, no. 28, 2012.

[55] P. Krogstrup, R. Popovitz-Biro, E. Johnson, M. H. Madsen, J. Nygård, and H. Shtrikman, "Structural phase control in self-catalyzed growth of GaAs nanowires on silicon (111)," *Nano Letters*, vol. 10, no. 11, pp. 4475–4482, 2010.

[56] D. Jacobsson, F. Panciera, J. Tersoff, M. C. Reuter, S. Lehmann, S. Hofmann, K. A. Dick, and F. M. Ross, "Interface dynamics and crystal phase switching in GaAs nanowires," *Nature*, vol. 531, no. 7594, pp. 317–322, 2016.

[57] K. Pemasiri, M. Montazeri, R. Gass, L. M. Smith, H. E. Jackson, J. Yarrison-Rice, S. Paiman, Q. Gao, H. H. Tan, C. Jagadish, X. Zhang, and J. Zou, "Carrier dynamics and quantum confinement in type II ZB-WZ InP nanowire homostructures," *Nano Letters*, vol. 9, no. 2, pp. 648–654, 2009.

Bibliography

[58] N. Vainorius, S. Lehmann, D. Jacobsson, L. Samuelson, K. A. Dick, and M. E. Pistol, "Confinement in Thickness-Controlled GaAs Polytype Nanodots," *Nano Letters*, vol. 15, no. 4, pp. 2652–2656, 2015.

[59] M. Heiss, S. Conesa-Boj, J. Ren, H. H. Tseng, A. Gali, A. Rudolph, E. Uccelli, F. Peiró, J. R. Morante, D. Schuh, E. Reiger, E. Kaxiras, J. Arbiol, and A. Fontcuberta i Morral, "Direct correlation of crystal structure and optical properties in wurtzite/zinc-blende GaAs nanowire heterostructures," *Physical Review B - Condensed Matter and Materials Physics*, vol. 83, no. 4, pp. 1–10, 2011.

[60] A. De and C. E. Pryor, "Predicted band structures of III-V semiconductors in the wurtzite phase," *Physical Review B - Condensed Matter and Materials Physics*, vol. 81, no. 15, p. 155210, 2010.

[61] B. Ketterer, M. Heiss, E. Uccelli, J. Arbiol, and A. Fontcuberta i Morral, "Untangling the electronic band structure of wurtzite GaAs nanowires by resonant Raman spectroscopy," *ACS Nano*, vol. 5, no. 9, pp. 7585–7592, 2011.

[62] N. Jeon, D. Ruhstorfer, M. Döblinger, S. Matich, B. Loitsch, G. Koblmueller, and L. J. Lauhon, "Connecting Composition-Driven Faceting with Facet-Driven Composition Modulation in GaAs-AlGaAs Core-Shell Nanowires," *Nano Letters*, vol. 18, no. 8, pp. 5179–5185, 2018.

[63] Y. Arakawa and H. Sakaki, "Multidimensional quantum well laser and temperature dependence of its threshold current," *Applied Physics Letters*, vol. 40, no. 11, pp. 939–941, 1982.

[64] M. A. Walling, J. A. Novak, and J. R. E. Shepard, "Quantum dots for live cell and in vivo imaging," *International Journal of Molecular Sciences*, vol. 10, no. 2, pp. 441–491, 2009.

[65] V. I. Klimov, a. a. Mikhailovsky, S. Xu, a. Malko, J. a. Hollingsworth, C. a. Leatherdale, H. Eisler, and M. G. Bawendi, "Optical Gain and Stimulated Emission in Nanocrystal Quantum Dots," *Science*, vol. 290, no. 5490, pp. 314–317, 2000.

[66] K. Yamaguchi, Y. Kunihiko, and T. Kaizu, "Stranski-Krastanov Growth of InAs Quantum Dots with Narrow Size Distribution," *Japanese Journal of Applied Physics*, vol. 39, no. 12A, p. L1245, 2000.

[67] K. Watanabe, N. Koguchi, and Y. Gotoh, "Fabrication of GaAs Quantum Dots by Modified Droplet Epitaxy," *Japanese Journal of Applied Physics*, vol. 39, no. 2, pp. 79–81, 2000.

[68] S. Sanguinetti, K. Watanabe, T. Tateno, M. Gurioli, P. Werner, M. Wakaki, and N. Koguchi, "Modified droplet epitaxy GaAs/AlGaAs quantum dots grown on a variable thickness wetting layer," *Journal of Crystal Growth*, vol. 253, no. 1-4, pp. 71–76, 2003.

[69] G. Juska, V. Dimastrodonato, L. O. Mereni, A. Gocalinska, and E. Pelucchi, "Towards quantum-dot arrays of entangled photon emitters," *Nature Photonics*, vol. 7, no. 7, pp. 527–531, 2013.

[70] S. T. Moroni, V. Dimastrodonato, T. H. Chung, G. Juska, A. Gocalinska, D. D. Vvedensky, and E. Pelucchi, "Indium segregation during III-V quantum wire and quantum dot formation on patterned substrates," *Journal of Applied Physics*, vol. 117, no. 16, 2015.

[71] T. H. Chung, G. Juska, S. T. Moroni, A. Pescaglini, A. Gocalinska, and E. Pelucchi, "Selective carrier injection into patterned arrays of pyramidal quantum dots for entangled photon light-emitting diodes," *Nature Photonics*, vol. 10, no. 12, pp. 782–787, 2016.

[72] E. Pelucchi, S. T. Moroni, V. Dimastrodonato, and D. D. Vvedensky, "Self-ordered nanostructures on patterned substrates: Experiment and theory of metalorganic vapor-phase epitaxy of V-groove quantum wires and pyramidal quantum dots," *Journal of Materials Science: Materials in Electronics*, vol. 29, no. 2, pp. 1–16, 2017.

[73] N. Somaschi, V. Giesz, L. De Santis, J. C. Loredo, M. P. Almeida, G. Hornecker, S. L. Portalupi, T. Grange, C. Antón, J. Demory, C. Gómez, I. Sagnes, N. D. Lanzillotti-Kimura, A. Lemaítre, A. Auffeves, A. G. White, L. Lanco, and P. Senellart, "Near-optimal single-photon sources in the solid state," *Nature Photonics*, vol. 10, no. 5, pp. 340–345, 2016.

[74] Y. Fontana, *Optically active quantum dots in bottom-up nanowires*. PhD thesis, École Polytechnique Fédérale de Lausanne, 2015.

[75] S. B. Nam, D. C. Reynolds, C. W. Litton, R. J. Almassy, T. C. Collins, and C. M. Wolfe, "Free-exciton energy spectrum in GaAs," *Physical Review B*, vol. 13, no. 2, pp. 761–767, 1976.

[76] R. Singh and G. Bester, "Nanowire Quantum Dots as an Ideal Source of Entangled Photon Pairs," *Phys. Rev. Lett.*, vol. 103, no. 6, p. 63601, 2009.

[77] D. Huber, M. Reindl, Y. Huo, H. Huang, J. S. Wildmann, O. G. Schmidt, A. Rastelli, and R. Trotta, "Highly indistinguishable and strongly entangled photons from symmetric GaAs quantum dots," *Nature Communications*, vol. 8, no. May, pp. 1–7, 2017.

[78] A. I. Tartakovskii, M. N. Makhonin, I. R. Sellers, J. Cahill, A. D. Andreev, D. M. Whittaker, J. P. R. Wells, A. M. Fox, D. J. Mowbray, M. S. Skolnick, K. M. Groom, M. J. Steer, H. Y. Liu, and M. Hopkinson, "Effect of thermal annealing and strain engineering on the fine structure of quantum dot excitons," *Physical Review B - Condensed Matter and Materials Physics*, vol. 70, no. 19, pp. 1–4, 2004.

[79] H. J. Kimble, M. Dagenais, and L. Mandel, "Photon antibunching in resonance fluorescence," *Physical Review Letters*, vol. 39, no. 11, pp. 691–695, 1977.

[80] P. Senellart, G. Solomon, and A. White, "High-performance semiconductor quantum-dot single-photon sources," *Nature Nanotechnology*, vol. 12, no. 11, pp. 1026–1039, 2017.

[81] L. Schweickert, K. D. Jöns, K. D. Zeuner, S. F. Covre Da Silva, H. Huang, T. Lettner, M. Reindl, J. Zichi, R. Trotta, A. Rastelli, and V. Zwiller, "On-demand generation of background-free single photons from a solid-state source," *Applied Physics Letters*, vol. 112, no. 9, 2018.

Bibliography

[82] D. B. Higginbottom, L. Slodička, G. Araneda, L. Lachman, R. Filip, M. Hennrich, and R. Blatt, "Pure single photons from a trapped atom source," *New Journal of Physics*, vol. 18, no. 9, 2016.

[83] M. J. Holmes, K. Choi, S. Kako, M. Arita, and Y. Arakawa, "Room-Temperature Triggered Single Photon Emission from a III-Nitride Site-Controlled Nanowire Quantum Dot," *Nano Letters*, vol. 14, no. 2, pp. 982–986, 2014.

[84] K. J. Vahala, "Optical microcavities," *Nature*, vol. 424, p. 829, 2003.

[85] E. M. Purcell, H. C. Torrey, and R. V. Pound, "Resonance Absorption by Nuclear Magnetic Moments in a Solid," *Phys. Rev.*, vol. 69, pp. 37–38, 1946.

[86] F. Liu, A. J. Brash, J. O'Hara, L. M. Martins, C. L. Phillips, R. J. Coles, B. Royall, E. Clarke, C. Bentham, N. Prtljaga, I. E. Itskevich, L. R. Wilson, M. S. Skolnick, and A. M. Fox, "High Purcell factor generation of indistinguishable on-chip single photons," *Nature Nanotechnology*, vol. 13, pp. 835–840, 2018.

[87] H. S. Nguyen, G. Sallen, C. Voisin, P. Roussignol, C. Diederichs, and G. Cassabois, "Ultracoherent single photon source," *Applied Physics Letters*, vol. 99, no. 26, p. 261904, 2011.

[88] M. H. Kolodrubetz and J. R. Petta, "Coherent holes in a semiconductor quantum dot," *Science*, vol. 325, no. 5936, pp. 42–43, 2009.

[89] K. A. Dick, J. Bolinsson, B. M. Borg, and J. Johansson, "Controlling the Abruptness of Axial Heterojunctions in III–V Nanowires: Beyond the Reservoir Effect," *Nano Lett.*, vol. 12, no. 6, pp. 3200–3206, 2012.

[90] N. Li, T. Y. Tan, and U. Gösele, "Transition region width of nanowire hetero- and pn-junctions grown using vapor–liquid–solid processes," *Appl. Phys. A*, vol. 90, no. 4, pp. 591–596, 2008.

[91] V. G. Dubrovskii, A. A. Koryakin, and N. V. Sibirev, "Understanding the composition of ternary III-V nanowires and axial nanowire heterostructures in nucleation-limited regime," *Materials and Design*, vol. 132, pp. 400–408, 2017.

[92] J. Claudon, J. Bleuse, N. S. Malik, M. Bazin, P. Jaffrennou, N. Gregersen, C. Sauvan, P. Lalanne, and J. M. Gérard, "A highly efficient single-photon source based on a quantum dot in a photonic nanowire," *Nature Photonics*, vol. 4, no. 3, pp. 174–177, 2010.

[93] E. Uccelli, M. Bichler, S. Nürnberger, G. Abstreiter, and A. F. I Morral, "Controlled synthesis of InAs wires, dot and twin-dot array configurations by cleaved edge overgrowth," *Nanotechnology*, vol. 19, no. 4, 2008.

[94] D. Rudolph, L. Schweickert, S. Morkötter, L. Hanschke, S. Hertenberger, M. Bichler, G. Koblmüller, G. Abstreiter, and J. J. Finley, "Probing the trapping and thermal activation dynamics of excitons at single twin defects in GaAs-AlGaAs core-shell nanowires," *New Journal of Physics*, vol. 15, no. 11, p. 113032, 2013.

[95] L. Mancini, Y. Fontana, S. Conesa-Boj, I. Blum, F. Vurpillot, L. Francaviglia, E. Russo-Averchi, M. Heiss, J. Arbiol, A. Fontcuberta i Morral, and L. Rigutti, "Three-dimensional nanoscale study of Al segregation and quantum dot formation in GaAs/AlGaAs core-shell nanowires," *Applied Physics Letters*, vol. 105, no. 24, p. 243106, 2014.

[96] L. Francaviglia, Y. Fontana, S. Conesa-Boj, G. Tütüncüoglu, L. Duchêne, M. B. Tanasescu, F. Matteini, and A. Fontcuberta i Morral, "Quantum dots in the GaAs/Al$_x$Ga$_{1-x}$As core-shell nanowires: Statistical occurrence as a function of the shell thickness," *Applied Physics Letters*, vol. 107, no. 3, p. 033106, 2015.

[97] L. Francaviglia, Y. Fontana, and A. Fontcuberta i Morral, "Chapter five - quantum dots in nanowires," in *Semiconductor Nanowires II: Properties and Applications* (S. A. Dayeh, A. F. i Morral, and C. Jagadish, eds.), vol. 94 of *Semiconductors and Semimetals*, pp. 159 – 184, Elsevier, 2016.

[98] C. Zheng, J. Wong-Leung, Q. Gao, H. H. Tan, C. Jagadish, and J. Etheridge, "Polarity-Driven 3-Fold Symmetry of GaAs/AlGaAs Core Multishell Nanowires," *Nano Lett.*, vol. 13, pp. 3742–3748, 2013.

[99] M. López and Y. Nomura, "Surface diffusion length of Ga adatoms in molecular-beam epitaxy on GaAs(100)–(110) facet structures," *Journal of Crystal Growth*, vol. 150, no. 110, pp. 68–72, 1995.

[100] S. Koshiba, Y. Nakamura, M. Tsuchiya, H. Noge, H. Kano, Y. Nagamune, T. Noda, and H. Sakaki, "Surface diffusion processes in molecular beam epitaxial growth of GaAs and AlAs as studied on GaAs (001)-(111)B facet structures," *Journal of Applied Physics*, vol. 76, no. 7, pp. 4138–4144, 1994.

[101] G. Biasiol and E. Kapon, "Mechanisms of Self-ordering of Quantum Nanostructures Grown on Nonplanar Surfaces," *Phys. Rev. Lett.*, vol. 81, pp. 2962–2965, 1998.

[102] N. Jeon, B. Loitsch, S. Morkoetter, G. Abstreiter, J. Finley, H. J. Krenner, K. G., and L. J. Lauhon, "Alloy Fluctuations Act as Quantum Dot-like Emitters in GaAs-AlGaAs Core–Shell Nanowires," *ACS Nano*, vol. 9, no. 8, pp. 8335–8343, 2015.

[103] P. M. Petroff, A. Y. Cho, F. K. Reinhart, A. C. Gossard, and W. Wiegmann, "Alloy Clustering in Ga$_{1-x}$Al$_x$As Compound Semiconductors Grown by Molecular Beam Epitaxy," *Physical Review Letters*, vol. 48, no. 3, pp. 170–173, 1982.

[104] T. Kuan, T. Kuech, W. Wang, and E. Wilkie, "Long-Range Order in Al$_x$Ga$_{1-x}$As," *Physical Review Letters*, vol. 54, no. 3, pp. 201–204, 1985.

[105] G. Bulgarini, M. E. Reimer, M. Hocevar, E. P. A. M. Bakkers, L. P. Kouwenhoven, and V. Zwiller, "Avalanche amplification of a single exciton in a semiconductor nanowire," *Nat. Photon.*, vol. 6, no. 7, pp. 455–458, 2012.

Bibliography

[106] C. Thelander, T. Mårtensson, M. T. Björk, B. J. Ohlsson, M. W. Larsson, L. R. Wallenberg, and L. Samuelson, "Single-electron transistors in heterostructure nanowires," *Appl. Phys. Lett.*, vol. 83, no. 10, pp. 2052–2054, 2003.

[107] C. Sun, M. T. Wade, Y. Lee, J. S. Orcutt, L. Alloatti, M. S. Georgas, A. S. Waterman, J. M. Shainline, R. R. Avizienis, S. Lin, B. R. Moss, R. Kumar, F. Pavanello, A. H. Atabaki, H. M. Cook, A. J. Ou, J. C. Leu, Y. H. Chen, K. Asanović, R. J. Ram, M. A. Popović, and V. M. Stojanović, "Single-chip microprocessor that communicates directly using light," *Nature*, vol. 528, no. 7583, pp. 534–538, 2015.

[108] J. Bleuse, J. Claudon, M. Creasey, N. S. Malik, J.-M. Gérard, I. Maksymov, J.-P. Hugonin, and P. Lalanne, "Inhibition, Enhancement, and Control of Spontaneous Emission in Photonic Nanowires," *Phys. Rev. Lett.*, vol. 106, p. 103601, mar 2011.

[109] M. Munsch, N. S. Malik, E. Dupuy, A. Delga, J. Bleuse, J. M. Gérard, J. Claudon, N. Gregersen, and J. Mørk, "Dielectric GaAs antenna ensuring an efficient broadband coupling between an inas quantum dot and a gaussian optical beam," *Physical Review Letters*, vol. 110, no. 17, pp. 1–5, 2013.

[110] G. Bulgarini, M. E. Reimer, M. Bouwes Bavinck, K. D. Jöns, D. Dalacu, P. J. Poole, E. P. A. M. Bakkers, and V. Zwiller, "Nanowire waveguides launching single photons in a Gaussian mode for ideal fiber coupling," *Nano Letters*, vol. 14, no. 7, pp. 4102–4106, 2014.

[111] G. Grzela, R. Paniagua-Domínguez, T. Barten, Y. Fontana, J. A. Sánchez-Gil, and J. Gómez Rivas, "Nanowire antenna emission," *Nano Letters*, vol. 12, no. 11, pp. 5481–5486, 2012.

[112] M. Munsch, J. Claudon, J. Bleuse, N. S. Malik, E. Dupuy, J.-M. Gérard, Y. Chen, N. Gregersen, and J. Mørk, "Linearly Polarized, Single-Mode Spontaneous Emission in a Photonic Nanowire," *Phys. Rev. Lett.*, vol. 108, no. 7, p. 77405, 2012.

[113] A. P. Foster, J. P. Bradley, K. Gardner, A. B. Krysa, B. Royall, M. S. Skolnick, and L. R. Wilson, "Linearly Polarized Emission from an Embedded Quantum Dot Using Nanowire Morphology Control," *Nano Lett.*, vol. 15, no. 3, pp. 1559–1563, 2015.

[114] T. Stettner, T. Kostenbader, D. Ruhstorfer, J. Bissinger, H. Riedl, M. Kaniber, G. Koblmüller, and J. J. Finley, "Direct Coupling of Coherent Emission from Site-Selectively Grown III-V Nanowire Lasers into Proximal Silicon Waveguides," *ACS Photonics*, vol. 4, no. 10, pp. 2537–2543, 2017.

[115] D. C. Watson, R. V. Martinez, Y. Fontana, E. Russo-Averchi, M. Heiss, A. Fontcuberta i Morral, G. M. Whitesides, and M. Lončar, "Nanoskiving Core–Shell Nanowires: A New Fabrication Method for Nano-optics," *Nano Lett.*, vol. 14, pp. 524–531, 2014.

[116] N. Rossi, F. R. Braakman, D. Cadeddu, D. Vasyukov, G. Tütüncüoglu, A. Fontcuberta i Morral, and M. Poggio, "Vectorial scanning force microscopy using a nanowire sensor," *Nature Nanotechnology*, vol. 12, no. 2, pp. 150–155, 2017.

[117] D. Tumanov, N. Vaish, H. A. Nguyen, Y. Curé, J. M. Gérard, J. Claudon, F. Donatini, and J. P. Poizat, "Static strain tuning of quantum dots embedded in a photonic wire," *Applied Physics Letters*, vol. 112, no. 12, 2018.

[118] M. Montinaro, G. Wüst, M. Munsch, Y. Fontana, E. Russo-Averchi, M. Heiss, A. Fontcuberta i Morral, R. J. Warburton, and M. Poggio, "Quantum Dot Opto-Mechanics in a Fully Self-Assembled Nanowire," *Nano Lett.*, vol. 14, no. 8, pp. 4454–4460, 2014.

[119] J. P. Garayt, J. M. Gérard, F. Enjalbert, L. Ferlazzo, S. Founta, E. Martinez-Guerrero, F. Rol, D. Araujo, R. Cox, B. Daudin, B. Gayral, L. Si Dang, and H. Mariette, "Study of isolated cubic GaN quantum dots by low-temperature cathodoluminescence," *Physica E: Low-Dimensional Systems and Nanostructures*, vol. 26, no. 1-4, pp. 203–206, 2005.

[120] T. Grange, N. Somaschi, C. Antón, L. De Santis, G. Coppola, V. Giesz, A. Lemaître, I. Sagnes, A. Auffèves, and P. Senellart, "Reducing Phonon-Induced Decoherence in Solid-State Single-Photon Sources with Cavity Quantum Electrodynamics," *Physical Review Letters*, vol. 118, no. 25, pp. 1–6, 2017.

[121] M. E. Reimer, G. Bulgarini, A. Fognini, R. W. Heeres, B. J. Witek, M. A. Versteegh, A. Rubino, T. Braun, M. Kamp, S. Höfling, D. Dalacu, J. Lapointe, P. J. Poole, and V. Zwiller, "Overcoming power broadening of the quantum dot emission in a pure wurtzite nanowire," *Physical Review B*, vol. 93, no. 19, pp. 1–9, 2016.

[122] J. Bao, D. C. Bell, F. Capasso, J. B. Wagner, T. Mårtensson, J. Trägårdh, L. Samuelson, J. Bao, D. C. Bell, F. Capasso, J. B. Wagner, T. Mårtensson, J. Trägårdh, and L. Samuelson, "Optical Properties of Rotationally Twinned Nanowire Superlattices," *Nano Letters*, vol. 8, pp. 836–841, 2008.

[123] M. A. Versteegh, M. E. Reimer, K. D. Jöns, D. Dalacu, P. J. Poole, A. Gulinatti, A. Giudice, and V. Zwiller, "Observation of strongly entangled photon pairs from a nanowire quantum dot," *Nature Communications*, vol. 5, 2014.

[124] K. D. Jöns, L. Schweickert, M. A. Versteegh, D. Dalacu, P. J. Poole, A. Gulinatti, A. Giudice, V. Zwiller, and M. E. Reimer, "Bright nanoscale source of deterministic entangled photon pairs violating Bell's inequality," *Scientific Reports*, vol. 7, no. 1700, pp. 1–11, 2017.

[125] Y. Fontana, P. Corfdir, B. Van Hattem, E. Russo-Averchi, M. Heiss, S. Sonderegger, C. Magen, J. Arbiol, R. T. Phillips, and A. Fontcuberta i Morral, "Exciton footprint of self-assembled AlGaAs quantum dots in core-shell nanowires," *Phys. Rev. B*, vol. 90, no. 7, p. 75307, 2014.

[126] M. Abbarchi, F. Troiani, C. Mastrandrea, G. Goldoni, T. Kuroda, T. Mano, K. Sakoda, N. Koguchi, S. Sanguinetti, A. Vinattieri, and M. Gurioli, "Spectral diffusion and line broadening in single self-assembled GaAs-AlGaAs quantum dot photoluminescence," *Applied Physics Letters*, vol. 93, no. 16, p. 162101, 2008.

Bibliography

[127] P. Corfdir, Y. Fontana, B. Van Hattem, E. Russo-Averchi, M. Heiss, A. Fontcuberta i Morral, and R. T. Phillips, "Tuning the g-factor of neutral and charged excitons confined to self-assembled (Al,Ga)As shell quantum dots," *Applied Physics Letters*, vol. 105, no. 22, p. 223111, 2014.

[128] B. D. Gerardot, S. Seidl, P. A. Dalgarno, R. J. Warburton, D. Granados, J. M. Garcia, K. Kowalik, O. Krebs, K. Karrai, A. Badolato, and P. M. Petroff, "Manipulating exciton fine structure in quantum dots with a lateral electric field," *Applied Physics Letters*, vol. 90, no. 4, pp. 1–4, 2007.

[129] N. Akopian, U. Perinetti, L. Wang, A. Rastelli, O. G. Schmidt, and V. Zwiller, "Tuning single GaAs quantum dots in resonance with a rubidium vapor," *Applied Physics Letters*, vol. 97, no. 8, 2010.

[130] Y. Varshni, "Temperature dependence of the energy gap in semiconductors," *Physica*, vol. 34, no. 1, pp. 149–154, 1967.

[131] G. Signorello, *Uniaxial Stress Effects in Zincblende and Wurtzite GaAs Nanowires: an Optical Spectroscopy Study.* PhD thesis, University of Basel, 2014.

[132] S. Adachi, "GaAs, AlAs, and $Al_xGa_{1-x}As$," *Journal of Applied Physics*, vol. 58, no. 3, 1985.

[133] D. Strauch and D. B, "Phonon dispersion in GaAs," *J. Phys.: Condens. Matter*, vol. 2, pp. 1457–1474, 1990.

[134] L. Francaviglia, A. Giunto, W. Kim, P. Romero-Gomez, J. Vukajlovic-Plestina, M. Friedl, H. Potts, L. Güniat, G. Tütüncüoglu, and A. Fontcuberta i Morral, "Anisotropic-Strain-Induced Band Gap Engineering in Nanowire-Based Quantum Dots," *Nano Letters*, vol. 18, no. 4, pp. 2393–2401, 2018.

[135] F. Amaduzzi, E. Alarcón-Lladó, H. Hautmann, R. Tanta, F. Matteini, G. Tütüncüoglu, T. Vosch, J. Nygård, T. Jespersen, E. Uccelli, and A. Fontcuberta i Morral, "Tuning the response of non-allowed Raman modes in GaAs nanowires," *Journal of Physics D: Applied Physics*, vol. 49, no. 9, 2016.

[136] A. K. Arora, M. Rajalakshmi, T. R. Ravindran, and V. Sivasubramanian, "Raman spectroscopy of optical phonon confinement in nanostructured materials," *Journal of Raman Spectroscopy*, vol. 38, no. 6, pp. 604–617, 2007.

[137] J. F. Nye, *Physical Properties of Cristals: Their Representation by Tensors and Matrices.* University Press Oxford, 1985.

[138] C. K. Williams, T. H. Glisson, J. R. Hauser, and M. A. Littlejohn, "Energy bandgap and lattice constant contours of III-V quaternary alloys of the form $A_xB_yC_zD$ or $AB_xC_yD_z$," *Journal of Electronic Materials*, vol. 7, no. 5, pp. 639–646, 1978.

[139] A. Denton and N. W. Ashcroft, "Vegard's law," *Physical Review A*, vol. 43, no. 6, pp. 3161–3164, 1991.

[140] I. Vurgaftman, J. R. Meyer, and L. R. Ram-Mohan, "Band parameters for III-V compound semiconductors and their alloys," *Journal of Applied Physics*, vol. 89, no. 11 I, pp. 5815–5875, 2001.

[141] T. H. Glisson, J. R. Hauser, M. A. Littlejohn, and C. K. Williams, "Energy bandgap and lattice constant contours of II-VI quaternary alloys," *Journal of Electronic Materials*, vol. 7, no. 1, pp. 1–16, 1978.

[142] J. A. Van Vechten and T. K. Bergstresser, "Electronic structures of semiconductor alloys," *Physical Review B*, vol. 1, no. 8, pp. 3351–3358, 1970.

[143] E. H. Li, "Material parameters of InGaAsP and InAlGaAs systems for use in quantum well structures at low and room temperatures," *Physica E: Low-Dimensional Systems and Nanostructures*, vol. 5, no. 4, pp. 215–273, 2000.

[144] H.-J. Briegel, W. Dür, J. I. Cirac, and P. Zoller, "Quantum Repeaters: The Role of Imperfect Local Operations in Quantum Communication," *Phys. Rev. Lett.*, vol. 81, no. 26, pp. 5932–5935, 1998.

[145] R. M. Camacho, M. V. Pack, J. C. Howell, A. Schweinsberg, and R. W. Boyd, "Wide-Bandwidth, Tunable, Multiple-Pulse-Width Optical Delays Using Slow Light in Cesium Vapor," *Phys. Rev. Lett.*, vol. 98, no. 15, p. 153601, 2007.

[146] N. Akopian, L. Wang, A. Rastelli, O. G. Schmidt, and V. Zwiller, "Hybrid semiconductor-atomic interface: slowing down single photons from a quantum dot," *Nature Photon.*, vol. 5, no. 4, pp. 230–233, 2011.

[147] C. Liu, Z. Dutton, C. H. Behroozi, and L. V. Hau, "Observation of coherent optical information storage in an atomic medium using halted light pulses," *Nature*, vol. 409, no. 6819, pp. 490–493, 2001.

[148] H. P. Komsa and A. Pasquarello, "Dangling bond charge transition levels in AlAs, GaAs, and InAs," *Applied Physics Letters*, vol. 97, no. 19, pp. 95–98, 2010.

[149] W. Bao, M. Staffaroni, J. Bokor, M. B. Salmeron, E. Yablonovitch, S. Cabrini, A. Weber-Bargioni, and P. J. Schuck, "Plasmonic near-field probes: a comparison of the campanile geometry with other sharp tips," *Optics Express*, vol. 21, no. 7, p. 8166, 2013.

[150] L. M. Otto, D. F. Ogletree, S. Aloni, M. Staffaroni, B. C. Stipe, and A. T. Hammack, "Visualizing the bidirectional optical transfer function for near-field enhancement in waveguide coupled plasmonic transducers," *Scientific Reports*, vol. 8, no. 1, pp. 1–6, 2018.

[151] B. G. Yacobi and D. B. Holt, *Cathodoluminescence Microscopy of Inorganic Solids*. Springer New York, 1990.

[152] H. Demers, N. Poirier-Demers, A. R. Couture, D. Joly, M. Guilmain, N. de Jonge, and D. Drouin, "Three-dimensional electron microscopy simulation with the CASINO Monte Carlo software," *Scanning*, vol. 33, no. 3, pp. 135–146, 2011.

Bibliography

[153] L. Samuelson and A. Gustafsson, "Imaging and spectroscopic studies of individual impurities in quantum structures," *Physical Review Letters*, vol. 74, no. 12, pp. 2395–2398, 1995.

[154] A. Gustafsson, J. Bolinsson, N. Sköld, and L. Samuelson, "Determination of diffusion lengths in nanowires using cathodoluminescence," *Applied Physics Letters*, vol. 97, no. 7, p. 072114, 2010.

[155] T. E. Everhart and P. H. Hoff, "Determination of kilovolt electron energy dissipation vs penetration distance in solid materials," *Journal of Applied Physics*, vol. 42, no. 13, pp. 5837–5846, 1971.

[156] B. Prévot and J. Wagner, "Raman characterization of semiconducting materials," *Prog. Crystal Growth and Charact.*, vol. 22, pp. 245–319, 1991.

[157] P. Y. Yu and M. Cardona, *Fundamentals of semiconductors : physics and materials properties.* Springer Berlin, 2010.

[158] I. Zardo, S. Conesa-Boj, F. Peiro, J. R. Morante, J. Arbiol, E. Uccelli, G. Abstreiter, and A. Fontcuberta i Morral, "Raman spectroscopy of wurtzite and zinc-blende GaAs nanowires: Polarization dependence, selection rules, and strain effects," *Physical Review B - Condensed Matter and Materials Physics*, vol. 80, no. 24, pp. 1–11, 2009.

[159] I. Zardo, S. Yazji, C. Marini, E. Uccelli, A. Fontcuberta i Morral, G. Abstreiter, and P. Postorino, "Pressure tuning of the optical properties of GaAs nanowires," *ACS Nano*, vol. 6, no. 4, pp. 3284–3291, 2012.

[160] D. B. Williams and C. B. Carter, *The Transmission Electron Microscope.* Springer US, 1996.

[161] Z. L. Wang, "Transmission Electron Microscopy of Shape-Controlled Nanocrystals and Their Assemblies," *The Journal of Physical Chemistry B*, vol. 104, no. 6, pp. 1153–1175, 2000.

[162] B. Fultz and J. Howe, *Transmission Electron Microscopy and Diffractometry of Materials.* Springer-Verlag Berlin Heidelberg, 2013.

[163] N. Sköld, J. B. Wagner, G. Karlsson, T. Hernán, W. Seifert, M.-E. Pistol, and L. Samuelson, "Phase Segregation in AlInP Shells on GaAs Nanowires," *Nano Lett.*, vol. 6, no. 12, pp. 2743–2747, 2006.

[164] K. A. Dick, C. Thelander, L. Samuelson, and P. Caroff, "Crystal phase engineering in single InAs nanowires," *Nano Letters*, vol. 10, no. 9, pp. 3494–3499, 2010.

[165] K. Kawaguchi, M. Heurlin, D. Lindgren, M. T. Borgstrm, M. Ek, and L. Samuelson, "InAs quantum dots and quantum wells grown on stacking-fault controlled InP nanowires with wurtzite crystal structure," *Applied Physics Letters*, vol. 99, no. 13, pp. 97–100, 2011.

[166] J. Wallentin, M. E. Messing, E. Trygg, L. Samuelson, K. Deppert, and M. T. Borgström, "Growth of doped InAsyP1-ynanowires with InP shells," *Journal of Crystal Growth*, vol. 331, no. 1, pp. 8–14, 2011.

[167] T. Xu, K. A. Dick, S. Plissard, T. H. Nguyen, Y. Makoudi, M. Berthe, J. P. Nys, X. Wallart, B. Grandidier, and P. Caroff, "Faceting, composition and crystal phase evolution in IIIV antimonide nanowire heterostructures revealed by combining microscopy techniques," *Nanotechnology*, vol. 23, no. 9, 2012.

[168] T. Rieger, M. Luysberg, T. Schäpers, D. Grützmacher, and M. I. Lepsa, "Molecular beam epitaxy growth of GaAs/InAs core-shell nanowires and fabrication of InAs nanotubes," *Nano Letters*, vol. 12, no. 11, pp. 5559–5564, 2012.

[169] M. Hjort, P. Kratzer, S. Lehmann, S. J. Patel, K. A. Dick, C. J. Palmstrøm, R. Timm, and A. Mikkelsen, "Crystal Structure Induced Preferential Surface Alloying of Sb on Wurtzite/Zinc Blende GaAs Nanowires," *Nano Letters*, vol. 17, no. 6, pp. 3634–3640, 2017.

[170] M. Zamani, G. Tütüncüoglu, S. Martí-Sánchez, L. Francaviglia, L. Güniat, L. Ghisalberti, H. Potts, M. Friedl, E. Markov, W. Kim, J.-B. Leran, V. G. Dubrovskii, J. Arbiol, and A. Fontcuberta i Morral, "Optimizing the yield of A-polar GaAs nanowires to achieve defect-free zinc blende structure and enhanced optical functionality," *Nanoscale*, 2018.

[171] M. E. Reimer, M. P. van Kouwen, M. Barkelid, M. Hocevar, M. H. M. van Weert, R. E. Algra, E. P. A. M. Bakkers, M. T. Björk, H. Schmid, H. Riel, L. P. Kouwenhoven, and V. Zwiller, "Single photon emission and detection at the nanoscale utilizing semiconductor nanowires," *J. Nanophoton.*, vol. 5, no. 1, pp. 53502–53512, 2011.

[172] T. Bryllert, L. E. Wernersson, L. E. Fröberg, and L. Samuelson, "Vertical high-mobility wrap-gated InAs nanowire transistor," *IEEE Electron Device Letters*, vol. 27, no. 5, pp. 323–325, 2006.

[173] C. Thelander, P. Agarwal, S. Brongersma, J. Eymery, L. F. Feiner, A. Forchel, M. Scheffler, W. Riess, B. J. Ohlsson, U. Gösele, and L. Samuelson, "Nanowire-based one-dimensional electronics," *Materials Today*, vol. 9, no. 10, pp. 28–35, 2006.

[174] J. P. Colinge, C. W. Lee, A. Afzalian, N. D. Akhavan, R. Yan, I. Ferain, P. Razavi, B. O'Neill, A. Blake, M. White, A. M. Kelleher, B. McCarthy, and R. Murphy, "Nanowire transistors without junctions," *Nature Nanotechnology*, vol. 5, no. 3, pp. 225–229, 2010.

[175] V. Mourik, K. Zuo, S. M. Frolov, S. R. Plissard, E. P. a. M. Bakkers, and L. P. Kouwenhoven, "Signatures of Majorana Fermions in," *Science*, vol. 336, no. 6084, p. 1003, 2012.

[176] R. M. Lutchyn, E. P. Bakkers, L. P. Kouwenhoven, P. Krogstrup, C. M. Marcus, and Y. Oreg, "Majorana zero modes in superconductor-semiconductor heterostructures," *Nature Reviews Materials*, vol. 3, no. 5, pp. 52–68, 2018.

Bibliography

[177] A. Fontcuberta i Morral, J. Arbiol, J. D. Prades, A. Cirera, and J. R. Morante, "Synthesis of silicon nanowires with wurtzite crystalline structure by using standard chemical vapor deposition," *Advanced Materials*, vol. 19, no. 10, pp. 1347–1351, 2007.

[178] F. J. Lopez, E. R. Hemesath, and L. J. Lauhon, "Ordered stacking fault arrays in silicon nanowires," *Nano Letters*, vol. 9, no. 7, pp. 2774–2779, 2009.

[179] D. Spirkoska, J. Arbiol, A. Gustafsson, S. Conesa-Boj, F. Glas, I. Zardo, M. Heigoldt, M. H. Gass, A. L. Bleloch, S. Estrade, M. Kaniber, J. Rossler, F. Peiro, J. R. Morante, G. Abstreiter, L. Samuelson, and A. Fontcuberta i Morral, "Structural and optical properties of high quality zinc-blende/wurtzite GaAs nanowire heterostructures," *Physical Review B*, vol. 80, no. 24, pp. 1–9, 2009.

[180] M. Hjort, S. Lehmann, J. Knutsson, R. Timm, D. Jacobsson, E. Lundgren, K. A. Dick, and A. Mikkelsen, "Direct imaging of atomic scale structure and electronic properties of GaAs wurtzite and zinc blende nanowire surfaces," *Nano Letters*, vol. 13, no. 9, pp. 4492–4498, 2013.

[181] I. Geijselaers, S. Lehmann, K. A. Dick, and M. Pistol, "Radial band bending at wurtzite–zincblende GaAs interfaces," *Nano Futures*, vol. 2, no. 3, 2018.

[182] C. Thelander, P. Caroff, S. Plissard, A. W. Dey, and K. A. Dick, "Effects of Crystal Phase Mixing on the Electrical Properties of InAs Nanowires," *Nano Lett.*, vol. 11, no. 6, pp. 2424–2429, 2011.

[183] M. Heigoldt, J. Arbiol, D. Spirkoska, J. M. Rebled, S. Conesa-Boj, G. Abstreiter, F. Peiró, J. R. Morante, and A. i Morral, "Long range epitaxial growth of prismatic heterostructures on the facets of catalyst-free GaAs nanowires," *J. Mater. Chem.*, vol. 19, no. 7, pp. 840–848, 2009.

[184] A. Trellakis, T. Zibold, T. Andlauer, S. Birner, R. K. Smith, R. Morschl, and P. Vogl, "The 3D nanometer device project nextnano: Concepts, methods, results," *Journal of Computational Electronics*, vol. 5, no. 4, pp. 285–289, 2006.

[185] S. Birner, T. Zibold, T. Andlauer, T. Kubis, M. Sabathil, A. Trellakis, and P. Vogl, "nextnano : General Purpose 3-D Simulations," *IEEE TRANSACTIONS ON ELECTRON DEVICES*, vol. 54, no. 9, pp. 2137–2142, 2007.

[186] S. Funk, A. Li, D. Ercolani, M. Gemmi, L. Sorba, and I. Zardo, "Crystal phase induced bandgap modifications in AlAs nanowires probed by resonant raman spectroscopy," *ACS Nano*, vol. 7, no. 2, pp. 1400–1407, 2013.

[187] C. Y. Yeh, S. H. Wei, and A. Zunger, "Relationships between the band gaps of the zinc-blende and wurtzite modifications of semiconductors," *Physical Review B*, vol. 50, no. 4, pp. 2715–2718, 1994.

[188] B. G. Yacobi and D. B. Holt, "Cathodoluminescence scanning electron microscopy of semiconductors," *Journal of Applied Physics*, vol. 59, no. 4, pp. R1–R24, 1986.

[189] N. Kumar Balla, C. Rendón-Barraza, L. M. Hoang, P. Karpinski, E. Bermúdez-Ureña, and S. Brasselet, "Polarized Nonlinear Nanoscopy of Metal Nanostructures," *ACS Photonics*, vol. 4, no. 2, pp. 292–301, 2017.

[190] J. L. Birman, "Simplified LCAO method for zincblende, wurtzite, and mixed crystal structures," *Physical Review*, vol. 115, no. 6, pp. 1493–1505, 1959.

[191] C. Chen, S. Shehata, C. Fradin, R. LaPierre, C. Couteau, and G. Weihs, "Self-directed growth of AlGaAs core-shell nanowires for visible light applications," *Nano Letters*, vol. 7, no. 9, pp. 2584–2589, 2007.

[192] D. Rudolph, L. Schweickert, S. Morkötter, L. Hanschke, S. Hertenberger, M. Bichler, G. Koblmüller, G. Abstreiter, and J. J. Finley, "Probing the trapping and thermal activation dynamics of excitons at single twin defects in GaAs-AlGaAs core-shell nanowires," *New Journal of Physics*, vol. 15, 2013.

[193] S. Conesa-Boj, H. I. Hauge, M. A. Verheijen, S. Assali, A. Li, E. P. Bakkers, and A. Fontcuberta i Morral, "Cracking the Si shell growth in hexagonal GaP-Si core-shell nanowires," *Nano Letters*, vol. 15, no. 5, pp. 2974–2979, 2015.

[194] P. Caroff, K. A. Dick, J. Johansson, M. E. Messing, K. Deppert, and L. Samuelson, "Controlled polytypic and twin-plane superlattices in III-V nanowires," *Nature Nanotechnology*, vol. 4, no. 1, pp. 50–55, 2009.

[195] V. Pankoke, P. Kratzer, and S. Sakong, "Calculation of the diameter-dependent polytypism in GaAs nanowires from an atomic motif expansion of the formation energy," *Physical Review B - Condensed Matter and Materials Physics*, vol. 84, no. 7, pp. 1–8, 2011.

[196] M. Rosini and R. Magri, "Surface Effects on the Atomic and Electronic Structure of Unpassivated GaAs Nanowires," *Acs Nano*, vol. 4, no. 10, pp. 6021–6031, 2010.

[197] A. Chomette, B. Deveaud, A. Regreny, and G. Bastard, "Observation of Carrier Localization in Intentionally Disordered GaAs/GaAlAs Superlattices," *Phys. Rev. Lett.*, vol. 57, pp. 1464–1467, 1986.

[198] X. Yuan, P. Caroff, J. Wong-Leung, L. Fu, H. H. Tan, and C. Jagadish, "Tunable Polarity in a III-V Nanowire by Droplet Wetting and Surface Energy Engineering," *Advanced Materials*, vol. 27, no. 40, pp. 6096–6103, 2015.

[199] P. Pfeffer, I. Gorczyca, and W. Zawadzki, "Theory of free-electron optical absorption in n-GaAs," *Solid State Communications*, vol. 51, no. 3, pp. 179–183, 1984.

[200] G. Signorello, E. Lörtscher, P. A. Khomyakov, S. Karg, D. L. Dheeraj, B. Gotsmann, H. Weman, and H. Riel, "Inducing a direct-to-pseudodirect bandgap transition in wurtzite GaAs nanowires with uniaxial stress," *Nature Communications*, vol. 5, no. 7491, 2014.

Bibliography

[201] P. Stepanov, M. Elzo-Aizarna, J. Bleuse, N. S. Malik, Y. Curé, E. Gautier, V. Favre-Nicolin, J.-M. Gérard, and J. Claudon, "Large and Uniform Optical Emission Shifts in Quantum Dots Strained along Their Growth Axis," *Nano Letters*, vol. 16, no. 5, pp. 3215–3220, 2016.

[202] M. Bouwes Bavinck, M. Zieliński, B. J. Witek, T. Zehender, E. P. A. M. Bakkers, and V. Zwiller, "Controlling a Nanowire Quantum Dot Band Gap Using a Straining Dielectric Envelope," *Nano Letters*, vol. 12, no. 12, pp. 6206–6211, 2012.

[203] F. Jansen, M. A. Machonkin, N. Palmieri, and D. Kuhman, "Thermomechanical properties of amorphous silicon and nonstoichiometric silicon oxide films," *J. Appl. Phys.*, vol. 62, no. 12, pp. 4732–4736, 1987.

[204] H. Tada, A. E. Kumpel, R. E. Lathrop, J. B. Slanina, P. Nieva, P. Zavracky, I. N. Miaoulis, and P. Y. Wong, "Thermal expansion coefficient of polycrystalline silicon and silicon dioxide thin films at high temperatures," *Journal of Applied Physics*, vol. 87, no. 9, pp. 4189–4193, 2000.

[205] M. E. Straumanis, J. P. Krumme, and M. Rubenstein, "Thermal Expansion Coefficients and Lattice Parameters between 10° and 65°C in the System GaP-GaAs," *Journal of The Electrochemical Society*, vol. 114, no. 6, pp. 640–641, 1967.

[206] M. Ettenberg and R. J. Paff, "Thermal expansion of AlAs," *Journal of Applied Physics*, vol. 41, no. 10, pp. 3926–3927, 1970.

[207] R. Trotta, J. Martín-Sánchez, J. S. Wildmann, G. Piredda, M. Reindl, C. Schimpf, E. Zallo, S. Stroj, J. Edlinger, and A. Rastelli, "Wavelength-tunable sources of entangled photons interfaced with atomic vapours," *Nature Communications*, vol. 7, pp. 1–7, 2016.

[208] J. A. Floro, S. J. Hearne, J. A. Hunter, P. Kotula, E. Chason, S. C. Seel, and C. V. Thompson, "The dynamic competition between stress generation and relaxation mechanisms during coalescence of Volmer-Weber thin films," *Journal of Applied Physics*, vol. 89, no. 9, pp. 4886–4897, 2001.

[209] L. Freund and S. Suresh, *Thin film materials.* Cambridge University Press New York, 2003.

[210] M. E. Messing, J. Wong-Leung, Z. Zanolli, H. J. Joyce, H. H. Tan, Q. Gao, L. R. Wallenberg, J. Johansson, and C. Jagadish, "Growth of straight InAs-on-GaAs nanowire heterostructures," *Nano Letters*, vol. 11, no. 9, pp. 3899–3905, 2011.

[211] M. T. Borgström, V. Zwiller, E. Müller, and A. Imamoglu, "Optically Bright Quantum Dots in Single Nanowires," *Nano Lett.*, vol. 5, pp. 1439–1443, 2005.

[212] D. Van Dam, D. R. Abujetas, R. Paniagua-Domínguez, J. A. Sánchez-Gil, E. P. Bakkers, J. E. Haverkort, and J. Gómez Rivas, "Directional and Polarized Emission from Nanowire Arrays," *Nano Letters*, vol. 15, no. 7, pp. 4557–4563, 2015.

[213] S. Mokkapati, D. Saxena, H. H. Tan, and C. Jagadish, "Optical design of nanowire absorbers for wavelength selective photodetectors," *Scientific Reports*, vol. 5, pp. 1–7, 2015.

[214] R. Yan, D. Gargas, and P. Yang, "Nanowire photonics," *Nat. Photon.*, vol. 3, no. 10, pp. 569–576, 2009.

[215] K. Hennessy, C. Högerle, E. Hu, A. Badolato, and A. Imamoğlu, "Tuning photonic nanocavities by atomic force microscope nano-oxidation," *Applied Physics Letters*, vol. 89, no. 4, pp. 1–4, 2006.

[216] R. Freeman and I. Willner, "Optical molecular sensing with semiconductor quantum dots (QDs)," *Chemical Society Reviews*, vol. 41, no. 10, p. 4067, 2012.

[217] S. Kumar, R. Trotta, E. Zallo, J. D. Plumhof, P. Atkinson, A. Rastelli, and O. G. Schmidt, "Strain-induced tuning of the emission wavelength of high quality GaAs/AlGaAs quantum dots in the spectral range of the 87Rb D2 lines," *Applied Physics Letters*, vol. 99, no. 16, pp. 161113–161118, 2011.

[218] U. Singh and S. Adenwalla, "Spatial mapping of focused surface acoustic waves in the investigation of high frequency strain induced changes," *Nanotechnology*, vol. 26, p. 255707, jun 2015.

[219] E. Uccelli, J. Arbiol, C. Magen, P. Krogstrup, E. Russo-Averchi, M. Heiss, G. Mugny, F. Morier-Genoud, J. NygaÅrd, J. R. Morante, and A. Fontcuberta i Morral, "Three-Dimensional Multiple-Order Twinning of Self-Catalyzed GaAs Nanowires on Si Substrates," *Nano Lett.*, vol. 11, no. 9, pp. 3827–3832, 2011.

[220] B. Welber, M. Cardona, C. K. Kim, and S. Rodriguez, "Dependence of the direct energy gap of GaAs on hydrostatic pressure," *Physical Review B*, vol. 12, no. 12, pp. 5729–5738, 1975.

[221] F. Amaduzzi, E. Alrcon-Llado, E. Russo-Averchi, F. Matteini, M. Heiss, G. Tütüncüoglu, S. Conesa-Boj, M. de la Mata, J. Arbiol, and A. Fontcuberta i Morral, "Probing inhomogeneous composition in core/shell nanowires by Raman spectroscopy," *Journal of Applied Physics*, vol. 116, no. 18, 2014.

[222] D. Rüffer, M. Slot, R. Huber, T. Schwarze, F. Heimbach, G. Tütüncüoglu, F. Matteini, E. Russo-Averchi, A. Kovács, R. Dunin-Borkowski, R. R. Zamani, J. R. Morante, J. Arbiol, A. F. i Morral, and D. Grundler, "Anisotropic magnetoresistance of individual cofeb and ni nanotubes with values of up to 1.4% at room temperature," *APL Materials*, vol. 2, no. 7, p. 076112, 2014.

[223] W. Hutchinson and Z. Suo, *Mixed mode cracking in layered materials*, vol. 29 of *Advances in Applied Mechanics*. Academic Press, 1991.

Bibliography

[224] B. Hua, J. Motohisa, Y. Ding, S. Hara, and T. Fukui, "Characterization of Fabry-Pèrot microcavity modes in GaAs nanowires fabricated by selective-area metal organic vapor phase epitaxy," *Applied Physics Letters*, vol. 91, no. 13, pp. 2–5, 2007.

[225] J. Zhu, Z. Yu, G. F. Burkhard, C.-M. Hsu, S. T. Connor, Y. Xu, Q. Wang, M. McGehee, S. Fan, and Y. Cui, "Optical Absorption Enhancement in Amorphous Silicon Nanowire and Nanocone Arrays," *Nano Letters*, vol. 9, no. 1, pp. 279–282, 2009.

[226] A. Schliwa, M. Winkelnkemper, and D. Bimberg, "Impact of size, shape, and composition on piezoelectric effects and electronic properties of In (Ga) AsGaAs quantum dots," *Physical Review B - Condensed Matter and Materials Physics*, vol. 76, no. 20, pp. 1–17, 2007.

[227] K. D. Jöns, R. Hafenbrak, R. Singh, F. Ding, J. D. Plumhof, A. Rastelli, O. G. Schmidt, G. Bester, and P. Michler, "Dependence of the Redshifted and Blueshifted Photoluminescence Spectra of Single $In_xGa_{1-x}As/GaAs$ Quantum Dots on the Applied Uniaxial Stress," *Phys. Rev. Lett.*, vol. 107, p. 217402, Nov 2011.

[228] C. E. Kuklewicz, R. N. E. Malein, P. M. Petroff, and B. D. Gerardot, "Electro-elastic tuning of single particles in individual self-assembled quantum dots," *Nano Letters*, vol. 12, no. 7, pp. 3761–3765, 2012.

[229] N. Lifshitz, A. Jayaraman, R. Logan, and R. Maines, "Pressure coefficient of the direct band gap of $Al_xGa_{1-x}As$ from optical absorption measurements," *Physical Review B*, vol. 20, no. 6, pp. 2398–2400, 1979.

[230] P. Wickboldt, E. Anastassakis, R. Sauer, and M. Cardona, "Raman phonon piezospectroscopy in GaAs: Infrared measurements," *Physical Review B*, vol. 35, no. 3, pp. 1362–1368, 1987.

[231] F. Cerdeira, C. J. Buchenauer, F. H. Pollak, and M. Cardona, "Stress-induced shifts of first-order Raman frequencies of diamond- and zinc-blende-type semiconductors," *Physical Review B*, vol. 5, no. 2, pp. 580–593, 1972.

[232] K. W. Adu, Q. Xiong, H. R. Gutierrez, G. Chen, and P. C. Eklund, "Raman scattering as a probe of phonon confinement and surface optical modes in semiconducting nanowires," *Applied Physics A: Materials Science and Processing*, vol. 85, no. 3, pp. 287–297, 2006.

[233] R. Gupta, Q. Xiong, G. D. Mahan, and P. C. Eklund, "Surface Optical Phonons in Gallium Phosphide Nanowires," *Nano Letters*, vol. 3, no. 12, pp. 1745–1750, 2003.

[234] R. Krahne, G. Chilla, C. Schüller, L. Carbone, S. Kudera, G. Mannarini, L. Manna, D. Heitmann, and R. Cingolani, "Confinement effects on optical phonons in polar tetrapod nanocrystals detected by resonant inelastic light scattering," *Nano Letters*, vol. 6, no. 3, pp. 478–482, 2006.

[235] D. Spirkoska, G. Abstreiter, and A. Fontcuberta i Morral, "Size and environment dependence of surface phonon modes of gallium arsenide nanowires as measured by Raman spectroscopy," *Nanotechnology*, vol. 19, no. 43, 2008.

[236] A. Tarraf, J. Daleiden, S. Irmer, D. Prasai, and H. Hillmer, "Stress investigation of PECVD dielectric layers for advanced optical MEMS," *Journal of Micromechanics and Microengineering*, vol. 14, no. 3, pp. 317–323, 2004.

[237] R. Timm, H. Eisele, A. Lenz, T. Y. Kim, F. Streicher, K. Pötschke, U. W. Pohl, D. Bimberg, and M. Dähne, "Structure of InAs/GaAs quantum dots grown with Sb surfactant," *Physica E: Low-Dimensional Systems and Nanostructures*, vol. 32, no. 1-2 SPEC. ISS., pp. 25–28, 2006.

[238] K. Onabe, "Unstable regions in III–V quaternary solid solutions composition plane calculated with strictly regular solution approximation," *Japanese Journal of Applied Physics*, vol. 21, no. 6, pp. L323–L325, 1982.

[239] G. B. Stringfellow, "Immiscibility and spinodal decomposition in III/V alloys," *Journal of Crystal Growth*, vol. 65, no. 1-3, pp. 454–462, 1983.

[240] J. W. Matthews and A. E. Blakeslee, "Defects in Epitaxial Multilayers. 1. Misfit Dislocations," *Journal of Crystal Growth*, vol. 27, no. DEC, pp. 118–125, 1974.

[241] M. Leyer, J. Stellmach, C. Meissner, M. Pristovsek, and M. Kneissl, "The critical thickness of InGaN on (0 0 0 1)GaN," *Journal of Crystal Growth*, vol. 310, no. 23, pp. 4913–4915, 2008.

[242] O. Salehzadeh, K. L. Kavanagh, and S. P. Watkins, "Geometric limits of coherent III-V core/shell nanowires," *Journal of Applied Physics*, vol. 114, no. 5, 2013.

[243] S. Raychaudhuri and E. T. Yu, "Calculation of critical dimensions for wurtzite and cubic zinc blende coaxial nanowire heterostructures," *Journal of Vacuum Science* & *Technology B: Microelectronics and Nanometer Structures*, vol. 24, no. 4, p. 2053, 2006.

[244] T. E. Trammell, X. Zhang, Y. Li, L. Q. Chen, and E. C. Dickey, "Equilibrium strain-energy analysis of coherently strained core-shell nanowires," *Journal of Crystal Growth*, vol. 310, no. 12, pp. 3084–3092, 2008.

[245] K. L. Kavanagh, "Misfit dislocations in nanowire heterostructures," *Semiconductor Science and Technology*, vol. 25, no. 2, 2010.

[246] M. De La Mata, C. Magén, P. Caroff, and J. Arbiol, "Atomic scale strain relaxation in axial semiconductor III-V nanowire heterostructures," *Nano Letters*, vol. 14, no. 11, pp. 6614–6620, 2014.

[247] F. Glas, "Critical dimensions for the plastic relaxation of strained axial heterostructures in free-standing nanowires," *Physical Review B - Condensed Matter and Materials Physics*, vol. 74, no. 12, pp. 2–5, 2006.

Bibliography

[248] F. Glas, "Lattice engineering," in *Lattice Engineering* (S. Wang, ed.), ch. 5, pp. 189–228, Taylor and Francis group, 2012.

[249] T. Kuykendall, P. Ulrich, S. Aloni, and P. Yang, "Complete composition tunability of InGaN nanowires using a combinatorial approach," *Nature Materials*, vol. 6, no. 12, pp. 951–956, 2007.

[250] M. De La Mata, R. Leturcq, S. R. Plissard, C. Rolland, C. Magén, J. Arbiol, and P. Caroff, "Twin-Induced InSb Nanosails: A Convenient High Mobility Quantum System," *Nano Letters*, vol. 16, no. 2, pp. 825–833, 2016.

[251] T. V. Hakkarainen, A. Schramm, J. Mäkelä, P. Laukkanen, and M. Guina, "Lithography-free oxide patterns as templates for self-catalyzed growth of highly uniform GaAs nanowires on Si(111)," *Nanotechnology*, vol. 26, no. 27, p. 275301, 2015.

[252] A. Fontcuberta i Morral, D. Spirkoska, J. Arbiol, M. Heigoldt, J. R. Morante, and G. Abstreiter, "Prismatic Quantum Heterostructures Synthesized on Molecular-Beam Epitaxy GaAs Nanowires," *Small*, vol. 4, no. 7, pp. 899–903, 2008.

[253] L. Francaviglia, G. Tütüncüoglu, F. Matteini, and A. Fontcuberta i Morral, "Tuning adatom mobility and nanoscale segregation by twin formation and polytypism," *Nanotechnology*, vol. 30, no. 5, p. 054006, 2019.

[254] P. Trebbia and N. Bonnet, "EELS elemental mapping with unconventional methods I. Theoretical basis: Image analysis with multivariate statistics and entropy concepts," *Ultramicroscopy*, vol. 34, no. 3, pp. 165–178, 1990.

[255] I. Jolliffe, *Principal Component Analysis.* Springer-Verlag New York, 2002.

[256] L. Balaghi, G. Bussone, R. Grifone, R. Hübner, J. Grenzer, and A. Krasheninnikov, "Up to 40 % reduction of the GaAs band gap energy via strain engineering in core / shell nanowires," *arXiv:1803.10873*, 2018.

[257] F. Boxberg, N. Søndergaard, and H. Q. Xu, "Elastic and piezoelectric properties of zincblende and wurtzite crystalline nanowire heterostructures," *Advanced Materials*, vol. 24, no. 34, pp. 4692–4706, 2012.

[258] J. Grönqvist, N. Søndergaard, F. Boxberg, T. Guhr, S. Åberg, and H. Q. Xu, "Strain in semiconductor core-shell nanowires," *Journal of Applied Physics*, vol. 106, no. 5, 2009.

[259] Y. Kim, H. J. Joyce, Q. Gao, H. H. Tan, C. Jagadish, M. Paladugu, J. Zou, and A. A. Suvorova, "Influence of nanowire density on the shape and optical properties of ternary InGaAs nanowires," *Nano Letters*, vol. 6, no. 4, pp. 599–604, 2006.

[260] D. E. Jesson, S. J. Pennycook, J.-M. Baribeau, and D. C. Houghton, "Step-driven lateral segregation and long-range ordering during $Si_x Ge_{1-x}$ epitaxial growth," *Phys. Rev. Lett.*, vol. 68, pp. 2062–2065, 1992.

[261] P. Ballet, J. B. Smathers, and G. J. Salamo, "Morphology of InAs self-organized islands on AlAs surfaces," *Applied Physics Letters*, vol. 75, no. 3, pp. 337–339, 1999.

[262] J. P. Jahn, M. Munsch, L. Béguin, A. V. Kuhlmann, M. Renggli, Y. Huo, F. Ding, R. Trotta, M. Reindl, O. G. Schmidt, A. Rastelli, P. Treutlein, and R. J. Warburton, "An artificial Rb atom in a semiconductor with lifetime-limited linewidth," *Physical Review B - Condensed Matter and Materials Physics*, vol. 92, no. 24, pp. 1–9, 2015.

[263] S. M. Ulrich, S. Weiler, M. Oster, M. Jetter, A. Urvoy, R. Löw, and P. Michler, "Spectroscopy of the D1 transition of cesium by dressed-state resonance fluorescence from a single (In,Ga)As/GaAs quantum dot," *Physical Review B - Condensed Matter and Materials Physics*, vol. 90, no. 12, pp. 1–4, 2014.

[264] M. Friedl, K. Cerveny, P. Weigele, G. Tütüncüoglu, S. Martí-Sánchez, C. Huang, T. Patlatiuk, H. Potts, Z. Sun, M. O. Hill, L. Güniat, W. Kim, M. Zamani, V. G. Dubrovskii, J. Arbiol, L. J. Lauhon, D. M. Zumbühl, and A. Fontcuberta i Morral, "Template-Assisted Scalable Nanowire Networks," *Nano Letters*, vol. 18, no. 4, pp. 2666–2671, 2018.

[265] J. Grecenkov, V. G. Dubrovskii, M. Ghasemi, and J. Johansson, "Quaternary Chemical Potentials for Gold-Catalyzed Growth of Ternary InGaAs Nanowires," *Crystal Growth and Design*, vol. 16, no. 8, pp. 4529–4530, 2016.

[266] E. D. Leshchenko, M. Ghasemi, V. G. Dubrovskii, and J. Johansson, "Nucleation-limited composition of ternary III-V nanowires forming from quaternary gold based liquid alloys," *CrystEngComm*, vol. 20, no. 12, pp. 1649–1655, 2018.

List of publications

1. <u>L. Francaviglia</u>, G. Tütüncüoglu, S. Martí-Sánchez, E. Di Russo, S. Escobar Steinvall, J. Segura Ruiz, H. Potts, M. Friedl, L. Rigutti, J. Arbiol and A. Fontcuberta i Morral, *Segregation scheme of indium in AlGaInAs nanowire shells*, submitted

2. <u>L. Francaviglia</u>, G. Tütüncüoglu, F. Matteini and A. Fontcuberta i Morral, *Tuning adatom mobility and nanoscale segregation by twin formation and polytypism*, Nanotechnology, **30**, 054006 (2019)

3. N. Bologna, S. Wirths, <u>L. Francaviglia</u>, M. Campanini, H. Schmid, V. Theofylaktopoulos, K. E. Moselund, A. Fontcuberta i Morral, R. Erni, H. Riel and M. D. Rossell, *Dopant-induced modifications of $Ga_x In_{(1-x)} P$ nanowire-based p-n junctions monolithically integrated on Si (111)*, ACS Appl. Mater. Interfaces, **10**(38), 32588 (2018)

4. M. Zamani, G. Tütüncüoglu, S. Martí-Sánchez, <u>L. Francaviglia</u>, E. Markov, W. Kim, L. Güniat, L. Ghisalberti, H. Potts, M. Friedl, J.-B. Leran, V. G. Dubrovskii, J. Arbiol and A. Fontcuberta i Morral, *Optimizing the yield of A-polar GaAs nanowires to achieve defect-free zinc blende structure and enhanced optical functionality*, Nanoscale, **10**, 17080 (2018).

5. D. Ramirez, J. I. Uribe, <u>L. Francaviglia</u>, P. Romero-Gomez, A. Fontcuberta i Morral and F. Jaramillo, *Photophysics behind highly luminescent two-dimensional hybrid perovskite $(CH_3 (CH_2)_2 NH_3)_2 (CH_3 NH_3)_2 Pb_3 Br_{10}$ thin films*, J. Mater. Chem. C, **6**, 6216 (2018)

6. <u>L. Francaviglia</u>, A. Giunto, W. Kim, P. Romero Gomez, J. Vukajlovic-Plestina, M. Friedl, H. Potts, L. Güniat, G. Tütüncüoglu and A. Fontcuberta i Morral, *Anisotropic-Strain-Induced Band gap Engineering in Nanowire-Based Quantum Dots*, Nano Lett. **18**, 2393 (2018)

7. W. Kim, V. G. Dubrovskii, J. Vukajlovic-Plestina, G. Tütüncüoglu, <u>L. Francaviglia</u>, L. Güniat, H. Potts, M. Friedl, J.-B. Leran and A. Fontcuberta i Morral, *Bistability of Contact Angle and Its Role in Achieving Quantum-Thin Self-Assisted GaAs nanowires*, Nano Lett. **18**, 49 (2018)

8. J. Vukajlović Pleština, V. Đerek, <u>L. Francaviglia</u>, F. Amaduzzi, H. Potts, M. Ivanda and A. Fontcuberta i Morral, *Nanoporous silicon tubes: the role of geometry in nanostructure*

formation and application to light emitting diodes, J. Phys. D: Appl. Phys. **50**, 265101 (2017)

9. M. Hetzl, J. Winnerl, <u>L. Francaviglia</u>, M. Kraut, M. Döblinger, S. Matich, A. Fontcuberta i Morral and M. Stutzmann, *Surface passivation and self-regulated shell growth in selective area-grown GaN-(Al,Ga)N core-shell nanowires*, Nanoscale, **9**, 7179 (2017)

10. M. Hetzl, M- Kraut, J. Winnerl, <u>L. Francaviglia</u>, M. Döblinger, S. Matich, A. Fontcuberta i Morral and M. Stutzmann, *Strain-induced Band Gap Engineering in Selectively Grown GaN-(Al,Ga)N Core-Shell Nanowire Heterostructures*, Nano Lett. **16**, 7098 (2016)

11. <u>L. Francaviglia</u>, Y. Fontana, S. Conesa-Boj, G. Tütüncüoglu, L. Duchêne, M. B. Tanasescu, F. Matteini and A. Fontcuberta i Morral, *Quantum dots in the GaAs/Al$_x$Ga$_{1-x}$As core-shell nanowires: statistical occurrence as a function of the shell thickness*, Appl. Phys. Lett. **107**, 033106 (2015)

12. <u>L. Francaviglia</u>, Y. Fontana and A. Fontcuberta i Morral, *Quantum dots in Nanowires*, Semiconductors and Semimetals, **94**, 159 (2016)

13. L. Mancini, Y. Fontana, S. Conesa-Boj, I. Blum, F. Vurpillot, <u>L. Francaviglia</u>, E. Russo-Averchi, M. Heiss, J. Arbiol, A. Fontcuberta i Morral and L. Rigutti, *Three-dimensional nanoscale study of Al segregation and quantum dot formation in GaAs/AlGaAs core-shell nanowires*, Appl. Phys. Lett. **105**, 243106 (2014)

Curriculum Vitae

Luca Francaviglia

lucafrancaviglia(at)live.it

Ch. du Bochet, 22	OrcID: 0000-0002-2138-0837
1024 Ecublens	ResearcherID: P-6651-2018
Switzerland	Google Scholar: Luca Francaviglia

Strengths

- Materials scientist specialized in semiconductor nanostructures
- Expert in optical and structural characterization techniques
- Planning and management of research projects, team work and communication skills

Eduacation and research experience

01/2015	*PhD Candidate in Materials Science and Engineering*
01/2019	Mechanisms shifting the emission energy of self-assembled quantum dots in nanowires
	Supervisor: Prof. Anna Fontcuberta i Morral
	École Polytechnique Fédérale de Lausanne EPFL (CH)

01/2014	*Master research project*
10/2014	Analysis of quantum dot formation in (Al)GaAs core-shell nanowires
	Supervisor: Prof. Leonida Miglio and Prof. Anna Fontcuberta i Morral
	École Polytechnique Fédérale de Lausanne EPFL (CH)

10/2012	*Master of Science (MS)*
10/2014	Solid-state physics
	Università degli Studi di Milano-Bicocca (Italy)

12/2009	*Bachelor of Science (BS)*
09/2012	Physics
	Università degli Studi di Milano-Bicocca (Italy)

Institutional responsibilities

01/2015	*Laboratory of Semiconductor Materials (EPFL)*
present	Co-responsible for an Attolight cathodoluminescence microscope (1 Mio CHF)

• Technical and safety (cryogenics) training of EPFL and external users
• Technical and scientific assistance to the users
• Interfacing Attolight and EPFL (operational issues, hardware and software installation)

01/2015	*Laboratory of Semiconductor Materials (EPFL)*
present	PhD student and research assistant

• Peer-reviewed publications: planning and running experiments and simulations, data analysis and interpretation, publication
• Teaching and laboratory assistant
• Planning and supervising projects for Bachelor and Master students
• Collaborations: among others, Martin Stutzmann group (Germany) and Marta D. Rosell group (Switzerland)

Supervision of students

07/2017	*Paula Garcia Moreno* (Universitat de Barcelona): Internship (full time)
09/2017	Exciton diffusion length of GaAs nanowires by cathodoluminescence
08/2016	*Andrea Giunto* (EPFL): Master project and Internship (full time)
01/2017	Bandgap engineering of quantum dots embedded in nanowires
04/2016	*Wonjong Kim* (École Polytechnique Paris): Master thesis (full time)
10/2016	Initial-stage study for high yield of vertical GaAs nanowires on Si substrate
02/2016	*Delphine Petri* (EPFL): Bachelor project (7h/week)
06/2016	Luminescence studies of quantum dots in nanowires
09/2015	*Till Koessler* (EPFL): Master project (10h/week)
01/2016	Cathodoluminescence characterization of quantum dots in nanowires

Teaching activities

2017	*Department of Physics (EPFL)*
	Examiner for the Master Course "Physics of photonic semiconductor devices" (July 2017)
2016 -2017	*Department of Materials Science and engineering (EPFL)*
	Teaching assistant (exercise classes): Functional properties of materials, 2 semesters
2016 -2017	*Department of Materials Science and engineering (EPFL)*
	Teaching assistant (exercise classes): Properties of semiconductors, 2 semesters
2015 -2017	*Civil engineering (EPFL)*
	Laboratory assistant: Shock flexibility test on notched bars (resilience), 3 semesters

Individual scientific reviewing activities

2017 - 2018	Peer-review upon invitation in *Superlattices and Microstructures (Elsevier)* and *ACS Applied Nano Materials*

Organization of conferences

06/2017	*NCCR QSIT Quantum Science and Technology*
	Organization of the QSIT junior meeting (3 days, 38 participants, 17k CHF budget)

Prizes and awards

02/2018	*IQST Science Slam Award at the 662nd WE-Heraeus-Seminar, Physikzentrum Bad Honnef*
09/2014	*Erasmus Placement for internship abroad, Università degli Studi di Milano-Bicocca*
06/2014	*EXTRA grant for Master Thesis abroad, Università degli Studi di Milano-Bicocca*

Personal skills

Materials characterization and fabrication
Cathodoluminescence (CL), photoluminescence (PL), photon-statistics measurements, Raman spectroscopy, scanning and transmission electron microscopy (SEM and TEM), X-ray energy dispersive spectroscopy (XEDS), plasma enhanced chemical vapor deposition (PECVD), molecular beam epitaxy (MBE)

Computer and IT
Nextnano (good knowledge); Matlab, Mathematica, Igor, Origin, Latex, Adobe Illustrator, Blender, MS Office (working knowledge); Python, Fortran, LabView (basic knowledge)

Languages
Italian (mother tongue), English (C2 – CAE certificate June 2008), French (B2/C1), German (A1)

Extracurricular activities

2017 - 2018   *Toastmaster international, UNIL-EPFL club: active member*

Personal information and interests

28 years old, Italian citizen (B permit in Switzerland), driving licenses A and B.
Running, gardening, travelling, beekeeping (active member EPFL association), climbing, swimming.